Fluid structure interaction in bioinspired locomotion problems

by

Gonzalo Arranz Fernández

in partial fulfillment of the requirements for the degree of Doctor in

Programa Interuniversitario en Mecánica de Fluidos

Universidad Carlos III de Madrid

Advisor 1:
Oscar Flores Arias

Advisor 2:
Manuel García-Villalba Navaridas

Tutor:
Oscar Flores Arias

Leganés, March 2021

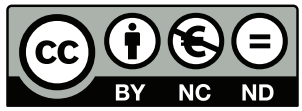

Acknowledgements

This thesis has been carried out in the Bioengineering and Aerospace Engineering Department at Universidad Carlos III de Madrid. The financial support has been provided by the Spanish Ministry of Economy and Competitiveness through grant DPI2016-76151-C2-2-R (AEI/FEDER, UE).

Published and submitted content

The following publications are fully included in Part II of this thesis:

Paper 1
Arranz, G., Flores, O. & García-Villalba, M., 2021. A weakly coupled immersed boundary method and dynamic algorithm for the fluid-structure interaction of multi-body systems, *J. Comput. Phys.*, *Under review.*

Paper 2
Arranz, G., Moriche, M., Uhlmann, M., Flores, O. & García-Villalba, M., 2018. Kinematics and dynamics of the auto-rotation of a model winged seed, *Bioinspir. Biomim.*, **13**(3), 036011. doi: 10.1088/1748-3190/aab144

Paper 3 Arranz, G., Gonzalo, A., Uhlmann, M., Flores, O. & García-Villalba, M., 2018. A numerical study of the flow around a model winged seed in auto-rotation, *Flow Turbul. Combust.*, **101**(2), 477–497. doi: 10.1007/s10494-018-9945-z

Paper 4
Arranz, G., Flores, O. & García-Villalba, M., 2020. Three-dimensional effects on the aerodynamic performance of flapping wings in tandem configuration, *J. Fluids Struct.*, **94**, 102893. doi: 10.1016/j.jfluidstructs.2020.102893

Paper 5
Arranz, G., Flores, O. & García-Villalba, M., 2021. Flow interaction of three-dimensional self-propelled flexible plates in tandem, *J. Fluid Mech.*, *Under review.*

Whenever material from these sources is included in this thesis, it is singled out with typographic means and an explicit reference.

Division of work between authors

Paper 1. The simulations and the analysis were performed by GA. The first version of the manuscript was written by GA. The final version of the manuscript included corrections and contributions from OF and MGV. The planning of the research was carried out by OF and MGV.

Paper 2. The simulations and the analysis were performed by GA. The code was implemented by MM. The first version of the manuscript was written by GA. The final version of the manuscript included corrections and contributions from OF, MGV and MU. The planning of the research was carried out by OF, MGV and MU.

Paper 3. The simulations were performed by GA. The analysis of the simulations was performed by GA and AG. The first version of the manuscript was written by GA. The final version of the manuscript included corrections and contributions from OF, MGV and MU. The planning of the research was carried out by OF, MGV and MU.

Paper 4. The simulations and the analysis were performed by GA. The first version of the manuscript was written by GA. The final version of the manuscript included corrections and contributions from OF and MGV. The planning of the research was carried out by OF and MGV.

Paper 5. The simulations and the analysis were performed by GA. The first version of the manuscript was written by GA. The final version of the manuscript included corrections and contributions from OF and MGV. The planning of the research was carried out by GA.

Other research merits

Publications

The content of the following publications, although related with the topic of the present thesis, is not included in this document:

Gonzalo, A., Arranz, G., Flores, O. & García-Villalba, M., 2018. From flapping to heaving: A numerical study of wings in forward flight, *J. Fluids Struct.*, **83**, p. 293–309. doi: 10.1016/j.jfluidstructs.2018.09.006

Jurado, R., Arranz, G., Flores, O., García-Villalba, M., 2020. Influence of the aspect ratio on the aerodynamic performance of apair of flapping wings, *J. Fluids Struct.*, *Under review.*

Proceedings

Arranz, G., Flores, O. & García-Villalba, M. Study of the efficiency of flapping and heaving wings in tandem configuration. *ERCOFTAC Workshop Direct and Large Eddy Simulation 12*, Madrid, Spain, 2019. 10.1007/978-3-030-42822-8_39

Arranz, G., Moriche, M., Uhlmann, M., Flores, O., & García-Villalba, M. The influence of the Reynolds number on the auto-rotation of samaras. *ERCOFTAC Workshop Direct and Large-Eddy Simulation 11*, Pisa, Italy, 2017. 10.1007/978-3-030-04915-7_54

A. Gonzalo, Arranz, G., Moriche, M., Flores, O., & García-Villalba, M. A numerical Study of low-aspect ratio flapping-wings in forward flight. *ERCOFTAC Workshop Direct and Large-Eddy Simulation 11*, Pisa, Italy, 2017. 10.1007/978-3-030-04915-7_53

Arranz, G., & Flores, O. Thrust generation in heaving and flapping wings in forward flight. *34th AIAA Applied Aerodynamics Conference*, Washington, USA, 2016. 10.2514/6.2016-3556

Conferences

The presenting author in underlined:

Arranz, G., Flores, O. & García-Villalba, M. Development of an algorithm for the fluid-structure interaction of bioinspired problems with multi-body systems. *APS Division Fluid Mechanics Annual Meeting*. Chicago, USA, 2020.

Jurado, R., Arranz, G., Flores, O. & García-Villalba, M. Aspect ratio effects on the aerodynamic performance of flapping wings in tandem configuration. *APS Division Fluid Mechanics Annual Meeting*. Chicago, USA, 2020.

Arranz, G., Flores, O. & García-Villalba, M. A numerical study of flapping wings in tandem configuration at low Reynolds number. *APS Division Fluid Mechanics Annual Meeting*. Seattle, USA, 2019.

Arranz, G., Flores, O. & García-Villalba, M. Implementation of an algorithm for the analysis of the fluid-structure interaction of multi-body systems. *Workshop on Fluid Mechanics*. Granada, Spain, 2019.

Arranz, G., Flores, O. & García-Villalba, M. Three dimensional effects in flapping wings in tandem configuration. *STAMS2019, First Colloquium of the Spanish Theoretical and Applied Mechanics Society*. Madrid, Spain, 2019.

Arranz, G., Gonzalo, A., Moriche, M., Uhlmann, M., Flores, O. & García-Villalba, M. On the stabilization of the leading edge vortex of an auto-rotating winged seed. *APS Division Fluid Mechanics Annual Meeting*. Atlanta, USA, 2018.

Arranz, G., Uhlmann, M., Flores, O., & García-Villalba, M The influence of the Reynolds number on the auto-rotation of samaras. *12th European Fluid Mechanics Conference*. Vienna, Austria, 2018.

Arranz, G. & Flores, O. From heaving to flapping: effect on thrust generation. *11th European Fluid Mechanics Conference 11*. Sevilla, Spain, 2016.

Abstract

Nature offers a vast amount of examples of efficient locomotion. Millions of years of evolution have allowed animals –such as fish, insects and birds–, and even plants –such as winged-seeds or dandelions– to achieve outstanding locomotive skills. Therefore, it is not a surprise that scientists and engineers have tried to replicate the flight and swimming capabilities of the former examples in order to develop efficient aerial and nautical robots. In fact, these efforts have led to the design and development of several successful bioinspired robots. However, their performance is still far below their living counterparts. One of the main reasons is that the understanding of the physics underlying biological locomotion is still limited. This is due to the complexity of the problem under consideration: the locomotion of a body through a fluid medium. This can be considered fluid structure interaction (FSI) problem where the dynamics of the specimens is the result from the hydrodynamic interaction with the surrounding fluid, which in turn is modified by the motion of the specimens. Consequently, the resulting problem is highly nonlinear and complex from a mathematical standpoint.

This dissertation attempts to contribute to further understand the fluid structure interactions in bioinspired locomotion problems. To that end, direct numerical simulations of several examples of bioinspired FSI problems are performed. These examples include the auto-rotation of a winged-seed, the flow interactions between the wings of a dragonfly, and the schooling patterns that emerge between two fish.

In the first part of this dissertation, the algorithm which has been developed to perform part of the aforementioned studies is presented. The proposed algorithm allows the study of the FSI of systems of connected rigid bodies –which serve as a model for the actual specimens– immersed in an incompressible fluid. It is built based on a preexisting flow solver, coupled with a robotic algorithm for the computation of the dynamics equations of the bodies. The use of robotic algorithms endows the proposed methodology with a great flexibility, allowing to simulate a large variety of problems with different geometries and configurations.

The second part of the thesis is devoted to the analysis of the aforementioned examples. In this regard, we first consider the flight of a winged-seed. This is a very interesting, yet complex, problem of fluid-dynamic interaction; in which the auto-rotative motion is the result of a subtle equilibrium between the aerodynamic forces and the inertia properties of the winged-seed. In our study, the dynamics and the flow surrounding the auto-rotating seed are characterized in a range of Reynolds numbers, Re. Specifically, we focus on the study of the leading edge vortex (LEV) that is developed on the upper surface of the seed's wing as it auto-rotates. Our findings suggest that, in the explored range $Re = [80 - 240]$, LEV's stability is not driven by vorticity transport along the spanwise direction nor viscous effects, as reported in the literature of rotating wings. Instead, fictitious accelerations (i.e., Coriolis and centrifugal accelerations) are the most suitable candidates to stabilize the LEV over the seed's wing.

In the second example, we study the effect of the three-dimensional (3D) interactions in the performance of two tandem wings, resembling those of a dragonfly. To that end, the wings undergo a two-dimensional (2D) optimum kinematics which is

a combination of heaving and pitching. We first analyze the effect of wings' aspect ratio, $\mathcal{AR}$, by comparing the 3D and 2D simulations. The results show that 3D vortical interactions are detrimental for the thrust production of the hindwing, but they do not significantly affect the propulsive efficiency of the tandem arrangement. Next, a more realistic flapping kinematics of the 3D is considered and compared to the previous heaving kinematics. We find a decrease in the propulsive efficiency of the flapping wings compared to their heaving counterparts, which has been linked to a non-desired shedding of vorticity on the inboard region of the wings.

The last bioinspired example corresponds to the collective motion of two self-propelled three-dimensional bodies. These bodies are idealized as rectangular, flat plates with flexibility along their chordwise direction, and that self-propels thanks to a prescribed vertical motion of their leading edges. We observe that tandem configurations emerge where both plates *swim* at a constant mean horizontal velocity and with a mean equilibrium horizontal distance. These configurations can be classified, attending to the resulting flow interactions, into compact and regular configurations. In the former, the performance of the upstream flapper is modified due to the close interaction with the downstream flapper. However, in the regular configurations, the performance of the upstream flapper is similar to that of an isolated flapper. Conversely, the performance of the downstream flapper is affected in both configurations by the interaction with the wake of the upstream flapper. We are able to link the changes in the downstream flapper's performance to its interaction with the vertical jet induced by vortex rings of the upstream flapper's wake. Finally, we propose a model to qualitatively predict the performance of a hypothetical downstream flapper based on the flow field of and isolated flapper, showing good agreement with the actual simulations.

Key words: bio-inspired locomotion, fluid structure interaction, direct numerical simulations.

Resumen

La naturaleza ofrece una gran cantidad de ejemplos de locomoción eficiente. Millones de años de evolución han permitido a animales –tales como peces, insectos o pájaros– e incluso plantas –como sámaras o dientes de león– lograr unas habilidades de lomoción excepcionales. Por lo tanto, no es una sorpresa que científicos e ingenieros hayan intentado replicar la capacidades de vuelo y nado de los anteriores ejemplos, con el objetivo de desarrollar robots aéreos y nadadores más eficientes. De hecho, estos esfuerzos han dado lugar al diseño y desarrollo exitoso de varios robots bioinsipirados. Sin embargo, el rendimiento de éstos es todavía muy inferior al de sus referentes biológicos. Una de las principales razones es que la comprensión de la física subyacente de la lomococión de sistemas biológicos es aún limitada. Esto es debido a la complejidad del problema, a saber, el movimiento de un cuerpo a través de un medio fluido. Este se puede considerar como un problema de interacción fluido estructura (FSI) donde la dinámica del espécimen es el resultado de la interacción fluidodinámica con el fluido de alrededor, el cual es a su vez modificado por el movimiento del cuerpo. Consecuentemente, el problema resultante es altamente no lineal y complejo desde un punto de vista matemático.

Con esta disertación se pretende contribuir a una mayor comprensión de la interacción fluido estructura en problemas de locomoción bioninspirados. Con tal propósito, se han realizado simulaciones numéricas directas de varios ejemplos bioinspirados de interacción fluido estructura. Estos ejemplos incluyen la autorrotación de una sámara, las interaccionés fluidas entre las alas de una libélula y los patrones de nado que surgen entre dos peces.

Durante la primera parte de esta disertación, se describe el algoritmo que ha sido desarrollado con el propósito de simular alguno de los problemas anteriormente citados. El algoritmo propuesto permite el estudio de la interacción fluido estructura de sistemas de cuerpos rígidos conectados –los cuales sirven como modelo de los especímenes reales– que están sumergidos en un fluido incompresible. Está construido sobre un solver fluido pre-existente, acoplado a un algoritmo robótico que se encarga de calcular las ecuaciones dinámicas de los cuerpos. El uso de algoritmos robóticos proporciona a la metodología propuesta una gran flexibilidad, permitiendo simular una gran variedad de problemas con diversas geometrías y configuraciones.

La segunda parte de esta tesis está dedicada al análisis de los ejemplos mencionados anteriormente. En este respecto, consideramos primero el vuelo de una sámara, el cual es un problema muy interesante, aunque complejo, de interacción fluido dinámica en el cual el movimiento autorrotativo es el resultado de un sutil equilibrio entre las fuerzas aerodinámicas y las propiedades inerciales de la semilla. En nuestro estudio, caracterizamos la dinámica y el flujo alrededor de la semilla autorrotante en un rango de números de Reynolds, Re. En concreto, nos centramos en el estudio del vórtice del borde de ataque (LEV) que se forma en la parte superior del ala de la sámara cuando ésta autorrota. Nuestros hallazgos sugieren que, en el rango explorado de $Re = [80 - 240]$, la estabilidad del LEV no se debe a un transporte de vorticidad a lo largo de la dirección de la envergadura del ala, ni a efectos viscosos –como se ha mencionado en la literatura de alas rotativas–, si no que las aceleraciones ficticias (es

decir, las aceleraciones centrífugas y de Coriolis), son las candidatas más probables responsables de la estabilización del LEV.

En el segundo ejemplo, se estudia el efecto de las interacciones tridimensionales (3D) en el rendimiento de dos alas en configuración tándem, basadas en las de una libélula. Para ello, se prescribe que el movimiento de las alas sea una combinación de cabeceo y oscilación vertical que es óptimo en 2 dimensiones (2D). Primero analizamos el efecto de la relación de aspecto de las alas, $\mathcal{R}$, comparando los resultados de las simulaciones en 3D y en 2D. Los resultados revelan que las interacciones vorticales en 3D son perjudiciales para la generación de empuje del ala trasera, pero estas interacciones no afectan de forma significativa a la eficiencia propulsiva del conjunto. Posteriormente, se considera un movimiento de batimiento más realista de las alas, y se compara su eficiencia con la obtenida previamente para las alas en movimiento oscilatorio vertical. Se observa una menor eficiencia de las alas en batimiento en comparación con las mismas alas en movimiento oscilatorio vertical. Este deterioro es asociado a un desprendimiento de estructuras vorticales cerca de los bordes marginales de las alas en batimiento.

El último ejemplo bioinspirado es el del movimiento colectivo de dos cuerpos tridimiensionales que se auto propulsan. Estos cuerpos se idealizan como placas planas rectangulares, siendo flexibles a lo largo de su cuerda, y que se auto propulsan gracias a un movimiento vertical impuesto de sus bordes de ataque. Los resultados muestran la aparición de configuraciones tándem donde sendas placas *nadan* con una velocidad media constante y separadas a una distancia de equilibrio que es también constante. Estas configuraciones son clasificadas –atendiendo a las interacciones fluidas– entre *compactas* y *regulares*. En las primeras, el rendimiento de la placa que nada aguas arriba (a la que llamaremos líder) se ve afectado por las interacciones cercanas con el cuerpo que nada aguas abajo (al que denominaremos seguidor). En cambio, en las configuraciones regulares el redimiento del líder es el mismo que el de una placa similar nadando de forma aislada. Por el contrario, el rendimiento del seguidor se ve afectado en ambas configuraciones debido a las interacciones con la estela del líder. Se ha podido relacionar estos cambios en la eficiencia del seguidor con la interacción con el chorro inducido por los anillos vorticales de la estela del líder. Finalmente, hemos propuesto un modelo que permite predecir, de forma cualitativa, el rendimiento de un seguidor hipotético basándonos en el campo fluido de una placa aislada. El modelo muestra una buena correlación con los datos obtenidos de las simulaciones numéricas.

Palabras clave: locomoción bioinspirada, interacción fluido estructura, simulaciones numéricas directas.

Contents

Acknowledgements iii

Published and submitted content iv

Other research merits vi

Abstract viii

Resumen x

Part I - Overview and summary

Chapter 1. Introduction 1
1.1. Objectives 3
1.2. Thesis structure 3

Chapter 2. Numerical methodology 5
2.1. Governing equations 5
2.2. Fluid structure interaction algorithms: the immersed boundary method 5
2.3. In-house code: TUCAN 7
2.3.1. Flow solver 7
2.3.2. Coupling the motion of the bodies 8
2.3.3. Main features of TUCAN 9

Chapter 3. Main contributions and conclusions 11
3.1. Paper highlights 12

Bibliography 15

Part II - Papers

Summary of the papers 21

Paper 1. A weakly coupled immersed boundary method and dynamic algorithm for the fluid-structure interaction of multi-body systems 23

Paper 2. Kinematics and dynamics of the auto-rotation of a model winged seed 55

Paper 3. A numerical study of the flow around a model winged seed in auto-rotation 83

Paper 4. Three-dimensional effects on the aerodynamic performance of flapping wings in tandem configuration 109

Paper 5. Flow interaction of three-dimensional self-propelled flexible plates in tandem 135

Part I

Overview and summary

Chapter 1

Introduction

When it comes to efficient means of locomotion, nature stands as the clear winner. One only needs to have a look at the numerous examples provided by animal kingdom. In the oceans and rivers, we find that the swimming capabilities of fish largely exceed those achieved by nautical science and technology (Triantafyllou & Triantafyllou 1995). For example, the Atlantic mackerel can reach burst speeds up to $18\,\mathscr{L}$/s (where $\mathscr{L}$ stands for body lengths); many fish species can sustain speeds of about $3\,\mathscr{L}$/s for over 600 min, whereas swimming at lower speeds with no signs of fatigue (Videler & Wardle 1991). Looking at the skies, a common barn swallow can roll five times faster than a highly acrobatic aircraft; while a common pigeon frequently attains flight speeds of $\sim 75\,\mathscr{L}/s$, widely exceeding the $32\,\mathscr{L}/s$ reached by a supersonic fighter (Shyy *et al.* 2013). Likewise, albatrosses are probably one of the most efficient flyers in terms of endurance: they are able to cover distances up to $15,000$ km in a single foraging trip (Jouventin & Weimerskirch 1990) by taking advantage of shear layers of wind over the ocean by means of the so-called dynamic soaring (Cone Jr 1964; Shaffer *et al.* 2001). Although previous examples have focused on animals, kingdom Plantae also offers striking examples of locomotion efficiency (Burrows 1975; Greene & Johnson 1990). Probably, one of the most well-known examples are winged seeds which, by virtue of their shape, are able to enter into auto-rotation as they fall from their tree and disperse from tens of meters to kilometers (Nathan 2006). Another noteworthy example are dandelions, which can achieve long dispersal distances (Tackenberg *et al.* 2003) owing to the interaction of their filaments with the surrounding air (Cummins *et al.* 2018).

Therefore, it is not surprising that we humans have tried to mimic nature and have developed robots inspired by some of the former examples. As an illustration, Triantafyllou & Triantafyllou (1995) were probably the first in developing a functional robotic fish, the *RoboTuna*. In the following years, a considerable amount of new prototypes were reported in the literature (see Aditi & Atul (2016) for a review on fish-inspired robots). A decade later, the first bioinspired flapping wings robot was presented by Wood (2008), followed by the *DelFly* by de Croon *et al.* (2009), and the *Nano Hummingbird* by Keennon *et al.* (2012). Likewise, auto-rotating winged seeds inspired the development of the *Samarai* (Fregene & Bolden 2010), and the robotic samara of Ulrich *et al.* (2010).

However, the performance of these bioinspired robots is still far from their living counterparts (Epps *et al.* 2009; Helbling & Wood 2018). Setting aside technological

limitations, one key factor is the need for a proper understanding of the fundamental physics underlying the locomotion of living creatures. In this regard, the mechanisms employed by fish, birds, insects or winged-seeds to achieve such performances are clearly different among one another. Nonetheless, all of them are based on manipulating the flow around them. This flow manipulation can be achieved by passive or active mechanisms. The former are related to the morphology of the specimen, like the uneven mass distribution of winged-seeds responsible for their auto-rotation (Norberg 1973); or the turbucles on the leading edges of Humpback whales, which provides them with an enhanced manoeuvrability (Miklosovic *et al.* 2004). In active flow control, the specimen directly modifies the flow with its movements: using its muscular activity (Fish & Lauder 2006).

Irrespective of the actual mechanism, from a physics standpoint these kind of problems can be considered as fluid structure interaction (FSI) problems between a body (or bodies) and a surrounding fluid. In these FSI problems, the dynamics of the bodies is the result of their hydrodynamic interaction with the surrounding fluid, which in turn is modified by the mechanisms employed by the bodies. This coupled interaction leads to a highly complex and nonlinear problem.

In order to gain a proper understanding of the physical mechanisms that govern these FSI problems, experiments and numerical simulations have proven to be very useful tools. On the one hand, experiments allow to study the actual problem in a controlled environment, as well as to perform large parametric studies. In particular, the advent of digital particle image velocimetry (DPIV) has allowed detailed examination of the flow structures produced by swimming and aerial animals (Birch & Dickinson 2001; Fish & Lauder 2006; Smits 2019). In spite of this, the amount of information that can be extracted from the fluid is still limited –usually restricted to the in-plane velocity in one or several planes without temporal resolution–, and force measurements in free motion is challenging (Hightower *et al.* 2017; Rival & Oudheusden 2017). On the other hand, from numerical simulations, the flow field (i.e., flow velocity and pressure) is known at each time instant, as well as the forces acting on the bodies without any kind of external interference. Nevertheless, this data availability comes at the expense of a high computational cost, as well as the complexity in modelling the coupled FSI problem.

In particular, the numerical simulation of this kind of FSI problems entails several challenges. First of all, the equations that govern the dynamics of the specimens must be derived and coupled with the flow equations, leading to a highly non-linear problem which must be solved. Secondly, the modelling of the geometry and kinematics of the specimens is complex: they may be composed of several "bodies" which have a relative motion among them (e.g., an insect can be decomposed into its thorax-abdomen, and its wings, which flap relative to the former); and additionally they can suffer from deformations due to the hydrodynamic interaction. This can further complicate the derivation of the dynamic equations and the solution of the whole system. Consequently, these problems are usually simplified to some extent. Sometimes, the dynamics of the bodies are not solved; instead the motion of the bodies is fully prescribed, leading to a one-way coupling in which the body modifies the surrounding fluid, but the flow does not modify the motion of the bodies. Alternatively, when the dynamics

of a specimen is computed from the FSI, the modelling of its inertia and geometric properties is simplified to reduce the complexity of the governing equations. One common simplification is to consider the specimen to be composed of several connected bodies. These bodies can be flexible, or assumed to be rigid, which reduces the computational complexity. Furthermore, there are numerous studies in which all the bodies except one are assumed to be massless (e.g., insect wings are usually modelled as massless). Thus leading to a simplified expression of the dynamic equations.

1.1. Objectives

The main objective of this thesis is to contribute to the understanding of the interactions among dynamics, elasticity and hydrodynamics in bioinspired problems, with the hope that this understanding paves the way for the development of more efficient, bioinspired aerial and swimming robots.

In order to achieve this global aim, three objectives are defined. Firstly, we study the auto-rotation of a winged-seed by means of numerical simulations to elucidate the coupled fluid-dynamic interaction of this passive mechanism.

Secondly, numerical simulations are performed to study the flow interactions of a collective of two bodies, with the objective of analyzing the effect of the kinematics and the elasticity of the bodies.

Finally, a computational tool to simulate the FSI problem of several systems of connected rigid body is developed and validated, in order to be able to fulfill the previous objective.

1.2. Thesis structure

The present document is organized in two parts, subdivided into chapters.

Part I provides an overall view and framework to the thesis. The present chapter (chapter 1) provides an introduction; chapter 2 summarizes the numerical methods used to accomplish the studies of this thesis; and chapter 3 summarizes the main contributions of this work.

Part II contains the original publications this dissertation led to. The first paper presents the numerical algorithm developed to compute the FSI of multi-body systems of rigid bodies. The second and the third articles are focused on the dynamics and the flow around a winged seed in auto-rotation, respectively. The fourth research article analyzes the flow interaction of two finite wings in *in-line* tandem configuration with a prescribed motion, resembling those of dragonflies. Finally, the last research item further explores the interaction of two tandem plates but which self-propel in an otherwise quiescent fluid:

Paper 1: A weakly coupled immersed boundary method and dynamic algorithm for the fluid-structure interaction of multi-body systems.

Paper 2: Kinematics and dynamics of the auto-rotation of a model winged seed.

Paper 3: A numerical study of the flow around a model winged seed in auto-rotation.

Paper 4: Three-dimensional effects on the aerodynamic performance of flapping wings in tandem configuration

Paper 5: Flow interaction of three-dimensional self-propelled flexible plates in tandem.

Chapter 2

Numerical methodology

2.1. Governing equations

The most general problem considered in the present thesis is depicted in figure 2.1. It consists of one or more rigid-bodies immersed in a fluid. For the biological locomotive problems considered herein, the fluid can be effectively considered as incompressible (Wang & Sun 2005).

Thus, the equations governing the motion of the surrounding fluid are the Navier-Stokes equations of an imcompressible, newtonian fluid:

$$\nabla \cdot \mathbf{u} = 0, \tag{2.1a}$$

$$\frac{\partial \mathbf{u}}{\partial t} + (\mathbf{u} \cdot \nabla)\mathbf{u} = -\frac{1}{\rho}\nabla p + \nu \nabla^2 \mathbf{u}, \tag{2.1b}$$

where $\mathbf{u}$ is the flow velocity, p is the pressure, and ρ and ν are the density and kinematic viscosity of the fluid, respectively. Equation (2.1) must be complemented with the boundary conditions of the particular problem, namely, the so-called non-slip boundary condition on the surface of the bodies:

$$\mathbf{u} = \mathbf{U}_{\partial\Gamma_i}(\mathbf{x}) \quad \forall \mathbf{x} \in \partial\Gamma_i, \quad \forall i \in B, \tag{2.2}$$

where $\partial\Gamma_i$ is the interface between the fluid and body, Γ_i; $B = \{1, \ldots, N_B\}$ is the set of bodies (being N_B the total number of bodies); and $\mathbf{U}_{\partial\Gamma_i}(\mathbf{x})$ is the velocity of Γ_i at its surface point, $\mathbf{x}$.

Note that, the value of $\mathbf{U}_{\partial\Gamma_i}$ is not necessarily known *a priori*, but it can be a function of the dynamics of the body due to the interaction with the fluid. This is assessed in section 2.3.2.

2.2. Fluid structure interaction algorithms: the immersed boundary method

There are many numerical procedures to solve the FSI problem posed in section 2.1. They can be broadly categorized according to its formulation into *monolithic* and *partitioned* (non-monolithic) formulations (Bazilevs *et al.* 2008; Hou *et al.* 2012); or according to the treatment of the solid-fluid interfaces as conforming mesh methods and non-conforming mesh methods (Deng *et al.* 2013).

Monolithic formulations treat both the fluid and the structure in the same mathematical framework, leading to a single discrete system of equations for the whole problem. They are robust and can achieve better accuracy, but they generally lead

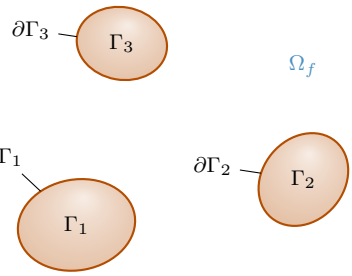

Figure 2.1: Sketch of the general problem under consideration: several bodies, Γ_i, immersed in a surrounding fluid of domain, Ω_f.

to large and poorly conditioned systems, which require the use of iterative solvers (Ryzhakov *et al.* 2010). As a result, they require substantially more resources. In contrast, in partitioned formulations the fluid and the structure are solved separately and the interfacial condition eq. (2.2) is used explicitly to ensure the compatibility between both systems (Hou *et al.* 2012). This allows to integrate existing, specialized codes for each subsystem. Moreover, the resulting systems of equations are generally better conditioned. Consequently, partitioned formulation has become a very popular option when solving FSI problems. Nevertheless, for specific cases, as for instance when the density of the fluid and the structure is very similar, partitioned schemes often show instability or poor converge (Ryzhakov *et al.* 2010).

Regarding the second categorization, in conforming mesh methods, the interface condition is treated as a physical boundary. Thus, as the solution advances in time, re-meshing of the fluid domain is necessary due to the movement of the bodies (i.e., the solid interface). On the contrary, a physical boundary between the bodies and the fluid does not exist in non-conforming methods, but constraints are imposed to eq. (2.1) for interface conditions to be fulfilled. As a consequence, re-meshing of the fluid domain is not required.

In the present thesis, a partitioned formulation with a non-conforming mesh method is used. The main motivation is that these approaches allow greater flexibility and simplicity in the implementation, and they are perfectly suited for the analysis of biological locomotion. In particular, a partitioned immersed boundary method (IBM) is used for all the studies presented in this thesis.

The main idea underlying IBM is depicted in figure 2.2. A Cartesian grid is defined which covers the fluid domain, considered to be a simply connected region, where eq. (2.1) is solved. Additionally, consider the surface of each body, $\partial\Gamma_i$, to be discretized into a set of points, $L(i) = \{1, ..., n_i\}$, each of which has an associated volume, $\Delta V_{i,j}$. The whole set of surface points is usually denoted as *Lagrangian force points*. The main idea behind IBM consists of adding a forcing term, $\mathbf{f}$, to eq. (2.1b), such that the fluid velocity interpolated at the Lagrangian force points satisfies eq. (2.2).

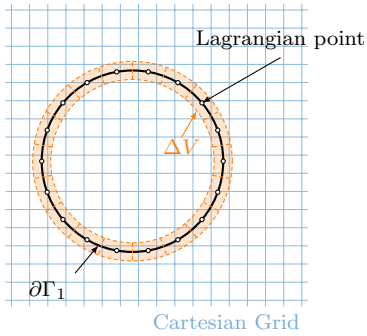

FIGURE 2.2: Sketch of the immersed boundary discretization of the fluid domain and the boundary of a body Γ_1 in two dimensions (or equivalently, a sectional view of a 3D space configuration).

Section 2.3 provides additional details on the IBM used in the present thesis. For further details in immersed methods for fluid structure interaction problems, reader is referred to Mittal & Iaccarino (2005); Griffith & Patankar (2020).

2.3. In-house code: TUCAN

The in-house code used in the present thesis was initially developed by Moriche (2017) during his PhD thesis; and several improvements were later introduced by Gonzalo (2018). Consequently, this section is intended to provide an overall description of the code. A more detailed description is provided in the aforementioned references. Likewise, the improvements to TUCAN developed during the present thesis are the subject of Paper 1.

2.3.1. *Flow solver*

The flow solver is similar to that presented in Uhlmann (2005). Equation (2.1) is solved using the projection method proposed by Brown *et al.* (2001) in order to enforce continuity. Spatial derivates are discretized by second order, centred finite differences on a staggered grid. Temporal marching is achieved by a three stage, low storage Runge-Kutta method, where non-linear terms are treated explicitly, and linear terms implicitly.

The resulting equations for a kth Runge-Kutta substep yield to be:

$$\tilde{\mathbf{u}} = \mathbf{u}^{k-1} + \Delta t \left(2\alpha_k \nu \nabla^2 \mathbf{u}^{k-1} - 2\alpha_k \rho^{-1} \nabla p^{k-1} - \gamma_k [(\mathbf{u}\cdot\nabla)\mathbf{u}]^{k-1} - \zeta_k [(\mathbf{u}\cdot\nabla)\mathbf{u}]^{k-2} \right), \tag{2.3a}$$

$$\tilde{\mathbf{U}}(\mathbf{X}_{i,j}) = \tilde{\mathbf{u}}(\mathbf{x}) \delta_h \left(\mathbf{x} - \mathbf{X}_{i,j} \right) \Delta V_{i,j}, \tag{2.3b}$$

$$\mathbf{F}^k(\mathbf{X}_{i,j}) = \frac{\mathbf{U}^{(d)}_{\partial\Gamma_i}(\mathbf{X}_{i,j}) - \tilde{\mathbf{U}}(\mathbf{X}_{i,j})}{\Delta t}, \tag{2.3c}$$

$$\mathbf{f}^k = \sum_{i\in B}\sum_{j\in L(i)} \mathbf{F}^k(\mathbf{X}_{i,j})\delta_h\left(\mathbf{x}-\mathbf{X}_{i,j}\right)\Delta V_{i,j}, \tag{2.3d}$$

$$\nabla^2\mathbf{u}^* - \frac{\mathbf{u}^*}{\alpha_k\nu\Delta t} = -\frac{1}{\nu\alpha_k}\left(\frac{\tilde{\mathbf{u}}}{\Delta t}+\mathbf{f}^k\right) + \nabla^2\mathbf{u}^{k-1}, \tag{2.3e}$$

$$\nabla^2\phi^k = \frac{\nabla\cdot\mathbf{u}^*}{2\alpha_k\Delta t}, \tag{2.3f}$$

$$\mathbf{u}^k = \mathbf{u}^* - 2\alpha_k\Delta t\nabla\phi^k, \tag{2.3g}$$

$$p^k = p^{k-1} + \rho\left(\phi^k - \alpha_k\nu\Delta t\nabla^2\phi^k\right), \tag{2.3h}$$

where the subscript indicates the substep at which the variable is evaluated; ϕ is the so-called pseudo-pressure; α_k, γ_k, ζ_k are the set of coefficients of the kth Runge-Kutta substep, given by Rai & Moin (1991); $\tilde{\mathbf{u}}$ is an estimate flow velocity for the forcing term calculation; and $\mathbf{u}^*$ is an intermediate flow velocity used in by the fractional step method.

The forcing of the IBM appears in eqs. (2.3b)–(2.3d). In eq. (2.3b), the fluid velocity is interpolated at the Lagrangian points. This interpolated velocity, $\tilde{\mathbf{U}}(\mathbf{X}_{i,j})$, is used, in conjunction with the surface velocity, $\mathbf{U}^{(d)}_{\partial\Gamma_i}$, in eq. (2.3c) to compute the forcing term at the Lagrangian point j of body Γ_i, namely $\mathbf{F}(\mathbf{X}_{i,j})$ (where the temporal superscript is dropped for convenience). This force is transferred to the grid points of the fluid mesh by means of eq. (2.3d). Interpolation from the Lagrangian points to the fluid mesh and vice-versa is performed using the regularized delta function, δ_h, introduced by Peskin (2002).

2.3.2. *Coupling the motion of the bodies*

When the motion of the bodies is prescribed, $\mathbf{U}^{(d)}_{\partial\Gamma_i}$ is known, and therefore the solution of eq. (2.3) can be computed at each time instant.

However, in a general problem where the motion of the bodies is the result of the fluid-structure interaction, $\mathbf{U}^{(d)}_{\partial\Gamma_i}$ is unknown *a priori*. Instead, in addition to eq. (2.1), the dynamic equations of motion of the bodies must be solved.

From classical mechanics, it is known that the equations of motion of a system of connected rigid bodies can be written in terms of its degrees of freedom (also known as generalized coordinates, defined herein as $\mathbf{q}$) as a system of ordinary differential equations:

$$\mathsf{H}\ddot{\mathbf{q}} + \mathsf{c} = \boldsymbol{\xi}, \tag{2.4}$$

where H is the so-called inertia matrix, c is a vector containing the effect of fictitious accelerations and gravity (if present), and $\boldsymbol{\xi}$ is the vector of generalized forces.

Solution of (2.4) at a given time yields the state of the system of bodies, namely $(\mathbf{q},\dot{\mathbf{q}})$, which after the corresponding mapping, leads to $(\mathbf{X},\mathbf{U}_{\partial\Gamma}(\mathbf{X}))$, allowing to evolve eq. (2.3c). The construction and method of solution of eq. (2.4), as well as the mapping and the coupling with the fluid equations is detailed in Paper 1.

Finally, when a single body is considered, eq. (2.4) can take the form of the Newton-Euler equations of motion. Namely,

$$m\dot{\mathbf{U}}_G = \mathbf{F}_{ext}, \tag{2.5}$$

$$\mathsf{I}_G\dot{\boldsymbol{\Omega}} + \boldsymbol{\Omega} \times \mathsf{I}_G\boldsymbol{\Omega} = \mathbf{M}_{G,ext}, \tag{2.6}$$

where m and I_G are the mass and inertia tensor of the body; $\mathbf{U}_G$ and $\boldsymbol{\Omega}$ are the linear and angular velocity of the body; and $\mathbf{F}_{ext}$ and $\mathbf{M}_{G,ext}$ are the external forces and moments acting on the body. The subscript G indicates that the magnitude is computed with respect to the gravity centre of the body. Note that, eq. (2.6) only holds when expressed in a body-fixed reference frame.

The dynamics of a winged-seed are computed in Paper 2 and Paper 3 by means of eqs. (2.5) and (2.6). Some of the mathematical details for the coupling of eqs. (2.5) and (2.6) with (2.3) are provided in Paper 2, whereas a complete description is available in Moriche *et al.* (2021).

2.3.3. *Main features of TUCAN*

In this section main features of TUCAN are highlighted. These features are presented in detail in Moriche (2017); Gonzalo (2018); thus, in this section we merely outline them and refer the interested reader to the aforementioned theses.

Equation (2.3) can be solved both in 2D and 3D. In the former, the computational domain is a rectangle, meanwhile in 3D it is a rectangular prism. This fluid domain is discretized into a structured staggered grid (see figure 2.3a). In this kind of grid, the pressure and velocities are not defined at the same mesh points, thus avoiding the odd-even decoupling between velocity and pressure that happens in a collocated mesh when central differences are used to discretize the diffusive terms (Hirsch 2007).

In the original version of TUCAN developed by Moriche (2017), the staggered grid can only be uniformly discretized. Due to the limitation $\Delta V \approx \Delta r^3$ imposed by the IBM (Uhlmann 2005), in a uniformly discretized grid the flow far away from the bodies is solved in a much finer mesh than required. Thus leading to larger computational time than actually required. To overcome these limitations, Gonzalo (2018) implemented the possibility of using a non-uniform grid in TUCAN. In particular, it allows to specify a rectangular prism with a uniform grid, where the bodies are expected to remain during the simulation. Outside this uniform grid, the grid is controlled by the *stretch factor* (see Gonzalo (2018) for further details). A schematic representation of this kind of grid is displayed in figure 2.3b.

TUCAN allows to impose Dirichlet, Neumann or periodic type boundary conditions in any boundary of the computational domain. In addition, for simulations where a free-stream inflow is imposed at one side of the domain, an advective type boundary condition can be set at the opposite side. This type of boundary condition allows strong vortical structures to leave the domain without reflections that would affect the whole domain if either Dirichlet or Neumann boundary conditions were imposed (Moriche 2017).

Parallelization is implemented in TUCAN by means of a block domain decomposition. The physical flow domain and the corresponding grid is split into smaller block

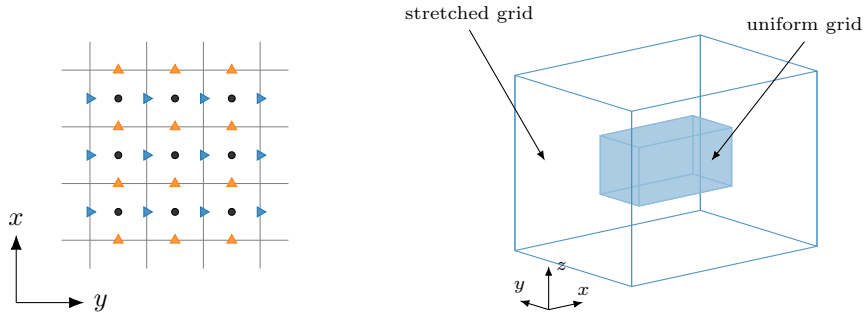

(a) (b)

Figure 2.3: (a) Sketch of a (x,y)-slice of a staggered grid. Pressure is computed at points (●), x component of the velocity is computed at points (▶), and y component of the velocity is computed at points (▲). (b) Sketch of a characteristic fluid domain. The discretized bodies are expected to move inside the uniform region.

domains (rectangular cuboids) and assigned to different processors. Communication among processors is based on the Message Passing Interface (MPI) standard.

Upon discretization, eq. (2.3e) and (2.3f) lead to three (one for each velocity component) and one, independent, linear systems, respectively, which are solved each substep. These systems are solved in parallel using the preconditioner library, Hypre (Chow *et al.* 1998; Falgout & Yang 2002). The discretized Poisson equation (eq. (2.3f)) is solved using the biconjugate gradient stabilized solver (BiCGSTAB) preconditioned with a parallel semicoarsening multigrid solver (PFMG). On the other hand, the discretized Helmholtz equation for each velocity component (eq. (2.3e)) is solved using a preconditioned conjugate gradient solver (PCG).

Input/Output (I/O) files that must be read/written by TUCAN are handled in the Hierarchical Data Format, version 5 (HDF5), designed for high volume and complex data management and compatible with MPI standards (Folk *et al.* 2011).

Finally, TUCAN has been thoroughly validated, and its scalability demonstrated. Validation test cases of fixed bodies and moving bodies with prescribed kinematics are presented in Moriche (2017); cases of free-falling single rigid bodies are presented with low detail in Paper 2 of the present thesis, and with much more detail in Moriche *et al.* (2021); and finally, the validation of the FSI of multibody systems is the subject of Paper 1.

Chapter 3

Main contributions and conclusions

The first contribution of the present thesis is the development of a computational framework for the study of biological locomotion. This is achieved by the implementation of a numerical solver capable of computing the fluid structure interaction of one or several systems of connected rigid bodies in an incompressible fluid.

The second contribution of this dissertation is the study of three examples of biological locomotion, displayed in figure 3.1, which exploit different mechanisms. First of all, the auto-rotation flight of a winged-seed was simulated. This exemplifies a passive mechanism for locomotion, in which the seed is not able to modify the flow by any active means, but its motion is solely determined by its inertia properties and the flow interaction. This study allowed the elucidation of the effect of Re on the auto-rotative flight; as well as to provide quantitative measurements of the forces and the flow around the seed in auto-rotation. Figure 3.1a displays the flow around the auto-rotating seed model, as well as the actual winged-seed the model is based on.

In a second block, two examples of bioinspired collective motion are studied. The flow interaction between two wings in tandem configuration with a prescribed motion are firstly analysed, motivated by the wings of dragonflies. This study focused on the characterization of the three-dimensional (3D) effects of the flow interaction between the wings, and the differences with the two-dimensional (2D) studies which are typically found in the literature. The main results showed that, 3D vortical interaction between the wings decrease force produced by the hindwing as compared to the 2D case. It was also found that a realistic flapping motion leads to a worse performance than the 2D idealized motion. For an illustration, figure 3.1b depicts the vortical structures developed by the two wings, as a simplified problem of the actual interaction between the fore- and hind-wing of a dragonfly.

The final case of study is that of two flexible plates in tandem configuration which self-propels, simulating the most simple schooling configuration. Note that this case might also be considered as a step forward in the study of the fluid structure interaction between the two bodies presented before: instead of prescribing the motion of the wings, the overall dynamics is determined by the flow interactions. This study allowed to characterize the stable schooling positions and their associated performance. Particularly, it was shown that the downstream body is able to benefit from the flow interactions if its instantaneous velocity is aligned with the one induced by the vortex rings of the upstream body's wake. As an example, figure 3.1c depicts the flow for a

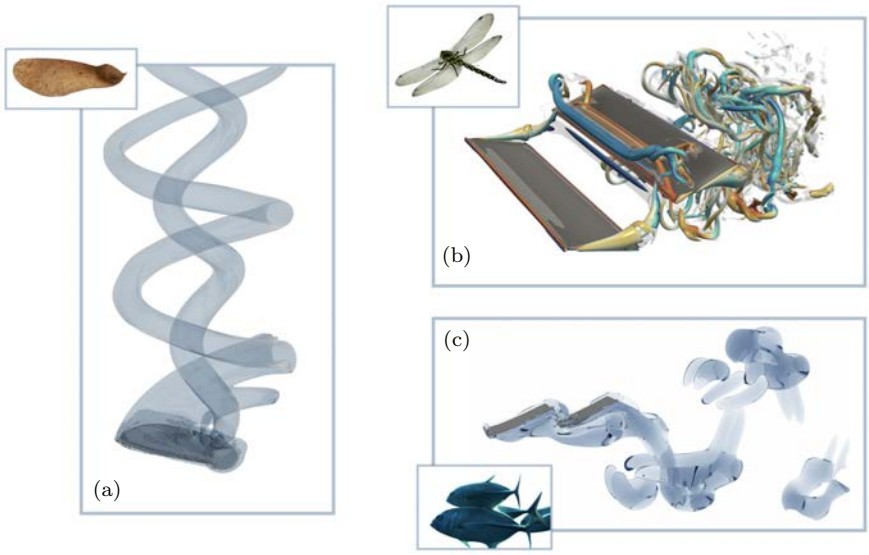

Figure 3.1: Flow visualization of the biological problem studied in this thesis. The inset attached to each panel displays the actual subject the problem is inspired in. (a) Auto-rotation of a winged-seed; (b) flapping motion of dragonfly's tandem wings; and (c) the collective motion of two self-propelled bodies.[1]

particular schooling configuration where the downstream body is interacting with the vortex ring just shed by the leading body.

In the following section the main conclusions of each paper are summarized.

3.1. Paper highlights

Paper 1

A weakly coupled immersed boundary method and dynamic algorithm for the fluid-structure interaction of multi-body systems

- A numerical methodology to solve the fluid-structure interaction problem with systems of connected rigid body is presented and validated.
- The proposed method follows a partitioned formulation. The flow equations are solved using a fractional-step method, and the non-slip boundary condition over the surface of the bodies is imposed by means of the immersed boundary method proposed by Uhlmann (2005).

[1] The dragonfly of panel (b) and the fish of panel (c) are extracted and adapted from www.pngimg.com and www.daily.jstor.org, respectively.

- The dynamic equations of the system of rigid bodies is computed in terms of reduced coordinates by means of the recursive algorithms proposed in Felis (2017). This endows the algorithm with great flexibility: allowing to simulate a great variety of different problems.
- Two bioinspired problems are presented to show the capabilities of the developed methodology: a 3D self-propelling flexible plate; and the flow around a flexible filament attached to an sphere, loosely inspired by the *ballooning* mechanism of spiders.

Paper 2

Kinematics and dynamics of the auto-rotation of a model winged seed

- Numerical simulations of the auto-rotation of a model winged-seed in the range of Reynolds number, $Re = 80 - 240$, with constant geometry and inertia properties are performed.
- It is found that the seed attains a stable auto-rotative state, with constant angular velocity and attitude angles. Additionally, it is found that the seed rotates while skidding (i.e., the angle between the horizontal projection of the spanwise axis of the seed and the centrifugal forces is different from zero).
- As Re increases, the angular velocity increases and the inclination of the winged-seed with respect to the horizontal plane decreases.
- Analysis of the aerodynamic forces and moments acting on the seed suggests that the vertical component is mainly due to pressure forces, whereas the components tangent to the wing seem to be related to viscous forces.

Paper 3

A Numerical Study of the Flow Around a Model Winged Seed in Auto-Rotation

- The flow around an auto-rotating seed is characterized in the range $Re = 80 - 240$. Three vortical structures are developed: a helical wing tip vortex; a vortex shed behind nut; and a leading edge vortex (LEV) above the wing surface which merges with the helical tip vortex.
- Three possible mechanisms for the stabilization of the LEV are studied:
  - No evidence for the first proposed mechanism, vorticity transport within the LEV, after a statistical analysis of fluid particle trajectories, is found.
  - Viscous stabilization could be a suitable mechanism only near the tips, however the flow topology at the tips makes it highly improbable.
  - Based on order of flow magnitudes, it was found that non-inertial accelerations could be a potential candidate for the stabilization of the LEV.
- The flow inside the LEV is described by characterizing the average spanwise vorticity, spanwise velocity and pressure. It is shown that, the flow for $Re = 160$ and 240 is qualitatively different to that for $Re = 80$, probably because the latter is close to the lower limit of auto-rotation (estimated to be $Re \lesssim 50$ for the considered seed).

Paper 4

Three-dimensional effects on the aerodynamic performance of flapping wings in tandem configuration

- Numerical simulations are performed to analyse the influence of 3D effects in the performance of tandem wings undergoing a 2D optimal kinematics.
- Aspect ratio effects are studied by considering wings of aspect ratio 2 and 4 undergoing a heaving and pitching motion. The results show that vortex breakdown leads to a thrust reduction on the hind-wing; however, the propulsive efficiency remains approximately constant and similar to that of the 2D case.
- The effect of a more realistic motion, namely a flapping motion, is addressed by comparing them with the previous results in heaving. The results show that there is a reduction in the forces and in the propulsive efficiency from a heaving to a flapping motion.
- The detrimental performance in flapping motion is more pronounced for the highest aspect ratio and it has been linked to a non-desired shedding vorticity on the inboard region of the wings.

Paper 5

Flow interaction of three-dimensional self-propelled flexible plates in tandem

- Numerical simulations are performed to explore the tandem configurations of two self-propelled flexible plates of finite span.
- Two main patterns of stable configurations are found: *compact* and *regular* configurations. The former are characterized by a close interaction between the flappers, which leads to a higher required power and propulsive speed than if they self-propelled in isolation. In regular configuration, the performance of the upstream flapper (leader) is not affected, but the performance of the downstream flapper (follower) is modified due to the interaction with the wake of the leader.
- Analysis reveals that the temporal evolution of the follower's required power can be linked to the vortex rings of the leader's wake. Specifically, the follower saves energy when it is moving in the same direction of the jet induced by the vortex ring it is interacting with.
- A model to qualitatively predict the performance of a hypothetical follower is presented. This model is based on the flow field of an isolated flapper and shows good agreement with the actual data from the simulations.

Bibliography

Aditi, R. & Atul, T. 2016 Fish-inspired robots: design, sensing, actuation, and autonomy—a review of research. *Bioinspir. Biomim.* **11** (3), 031001.

Bazilevs, Y., Calo, V. M., Hughes, T. J. R. & Zhang, Y. 2008 Isogeometric fluid-structure interaction: theory, algorithms, and computations. *Comput. Mech.* **43** (1), 3–37.

Birch, J. M. & Dickinson, M.l H. 2001 Spanwise flow and the attachment of the leading-edge vortex on insect wings. *Nature* **412** (6848), 729–733.

Brown, D. L., Cortez, R. & Minion, M. L. 2001 Accurate projection methods for the incompressible Navier–Stokes equations. *J. Comput. Phys.* **168** (2), 464–499.

Burrows, F. M. 1975 Wind-borne seed and fruit movement. *New Phytol.* **75** (2), 405–418.

Chow, E., Cleary, A. J. & Falgout, R. D. 1998 Design of the hypre preconditioner library. In *In SIAM Workshop on Object Oriented Methods for Inter-operable Scientific and Engineering Computing*, pp. 106–116. SIAM.

Cone Jr, C. D. 1964 A mathematical analysis of the dynamic soaring flight of the albatross with ecological interpretations. *Tech. Rep.* Virginia Institute of Marine Science.

de Croon, G. C. H. E., de Clercq, K. M. E., Ruijsink, R., Remes, B. & de Wagter, C. 2009 Design, aerodynamics, and vision-based control of the delfly. *Int. J. Micro Air Veh.* **1** (2), 71–97.

Cummins, C., Seale, M., Macente, A., Certini, D., Mastropaolo, E., Viola, I. M. & Nakayama, N. 2018 A separated vortex ring underlies the flight of the dandelion. *Nature* **562** (7727), 414–418.

Deng, H.-B., Xu, Y.-Q., Chen, D.-D., Dai, H., Wu, J. & Tian, F.-B. 2013 On numerical modeling of animal swimming and flight. *Comput. Mech.* **52** (6), 1221–1242.

Epps, B. P., Valdivia y Alvarado, P., Youcef-Toumi, K. & Techet, A. H. 2009 Swimming performance of a biomimetic compliant fish-like robot. *Exp. Fluids* **47** (6), 927.

Falgout, R. D. & Yang, U. M. 2002 hypre: A library of high performance preconditioners. In *Computational Science — ICCS 2002*, pp. 632–641.

Felis, M. 2017 RBDL: an efficient rigid-body dynamics library using recursive algorithms. *Auton. Robot.* **41** (2), 495–511.

Fish, F.E. & Lauder, G.V. 2006 Passive and active flow control by swimming fishes and mammals. *Ann. Rev. Fluid Mech.* **38** (1), 193–224.

Folk, M., Heber, G., Koziol, Q., Pourmal, E. & Robinson, D. 2011 An overview of the HDF5 technology suite and its applications. In *Proceedings of the EDBT/ICDT 2011 Workshop on Array Databases*, pp. 36–47. Association for Computing Machinery.

Fregene, K. & Bolden, C. L. 2010 Dynamics and control of a biomimetic single-wing nano air vehicle. In *American Control Conference (ACC), 2010*, pp. 51–56. IEEE.

Gonzalo, A. 2018 Aerodynamic forces and vortex structures of flapping wings in forward flight. PhD thesis, Univ. Carlos III Madrid.

Greene, D. F. & Johnson, E. A. 1990 The aerodynamics of plumed seeds. *Funct. Ecol.* pp. 117–125.

Griffith, B. E. & Patankar, N. A. 2020 Immersed methods for fluid–structure interaction. *Annu. Rev. Fluid Mech.* **52** (1), 421–448.

Helbling, E. F. & Wood, R. J. 2018 A review of propulsion, power, and control architectures for insect-scale flapping-wing vehicles. *Appl. Mech. Rev.* **70** (1), 010801.

Hightower, B. J., Ingersoll, R., Chin, D. D., Lawhon, C., Haselsteiner, A. F. & Lentink, D. 2017 Design and analysis of aerodynamic force platforms for free flight studies. *Bioinspir. Biomim.* **12** (6), 064001.

Hirsch, C. 2007 *Numerical computation of internal and external flows: The fundamentals of computational fluid dynamics*. Elsevier.

Hou, G., Wang, J. & Layton, A. 2012 Numerical methods for fluid-structure interaction – a review. *Commun. Comput. Phys.* **12** (2), 337–377.

Jouventin, P. & Weimerskirch, H. 1990 Satellite tracking of wandering albatrosses. *Nature* **343** (6260), 746–748.

Keennon, M., Klingebiel, K. & Won, H. 2012 Development of the nano hummingbird: A tailless flapping wing micro air vehicle. In *50th AIAA Aerospace Sciences Meeting including the New Horizons Forum and Aerospace Exposition*. American Institute of Aeronautics and Astronautics.

Miklosovic, D. S., Murray, M. M., Howle, L. E. & Fish, F. E. 2004 Leading-edge tubercles delay stall on humpback whale (Megaptera novaeangliae) flippers. *Phys. Fluids* **16** (5), L39–L42.

Mittal, R. & Iaccarino, G. 2005 Immersed boundary methods. *Annu. Rev. Fluid Mech.* **37** (1), 239–261.

Moriche, M. 2017 A numerical study on the aerodynamic forces and the wake stability of flapping flight at low reynolds number. PhD thesis, Univ. Carlos III Madrid.

Moriche, M., Uhlmann, M. & Dŭsek, J. 2021 A single oblate spheroid settling in unbounded ambient fluid: a benchmark for simulations in steady and unsteady wake regimes. *Int. J. Multiphase Flow* p. 103519.

Nathan, R. 2006 Long-distance dispersal of plants. *Science* **313** (5788), 786–788.

Norberg, R. 1973 Autorotation, self-stability, and structure of single-winged fruits and seeds (samaras) with comparative remarks on animal flight. *Biol. Rev.* **48** (4), 561–596.

Peskin, C. S. 2002 The immersed boundary method. *Acta Numer.* **11**, 479–517.

Rai, M. & Moin, P. 1991 Direct simulations of turbulent flow using finite-difference schemes. *J. Comput. Phys.* **96** (1), 15–53.

Rival, D. E. & Oudheusden, B. v. 2017 Load-estimation techniques for unsteady incompressible flows. *Exp. Fluids* **58** (3), 20.

Ryzhakov, P. B., Rossi, R., Idelsohn, S. R. & Oñate, E. 2010 A monolithic lagrangian approach for fluid–structure interaction problems. *Comput. Mech.* **46** (6), 883–899.

Shaffer, S. A., Costa, D. P. & Weimerskirch, H. 2001 Behavioural factors affecting foraging effort of breeding wandering albatrosses. *J. Anim. Ecol.* **70** (5), 864–874.

Shyy, W., Aono, H., Kang, C.-K. & Liu, H. 2013 *An introduction to flapping wing aerodynamics*, , vol. 37. Cambridge University Press.

Smits, A. J. 2019 Undulatory and oscillatory swimming. *J. Fluid Mech.* **874**, P1.

Tackenberg, O., Poschlod, P. & Kahmen, S. 2003 Dandelion seed dispersal: The

horizontal wind speed does not matter for long-distance dispersal - it is updraft! *Plant Biol.* **5** (5), 451–454.

Triantafyllou, M. S. & Triantafyllou, G. S. 1995 An efficient swimming machine. *Sci. Am.* **272** (3), 64–70.

Uhlmann, M. 2005 An immersed boundary method with direct forcing for the simulation of particulate flows. *J. Comput. Phys.* **209** (2), 448–476.

Ulrich, E. R., Darryll, P. & Humbert, J. S. 2010 From falling to flying: the path to powered flight of a robotic samara nano air vehicle. *Bioinspir. Biomim.* **5** (4), 045009.

Videler, J. J. & Wardle, C. S. 1991 Fish swimming stride by stride: speed limits and endurance. *Rev. Fish Biol. Fisheries* **1** (1), 23–40.

Wang, Z. J. 2005 Dissecting insect flight. *Ann. Rev. Fluid Mech.* **37** (1), 183–210.

Wood, R. J. 2008 The first takeoff of a biologically inspired at-scale robotic insect. *IEEE Trans. Rob.* **24** (2), 341–347.

Part II

Papers

Summary of the papers

Paper 1

A weakly coupled immersed boundary method and dynamic algorithm for the fluid-structure interaction of multi-body systems

Paper 2

Kinematics and dynamics of the auto-rotation of a model winged seed

Paper 3

A numerical study of the flow around a model winged seed in auto-rotation

Paper 4

Three-dimensional effects on the aerodynamic performance of flapping wings in tandem configuration

Paper 5

Flow interaction of three-dimensional self-propelled flexible plates in tandem

1

Paper 1

A weakly coupled immersed boundary method and dynamic algorithm for the fluid-structure interaction of multi-body systems

G. Arranz[1], **O. Flores**[1], **M. García-Villalba**[1]

[1] Universidad Carlos III de Madrid, Spain

Journal Computational Physics (Under review) (2021)

We present a method for computing fluid-structure interaction problems for multi-body systems. The fluid flow equations are solved using a conventional fractional-step method with the immersed boundary method proposed by Uhlmann [J. Comput Phys. 209 (2005) 448]. The equations of the rigid bodies are solved using recursive algorithms proposed by Felis [Auton. Robot 41 (2017) 495]. The two systems of equations are weakly coupled, so that the resulting method is cost-effective. The accuracy of the method is demonstrated by comparison with two-dimensional cases of the literature: the flapping of a flexible airfoil and the self-propulsion of a plunging flexible plate. As an illustration of the capabilities of the proposed method, two three-dimensional bio-inspired problems are presented: an extension to three dimensions of the plunging flexible plate and a simple model of spider ballooning.

Key words: immersed boundary method, multi-body system, Navier–Stokes equations, fluid-structure interaction, bioinspired locomotion

1. Introduction

The understanding of the mechanisms of biological motion, such as insect flight, fish swimming, bacteria swarming or seed dispersal by wind, has shown to be important for scientific and engineering applications. Clear examples are the recent developments in micro-air vehicles (de Croon *et al.* 2009; Richter & Lipson 2011; Keennon *et al.* 2012) or swimming robots (Triantafyllou & Triantafyllou 1995; Hirata *et al.* 2000; Yu *et al.* 2004). However, despite these advances, there is still a lack of proper knowledge about the physics underlying the motion of biological systems. This restricts artificial systems from achieving the performance of biological systems.

In particular, one of the shortcomings associated to the modelling of biological motion is that it is computationally challenging. From a physical point of view, it can be envisaged as a fluid-structure interaction (FSI) problem, in which one or more bodies are immersed in a fluid. The dynamics of the bodies is a direct result of their hydrodynamic interaction with the surrounding fluid. As a consequence, the resulting problem is a highly non-linear problem consisting of the coupling between the equations of the fluid motion and the equations of motion of the bodies. An additional aspect to be considered is the geometrical variability of the bodies found in

applications: they may have mobile appendages (e.g., the wings of flying animals or robots, fins of aquatic swimmers, etc.), they may be deformable and subject to large deformations, etc. This poses additional complexities in order to model this kind of problems. First, the fluid-solid interface changes with time. Second, the equations of the body dynamics can become complex to derive and to solve.

In computational fluid dynamics, solid-fluid interfaces can be represented with two families of procedures that differ in the spatial discretization of the fluid near the solid: conforming mesh methods and non-conforming mesh methods (Deng *et al.* 2013). In the former, the interface condition is treated as a physical boundary, which requires the re-meshing of the fluid domain due to the movement of the bodies as time evolves. The Arbitrary Eulerian-Lagrangian (ALE) method in Donea *et al.* (2017) is an example of conforming mesh methods. On the other hand, in non-conforming mesh methods, a physical boundary between the bodies and the fluid does not exist, but constraints are imposed to the fluid equations such that interface conditions are fulfilled at the boundaries. As a consequence, re-meshing of the fluid domain is not required. In this regard, immersed methods such as immersed boundary methods (IBM) have proven to be a very useful tool to reproduce the arbitrary motion of solids immersed in a fluid (Mittal & Iaccarino 2005; Griffith & Patankar 2020; Uhlmann 2005; Pinelli *et al.* 2010; Breugem 2012; Kempe & Fröhlich 2012).

Regarding the modelling of the dynamics of the bodies, in some situations, a feasible approach is to approximate a given complex body as a set of rigid bodies connected among them by kinematic constraints (see for example Liu (2009); Suzuki *et al.* (2015)). Under this approach, the dynamics of the bodies are represented as a system of non-linear differential equations which is influenced by the inertia properties of the rigid bodies and the connections among them. Note that there is a large variability of possible system configurations so that, in general, the system of non-linear differential equations needs to be re-derived every time the configuration is modified (i.e., adding a body, such as a tail, or changing the type of links between bodies). In this regard, robotic algorithms stand as an outstanding choice to compute the dynamics of a complex system of rigid bodies with a semi-automatic procedure (Featherstone 2014).

Most of the works which study the FSI of multi-body system derived the equations of motion specifically for the problem under consideration (Zhang *et al.* 2013; Arora *et al.* 2018; Suzuki *et al.* 2019; Yao & Yeo 2019). On the contrary, few works are found in the literature which are able to compute the interaction problem of a generic multi-body system with a surrounding flow. For example, Wang & Eldredge (2015) reported a vorticity-based immersed boundary projection method with a strong coupling of the dynamics equations. More recently, Li *et al.* (2018) coupled a multi-body algorithm with the existing finite volume method of the commercial software, Ansys, to solve the flow around the bodies. In this case, only rotations where allowed between the bodies conforming the multi-body system. The time coupling between both algorithm was accomplished in a staggered fashion, leading to a weak coupling of both systems. Finally, Bernier *et al.* (2019) recently developed a 2D vortex particle method coupled with a multi-body solver, extending the work by Gazzola *et al.* (2011).

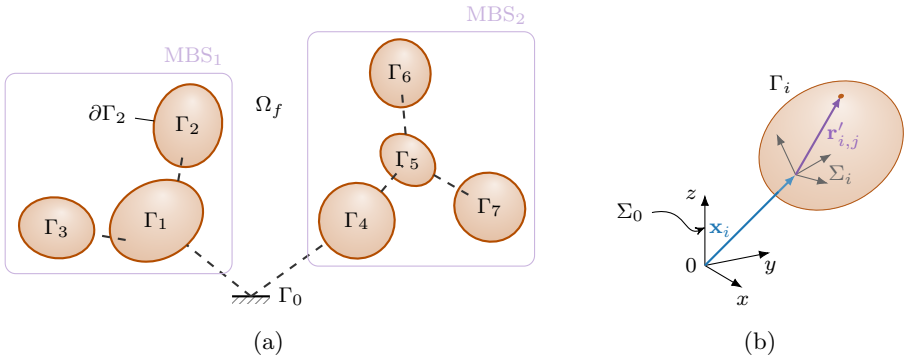

FIGURE 1: (a) Schematic representation of the interaction of two multi-body systems (MBS$_1$ and MBS$_2$) of rigid bodies, Γ_i, with a surrounding fluid domain, Ω_f. The connections among the bodies are represented as dashed lines. Γ_0 is a fixed inertial reference base. (b) Definition of the reference systems, Σ, and vectors used to define the position and orientation of a given body Γ_i.

In this article, we present a methodology to compute the dynamics of multi-body systems immersed in an incompressible Newtonian fluid using a partitioned (non monolithic) approach. The flow equations are solved by means of Direct Numerical Simulation (DNS) where the presence of the bodies is modelled using the IBM proposed by Uhlmann (2005). The dynamics of the multi-body systems is solved using recursive dynamic algorithms in reduced coordinates developed by Felis (2017).

The structure of the paper is as follows: the methodology is presented in § 2; a validation of the methodology with existing cases reported in the literature is found in § 3; in § 4, two illustrative problems solved using this methodology are presented; and, finally, the major conclusions of this study are gathered in § 5.

2. Methodology

2.1. *Problem description*

The physical problem considered in the present work is the interaction of a multi-body system (MBS) of rigid bodies with a surrounding fluid. In this MBS, the rigid bodies are connected among them by joints (i.e., kinematic constraints) and are subject to the hydrodynamic forces and torques exerted by the surrounding fluid. Note that a collection of MBSs can also be handled by the proposed method. This is illustrated with a sketch in Figure 1a, where Γ_i stands for the ith rigid body of the MBS. Note that Γ_0 in the sketch does not represent a rigid body, but a fixed inertial base. Consequently, the joints connecting Γ_1 and Γ_4 to Γ_0 do not necessarily restrict any degree of freedom (i.e., free body motion).

The fluid is modelled as incompressible and Newtonian, whose governing equations are

$$\nabla \cdot \mathbf{u} = 0, \tag{1a}$$

$$\frac{\partial \mathbf{u}}{\partial t} + (\mathbf{u} \cdot \nabla)\mathbf{u} = -\frac{1}{\rho}\nabla p + \nu \nabla^2 \mathbf{u} + \mathbf{f}, \tag{1b}$$

where $\mathbf{u}$ is the fluid velocity field, ρ is the fluid density, p is the pressure, ν is the kinematic viscosity, and $\mathbf{f}$ is a forcing term. The latter is calculated to fulfill the *non-slip boundary condition* on the surface of the bodies,

$$\mathbf{u}(\mathbf{x}) = \mathbf{U}_{\partial\Gamma_i}(\mathbf{x}) \quad \forall \mathbf{x} \in \partial\Gamma_i, \quad \forall i \in B, \tag{2}$$

where $\mathbf{U}_{\partial\Gamma_i}$ is the velocity on the surface of the rigid body Γ_i, and $B = \{1, ..., N_B\}$, is the set of rigid bodies, being N_B the total number of them.

Concerning the equations that govern the dynamics of the MBS, recall that six scalar equations, the so-called Newton-Euler equations, are needed to represent the dynamics of a single rigid body in three dimensions (3D). Thus, in principle $6 \times N_B$ equations fully describe the dynamics of the MBS. However, the joints connecting bodies usually constrain their relative motion. Consequently, it is possible to reduce the number of equations to the number of the degrees of freedom (N_{dof}) of the MBS. Although several methodologies can be adopted to find these equations (Greenwood 2006), the final result leads to a system of ordinary differential equations which can be written in the form Featherstone (2014):

$$\mathsf{H}(\mathbf{q})\ddot{\mathbf{q}} + \mathsf{c}(\mathbf{q}, \dot{\mathbf{q}}) = \boldsymbol{\xi} + \boldsymbol{\xi}_h, \tag{3}$$

where $\mathbf{q}$ is the vector of the generalized coordinates (of size $N_{dof} \times 1$), H is the joint space or generalized inertia matrix, c is the generalized bias force (accounting for gravity, Coriolis and centrifugal forces), $\boldsymbol{\xi}$ is the vector of generalized forces (e.g., springs and/or dampers in the joints, *etc.*), and $\boldsymbol{\xi}_h$ is the vector of generalized forces due to the surrounding fluid (i.e., hydrodynamic forces). Note that, although only the dependence on $\mathbf{q}$ and $\dot{\mathbf{q}}$ of H and c is made explicit in eq. (3), both also depend on the inertia properties of the bodies. Note also that, $\mathbf{q}$ represents the configuration of the MBS at a given time instant in the N_{dof}-dimensional *configuration* space (Greenwood 2006; Boyer & Porez 2015).

In the following subsections, the solver employed to solve eq. (1) and eq. (3) are described (in § 2.2 and § 2.3, respectively), followed by the description of the algorithm coupling both solvers (§ 2.4).

2.2. *Flow solver*

Equation (1) is solved using the numerical method proposed by Uhlmann (2005), where the forcing term is modelled using Uhlmann's immersed boundary method (IBM). The method requires the use of two grids. First, the fluid domain, Ω_f, is discretized into a fixed, Cartesian grid, the so-called Eulerian grid. Second, the surface of each rigid-body, $\partial\Gamma_i$, is discretized into n_i evenly distributed points. Therefore, the set of surface points for a body Γ_i is defined as $L(i) = \{1, ..., n_i\}$, and the position of grid points on $\partial\Gamma_i$ is labelled as $\mathbf{X}_{i,j}$, $j \in L(i)$. This is the so-called Lagrangian grid.

The equations (1) are solved using a fractional step method. The spatial derivatives are discretized with 2nd order finite differences in a staggered grid. The temporal scheme is a 3-stage low-storage, semi-implicit Runge-Kutta, in which the convective terms are treated explicitly and the viscous terms are treated implicitly. For completeness, the discretized equations at the kth Runge-Kutta substep are provided below:

$$\tilde{\mathbf{u}} = \mathbf{u}^{k-1} + \Delta t \left(2\alpha_k \nu \nabla^2 \mathbf{u}^{k-1} - 2\alpha_k \rho^{-1} \nabla p^{k-1} - \gamma_k [(\mathbf{u}\cdot\nabla)\mathbf{u}]^{k-1} - \zeta_k [(\mathbf{u}\cdot\nabla)\mathbf{u}]^{k-2}\right), \tag{4a}$$

$$\nabla^2 \mathbf{u}^* - \frac{\mathbf{u}^*}{\alpha_k \nu \Delta t} = -\frac{1}{\nu \alpha_k}\left(\frac{\tilde{\mathbf{u}}}{\Delta t} + \mathbf{f}^k\right) + \nabla^2 \mathbf{u}^{k-1}, \tag{4b}$$

$$\nabla^2 \phi^k = \frac{\nabla \cdot \mathbf{u}^*}{2\alpha_k \Delta t}, \tag{4c}$$

$$\mathbf{u}^k = \mathbf{u}^* - 2\alpha_k \Delta t \nabla \phi^k, \tag{4d}$$

$$p^k = p^{k-1} + \rho\left(\phi^k - \alpha_k \nu \Delta t \nabla^2 \phi^k\right), \tag{4e}$$

where $\tilde{\mathbf{u}}$ is an estimated velocity without the forcing term (i.e., disregarding the solid surfaces), ϕ is the pseudo-pressure and the the Runge-Kutta coefficients (α_k, γ_k and ζ_k) are taken from Rai & Moin (1991).

The forcing term in eq. (4b), $\mathbf{f}^k$, is obtained from estimating the necessary force to fulfil the boundary condition given by eq. (2):

$$\mathbf{F}^k(\mathbf{X}_{i,j}) = \frac{\mathbf{U}^{k-1}_{\partial\Gamma_i}(\mathbf{X}_{i,j}) - \tilde{\mathbf{U}}(\mathbf{X}_{i,j})}{\Delta t}, \quad \forall j \in L(i), i \in B. \tag{5}$$

In this equation, $\tilde{\mathbf{U}}$ corresponds to $\tilde{\mathbf{u}}$ interpolated to the Lagrangian points. Note that this implementation of the IBM requires interpolations from the Eulerian grid to the Lagrangian grid ($\tilde{\mathbf{u}} \mapsto \tilde{\mathbf{U}}$), as well as a spreading operator from the Lagrangian grid to the Eulerian grid ($\mathbf{F}^k \mapsto \mathbf{f}^k$). These two operators are defined using the regularized delta functions introduced by Peskin (2002), which satisfy the necessary conditions in terms of conservation of momentum, force and torque in the interpolation and spreading operations.

For further details on the immersed boundary method described above, the reader is referred to Uhlmann (2005). This algorithm has been implemented in a code called TUCAN, which has been successfully used for the simulation of rigid-bodies with prescribed kinematics (Moriche *et al.* 2016, 2017; Gonzalo *et al.* 2018; Arranz *et al.* 2020). Likewise, the free motion of a single-rigid body immersed in a fluid has been also successfully simulated (Arranz *et al.* 2018*b*,*a*), using the coupling method presented in Uhlmann (2005).

2.3. *Multi-body solver*

The temporal integration of eq. (3) provides the generalized velocities, which in turn, are integrated to compute the generalized coordinates at a given time instant, t. Nonetheless, the kinematics of several DoFs are often known as a prescribed function

of time (e.g., the motion of a wing with respect to the flyer's body). Therefore, it is convenient to write $\mathbf{q}$ as $\mathbf{q} = \begin{bmatrix}\mathbf{q}_u^\mathsf{T} & \mathbf{q}_p^\mathsf{T}\end{bmatrix}^\mathsf{T}$, where $\mathbf{q}_p$ contains the generalized coordinates whose temporal evolution is prescribed. Likewise,

$$\mathsf{H} = \begin{bmatrix}\mathsf{H}_u & \mathsf{H}_{up} \\ \mathsf{H}_{pu} & \mathsf{H}_p\end{bmatrix}, \qquad \mathsf{c} = \begin{bmatrix}\mathsf{c}_u \\ \mathsf{c}_p\end{bmatrix}, \qquad \boldsymbol{\xi} = \begin{bmatrix}\boldsymbol{\xi}_u \\ \boldsymbol{\xi}_p\end{bmatrix}, \qquad \boldsymbol{\xi}_h = \begin{bmatrix}\boldsymbol{\xi}_{h,u} \\ \boldsymbol{\xi}_{h,p}\end{bmatrix} \tag{6}$$

Therefore, a reduced system for the unknown generalized accelerations is found,

$$\mathsf{H}_u(\mathbf{q})\ddot{\mathbf{q}}_u = \boldsymbol{\xi}_u - \mathsf{c}_u^*(\mathbf{q}, \dot{\mathbf{q}}) + \boldsymbol{\xi}_{h,u}, \tag{7}$$

where $\mathsf{c}_u^* = \mathsf{c}_u + \mathsf{H}_{up}\ddot{\mathbf{q}}_p$. The reduced system of eq. (7) has the same form as eq. (3) but consists of $N_{dof} - N_p$ algebraic equations (where N_p is the number of DoF whose motion is prescribed). Note also that H_u and c_u^* depend on all generalized coordinates, prescribed and otherwise.

Equation (7) is discretized using the same temporal scheme used for the convective terms in eq. (1),

$$\dot{\mathbf{q}}_u^k = \dot{\mathbf{q}}_u^{k-1} + \Delta t \left(\gamma_k[\mathsf{H}_u^{-1}(\boldsymbol{\xi}_u - \mathsf{c}_u^*)]^{k-1} + \zeta_k[\mathsf{H}_u^{-1}(\boldsymbol{\xi}_u - \mathsf{c}_u^*)]^{k-2} + [\mathsf{H}_u^{-1}]^{k-1}\boldsymbol{\xi}_{h,u}^k\right), \tag{8}$$

where the inverse of the reduced joint space matrix (H_u) is computed using the Cholesky factorization. On the other hand, $\boldsymbol{\xi}_{h,u}^k$ are the generalized forces mapped from the physical hydrodynamic forces computed from $\mathbf{F}^k$ of eq. (5) as explained in the following section.

The generalized coordinates are computed implicitly, as in the coupling method proposed in Uhlmann (2005), using the same scheme as for the viscous terms in eq. (4),

$$\mathbf{q}_u^k = \mathbf{q}_u^{k-1} + \Delta t \alpha_k(\dot{\mathbf{q}}_u^k + \dot{\mathbf{q}}_u^{k-1}). \tag{9}$$

As mentioned in the introduction, several methods can be used to derive eq. (3) and compute the corresponding joint space inertia matrix, H, and the bias force vector, c. In the present work, the open-source Rigid Body Dynamics Library (RBDL) developed by Felis (2017) has been employed. In particular, c is computed using the Recursive Newton-Euler algorithm (RNEA), and H is computed by means of the Composite Rigid-Body algorithm (CRBA) (Featherstone 2014; Felis 2017). These matrices are then reordered into eq. (6) to obtain H_u and c_u^*. Lastly, the expression for the generalized forces is discussed in next section and in B.2.

Finally, it is worth mentioning that several degrees of freedom are allowed between two connected bodies. In these cases, the joint that links the bodies is usually denoted as *multiple DoF joint*. Depending on the involved degrees of freedom, the definition of these joints can become cumbersome. Therefore, for a higher versatility of the algorithm, multiple DoF joints are simulated using single DoF joints (i.e., prismatic or revolute joints) with *virtual* bodies whose mass and inertia is zero (Felis 2017) (see Appendix A for further details). The only exceptions are spherical joints (3 rotations), which are simulated using a quaternion formulation to avoid singularities (Featherstone 2014).

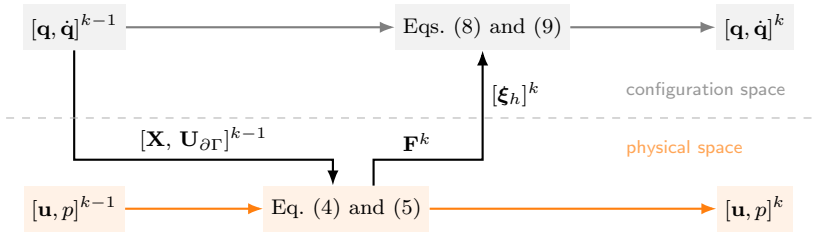

FIGURE 2: Schematic diagram of the coupling between the fluid solver and the dynamic algorithm during a Runge-Kutta substep. these are used to compute the new state of the multi-body system.

2.4. *Coupling*

The coupling of the algorithms corresponding to the fluid phase and to the MBS is depicted in Fig. 2. Let the state of fluid phase and MBS be known at Runge-Kutta substep $k-1$. The steps are as follows:

1. The generalized coordinates and velocities ($\mathbf{q}^{k-1}$ and $\dot{\mathbf{q}}^{k-1}$) are used to compute the position and velocity of *the Lagrangian points*, namely, $\mathbf{X}_{i,j}$ and $\mathbf{U}^{k-1}_{\partial\Gamma_i}(\mathbf{X}_{i,j})$.
2. The latter is used in eq. (5) to compute $\mathbf{F}^k$, which is then transferred to the Eulerian grid, $\mathbf{F}^k \mapsto \mathbf{f}^k$.
3. With $\mathbf{f}^k$, eq. (4) can be solved to obtain the state of the fluid phase at substep k, namely, $\mathbf{u}^k$ and p^k inside Ω_f.
4. The hydrodynamic forces and moments acting on the bodies ($\mathcal{F}$, $\mathcal{M}$) are computed from $\mathbf{F}^k$, as detailed below.
5. ($\mathcal{F}$, $\mathcal{M}$) are mapped as generalized external forces, $\boldsymbol{\xi}_h$. Then, eq. (8) is solved, yielding $\dot{\mathbf{q}}^k$.
6. Finally, $\mathbf{q}^k$ is computed from eq. (9), fully determining the state of the bodies at substep k.

Note that, in the fluid solver, $\mathbf{X}$ and $\mathbf{U}_{\partial\Gamma}$ are treated explicitly (i.e., at $k-1$), while in the multi-body solver $\boldsymbol{\xi}_h$ represents the hydrodynamic force integrated between $k-1$ and k. This leads to a *weak coupling* of the sub-systems, where the flow field at the solid interface may not be fully compatible with the solid's interface velocity at the end of the time step (Uhlmann 2005).

To build the mapping $(\mathbf{q}, \dot{\mathbf{q}}) \mapsto (\mathbf{X}_{i,j}, \mathbf{U}_{\partial\Gamma_i}(\mathbf{X}_{i,j}))$, it is necessary to know the position of a control point of Γ_i, $\mathbf{x}_i$; the orientation of Γ_i with respect to the inertial coordinate basis, Σ_0 (given by the rotation matrix E_i); and the angular and linear velocity of the control point, $\boldsymbol{\omega}_i$ and $\mathbf{v}_i$, respectively. Thus,

$$\mathbf{X}_{i,j} = \mathbf{x}_i^0 + \mathsf{E}_i \mathbf{r}'_{i,j}, \tag{10a}$$

$$\mathbf{U}_{\partial\Gamma_i} = \mathbf{v}_i^0 + \boldsymbol{\omega}_i^0 \times \mathsf{E}_i \mathbf{r}'_{i,j}, \tag{10b}$$

where the superscripts indicate the coordinate basis in which the vector is expressed, and $\mathbf{r}'_{i,j}$ is the relative position of the point $j \in L(i)$ on the surface of the ith body, with respect to the body's control point expressed in Σ_i (hence, it is a fixed quantity

for a rigid body). Note that, $\mathbf{x}_i^0$ and E_i can be calculated from the rotation matrices and position vectors of the joints that link Γ_i to the ground. Likewise, $\boldsymbol{\omega}_i$ and $\mathbf{v}_i$ can be expressed as functions $f(\mathbf{q}, \dot{\mathbf{q}})$. In the present case, these variables can directly be extracted from the multi-body library, RBDL. For the interested reader, B.1 provides the expressions to compute $\mathbf{x}_i^0$, $\boldsymbol{\omega}_i$ and $\mathbf{v}_i$.

The hydrodynamic forces and moments acting upon the body Γ_i, namely, $\mathcal{F}_i$ and $\mathcal{M}_i$, can be shown to be (Uhlmann 2005):

$$\mathcal{F}_i = \underbrace{-\rho \sum_{j \in L(i)} \mathbf{F}(\mathbf{X}_{i,j}) \Delta V_j}_{\mathcal{G}_i} + \frac{\rho}{\rho_i} m_i \ddot{\mathbf{x}}_{G,i}, \tag{11a}$$

$$\mathcal{M}_i = \underbrace{-\rho \sum_{j \in L(i)} (\mathbf{X}_{i,j} - \mathbf{x}_i) \times \mathbf{F}(\mathbf{X}_j) \Delta V_j}_{\mathcal{N}_i} + \rho \int_{\partial \Gamma_i} (\mathbf{x} - \mathbf{x}_i) \times \mathbf{u} \, \mathrm{d}\mathbf{x}, \tag{11b}$$

where ρ_i, m_i and $\mathbf{x}_{G,i}$ are the density, mass and position of the gravity centre of Γ_i, respectively. The integral term of eq. (11b) represents the rate of change of angular momentum of the fluid inside Γ_i whose value has to be computed by numerical integration, as in other works (Tschisgale *et al.* 2017). However, in the present work this term is approximated by supposing rigid-body motion of the fluid inside Γ_i, for efficiency reasons, as in Uhlmann (2005). This entails that the contribution of the last term of eq. (11) can be embedded in H and c if they are built using an effective density for each body equal to $(\rho_i - \rho)$, in a similar fashion as for single rigid bodies in Uhlmann (2005). This imposes a lower limit of the density ratios that can be simulated using the present approach of approximately $\rho_i/\rho \geq 1.2$, based on Uhlmann (2005). The remaining terms of eq. (11), namely $\mathcal{G}_i$ and $\mathcal{N}_i$, constitute then $\boldsymbol{\xi}_h$ of eq. (3) after mapped to the space of generalized forces (see B.2 for further details).

3. Validation

As detailed in § 2, the multi-body algorithm developed herein has been coupled with a pre-existing flow solver which has already been used to solve the coupled fluid-structure interaction of single rigid bodies (Arranz *et al.* 2018*b*,*a*). Since the multi-body algorithm can be also used to simulate the problem of a single rigid body with several DoFs (i.e., by defining virtual, mass-less bodies, linked by the single DoFs joints described in appendix Appendix A), we can compare the results of the multi-body algorithm with those obtained with the pre-existing algorithm. Since the flow solver is the same, the only differences should arise from the construction and solution of the dynamic equations. Several test cases have been performed following this methodology (both in 2D and 3D), including the free fall of circular cylinders (2D) and spheroids (3D), and the auto-rotation of a winged *samara* seed (Arranz *et al.* 2018*b*), yielding an excellent agreement between the multi-body and single-rigid-body algorithms. These tests are not presented herein for the sake of brevity, and instead, we validate our multi-body solver against 2D multi-body problems previously reported in the literature.

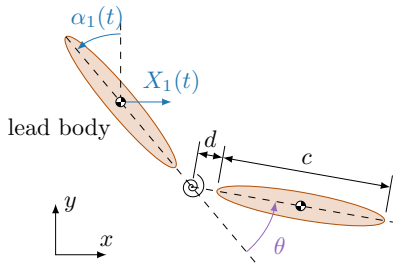

FIGURE 3: Sketch of the validation case adapted from Toomey & Eldredge (2008).

3.1. *Flapping of a flexible airfoil*

The first validation case is extracted from Toomey & Eldredge (2008). A sketch of the problem is shown in Fig. 3. It consists of two 2D rigid bodies connected by a torsional spring and a damper, immersed in a quiescent fluid. Both bodies are ellipses of aspect ratio $5:1$ of major axis c. The distance between each body and the torsional spring is $d = 0.05c$. The motion of the lead body is fully prescribed and given by the linear displacement of its centre of mass, $X_1(t)$, and the orientation angle, $\alpha_1(t)$. The motion of the follower body is given by the deflection angle, $\theta(t)$, between the follower and the lead body (see Fig. 3), which results from the dynamic interaction with the lead body and the surrounding fluid. Hence, the degrees of freedom of the MBS are X_1, α_1 and θ, while the only unknown degree of freedom is θ. Consequently, the vectors of generalized coordinates are $\mathbf{q}_p = [X_1,\, \alpha_1]$ and $\mathbf{q}_u = \theta$. The prescribed motion of the lead body follows the time laws

$$X_1(t) = \frac{A_0}{2}\frac{G_t(ft)C(ft)}{\max\left(G_t\right)}, \qquad \alpha_1(t) = -\beta\frac{G_r(ft)}{\max\left(G_r\right)},$$

where f is the frequency of oscillation ($T = 1/f$ is the period of oscillation), and the translational and angular amplitudes are set to $A_0/c = 1.4$ and $\beta = \pi/4$, respectively. Furthermore,

$$G_t(t) = \int_t \tanh\left(\sigma\cos 2\pi t'\right)dt', \qquad G_r(t) = \tanh\left(\sigma\cos 2\pi t\right),$$

$$C(t) = \frac{\tanh\left(8t-2\right) + \tanh 2}{1+\tanh 2}.$$

Two cases from Toomey & Eldredge (2008) are considered: Case 1 ($\sigma = 0.628$) and Case 4 ($\sigma = 3.770$). Fig. 4 depicts the kinematics of the lead body for both cases. The rest of parameters that fully define the problem are the rotation Reynolds number, $Re_r = \dot{\alpha}_M c^2/\nu = 100$ (where $\dot{\alpha}_M$ is the maximum angular velocity); the body-to-fluid density ratio, $\rho_s/\rho = 5$; the dimensionless spring stiffness, $K^* = K/(\rho f^2 c^4) = 456$; and the damping coefficient, $R^* = R/(\rho f c^4) = 3.95$.

The results obtained with the present algorithm are compared with the results reported by Toomey & Eldredge (2008) using a viscous vortex particle method, and with the results reported by Wang & Eldredge (2015) using the IB-projection method.

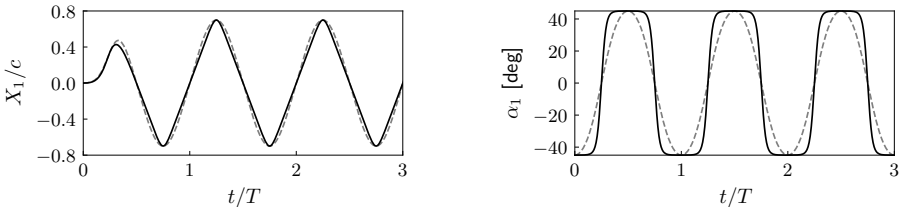

FIGURE 4: (a) Horizontal position and (b) pitch angle of the lead body as a function of time. (- - -) Case 1; (——) Case 4.

Note that both cases use strongly coupled body dynamics, while in the present algorithm the body dynamics are weakly coupled with the fluid solver.

In the present simulations, the computational domain is a square of side $32c$ (like in Wang & Eldredge (2015)) with periodic boundary conditions. At $t = 0$, the centre of mass of the lead body is located at $8c$ from the top wall and centred in the horizontal direction. The fluid domain is discretized with a uniform mesh of grid spacing $\Delta x = c/64$. This is a slightly coarser resolution than the one used in previous studies (Toomey & Eldredge 2008; Wang & Eldredge 2015) ($\Delta x \approx c/100$). The time step is set to $\Delta t = 5 \cdot 10^{-4} T$, leading to $CFL \leq 0.4$. Finally, the bodies are discretized using a Lagrangian mesh with evenly spaced points with distance Δx.

Fig. 5 depicts the comparison of the deflection angle, θ, and the vertical force, F_y, between the current results and the existing literature. A good agreement of the evolution of the deflection angle, and the non-dimensional vertical force is observed for both cases despite the different numerical approaches and computational details.

3.2. *Self-propelling flexible plate*

The second validation case is taken from Arora *et al.* (2018) and consists of a 2D self-propelling flexible plate. The plate is modelled using a lumped-torsional flexibility model as shown in Fig. 6a. In particular, the plate of chord C and thickness $e/C = 0.02$ is divided into five rectangular rigid bodies, of uniform density, ρ_s, separated by a distance $2d = e$, joint by torsional springs of torsional stiffness, K. The plate is free to move in the horizontal direction, whereas the vertical position of the leading edge is prescribed as:

$$Y(t) = A\cos(2\pi f t) \tag{12}$$

The relative deflection angle of body i with respect its predecessor, $i-1$, is defined as θ_i (see Fig. 6a). Consequently, the generalized vectors of the multi-body system are $\mathbf{q}_p = Y$ and $\mathbf{q}_u = [X, \theta_1, ..., \theta_5]$, where X is the horizontal coordinate of the leading edge of the plate.

The parameters that govern the present problem are the non-dimensional amplitude, $A/C = 0.6$; the Reynolds number, $Re = AfC/\nu = 100$; the body-to-fluid density ratio, $\rho_s/\rho = 10$; and the non-dimensional torsional stiffness, $K^* = K/\rho f^2 C^4 = 52.242$.

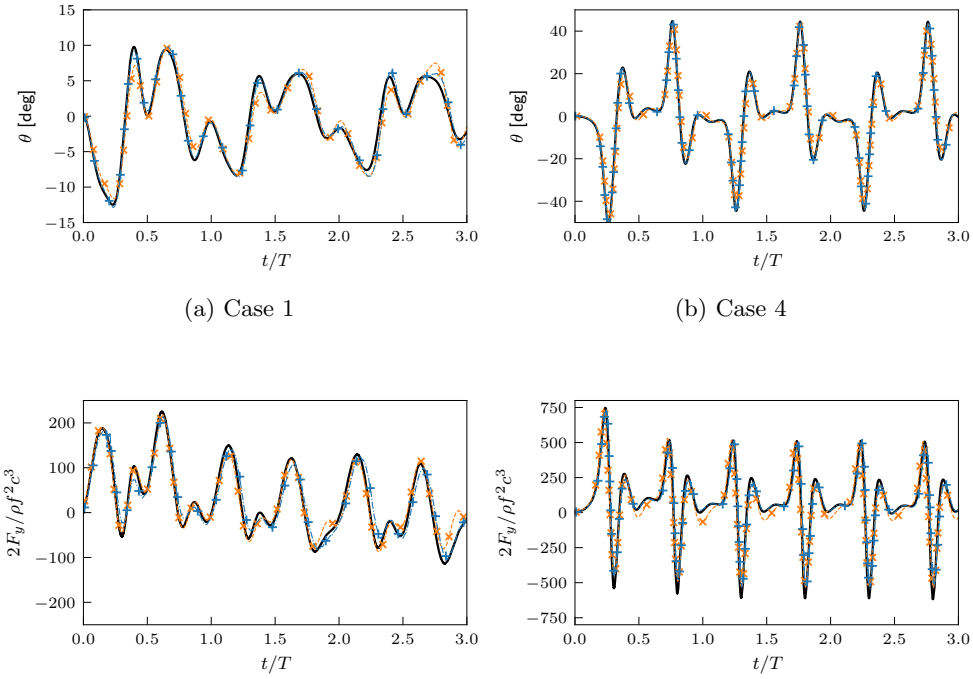

(a) Case 1 (b) Case 4

(c) Case 1 (d) Case 4

FIGURE 5: (a-b) Deflection angle of the follower body, and (c-d) total vertical force acting upon the multi-body system as a function of time. Note the difference in scale between cases 1 and 4. (——) present results, (-+-) Toomey & Eldredge (2008), and (-*-) Wang & Eldredge (2015).

The chosen parameters correspond to the case $\psi = A\rho/(e\rho_s) = 3$, $\omega^* = \omega_n/(2\pi f) = 3.5$ (where ω_n is the first natural frequency of the multi-body system), shown in Arora *et al.* (2018, Fig. 15 and 16).

The simulations are performed in a rectangular domain of size $20C \times 12C$ uniformly discretized with a grid size $\Delta x = 0.004C$. Note that, due to the plunging motion of the plate's LE, it moves horizontally at an instantaneous speed $\dot{X}(t)$. Therefore, the plate travels an horizontal distance $U_p T$ (where $U_p = f \int_{T-1}^{T} \dot{X} \mathrm{d}t$ is the mean propulsive speed), over a cycle. In order for the plate not to leave the computational domain, the plate is immersed in a uniform stream flow of intensity U_∞, such that $U_\infty \approx U_p$ and the mean horizontal displacement of the plate with respect to the computational domain is as small as possible. Consequently, Dirichlet boundary conditions are imposed at the inflow and lateral walls, namely, $u = U_\infty$ and $v = 0$ (where u and v are the horizontal and vertical fluid velocities, respectively, and U_∞ equals the estimated mean propulsive velocity extracted from (Arora *et al.* 2018, Fig. 14)); and an advective

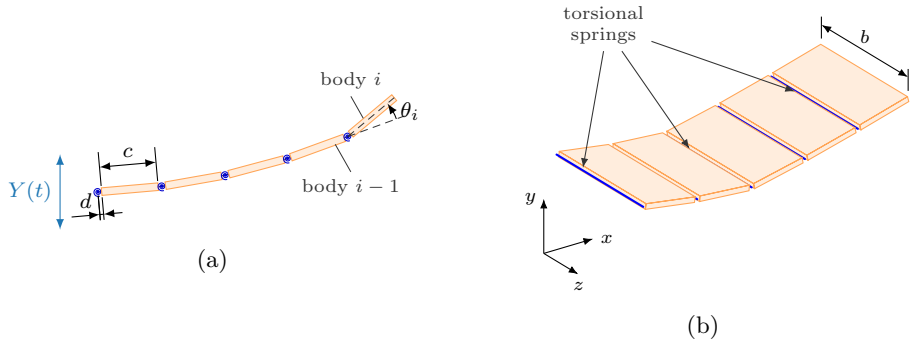

FIGURE 6: (a) Lumped-torsional flexibility model of the flexible plate based on Arora *et al.* (2018) consisting of 5 rectangular rigid bodies joined by torsional springs. (b) Extension of the model of Arora *et al.* (2018) to three-dimensions by considering rectangular plates of width b.

boundary condition is imposed at the outflow boundary. The bodies are discretized using a Lagrangian grid with equidistant points separated $\Delta x = 0.004C$ and the time step is $\Delta t = 5 \cdot 10^{-5} T$ (where $T = f^{-1}$). On the other hand, simulations in Arora *et al.* (2018) are performed using a Lattice-Boltzmann method with a computational domain $50C \times 20C$ and spatial discretization $\Delta x = 0.005C$.

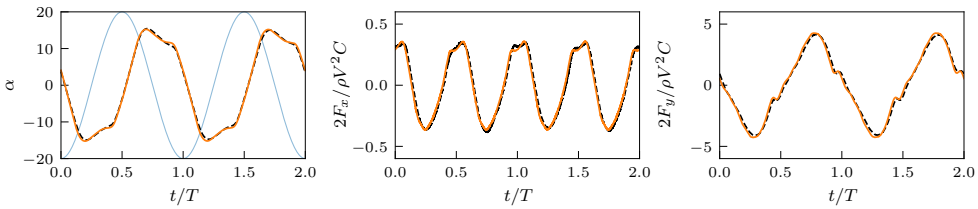

FIGURE 7: Comparison of the (a) tip deflection angle, (b) horizontal force and (c) vertical force: (——) present results, and (- - -) Arora *et al.* (2018). In Fig. 7a, (——) corresponds to the Y-position of the leading edge (without scale).

Fig. 7a depicts the time evolution during two cycles of the tip deflection angle (defined as the angle between the horizontal and the line that joins the leading edge and the trailing edge). Fig. 7b-c shows the time evolution of the horizontal and vertical forces exerted on the plate normalized by $\frac{1}{2}\rho V^2 C$, where $V = 2\pi f A$ is the maximum vertical velocity of the leading edge. It should be pointed out that results from Arora *et al.* (2018) correspond to cycles $48 - 49$, whereas the present results are for cycles $12 - 13$, since no changes were observed with respect to previous cycles. Nevertheless,

a good agreement is observed between the present simulations and those from Arora *et al.* (2018), with relative differences in the peak-to-peak amplitudes of the forces of less than 3%, and an absolute difference of the maximum tip-deflection angle lower than 0.19°.

4. Results

In the next sections, two examples of the capabilities of the proposed methodology are presented. In §4.1 the study from Arora *et al.* (2018) presented in §3.2 for validation is extended to a 3D configuration. In §4.2 the proposed algorithm is employed to model a deformable filament attached to a sphere, as an idealized model of the *spider ballooning* problem.

4.1. *Self propelling finite aspect ratio plate*

We now extend the study of Arora *et al.* (2018) by considering a flexible plate of finite span, $b = 0.5C$, undergoing the same plunging motion given by eq. (12). The flexible plate with finite aspect ratio ($\mathcal{AR} = 0.5$) is modelled using the lumped-torsional model of Arora *et al.* (2018) (see Fig. 6a) extended to three dimensions, as depicted in Fig. 6b.

In order to reduce the computational cost of the 3D configuration, a lower Re than in § 3.2 is considered, allowing for a coarser spatial grid. Hence, both 2D and 3D flexible plates are simulated, to compare both configurations under the same conditions. The Reynolds number and the plunging amplitude in eq. (12) are set to $Re = 20$ and $A/C = 0.6$, respectively. On the other hand the plunging frequency is selected as that of maximum propulsive speed for the 2D plate, namely $\omega^* = \omega_n/(2\pi f) \approx 5$ (Arora *et al.* 2018). This leads to a torsional stiffness parameter $K^* = 106.617$ for the 2D plate and a torsional stiffness parameter $K^*_{3D} = K_{3D}/(\rho f^2 C^5) = K^* \mathcal{AR} = 53.309$ for the torsional springs of the 3D plate.

4.1.1. *Computational set-up*

Since the Reynolds number of these cases is five times smaller than that of the validation case discussed in 3.2, a grid refinement study is performed for the 2D configuration to select the grid spacing, Δx, and the size of the computational domain.

Figure 8a displays the tip deflection angle during a cycle for 3 different values of Δx in a computational domain of size $16C \times 8C$. As it can be appreciated, the trend of the tip angle is well captured even for the lowest grid resolution, $\Delta x = 0.02C$. In particular, the relative error in the maximum tip angle is of 2% and 0.5% for $\Delta x = 0.02C$ and $0.0125C$, respectively. Likewise, the effect of the external boundaries is evaluated by considering two sizes of the computational domain, $16C \times 8C$ and $40C \times 16C$, both discretized with a uniform grid spacing $\Delta x = 0.02C$. The evolution of the tip angle during a cycle is displayed in Fig. 8b for both computational domains. The variation of the maximum tip angle with the fluid domain is less than 1%. Therefore, it is clearly observed that the location of the far field boundaries is not affecting the computed solution.

In sight of the previous results, the computational domain is chosen to be $16C \times 8C$ for the 2D simulation and $16C \times 8C \times 8C$ for the 3D simulation. This computational

domain is uniformly discretized with a grid size $\Delta x = 0.0125C$ for the 2D simulations. On the other hand, for the 3D simulation, a grid spacing $\Delta x = 0.02C$ is used to discretized a refined region which contains the plate, whereas outside this region, a constant stretching factor of 1% is applied to the grid in all directions. The size of the refined region is $4C \times 2C \times 2C$, being centred along the y and z directions and starting at $3C$ from the inflow boundary along the streamwise direction.

The boundary conditions of the 2D case are those reported in section 3.2. For the 3D simulation, free-slip boundary conditions are imposed at all lateral boundaries, uniform streamwise flow of intensity U_∞ at the inflow boundary, and an advective boundary condition at the outflow boundary. Note that, while U_p is known from Arora *et al.* (2018) for the 2D case and we can set $U_\infty = U_p$; it is not known *a priori* for its 3D counterpart. In order to estimate U_∞ such that the plate remains at a constant mean horizontal position within the computational domain, simulations fixing the horizontal position of the 3D plate are performed in which the U_∞ is varied until the mean horizontal force over a cycle was approximately zero. Then, the simulation is restarted with this value of U_∞, allowing the horizontal displacement of the flapper. Hence, the propulsive speed can be computed as:

$$U_p = U_\infty - \langle \dot{X} \rangle = U_\infty - \frac{1}{T} \int_{T-1}^{T} \dot{X} \mathrm{d}t, \tag{13}$$

where $\dot{X}$ is the instantaneous velocity of the leading edge of the plate with respect to the computational domain.

In terms of the IBM, all the surfaces are discretized into evenly distributed points separated by a distance Δx. The simulations are run until the forces on the plate are periodic and the value of U_p, computed with eq. (13), does not vary with respect to the previous cycle.

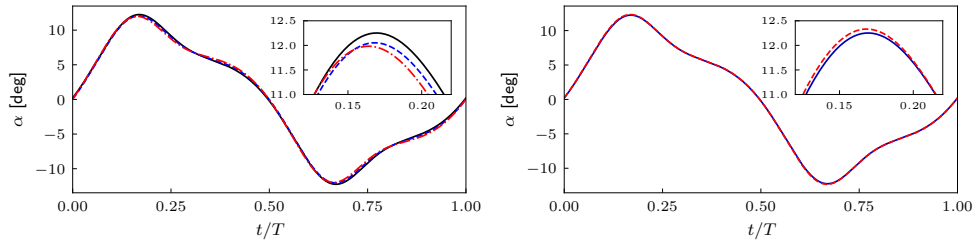

FIGURE 8: (a) Grid sensitivity analysis on the tip deflection angle, α: (——) $\Delta x = 0.02C$, (- - -) $\Delta x = 0.0125C$, and (-·-·-) $\Delta x = 0.00625C$. (b) Effect of the fluid domain on α: (——) $16C \times 8C$, and (- - -) $40 \times 16C$.

	U_p^*	$\langle P_i^* \rangle$	ε
2D	1.50	2.52	0.60
3D	0.48	1.44	0.33

TABLE 1: Non-dimensionalized values of the propulsive speed, U_p^*, average input power, $\langle P_i^* \rangle$, and effectiveness, ε, for both cases.

4.1.2. *Discussion of the results*

One of the most noticeable differences between both cases is the change of the mean propulsive speed, U_p, which significantly decreases from the 2D configuration to the finite aspect ratio case. This result is consistent with findings of Yeh & Alexeev (2016) for plunging flexible plates with smaller plunging amplitude $A/C = 0.1$ and at slightly higher Re than the present one. Yeh & Alexeev (2016) reported that, for a given ω^*, the propulsive speed decreased with decreasing b/C (note that the 2D case would correspond to $\mathit{AR} \to \infty$). Table 1 shows that $U_p^* = U_p/V$ is three times lower for the $\mathit{AR} = 0.5$ flapper. Thus, it is remarkable that the maximum tip deflection angle is similar for both cases, as shown in Fig. 9a. Nonetheless, the phase-shift between the vertical position of the leading edge and the tip deflection angle differs between both cases: for the 2D case this phase-shift is close to $\pi/2$ ($\alpha \approx 0$ when Y is maximum) meanwhile it is lower for the 3D case.

The aerodynamic forces also differ significantly from the 2D to the 3D scenario. This is appreciated in Fig. 9b and 9c, which depict the aerodynamic forces normalized with the maximum vertical velocity and the reference surface, S. This reference surface is C for the 2D case (since F_x are forces per unit span) and bC for the 3D case. In both cases, the tip deflection angle and the vertical force are in phase, suggesting that both, tip deflection and lift force, are direct consequences of the pressure difference between the upper and lower pressure acting upon the plate. A similar rationale holds for the horizontal force (Fig. 9b); in both cases the peak thrust (negative F_x) occurs at the maximum tip deflection, meanwhile the drag (positive F_x) is maximum for $\alpha \approx 0$. Nonetheless, it can be observed that the drag and thrust peak have a similar amplitude for the 2D case, whereas the thrust peak for the 3D case is less pronounced. The smaller amplitude of F_x in the 3D case is directly linked to a more steady instantaneous horizontal velocity (not shown).

Figure 10 displays the vortical structures around the 3D flapper at the beginning of the downstroke (Fig. 10a) and roughly at mid-downstroke (Fig. 10b). The observed structures are qualitatively similar to those reported in the literature of similar flexible flappers but at post-resonance plunging frequencies (Yeh & Alexeev 2014, 2016). In particular, a leading edge vortex (LEV) and a pair of side tip vortices (STV) are developed at each stroke of the flapper. These vortices are shed at the end of each stroke and become a vortex ring which is convected downstream.

In order to compare the flow structure in both configurations, Fig. 11 depicts the spanwise vorticity ω_z and the pressure for the 2D case and for the mid-span ($z = 0$) plane of the 3D case. It can be appreciated that the flow clearly differs between both scenarios. In particular, the 2D wake topology is different from the 3D wake

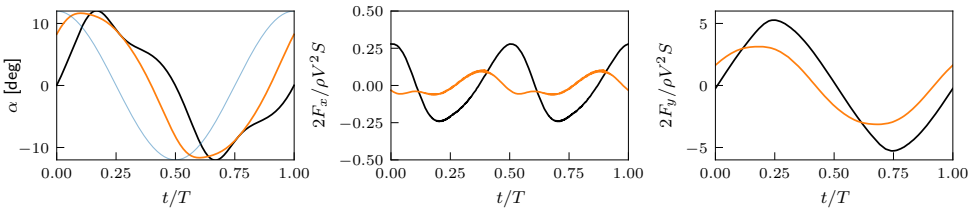

(a) (b) (c)

FIGURE 9: Comparison of the (a) tip deflection angle, (b) horizontal force and (c) vertical force: (——), 2D configuration and (——) $\mathcal{AR} = 0.5$ plate. In the normalization of the forces, $S = C$ for the 2D case and $S = bC$ for the 3D cases. In Fig. 9a, (——) corresponds to the position of the leading edge (without scale).

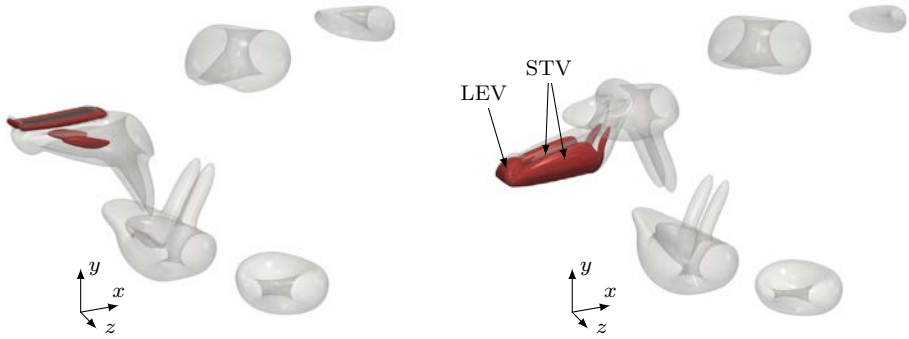

(a) $t/T = 0$ (b) $t/T = 0.24$

FIGURE 10: Visualization of the flow structures around the $\mathcal{AR} = 0.5$ flapper at two time instants. Vortical structures are displayed as iso-contours of the Q criterion (Hunt *et al.* 1988): light grey structures correspond to $Q = 0.004V^2/C^2$ and red structures to $Q = 7V^2/C^2$.

described in the previous paragraph. Instead of a succession of vortex dipoles observed in the 3D case (which correspond to the intersection of the vortex rings at $z = 0$), two consecutive vortices with the same vorticity orientation are shed during each stroke; namely: an LEV and a trailing edge vortex (TEV). The higher U_p can be appreciated as a larger separation between vortices shed during each stroke in the 2D scenario, as compared to the 3D wake. In the 2D case, the LEV developed during upstroke (LEV_u) is shed at mid-downstroke, right before the shedding of the TEV that develops during the downstroke (TEV_d), as depicted in Fig. 11b.

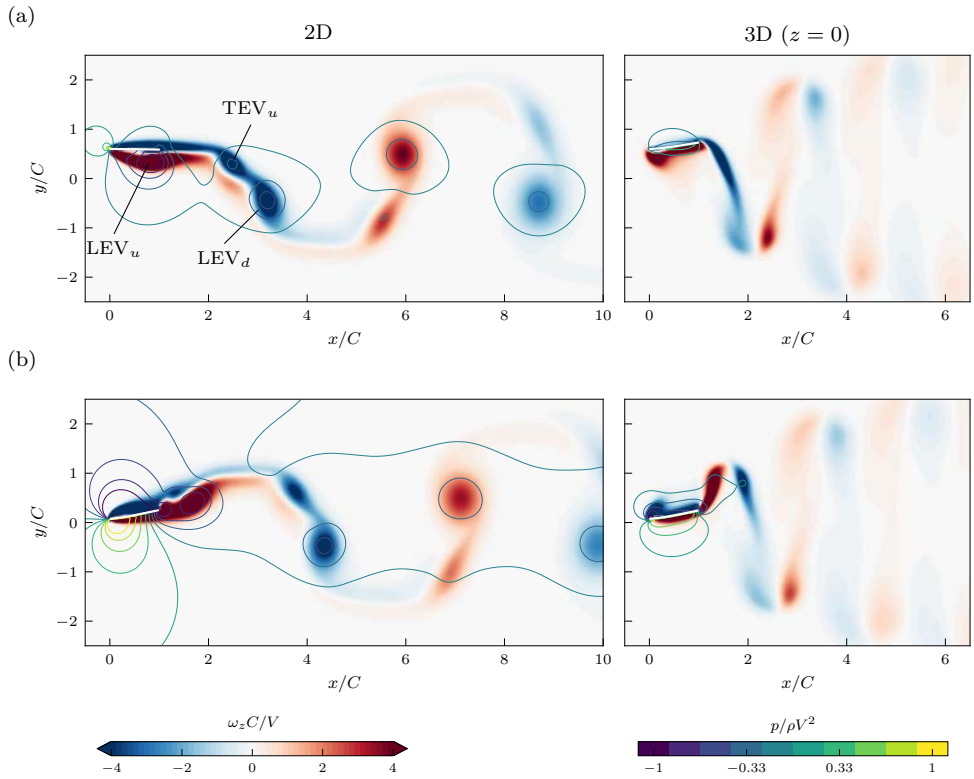

FIGURE 11: Spanwise vorticity, ω_z, and pressure contours for the 2D case and at mid-span of the 3D case at (a) beginning of the downstroke ($t/T = 0$) and (b) mid-downstroke ($t/T = 0.24$).

The LEV developed by the 2D plate is more intense, with a lower pressure associated to it, than to its 3D counterpart (see Fig. 11a). Indeed, this lower pressure region associated to the 2D LEV explains the smaller wing tip deflection at the beginning of a stroke; Fig. 11a reveals that at $t/T = 0$, the 2D LEV$_u$ is close to the trailing edge, making the plate to remain nearly horizontal. On the contrary, the absence of LEV$_u$ at the trailing of the 3D flapper, leads to a higher pressure (i.e, weaker suction) at the lower surface, yielding a higher tip deflection.

Finally, it is interesting to analyse the variation in the performance of the flappers. To that end, the *effectiveness*, or *swimming economy* of each plate is computed as (Yeh & Alexeev 2014, 2016):

$$\varepsilon = \frac{U_p^*}{\langle P_i^* \rangle}, \tag{14}$$

where $\langle P_i^* \rangle$ is the average non-dimensional input power, namely, $P_i^* = 2F_y\dot{Y}/(\rho V^3 S)$, over the last cycle (Arora *et al.* 2018). The values of $\langle P_i^* \rangle$ and ε for both cases are

gathered in Table 1. Although the required input power for the finite aspect ratio plate is lower than for its 2D counterpart, the reduction is not large enough to compensate for the lower propulsive speed. As a consequence, the *swimming economy* of the finite plate is significantly smaller than that of the 2D plate. Previous studies have linked the detriment of the swimming performance with decreasing $\mathit{\AE}$ with the STV (Raspa *et al.* 2014; Yeh & Alexeev 2016). The absence of STV in the 2D case ($\mathit{\AE} \to \infty$), together with its greater performance, are in agreement with this hypothesis.

4.2. *Spider ballooning*

The second example of application of the methodology proposed here is inspired by the ability of some spiders to disperse aerially by releasing one or several silk filaments. These filaments act as *drag lines* when they encounter a wind current, allowing spiders to achieve long dispersal distances. This mechanism is usually known as *spider ballooning* (Humphrey 1987; Zhao *et al.* 2017; Cho *et al.* 2018). Several studies addressing this phenomena, both experimentally (Suter 1991; Cho *et al.* 2018; Courtney *et al.* 2020) and numerically (restricted to 2D) (Humphrey 1987; Reynolds *et al.* 2006; Zhao *et al.* 2017), are found in the literature. These studies are mostly focused on characterizing the dispersal properties (in terms of dispersal length, terminal descent velocity, effective length of the filaments, *etc.*) of spider ballooning, both with actual samples or simplified models.

Motivated by this problem, a fundamental study is devised where the flow around a fixed sphere of diameter D, which has a filament of length L attached to it, is studied. In particular, the objective of the study is to determine what is the effect of the filament on the flow around the sphere, as well as the fluid forces acting upon it. From the point of view of the filament, this problem can be classified as an *extraneously induced excitation* (EIE) fluid-induced vibration problem (Paidoussis 1998; Yu *et al.* 2019).

Two simulations are performed: a fixed sphere immersed in a uniform flow, and the same problem but with a filament attached to the surface of the sphere. For the sake of clarity, the first case is labelled as S and the second case is labelled as F. The filament is modelled as N rigid links connected among them by joints which do not restrain the rotation (see Fig. 12a). For the dynamical model, the links are modelled as cylindrical rods of constant density $\rho_s = 6\rho$, length $l = L/N$ and diameter, $d = \Delta x$ (where Δx is the grid size). For the fluid coupling, each link is discretized into a 1D array of $l/\Delta x$ points evenly distributed. Consequently, the fluid does not exert any torque along the longitudinal axis of the filament. This enables to define the position of a given link i with respect to its predecessor by means of two angles, θ_i and φ_i (see Fig. 12b), instead of 3, as should be required to define the orientation of a rigid body. Accordingly, the joint connecting a given link, i, with its predecessor, $i-1$, is a multi-DOF joint consisting of a revolute joint about the y_i-axis, followed by another revolute joint about the rotated z_i-axis, namely, z_i', as sketched in Fig. 12b.

The sphere is immersed in a uniform flow parallel to the x-axis (see Fig. 12a) of magnitude U. The point at which the filament is attached is $x = -D/2$, that is, downstream the of sphere. For the present study, $L = 5D$, $Re = DU/\nu = 300$, and $N = 24$. This Reynolds number corresponds to a flow regime for the case of the

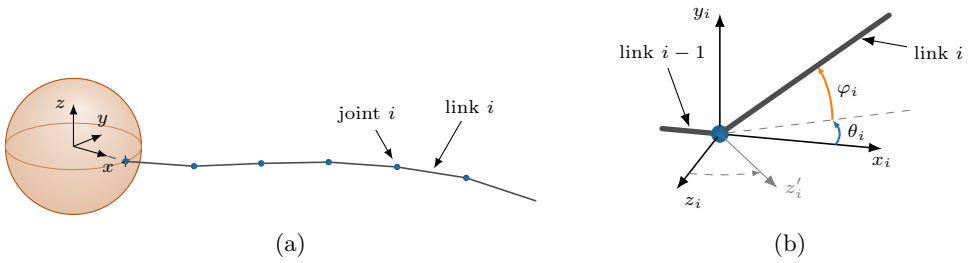

FIGURE 12: (a) Sketch of the multi-body system composed of a fixed sphere and filament consisting of $N = 6$ links. The reference frame depicted corresponds to the inertial reference frame. (b) Schematic view of the parameters that define the joint between two linkages. The Cartesian frame $x_i y_i z_i$ is fixed to the link $i - 1$.

isolated sphere in which vortex shedding starts to occur (Bouchet *et al.* 2006). It has been selected to explore if interference between the filament and the shed vortices is found.

4.2.1. *Computational set-up*

For both simulations, the computational domain is a rectangular prism of dimensions $14D \times 8D \times 8D$ in the streamwise and lateral directions, respectively. A uniform refined region of size $7D \times 2D \times 2D$ is defined, with a grid spacing $\Delta x = D/48$. This region is located $3D$ downstream of the inflow, centered within the lateral directions of the computational domain. Outside of this region, a stretching factor of 1% is applied in all directions. A uniform free stream of magnitude U is imposed at the inflow boundary, free-slip boundary conditions are imposed at the lateral boundaries and an advective boundary conditions is implemented at the outflow boundary.

For the IBM, the sphere is discretized into N_s evenly distributed points, such that $N_s \approx \pi D^2/\Delta x^2$, similarly to (Uhlmann 2005). On the other hand, each segment of the filament is discretized by equally spaced points, separated a distance Δx, without gaps between adjacent segments.

The time step is fixed to $\Delta t = 0.0025U/D$, ensuring $CFL < 0.2$. Finally, the simulation of the isolated sphere (case S) is started from scratch, whereas the sphere with the attached filament (case F) is started from a flow field of case S when vortex shedding was present.

4.2.2. *Discussion of the results*

At the selected Reynolds number, the flow over the sphere exhibits periodic shedding of vortices after an initial transient. Fig. 13 displays an snapshot of the wake of the sphere after the onset of vortex shedding. This leads to oscillatory hydrodynamic forces over the sphere, as observed from Fig. 14a, which depicts the non-dimensional streamwise (i.e., drag) force, $F_x^* = F_x/(\rho U^3 \pi D^2/8)$. It can also be observed that the mean value of F_x^* increases after the onset of vortex shedding. The oscillation

FIGURE 13: Instantaneous visualization of the flow structures around the isolated sphere at $Re = 300$. Vortical structures correspond to iso-contours of the Q-criterion, $Q = 0.2U^2/D^2$.

frequency is found to be $0.135U/D$, in agreement with existing literature at the same Reynolds number (Tomboulides *et al.* 1993; Johnson & Patel 1999). Furthermore, the non-axisymmetric wake leads to the appearance of a transversal force contained in the plane of symmetry of the wake. Note that the location of this plane of symmetry with respect to the inertial axis arises naturally, only forced by numerical biases (Johnson & Patel 1999). In the present case, the angle between the $(x, y)-$plane and the symmetry plane is approximately 67.7°. This angle, is computed by a least square regression of the transversal forces, as shown in in Fig. 14b. Figure 14c depicts the transverse force when expressed in parallel ($F_{\parallel}$) and perpendicular ($F_{\perp}$) components with respect to the symmetry plane of the wake. The plot shows oscillations of $F^*_{\parallel}$, with the same frequency of oscillation as F^*_x, and a net non-zero $F^*_{\parallel}$ when averaged over several periods.

When the deformable filament is attached to the posterior part of the sphere, the flow topology is greatly modified. If the simulation is started from a flow field with vortical structures (Fig. 15a) the filament starts oscillating, and after 2-3 shedding cycles, vortex shedding is suppressed, and a stable flow around the sphere-filament is developed (Fig. 15b). If the simulations are started from scratch, no vortex shedding occurs. The topology of the flow in this new regime is characterized by the development of an axisymmetric recirculation region attached to the sphere, similarly to the case of the isolated sphere at $Re < 210$ (Johnson & Patel 1999). This can be clearly appreciated in Fig. 16, which depicts the instantaneous streamlines past the sphere and the filament. Note that a shear layer is developed along the filament, which changes direction in the recirculation bubble.

The vortex shedding inhibition has a noticeable effect on the forces acting over the sphere. Firstly, the mean drag force acting over the sphere is reduced and the oscillations are hindered, as shown in Fig. 14a, leading to a steady value of the drag force over the sphere. However, the total drag force (i.e., sphere + filament) increases, due to the skin friction of the filament, which acts as a *drag line*. Secondly, the amplitude of the oscillations of the transverse force decreases with respect to the case of the isolated sphere, as shown in Fig. 14c. The frequency of oscillation of the

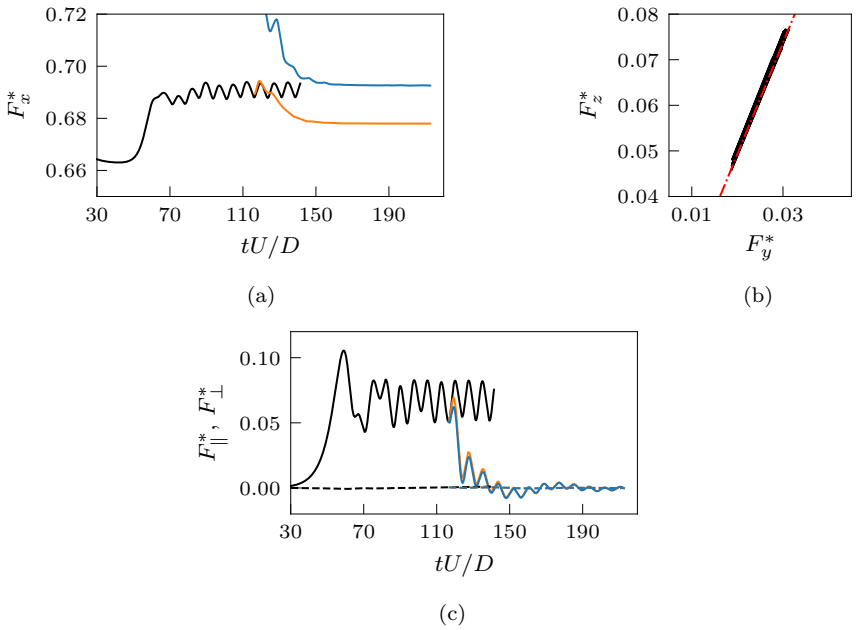

FIGURE 14: (a) Temporal evolution of the non-dimensional streamwise force. (——) case S; (——) case F (force over the sphere); (——) case F (force over the sphere and the filament). (b) (——) Non-dimensional transverse force on the sphere for case S for $t > 90D/U$ (after onset of vortex shedding); and its (-·-·-) least square regression. (c) Temporal evolution of the non-dimensional transverse forces expressed into its parallel and normal components. Color legend is as 14a, line styles stands for (——) $F_\parallel^*$, and (- - -) $F_\perp^*$.

FIGURE 15: Instantaneous visualization of the flow structures around the sphere with the deformable filament at (a) initial time instants, and (b) after reaching and stable state. Vortical structures correspond to iso-contours of the Q-criterion, $Q = 0.2U^2/D^2$, as in Fig. 13.

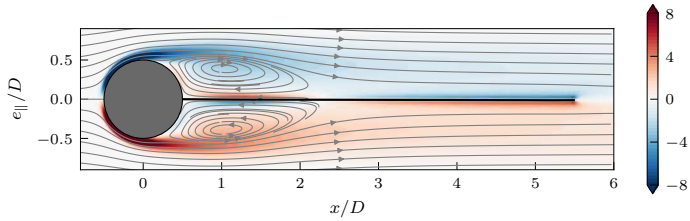

FIGURE 16: Instantaneous streamlines past the sphere and the filament in the $(x, e_{\parallel})$-plane, together with the vorticity perpendicular to the plane.

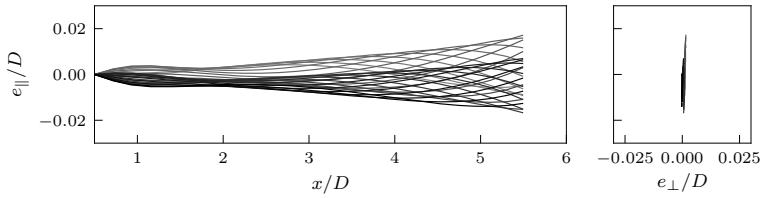

FIGURE 17: Oscillation pattern of the filament during the last two oscillation cycles of the transverse forces. Line color indicates the time instant (from grey to black). Note the difference in the scale of the axes.

transverse forces (which was previously linked to the shedding frequency of vortices over the sphere) is also reduced, from $0.135U/D$ without the filament to $0.120U/D$ with the filament.

In addition, the mean value of the transverse force over an oscillation cycle has a zero mean value (Fig. 14c), which suggest that the flow becomes symmetric, in a time-average sense, across the $(x, e_{\parallel})-$plane (where $e_{\parallel}$ is the direction perpendicular to $x-$axis and contained in the wake's symmetry plane).

Regarding the dynamics of the filament, Fig. 17 depicts its deformation pattern during the last two oscillation cycles of the transverse force. It can be observed that the filament is not steady but it oscillates with a low amplitude. It is interesting to note that these oscillations are contained in a plane, which correspond to the symmetry plane of the wake of the isolated sphere.

5. Conclusions

A methodology to solve fluid-structure interaction problems with multi-body systems has been presented. The proposed methodology follows a partitioned approach. The flow is solved using a conventional fractional-step method while the presence of the bodies of the MBS in the fluid is performed by means of the immersed boundary method proposed by Uhlmann (2005). On the other hand, the dynamic equations

of the rigid bodies are computed in terms of the reduced coordinates of the MBS by the CRBA and RNEA recursive algorithms proposed by Felis (2017). The coupling between flow equations and the MBS equations is *weak*, extending the approach of Uhlmann (2005) for single rigid bodies to MBSs.

Two cases from the literature have been selected to validate the present methodology. Since the flow solver has been already validated elsewhere, the validation focuses on the multi-body dynamics and the coupling. The first validation case corresponds to a system of two bodies joined by a torsional spring. Very good agreement is obtained when comparing to a vortex particle method (Toomey & Eldredge 2008) and to a vorticity-based IBM with strong coupling (Wang & Eldredge 2015). The second case is that of a flexible, self-propelled plate modelled as several rigid bodies connected by torsional springs (Arora *et al.* 2018). The obtained results show again very good agreement with those obtained from a Lattice-Boltzmann simulation (Arora *et al.* 2018).

Two additional bio-inspired examples are provided to illustrate the capabilities of the methodology. The first example is a three-dimensional extension of the case presented by Arora *et al.* (2018). It is observed that 3D effects are detrimental in terms of propulsive speed and efficiency, although the deflection of the plate is not significantly modified. The results are in accordance with those reported by Yeh & Alexeev (2014) for flexible self-propelled plates. The second example is loosely inspired by the *ballooning* mechanism of several spiders to disperse aerially. The problem is modelled as a deformable filament attached to a fixed sphere and immersed in a free-stream. The flexibility of the filament is modelled as a chain of rigid links connected with multi-DoF joints. When compared to an isolated sphere at the same Reynolds number, it is shown that the vortex shedding is suppressed, despite the very low amplitude of oscillation of the filament. The reduction in the unsteadiness of the flow results in a decrease of the drag contribution from the sphere, but a larger total drag due to the extra friction introduced by the filament.

In summary, it has been shown that the proposed methodology allows the definition and analysis of a multitude of diverse configurations of MBS, thanks to the use of generalised recursive algorithms. Moreover, the coupling between the flow equations and the MBS equations is very simple, yet robust enough to provide very good agreement with existing results from the literature. Nonetheless, the *weak coupling* imposes a lower limit on the density ratios of the bodies which can be simulated with the present methodology. Although, recent works have proven to successfully tackle arbitrary density ratios for single rigid bodies using a non-iterative version of the *weak coupling* approach presented in Tschisgale *et al.* (2017), the technical details are not trivial for arbitrary geometries so that this extension of the methodology is left for future work.

Acknowledgements

This work was supported by grant DPI2016-76151-C2-2-R (AEI/FEDER, UE). The computations were partially performed at the supercomputer Caesaraugusta from the *Red Española de Supercomputación* in activity IM-2020-1-0008. We thank Dr. N.

Arora, Dr. A. Gupta and Dr. J. Eldredge for providing their data in electronic form and for fruitful discussions.

Appendix A. Joint modelling

A joint that connect two bodies can also be regarded as the constraint of the relative motion between two Cartesian reference frames, attached to each body Featherstone (2014). Figure 18a illustrates this concept: body Γ_i has an attached reference frame, Σ_i, and is linked to its predecessor body, Γ_k, which has its own attached reference frame, Σ_k. Therefore, a joint can be defined by the rotation matrix, $\mathsf{E}_{k,i}$, from Σ_i to Σ_k; and the vector $\mathbf{s}_i$, which links the origin of both Cartesian frames and is implicitly expressed in Σ_k. Note that $\mathsf{E}_{k,i}$ and $\mathbf{s}_i$ only depend on the degrees of freedom allowed by the joint, but their definition depend on the kind of joint.

Single DoF joints of two types are considered: prismatic (i.e., translation) joints along any axis of Σ_k; and revolute (i.e. rotation) joints about any axis of Σ_k. For a prismatic joint which allows translation along the x-axis of Σ_k, $\mathsf{E}_{k,i}$ is the identity matrix of size 3; and $\mathbf{s}_i(q_i) = q_i\mathbf{e}_x$, where $\mathbf{e}_x$ is the unitary vector parallel to x-axis, and q_i is the joint's degree of freedom and corresponds to the magnitude of the translation. Then, the relative velocity of body Γ_i with respect to Σ_k is:

$$\boldsymbol{\omega}_i' = \mathbf{0}, \qquad \mathbf{v}_i' = \dot{\mathbf{s}}_i = \dot{q}_i\mathbf{e}_x.$$

On the other hand, for a joint which allows the rotation about the x-axis, $\mathsf{E}_{k,i}(q_i)$ is a matrix belonging to the 3D rotation group, $SO(3)$, namely

$$\mathsf{E}_{k,i}(q_i) = \begin{bmatrix} 1 & 0 & 0 \\ 0 & \cos q_i & -\sin q_i \\ 0 & \sin q_i & \cos q_i \end{bmatrix};$$

and $\mathbf{s}_i$ is a constant vector. Note that, in this case q_i stands for the rotation angle. In this case, the relative velocity of body Γ_i with respect to Σ_k takes the form:

$$\boldsymbol{\omega}_i' = \dot{q}_i\mathbf{e}_x, \qquad \mathbf{v}_i' = \boldsymbol{\omega}_i' \times \mathbf{s}_i.$$

Similar definitions stand for translations and rotations about y and z axes.

In order to model joints which allow multiple degrees of freedom between two bodies, several virtual bodies can be linked sequentially using single DoF joints (prismatic or revolute), as illustrated in Fig. 18b. For the dynamical model, these virtual bodies have no mass; and for the fluid coupling, they have no associated Lagrangian points (i.e., no volume). Under this approach, the connection between the two physical bodies is equivalent to a multi DoF joint. Hence, the present methodology allows a simple implementation of any kind of kinematic joint with a negligible increase of the computational cost.

Appendix B. Mapping between generalized and physical coordinates

B.1. *From generalized coordinates to physical coordinates*

Computation of $\mathbf{X}_{i,j}$ and $\mathbf{U}_{\partial\Gamma_i}$, according to eq. (10), requires the calculation of E_i, $\mathbf{x}_i^0$, $\mathbf{v}_i^0$, and ω_i^0. These variables can be derived from the joint variables derived in

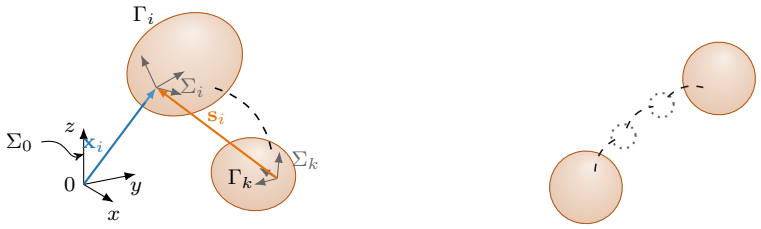

FIGURE 18: (a) Sketch of body Γ_i and its predecessor, Γ_k, illustrating the elements that define the joint between them. (b) Representation of a joint with 3 DoF, simulated by means of 2 virtual bodies (represented as dashed circles) which have no mass and associated Lagrangian points.

Appendix A. To that end, we exploit the fact that, for a *kinematic tree* like the one considered in Fig. 1a, we can define a unique predecessor for each body, Γ_i, which can be hence denoted as $\Gamma_{\lambda(i)}$. Likewise, a set $\mu(i)$ can be defined containing all the bodies which precede Γ_i. As an example, for body Γ_7 in Fig. 1a, $\mu(7) = \{4, 5, 7\}$. Under these definitions, the rotation matrix of body Γ_i is computed as:

$$\mathsf{E}_i = \prod_{j \in \mu(i)} \mathsf{E}_{\lambda(j),j} \tag{15}$$

Likewise,

$$\mathbf{x}_i^0 = \sum_{j \in \mu(i)} \mathsf{E}_{\lambda(j)} \mathbf{s}_j(q_j), \tag{16}$$

whereas, $\mathbf{v}_i^0$ and $\boldsymbol{\omega}_i^0$ can be computed from eq. (16) by substituting $\mathbf{s}_j$ by $\mathbf{v}_j'$ and $\boldsymbol{\omega}_j'$, respectively.

B.2. *From physical coordinates to generalized coordinates*

In order to compute $\boldsymbol{\xi}_h$ to solve eq. (7), the hydrodynamic forces acting upon the bodies must be expressed in terms of generalized coordinates. Note that, with the present coupling, the component of the hydrodynamic forces that have to be mapped are $\mathcal{G}_i$ and $\mathcal{N}_i$ from eq. (11a) and eq. (11b), respectively. For the sake of efficiency, it is convenient to gather both forces and moments acting on body Γ_i into a single vector:

$$\hat{\mathbf{f}}_i^h = \begin{bmatrix} \mathcal{N}_i \\ \mathcal{G}_i \end{bmatrix}, \tag{17}$$

where it is implicitly assumed that both $\mathcal{N}_i$ and $\mathcal{G}_i$ are expressed in Σ_0 and moments are computed about the origin.

We also define the matrix transform of Γ_i as:

$$\mathbf{X}_i^* = \begin{bmatrix} \mathsf{E}_i^\top & -\mathsf{E}_i^\top \mathbf{x}_i^{0\times} \\ \mathsf{0} & \mathsf{E}_i^\top \end{bmatrix}, \tag{18}$$

where $\mathbf{x}_i^0\times$ is a skew-symmetric matrix belonging to the Lie algebra of the $SO(3)$ rotation group.

With the previous definitions, a simplified version of the RNEA can be implemented to compute the components of $\boldsymbol{\xi}_h$, namely:

for $i \leftarrow 1, N_B$ **do**
  $\hat{\mathbf{g}}_i = \mathbf{X}_i^* \hat{\mathbf{f}}_i^h$
end for
for $i \leftarrow N_B, 1$ **do**
  $\xi_{h,i} = \mathbf{S}_i^\top \hat{\mathbf{g}}_i$
  if $\lambda(i) \neq 0$ **then**
    $\hat{\mathbf{g}}_{\lambda(i)} = \hat{\mathbf{g}}_{\lambda(i)} + \mathbf{X}^*_{\lambda(i)} \hat{\mathbf{f}}_i^h$
  end if
end for

where $\lambda(i)$ is the index of the predecessor body of Γ_i. The previous algorithm simply transfers the forces acting upon a given body across its supporting tree (i.e., the set of bodies that connect it to base, Σ_0). Note that, $\mathbf{S}_i$ is the motion subspace of the joint. For prismatic and revolute joints, $\mathbf{S}_i$ is a unitary column vector of size 6×1, whose only non-zero component is the axis along which rotation/translation is allowed. In particular, its first 3 components are associated to rotations about the x, y or z axes of the joints; meanwhile its 3 last components are associated with translations along the aforementioned axes.

References

Arora, N., Kang, C.-K., Shyy, W. & Gupta, A. 2018 Analysis of passive flexion in propelling a plunging plate using a torsion spring model. *J. Fluid Mech.* **857**, 562–604.

Arranz, G., Flores, O. & García-Villalba, M. 2020 Three-dimensional effects on the aerodynamic performance of flapping wings in tandem configuration. *J. Fluids Struct.* **94**, 102893.

Arranz, G., Gonzalo, A., Uhlmann, M., Flores, O. & García-Villalba, M. 2018*a* A numerical study of the flow around a model winged seed in auto-rotation. *Flow Turbul. Combust.* **101** (2), 477–497.

Arranz, G., Moriche, M., Uhlmann, M., Flores, O. & García-Villalba, M. 2018*b* Kinematics and dynamics of the auto-rotation of a model winged seed. *Bioinspir. Biomim.* **13**, 036011.

Bernier, C., Gazzola, M., Ronsse, R. & Chatelain, P. 2019 Simulations of propelling and energy harvesting articulated bodies via vortex particle-mesh methods. *J. Comput. Phys.* **392**, 34 – 55.

Bouchet, G., Mebarek, M. & Dušek, J. 2006 Hydrodynamic forces acting on a rigid fixed sphere in early transitional regimes. *Eur. J. Mech.-B/Fluids* **25** (3), 321–336.

Boyer, F. & Porez, M. 2015 Multibody system dynamics for bio-inspired locomotion: From geometric structures to computational aspects. *Bioinspir. Biomim.* **10** (2), 1–21.

Breugem, W.-P. 2012 A second-order accurate immersed boundary method for fully resolved simulations of particle-laden flows. *J. Comput. Phys.* **231** (13), 4469–4498.

Cho, M., Neubauer, P., Fahrenson, C. & Rechenberg, I. 2018 An observational study of ballooning in large spiders: Nanoscale multifibers enable large spiders' soaring flight. *PLOS Biol.* **16** (6), 1–27.

Courtney, R. J., Stevens, T., Zhang, W. & Zhao, L. 2020 Flying spiders: What is the drag acting on a spider-dragline in free-fall? AIAA Scitech 2020 Forum. AIAA 2020-1539.

de Croon, G.C.H.E., de Clercq, K.M.E., Ruijsink, R., Remes, B. & de Wagter, C. 2009 Design, aerodynamics, and vision-based control of the DelFly. *Int. J. Micro Air Veh.* **1** (2), 71–97.

Deng, H.-B., Xu, Y.-Q., Chen, D.-D., Dai, H., Wu, J. & Tian, F.-B. 2013 On numerical modeling of animal swimming and flight. *Comput. Mech.* **52** (6), 1221–1242.

Donea, J., Huerta, A., Ponthot, J.-P. & Rodríguez-Ferran, A. 2017 Arbitrary Lagrangian–Eulerian Methods. In *Encyclopedia of Computational Mechanics Second Edition*, pp. 1–23. Wiley Online Library.

Featherstone, R. 2014 *Rigid body dynamics algorithms*. Springer.

Felis, M. 2017 RBDL: an efficient rigid-body dynamics library using recursive algorithms. *Auton. Robot.* **41** (2), 495–511.

Gazzola, M., Chatelain, P, Wim, M. [van Rees] & Koumoutsakos, P. 2011 Simulations of single and multiple swimmers with non-divergence free deforming geometries. *J. Comput. Phys.* **230** (19), 7093 – 7114.

Gonzalo, A., Arranz, G., Moriche, M., García-Villalba, M. & Flores, O. 2018 From flapping to heaving: A numerical study of wings in forward flight. *J. Fluids Struct.* **83**, 293–309.

Greenwood, D. 2006 *Advanced dynamics*. Cambridge University Press.

Griffith, B. E. & Patankar, N. A. 2020 Immersed methods for fluid–structure interaction. *Annu. Rev. Fluid Mech.* **52** (1), 421–448.

Hirata, K., Takimoto, T. & Tamura, K. 2000 Study on turning performance of a fish robot. In *Proc. 1st Int. Symp. Aqua Bio-Mechanisms*, pp. 287–292.

Humphrey, J. A. C. 1987 Fluid mechanic constraints on spider ballooning. *Oecologia* **73** (3), 469–477.

Hunt, J. C. R., Wray, A. A. & Moin, P. 1988 Eddies, stream, and convergence zones in turbulent flows. *Center For Turbulence Research* **Report CTR-S88**.

Johnson, T. A. & Patel, V. C. 1999 Flow past a sphere up to a Reynolds number of 300. *J. Fluid Mech.* **378**, 19–70.

Keennon, M., Klingebiel, K. & Won, H. 2012 Development of the nano hummingbird: A tailless flapping wing micro air vehicle. In *50th AIAA Aerospace Sciences Meeting including the New Horizons Forum and Aerospace Exposition*, pp. 1 – 12.

Kempe, T. & Fröhlich, J. 2012 An improved immersed boundary method with direct forcing for the simulation of particle laden flows. *J. Comput. Phys.* **231** (9), 3663–3684.

Li, R., Xiao, Q., Liu, Y., Hu, J., Li, L., Li, G., Liu, H., Hu, K. & Wen, L. 2018 A multi-body dynamics based numerical modelling tool for solving aquatic biomimetic problems. *Bioinspir. Biomim.* **13** (5), 056001.

Liu, H. 2009 Integrated modeling of insect flight: From morphology, kinematics to aerodynamics. *J. Comput. Phys.* **228** (2), 439 – 459.

Mittal, R. & Iaccarino, G. 2005 Immersed boundary methods. *Annu. Rev. Fluid Mech.* **37** (1), 239–261.

Moriche, M., Flores, O. & García-Villalba, M. 2016 Three-dimensional instabilities in the wake of a flapping wing at low Reynolds number. *Int. J. Heat Fluid Flow* **62A**, 44–55.

Moriche, M., Flores, O. & García-Villalba, M. 2017 On the aerodynamic forces on heaving and pitching airfoils at low Reynolds number. *J. Fluid Mech.* **828**, 395–423.

Paidoussis, M. P 1998 *Fluid-structure interactions: slender structures and axial flow*, , vol. 1. Academic press.

Peskin, C. 2002 The immersed boundary method. *Acta Numerica* **11**, 479–51.

Pinelli, A., Naqavi, I. Z., Piomelli, U. & Favier, J. 2010 Immersed-boundary methods for general finite-difference and finite-volume Navier–Stokes solvers. *J. Comput. Phys.* **229** (24), 9073–9091.

Rai, M. & Moin, P. 1991 Direct simulations of turbulent flow using finite-difference schemes. *J. Comput. Phys.* **96** (1), 15–53.

Raspa, V., Ramananarivo, S., Thiria, B. & Godoy-Diana, R. 2014 Vortex-induced drag and the role of aspect ratio in undulatory swimmers. *Phys. Fluids* **26** (4), 041701.

Reynolds, A. M., Bohan, D. A. & Bell, J. R. 2006 Ballooning dispersal in arthropod taxa with convergent behaviours: dynamic properties of ballooning silk in turbulent flows. *Biol. Lett.* **2** (3), 371–373.

Richter, C. & Lipson, H. 2011 Untethered hovering flapping flight of a 3D-printed mechanical insect. *Artif. Life* **17** (2), 73–86.

Suter, R. B. 1991 Ballooning in spiders: results of wind tunnel experiments. *Ethol. Ecol. Evol.* **3** (1), 13–25.

Suzuki, K., Minami, K. & Inamuro, T. 2015 Lift and thrust generation by a butterfly-like flapping wing–body model: immersed boundary–lattice Boltzmann simulations. *J. Fluid Mech.* **767**, 659 – 695.

Suzuki, K., Okada, I. & Yoshino, M. 2019 Effect of wing mass on the free flight of a butterfly-like model using immersed boundary–lattice Boltzmann simulations. *J. Fluid Mech.* **877**, 614–647.

Tomboulides, A., Orszag, S. & Karniadakis, G. 1993 Direct and large-eddy simulations of axisymmetric wakes. In *31st Aerospace Sciences Meeting*, p. 546.

Toomey, J. & Eldredge, J. D. 2008 Numerical and experimental study of the fluid dynamics of a flapping wing with low order flexibility. *Phys. Fluids* **20** (7), 073603.

Triantafyllou, M. S. & Triantafyllou, G. S. 1995 An efficient swimming machine. *Sci. Am.* **272** (3), 64–70.

Tschisgale, S., Kempe, T. & Fröhlich, J. 2017 A non-iterative immersed boundary method for spherical particles of arbitrary density ratio. *J. Comput. Phys.* **339**, 432 – 452.

Uhlmann, M. 2005 An immersed boundary method with direct forcing for the simulation of particulate flows. *J. Comput. Phys.* **209** (2), 448–476.

Wang, C. & Eldredge, J. D. 2015 Strongly coupled dynamics of fluids and rigid-body systems with the immersed boundary projection method. *J. Comput. Phys.* **295**, 87–113.

Yao, J. & Yeo, K. S. 2019 Free hovering of hummingbird hawkmoth and effects of wing mass and wing elevation. *Comput. Fluids* **186**, 99 – 127.

Yeh, P. D. & Alexeev, A. 2014 Free swimming of an elastic plate plunging at low Reynolds number. *Phys. Fluids* **26** (5), 053604.

Yeh, P. D. & Alexeev, A. 2016 Effect of aspect ratio in free-swimming plunging flexible plates. *Comput. Fluids* **124**, 220–225.

Yu, J., Tan, M., Wang, S. & Chen, E. 2004 Development of a biomimetic robotic fish and its control algorithm. *IEEE Transactions on Systems, Man, and Cybernetics, Part B (Cybernetics)* **34** (4), 1798–1810.

Yu, Y., Liu, Y. & Amandolese, X. 2019 A review on fluid-induced flag vibrations. *Appl. Mech. Rev.* **71** (1).

Zhang, S., Yu, J., Zhang, A. & Zhang, F. 2013 Spiraling motion of underwater gliders: Modeling, analysis, and experimental results. *Ocean Eng.* **60**, 1–13.

Zhao, Longhua, Panayotova, Iordanka N., Chuang, Angela, Sheldon, Kimberly S., Bourouiba, Lydia & Miller, Laura A. 2017 Flying spiders: Simulating and modeling the dynamics of ballooning. In *Women in Mathematical Biology* (ed. Anita T. Layton & Laura A. Miller), pp. 179–210.

Paper 2

2

Kinematics and dynamics of the auto-rotation of a model winged seed

G. Arranz[1], M. Moriche[1], M. Uhlmann[2], O. Flores[1], M. García-Villalba[1]

[1] Universidad Carlos III de Madrid, Spain
[2] Karlsruhe Institute of Technology, Germany

Bioinspiration & Biomimetics (2018), vol. **13** (3), 036011

Numerical simulations of the auto-rotation of a model winged seed are presented. The calculations are performed by solving simultaneously the Navier-Stokes equations for the flow surrounding the seed and the rigid-body equations for the motion of the seed. The Reynolds number based on the descent speed and a characteristic chord length is varied in the range $80 - 240$. Within this range, the seed attains an asymptotic state with finite amplitude auto-rotation, while for smaller values of the Reynolds number no auto-rotation is observed. The motion of the seed is characterized by the coning and pitch angles, the angular velocity and the horizontal translation of the seed. The values obtained for these quantities are qualitatively similar to those reported in the literature in experiments with real winged seeds. When increasing the Reynolds number, the seed tends to rotate at higher speeds, with less inclination with respect to the horizontal plane, and with a larger translation velocity. With respect to the aerodynamic forces, it is observed that, with increasing Reynolds number, the horizontal components decrease in magnitude while the vertical component increases. The force distribution along the wing span is characterized using both global and local characteristic speeds and chord lengths for the non-dimensionalisation of the force coefficients. It is found that the vertical component does not depend on the Reynolds number when using local scaling, while the chordwise component of the force does.

Key words: winged-seed, auto-rotation, numerical simulation

1. Introduction

Nature has shown to be an excellent engineer. Therefore, it is not surprising that several tree species are able to take advantage of wind and turbulent gusts to disperse their seeds thanks to their suitable shapes. More surprising is the fact that this dispersal can range from tens of meters to kilometers (Nathan 2006). Some of these seeds, often called straying seeds, rely on their small weight to surface ratio to perform a parachuting flight thanks to the drag force acting on them (Burrows 1975; Minami & Azuma 2003). However, there are other kind of seeds which are able to create lifting forces opposite to gravity to reduce their descent speed and increase their dispersal distance under lateral winds. This type of seeds, usually known as winged seeds, or

samaras, generate these aerodynamic forces executing auto-rotational flight as they fall (Azuma 1992, chapter 6). Thus, samaras have much larger wing loading (weight to exposed surface ratio) than straying seeds (Minami & Azuma 2003).

Winged seeds from different species have different size and shape, but all of them exhibit a similar physical structure: a thin, leaf-like wing with a thicker leading edge; and a nut (or embryo) at one side of the wing. These seeds have received a lot of attention from the scientific community during the last decades (Norberg 1973; Green 1980; Azuma & Yasuda 1989; Rosen & Seter 1991; Seter & Rosen 1992; Yasuda & Azuma 1997). The reasons for this attention are mainly two. First, the reduction of the descent speed in auto-rotation compared to the free falling velocity, which has obvious engineering applications. Second, winged seeds have high auto-rotation stability, meaning that they are able to sustain auto-rotation when they encounter wind disturbances (Lee & Choi 2017), and when their shape is drastically changed (Varshney *et al.* 2012). The gist of this stable auto-rotation is a subtle coupling between seed's inertia and aerodynamic forces (Varshney *et al.* 2012). In this fashion, samaras possess self-stability governed just by their structural pattern, without the need of any active actuator, like neuromuscular control in animal flight (Norberg 1973).

These natural abilities have fostered the development of aerial vehicles based on samaras. Examples of these are the *Samarai* developed by Lockheed-Martin (Obradovic *et al.* 2012; Fregene & Bolden 2010) and the robotic samara developed by Ulrich *et al.* (2010), which have a propeller installed to be remotely controlled. Similarly, Pounds & Singh (2015) present a sensor based on the shape of a winged seed to exploit the dispersal capabilities of these seeds. In this fashion, several of these sensors are deployed from an aerial vehicle with the scope of monitoring a target area.

However, the design of efficient vehicles entails a more detailed comprehension of the auto-rotation phenomena, which is difficult to study. The coupling between the seed's inertia and aerodynamic forces poses several difficulties in order to analyse the problem from a theoretical perspective. The descent speed, angular velocity, and attitude of the seed as it auto-rotates will be largely defined by the aerodynamic forces, which in turn will vary depending on the former parameters. Hence, a theoretical approach of the problem entails, ineluctably, a model of the aerodynamic forces based on seed's kinematics. The vast majority of these models are simplified models based on the *blade element theory*, which do not consider the existence of a leading edge vortex (LEV), or three dimensional effects of the flow, among others (Azuma & Yasuda 1989; Seter & Rosen 1992*b*).

On the other extreme, thanks to advances in flow visualization techniques such as digital particle image velocimetry (DPIV), it is possible to measure the velocity field around an actual samara in auto-rotation. In fact, this technique allowed Lentink *et al.* (2009) to visualize a stable LEV created on the upper surface of winged seeds as they auto-rotate. Nonetheless, although DPIV allows to study the flow field, the force distribution is not easily measured experimentally. Consequently, force distributions are usually extrapolated from the velocity field as in Lentink *et al.* (2009), Salcedo *et al.* (2013) and Limacher & Rival (2015).

These difficulties can be overcome with the use of Direct Numerical Simulations (DNS) with a 2-way coupling between the fluid and the solid dynamics, where the

aerodynamic forces are directly obtained and hence do not need to be modelled (Uhlmann 2005). Moreover, systematic variations of a single parameter of the problem (e.g., seed's inertia, density ratio or Reynolds number) are easily performed using DNS, allowing to study the isolated effect of these parameters on the auto-rotation of the seed.

In the present study we take advantage of this latter approach, and perform DNS of the auto-rotation of a winged-seed at different Reynolds numbers, $Re = w_d c/\nu$ (where w_d is the descent speed, c is the characteristic chord of the seed's wing, and ν is the dynamic viscosity of air). The objective is to investigate auto-rotation at lower Reynolds number than typical values found in nature (which are of the order of $Re \sim 700$), studying the change of the kinematics and the aerodynamic forces with Re while keeping the seed's geometry and inertia constant. The analysis focuses on the motion and attitude of the model winged seed, and on the resulting aerodynamic forces. The analysis of the flow surrounding the seed is reported elsewhere (Arranz *et al.* 2018). The structure of the paper is as follows. Section 2 presents the methodology used for the simulations, including the numerical methods, geometric and inertial model of the seed, etc. The results of the simulations are presented and discussed in section 3 in terms of the seed kinematics and the distribution of aerodynamic forces. Finally, the conclusions are presented in section 4.

2. Methodology

2.1. *Numerical model*

The problem under study is the motion of a winged seed immersed in ambient fluid. Four different reference frames are used in the present analysis: Σ_L, Σ_p, Σ_c and Σ_R. Σ_L is the laboratory reference frame: an inertial reference frame with axes x_L, y_L and z_L, the latter pointing upwards. Σ_p is a body-fixed reference frame centered at the seed's gravity centre, G, whose axes coincide with the principal axes of inertia of the seed. Both Σ_L and Σ_p are sketched in figure 1a, and are used to solve the equations of motion of the seed, as discussed in the next paragraph. The other two reference frames sketched in figure 1b, Σ_c and Σ_R, are defined in terms of the seed's geometry and are used for analysing and visualizing purposes. Σ_c is a body fixed reference frame centered at the centre of the nut; with z_c normal to the wing of the seed and y_c pointing towards the tip of the wing. On the other hand Σ_R is a non-inertial reference frame whose attitude is defined by its axes z_R, parallel to z_L, and y_R, which is the projection of y_c on the horizontal plane ($z_L = 0$).

We define $\mathbf{i}$, $\mathbf{j}$ and $\mathbf{k}$ to be the unit vectors in the x, y and z directions, respectively. The subscript of these vectors indicate the reference frame they belong to, e.g.: $\mathbf{i}_L$ is the unit vector of x_L. On the other hand, to specifically indicate that a vector is expressed in a certain basis, the superscript notation, $\mathbf{x}^Y$, is used, where Σ_Y is the basis. Therefore, $\mathbf{x}^Y$ indicates that the components of $\mathbf{x}^Y$, namely, (x_1, x_2, x_3) are $x_1 = \mathbf{x} \cdot \mathbf{i}_Y$, $x_2 = \mathbf{x} \cdot \mathbf{j}_Y$ and $x_3 = \mathbf{x} \cdot \mathbf{k}_Y$.

The equations that govern the motion of the seed are:

$$m_s \dot{\mathbf{u}}_G = \mathbf{F}_{ext}, \tag{1}$$

$$\mathsf{I}_G \dot{\boldsymbol{\Omega}} + \boldsymbol{\Omega} \times \mathsf{I}_G \boldsymbol{\Omega} = \mathbf{M}_G. \tag{2}$$

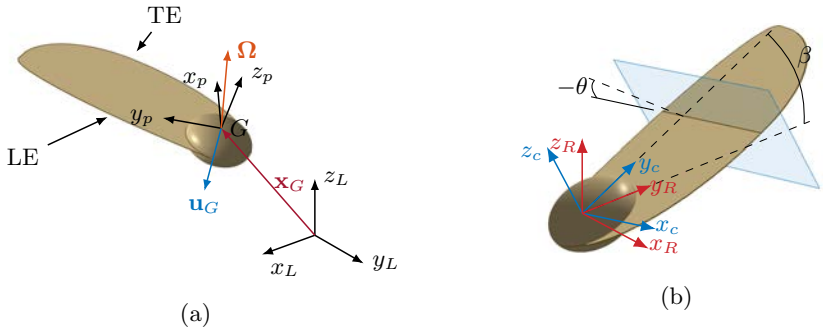

FIGURE 1: (a) Sketch of Σ_L and Σ_p. The position vector of the gravity centre, $\mathbf{x}_G$, the velocity vector of G, $\mathbf{u}_G$, and the angular velocity vector, $\mathbf{\Omega}$, are also displayed. LE and TE stands for the leading edge and the trailing edge of the wing seed, respectively. (b) Sketch of Σ_c and Σ_R. The two angles that define the attitude of the seed, the coning angle, β, and the pitch angle, θ, are also displayed.

In eq. (1) and eq. (2), dot indicates time derivative, m_s is the mass of the seed, $\mathbf{u}_G$ is the absolute velocity of the gravity centre (i.e. with respect to Σ_L), $\mathbf{F}_{ext}$ are the external forces acting upon the seed, $\mathbf{\Omega}$ is the angular velocity, I_G is the tensor of inertia about the gravity centre of the seed and $\mathbf{M}_G$ are the moments about the gravity centre. Note that eq. (2) is expressed in a body-fixed frame of reference. The external forces are the gravity, $-m_s g \mathbf{k}_L$, where g is the gravity acceleration; buoyant force, $m_s \rho / \rho_s g \mathbf{k}_L$, where ρ and ρ_s are the fluid and seed densities, respectively; and aerodynamic forces, $\mathbf{F}$. On the other hand, we consider that the moment $\mathbf{M}_G$ is only due to the aerodynamic forces, which is strictly true for a samara of uniform density.

Equation (1) is solved in the inertial reference frame Σ_L, whereas eq. (2) is solved in the body reference frame Σ_p. The latter simplifies the resolution of eq. (2) since the tensor I_G, when expressed in Σ_p, is constant and diagonal, with the elements of this diagonal corresponding to the principal moments of inertia of the seed.

In order to solve eq. (1) and eq. (2), the attitude of Σ_p with respect Σ_L must be known. This is done here with the quaternion formulation, which avoids the possible singularities that may arise with the Euler angles (see Tewari 2007). The quaternion, $\mathbf{Q} = (Q_1, Q_2, Q_3, Q_4)$, is defined as:

$$Q_i = e_i \sin\left(\frac{\varphi}{2}\right) \quad (i = 1, 2, 3) \quad \text{and} \tag{3}$$

$$Q_4 = \cos\left(\frac{\varphi}{2}\right), \tag{4}$$

where $\mathbf{e} = (e_1, e_2, e_3)$ is a unit vector along the rotation axis and φ is the angle of rotation. Hence, the quaternion $\mathbf{Q}$ defines a rotation that converts Σ_L into Σ_p. It is possible to show that the time evolution of $\mathbf{Q}$ is:

$$\frac{\mathrm{d}\mathbf{Q}}{\mathrm{d}t} = \frac{1}{2}\Omega\mathbf{Q}, \tag{5}$$

where Ω depends on $\mathbf{\Omega}^p = (p, q, r)$ (superscript p indicates that $\mathbf{\Omega}$ is expressed in Σ_p), namely:

$$\Omega = \begin{pmatrix} 0 & r & -q & p \\ -r & 0 & p & q \\ q & -p & 0 & r \\ -p & -q & -r & 0 \end{pmatrix}. \tag{6}$$

For further details about quaternion formulation the reader is referred to Tewari (2007).

The solution to the system of equations eq. (1), eq. (2) and eq. (5) yields the evolution of the seed's dynamics. However, the aerodynamic forces and moments acting on the seed must be known. To compute them, we solve the incompressible Navier-Stokes equations,

$$\nabla \cdot \mathbf{u} = 0, \tag{7a}$$

$$\frac{\partial \mathbf{u}}{\partial t} + (\mathbf{u} \cdot \nabla)\mathbf{u} = -\frac{1}{\rho}\nabla p_f + \nu \nabla^2 \mathbf{u}, \tag{7b}$$

where $\mathbf{u}$ is the fluid velocity, p_f is the pressure and ν is the kinematic viscosity of the fluid. Equations eq. (7a) and eq. (7b) are solved in the inertial reference frame, Σ_L.

Direct numerical simulations are carried out to solve eq. (7a) and eq. (7b) with TUCAN: an in-house solver of the Navier-Stokes equations that uses a fractional step method and centered, second-order finite differences for spatial derivatives in a staggered grid; time evolution is performed by a semi-implicit three stages Runge-Kutta method; and the presence of the body inside the fluid is modelled by means of an Immersed Boundary Method (IBM) (Uhlmann 2005). The code is described in Moriche (2017) and it has been extensively validated and applied to aerodynamic flows (Moriche *et al.* 2016, 2017).

The coupling between the equations of motion and the Navier-Stokes equations is implemented as in Uhlmann (2005). It is a weak coupling, in which at each Runge-Kutta stage, the flow is solved first to obtain $\mathbf{F}$, and then the seed dynamics are updated. The difference with Uhlmann (2005) is that eq. eq. (2) is expressed in the principal axes of inertia, entailing the computation of eq. (5). On the contrary, Uhlmann (2005) modelled spheres which have isotropic inertia properties, so that I_G is constant regardless of the reference frame, and there is no need to keep track of the orientation of the sphere.

To validate the present algorithm, we have computed the motion of an oblate spheroid of aspect ratio 1.5 and density ratio $\rho_s/\rho_f = 2.14$ settling under gravity in ambient fluid. For this configuration, high-fidelity data from a boundary-conforming spectral-element method is available (Chrust 2012). Using a grid resolution of 24 points per major axis, we have reproduced the instability regimes described in Chrust (2012), and their transitions with increasing the Galileo number, $Ga = \sqrt{(\rho_s/\rho_f - 1)gV}/\nu$, where V is the volume of the spheroid. Particularly, our validation runs show a steady vertical trajectory for $Ga = 96$, steady oblique for $Ga = 110$, oscillating oblique for $Ga = 122$ and vertical with lateral oscillations for $Ga = 150$.

(a) (b)

FIGURE 2: (a) *Tipuana Tipu* seed. (b) Simplified model of *Tipuana Tipu* seed used in the simulations. Top view and side view of the model. C is the geometric centre of the nut, and G is the gravity centre of the seed. For reference Σ_p and Σ_c are also sketched.

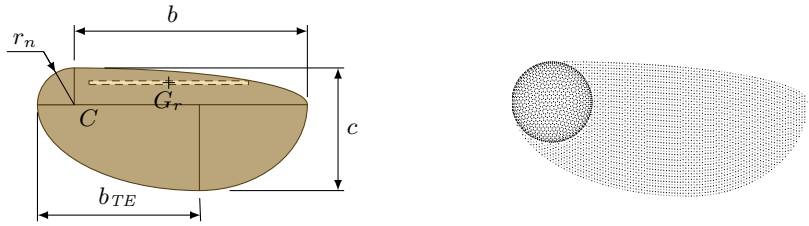

(a) (b)

FIGURE 3: (a) Sketch of the wing planform together with the fictitious rod and its gravity centre position, G_r. (b) Discretization of the samara seed.

2.2. *Geometric, inertial and aerodynamic model*

For the simulations, we use a simplified model based on the *Tipuana Tipu* seed shown in figure 2a. The use of a simplified model instead of replicating the actual shape of a real samara is well justified if one looks at the vast variety of winged-seed's geometries that exist in Nature (Azuma & Yasuda 1989; Green 1980). This simplified model consists of a nut, which is modelled as an oblate spheroid, and a wing modelled as a flat plate (see figure 2b).

The shape of the wing consists of four quarters of ellipse which are tangent to each other, following the same approach as Pedersen & Żbikowski (2006) to model insect wings (figure 3a). Note that similarities between winged seeds and animal wings were already reported by Norberg (1973) and have been recently analysed by Ortega-Jiménez *et al.* (2017) in terms of their auto-rotation.

We define the characteristic chord of the wing to be c (see figure 3a). The dimensions of the wing are $b/c = 1.9$, $b_{TE}/c = 1.32$ and $r_n/c = 0.3$, as shown in figure 3a. Note that r_n is the semi-major axis of the nut, whose aspect ratio is 0.6 (i.e. ratio between the semi-minor axis and the semi-major axis of the ellipsoid).

For the inertia model, we assume that the seed has constant density ρ_s, the oblate spheroid is solid, and the wing is a flat plate of thickness $t = 0.005c$. Moreover, the effect of the thick leading edge –which plays a role of the utmost importance in auto-rotation stability (Norberg 1973; Seter & Rosen 1992; Yasuda & Azuma 1997), is also accounted for with a fictitious rod, shown in figure 3a. The dimensions of this fictitious rod are adjusted so that for the spanwise sections of the wing affected by the rod, the distance from the leading edge to the mass centre is smaller than 30% of $c(y_c)$, in accordance to Norberg (1973). The rod is defined by its radius $r_r = 0.05c$ and length $l_r = 1.54c$, the position of its gravity centre, $\mathbf{CG_r} = -0.25c\mathbf{i}_c + 0.77c\mathbf{j}_c$ (where $\mathbf{CG_r}$ denotes the vector from C to G_r), and the orientation of its longitudinal axis, parallel to y_c (see figure 3a). In this fashion, the resulting inertia tensor of the seed with respect to C expressed in Σ_c, namely, I_C^c, is:

$$\mathsf{I}_C^c = \begin{bmatrix} 19.26 & -0.99 & 0 \\ -0.99 & 3.20 & 0 \\ 0 & 0 & 21.57 \end{bmatrix} \cdot 10^{-3}\rho_s c^5,$$

and the gravity centre of the seed with respect to Σ_c turns out to be, $\mathbf{CG} = -0.018c\mathbf{i}_c + 0.185c\mathbf{j}_c$. The principal tensor of inertia turns out to be:

$$\mathsf{I}_G^p = \begin{bmatrix} 16.29 & 0 & 0 \\ 0 & 3.17 & 0 \\ 0 & 0 & 18.56 \end{bmatrix} \cdot 10^{-3}\rho_s c^5.$$

2.3. *Computational set-up*

To perform the simulations, the seed is placed in a cubic fluid domain of side $10.66c$. Periodic boundary conditions are imposed at the lateral boundaries, whereas a uniform inflow is imposed at the bottom boundary ($z^L = -3.66c$), and an advective boundary condition is imposed at the top boundary. The computational domain is discretized with a uniform Cartesian grid of 512^3 points, which corresponds to 48 grid points per length c. This resolution has been set after performing a grid refinement study, presented in Appendix Appendix A. Likewise, the seed is also discretized into points (see figure 3b) whose resolution is based on the requirements of the immersed boundary method (Uhlmann 2005). Particularly, the seed consists of 5674 points. Since the wing thickness t is much smaller than the grid spacing, $\Delta = c/48$, the wing is modelled as a flat surface. The time step, Δt, has been selected so that $CFL = u_{max}\Delta t/\Delta \leq 0.2$, where u_{max} is the maximum velocity in the flow field.

The seed is free to rotate and its gravity centre can move on an horizontal plane, but we restrain its motion in the vertical direction. Note that fixing $z_G^L = 0$ (and $w_G^L = \dot{w}_G^L = 0$) and imposing a constant inflow velocity w_d results in a configuration that is analogous to the *natural* configuration: a seed descending at a constant speed w_d in a fluid at rest. The advantage of this procedure is that it allows a finer control of the simulation parameters (note that in the *natural* configuration the descent velocity

of the seed, w_d, is unknown), and a simpler set-up of the computational domain: in the *natural* configuration, when the inflow velocity is not exactly equal to w_d, the seed is eventually advected outside of the computational domain.

Finally, it should be noted that fixing the vertical position of the gravity centre of the seed means that the the vertical component of eq. (1) is not solved, which is the only equation involving the gravity acceleration, g. Indeed, once the seed has reached a stable auto-rotative state, we can use the value of F_z^L obtained in the simulation to estimate the value of g required to have a equilibrium of forces in the vertical direction,

$$g = \frac{F_z^L}{m_s} \frac{\varrho}{\varrho - 1}, \tag{8}$$

where F_z^L is the vertical component of $\mathbf{F}^L$, and $\varrho = \rho_s/\rho_f$ is the density ratio. Then, the simulation can be restarted in the *natural* configuration (i.e., solving all components of eq. (1) and allowing the seed to move freely in the domain) using the value of g computed in eq. (8). This approach is proposed by Uhlmann & Dušek (2014). We followed this procedure for a single case, obtaining a dynamical response of the samara in the *natural* configuration virtually indistinguishable to the results reported in section 3.

When fixing $z_G^L = 0$, the problem depends on two non-dimensional numbers, the density ratio, ϱ, and the Reynolds number, Re. In our simulations $\varrho = 300$ (which is a reasonable value close to reality) and we vary the Reynolds number, $Re = [80, 160, 240]$. Note that these Re are on the lower limit of typical Reynolds number of actual winged-seeds, which ranges from $Re \simeq 350$ to 1540 (Green 1980; Azuma & Yasuda 1989; Salcedo *et al.* 2013).

To trigger the auto-rotation of the seed, the simulations are started with initial conditions: $\mathbf{\Omega}_0 = \Omega_0 \mathbf{k}_L = c/w_d \mathbf{k}_L$, $\mathbf{u}_G = 0$, and z_p parallel to z_L, which is equivalent to an initial rotation about G. To check the effect of the value Ω_0 on the final auto-rotative steady state, we also started a simulation with $\Omega_0 = \frac{1}{2} c/w_d$, yielding the same auto-rotative state. It should be highlighted that in both cases, the initial angular velocity is lower than the final angular velocity.

The previous procedure is followed to start the simulation with $Re = 240$ and with a lower resolution, $256 \times 256 \times 256$ grid points, to save computational time. Once the seed has performed several cycles, at a given time t_1, the flow field is interpolated into a finer grid of $512 \times 512 \times 512$ grid points and the simulation is restarted with this denser mesh. For $Re = 80$ and 160, we use the flow field and the seed attitude at t_1 to restart the simulation with the desired Re at the reduced resolution. After the seed has performed several cycles with the new Reynolds number, the field is interpolated into the finer mesh, as explained previously, and the simulations are continued.

3. Results

For all cases under study the seed attained an asymptotic state with finite amplitude auto-rotation. We performed additional simulations at $Re \leq 80$. First, the simulation was started directly at $Re = 80$ with the initial condition described in section 2.3. In this case the seed failed to auto-rotate, suggesting that the problem presents hysteresis. Likewise, starting with the auto-rotating simulation at $Re = 80$, we successively

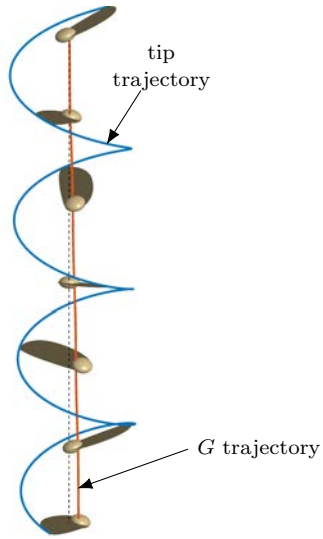

FIGURE 4: Three dimensional view of the seed's trajectory for $Re = 240$. (——) Trajectory of the wing's tip, (——) trajectory of the gravity centre. The attitude of the seed is depicted at different equidistant time instants. The dotted line is a vertical axis parallel to $\mathbf{k}_L$.

decreased the Reynolds number and it was observed that there may be a lower limit $Re \approx 50$ below which auto-rotation is no longer possible. Nevertheless, the aim of this study is not to determine what is the exact Reynolds number at which auto-rotation is no longer possible so that additional simulations should be performed in the future in order to establish this value accurately.

For a visualization of the simulations, figure 4 shows the trajectory and orientation of the seed at $Re = 240$ descending at a constant speed w_d. The seed is depicted at equispaced time instants. In addition, the trajectory of the wing tip and G are also displayed.

Although in figure 4 only $Re = 240$ is shown, the motion is qualitatively similar for all Re under study. From figure 4, one can infer that the seed spins about a vertical axis; thus, $\mathbf{\Omega}$ is parallel to $\mathbf{k}_L$ (except for small deviations which never exceed 2°). As a result, the wing tip describes a helical path. On the contrary, G follows almost a vertical path (with small displacements in x_L and y_L), suggesting that the rotation axis is very close to G.

As mentioned in section 1, auto-rotation is due to a tight coupling between the aerodynamic forces and the seed's motion. In turn, aerodynamic forces are greatly dependent on flow structures, which are represented in figure 5. This figure displays iso-surfaces of the second invariant of the velocity gradient tensor, Q, for the case with $Re = 240$ (i.e. the Q-criterion of Hunt *et al.* 1988 for the identification of vortical structures). Three main vortical structures can be identified: the wing tip vortex; the

FIGURE 5: Iso-surfaces of the Q-criterion for $Re = 240$. Light blue iso-surface $\tilde{Q} = 0.5$, dark blue iso-surface $\tilde{Q} = 5$, where $\tilde{Q} = Qc^2/w_d^2$.

wake shed by the nut; and the LEV (i.e, leading edge vortex) which is formed above the wing and corresponds to the darker blue surface in figure 5. As a consequence of the rotation, the wing tip vortex wraps about a vertical axis, forming a helical structure, similar to the trajectory of the wing tip shown in figure 4. The vortex shed by the nut has also a helical shape, but with a smaller radius. A more detailed analysis of the corresponding flow fields is reported in Arranz *et al.* (2018).

Figure 4 shows that the seed reaches a quasi-stationary state. Consequently, in the following sections we will discuss time averaged quantities over the last 4 periods of the simulations. These averaged quantities are denoted with angular brackets, e.g.: $\langle x \rangle$. Likewise, non-dimensional variables are denoted as $\tilde{x}$.

3.1. *Seed kinematics*

Quantitatively, the effect of the Reynolds number on the motion of the seed is assessed by the change of the coning angle, β, and the pitch angle, θ, the angular velocity, $\mathbf{\Omega}$, and the displacement of G. β is the angle between $\mathbf{j}_c$ and the horizontal plane, and it gives an indication of how tilted the winged seed is with respect to the horizontal plane. On the other hand, θ is the angle between $\mathbf{i}_c$ and $\mathbf{i}_R$ and it can be seen as a geometric angle of attack. The definitions of both β and θ are depicted in figure 1b. Mathematically, β and θ are defined as:

$$\beta = \cos^{-1}\left(\mathbf{j}_c \cdot \mathbf{j}_R\right) \tag{9}$$

$$\theta = -\mathrm{sgn}(\mathbf{i}_c \cdot \mathbf{k}_L)\cos^{-1}\left(\mathbf{i}_c \cdot \mathbf{i}_R\right) \tag{10}$$

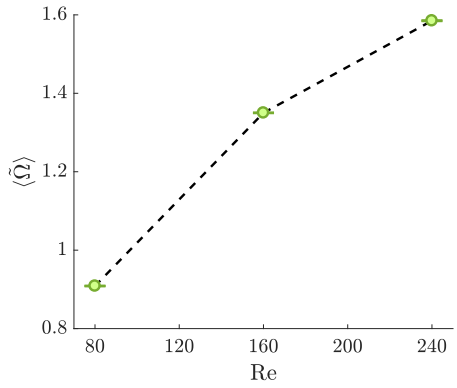

FIGURE 6: Evolution of $\tilde{\Omega}$ averaged over the last four periods, $\langle\tilde{\Omega}\rangle$, as a function of Re. The standard deviation is depicted with error bars.

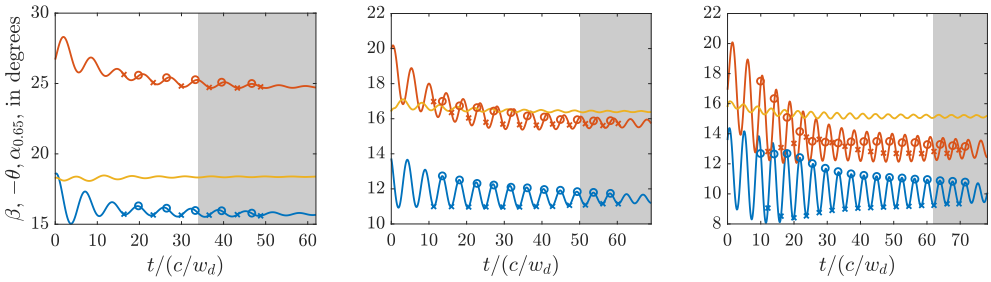

(a) $Re = 80$ (b) $Re = 160$ (c) $Re = 240$

FIGURE 7: Temporal evolution of β (——); θ (——); and the angle of attack at $0.65b$, $\alpha(y_c = 0.65b)$ (——). Symbol ()rresponds to the time instant when fluid relative velocity is local maximum; ()e the time instants when fluid relative velocity is local minimum. The shaded region correspond to the last four periods, where the averages are calculated.

Figure 6 displays the average of the modulus of the non-dimensional angular velocity (namely, $\tilde{\Omega} = \Omega c/w_d$) as a function of Re, together with its standard deviation. In figure 6 one can appreciate that the standard deviation for all the cases is very small, indicating that $\tilde{\Omega}$ is indeed rather constant. Looking at the evolution of $\langle\tilde{\Omega}\rangle$ with Re, one can observe that it increases with Re, i.e. the seed spins faster as the Reynolds number increases. The values of $\langle\tilde{\Omega}\rangle$ are also gathered in table 1.

Figure 7 shows the temporal evolution of β and θ for the different Reynolds numbers. The time $t = 0$ corresponds to the time when the simulations are started on

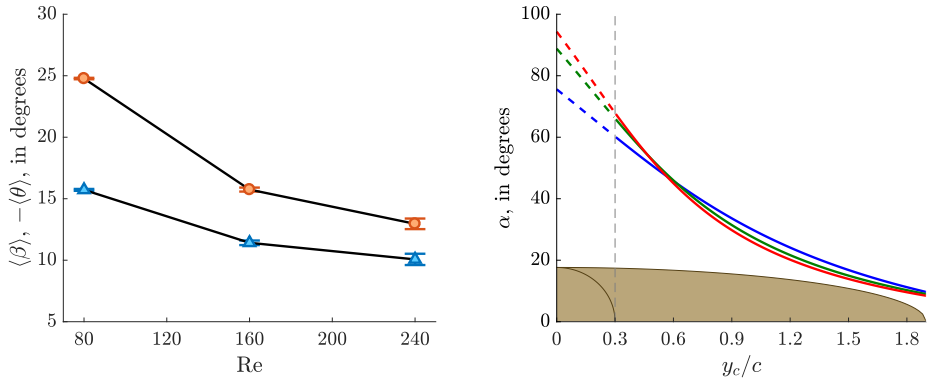

FIGURE 8: (a) Evolution of $\langle\beta\rangle$ (▲), and $-\langle\theta\rangle$ (●) as a function of Re. The standard deviation of β and $-\theta$ is depicted with error bars. (b) Angle of attack distribution along the span of the seed's wing. (——) $Re = 80$, (——) $Re = 160$ and (——) $Re = 240$. The dashed vertical line depicts the start of the nut.

the fine grid. Regardless of Re, both angles show an oscillatory behaviour about a mean value after an initial transient. The initial variation is caused by the change of the resolution, as explained in section 2.3. Nonetheless, the oscillation of both angles is small, not exceeding 2°. Note that there is a phase shift of approximately $\pi/2$ between β and θ. Also, the oscillations observed in figure 7 have a fixed frequency. This frequency is equal to $\Omega/2\pi$ for all Reynolds numbers, meaning that the period of the oscillations is the period of the rotation. It is interesting to recall that this oscillatory behaviour has also been observed experimentally (Ulrich & Pines 2012). This issue will be discussed further below.

Figure 8a shows the evolution of the mean coning angle, $\langle\beta\rangle$, and the mean pitch angle, $\langle\theta\rangle$, with the Reynolds number. The angles are averaged over the last 4 periods (shaded region in figure 7), and their standard deviation is also depicted in the plot by means of vertical bars. One should recall that θ is always negative, and that is why both figure 7 and figure 8a show $-\theta$. A negative pitch angle means that if the axis y_c would lie on the horizontal plane, the leading edge of the seed would be below this horizontal plane. As the Reynolds number is increased both the coning and the pitch angle decrease (in absolute magnitude). Thus, the wing of the seed tends to be more parallel to the horizontal plane as Re is increased. Note that the growth of the standard deviation with Re means that the amplitude of the oscillations increases, a fact that one can appreciate in figure 7. The values of $\langle\beta\rangle$ and $\langle\theta\rangle$ are also gathered in table 1.

We now proceed to compare our results with the kinematics of actual seeds. To do so, table 1 shows experimental values of the coning angle, the pitch angle and the tip speed ratio, λ, found in the literature. Since in all the references the Reynolds

	Species	Re	$\widehat{Re}$	$\langle\tilde{\Omega}\rangle$	$\langle\beta\rangle$	$-\langle\theta\rangle$	$\langle\tilde{r}_{GR}\rangle$	λ
Present simulations	–	80	63	0.91	15.72	24.77	$2.7 \cdot 10^{-2}$	1.66
	–	160	126	1.35	11.49	15.82	$1.2 \cdot 10^{-2}$	2.52
	–	240	188	1.58	10.06	13.06	$0.8 \cdot 10^{-2}$	2.96
Green (1980)	*Acer rublum*	–	723	–	36.3	12.5	–	2.89
	Acer saccharum	–	1673	–	12.9	9.0	–	3.32
	Acer saccharinum	–	1880	–	27.3	10.6	–	4.28
Azuma & Yasuda (1989)	*Acer palmatum Thunb*	–	276	–	15.0	0.90	–	2.04
	Acer palmatum Thunb. var	–	457	–	27.6	1.39	–	2.27
	Acer diabolicum Blume	–	459	–	23.7	1.17	–	3.57
Salcedo *et al.* (2013)	*Swietenia macrophylla*	–	1670	–	20.2	–	–	2.21

TABLE 1: Average values of the kinematics ($\langle\tilde{\Omega}\rangle$, $\langle\beta\rangle$, $\langle\theta\rangle$, $\langle\tilde{r}_{GR}\rangle$ and λ) as function of Re. $\langle\beta\rangle$ and $\langle\theta\rangle$ are given in degrees. For comparison, the table gathers experimental values from the existing literature for different species.

number is based on the mean chord, $\hat{c} = S/b_w$, where S is the total surface of the wing and b_w is the total span of the wing ($b_w = b + r_n$ in our case), we define a new Reynolds number for the comparison, $\widehat{Re} = w_d\hat{c}/\nu$. It should be noted that the seeds reported in table 1 belong to different species, having different geometries and inertias. This precludes a quantitative comparison with our results. For the same reason, an analysis of the effect of the Re on the kinematics of the seeds cannot be assessed with the experimental values of table 1. This analysis has to rely only on the present simulation data.

Despite the simplifications of our model (flat wing, no surface roughness, imposed inertia tensor), the kinematics of the seed are qualitatively similar to experiments found in existing literature. The coning angle of the different seeds ranges between 12° and 36°. Nonetheless, table 1 shows that within our simulations $\langle\beta\rangle$ agrees with the lower limit of the coning angle measured in experiments. However, the trend exhibited in figure 8a is a decrease of $\langle\beta\rangle$ with the Reynolds number. If this tendency is followed, lower $\langle\beta\rangle$ would be expected for higher Re, in disagreement with experiments. This discrepancy could be attributed to the simplifications of the model. However, the behaviour of this trend might change for higher Re.

Comparison of the pitch angle is more cumbersome due to the difficulty in measuring it experimentally. Moreover, there is no consensus of the definition of θ. For instance, Green (1980) defines θ as "tilt of wing in plane of rotation", whereas Azuma & Yasuda (1989) defines θ at a given spanwise section. Therefore, we limit the comparison to the sign of $\langle\theta\rangle$, which is always negative in both the experiments and in our results.

In order to compare the angular velocity, the tip speed ratio, λ, is used (Miller *et al.* 1997). This parameter is computed as the ratio between the tip speed due to angular velocity (roughly $b\langle\tilde{\Omega}\rangle\cos\langle\beta\rangle$) and the descent speed, w_d. The tip speed ratio is gathered in table 1. In the literature, λ ranges from approximately 2 to 3.3. The values of the simulations are within the experimental range (except the case $Re = 80$, which is slightly lower).

The combined effect of β, θ and $\mathbf{\Omega}$ determines the angle of attack, $\alpha(y_c)$, which is an important quantity in aerodynamics. Mathematically, α can be expressed as

$$\alpha(y_c) = \tan^{-1}\left(\frac{\mathbf{u}_e(y_c)\cdot\mathbf{k}_c}{\mathbf{u}_e(y_c)\cdot\mathbf{i}_c}\right), \tag{11}$$

where $\mathbf{u}_e(y_c) = w_d\mathbf{k}_L - \mathbf{u}_G - \mathbf{\Omega}\times(y_c\mathbf{j}_c)$ is the effective velocity at each spanwise section. Figure 8b depicts the angle of attack distribution along the span for the different Re. It is found that the angle of attack distribution is very similar for the three Re, specially for $y_c > 0.6c$. For the outer spanwise positions, the local angle of attack slightly decreases with the Reynolds number. The temporal evolution of α is similar to β and θ, namely, it oscillates with a frequency of $\Omega/2\pi$. However, the amplitude of the oscillations is one order of magnitude smaller than those of β and θ, although they also increase with Re. This phenomenon is illustrated in figure 7, where the temporal evolution of α at $y_c = 0.65b$ is depicted. The selection of this particular spanwise section is somewhat arbitrary, but similar plots are obtained for other sections (specially in terms of the effect of the Reynolds numbers).

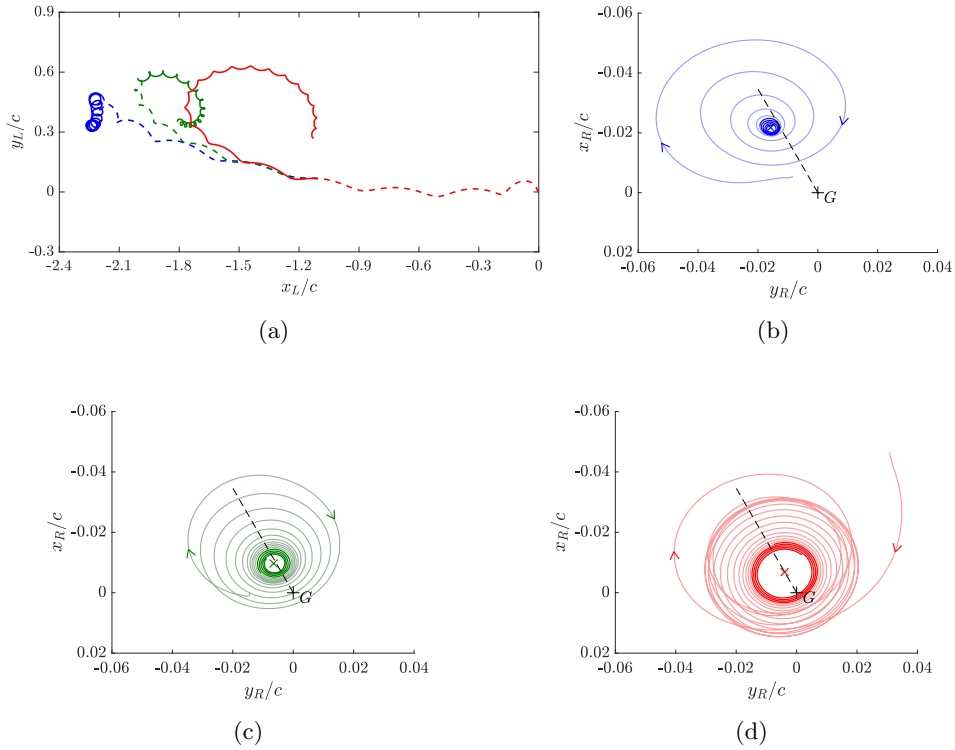

FIGURE 9: (a) Trajectory of the gravity centre, G on the horizontal plane. Line style: (- - -) Resolution $256 \times 256 \times 256$ grid points, (——) resolution $512 \times 512 \times 512$ grid points. (——) $Re = 80$, (——) $Re = 160$ and (——) $Re = 240$. (b) (c) and (d) Intersection of the *moving axoid* with the horizontal plane $z_L/c = 0$. (b) $Re = 80$, (c) $Re = 160$, and (d) $Re = 240$. The intersection during the last four periods is highlighted. () the mean position of the rotation axis averaged over the last four periods. The dashed line makes 120° with respect to y_c

We turn now our attention to the motion of G in the horizontal plane. Recall that, as discussed in figure 4, the velocity of G in the horizontal plane is not zero. Indeed figure 9a shows the trajectory of the gravity centre on the horizontal plane for the different Reynolds numbers. For $Re = 80$, after the initial transient (shown in dashed line), the gravity centre seems to rotate about an axis which tends to be at a fixed position. For $Re = 160$ and 240 the trajectories shown in figure 9a seems to suggest that for these Reynolds numbers the axis of rotation does not tend to a fixed position. This is reminiscent of the different regimes of sedimentation observed for simpler bodies, like spheres, disks and spheroids (Ern *et al.* 2012).

To better understand the motion described by the seed in figure 9a, we compute the *moving axoid*, which is the locus of the instantaneous axis of rotation seen from a body fixed reference frame (Beju *et al.* 1983). Note that the instantaneous axis of rotation is always parallel to $\mathbf{\Omega}$, which in turn is parallel to $\mathbf{k}_L$ (except for small deviations, as previously commented). Therefore, the *moving axoid* is a ruled surface which can be characterized by its intersection with the plane $z_L = z_R = 0$.

Figure 9b-d depicts the intersection of the *moving axoid* with the plane $z_R = 0$ for the different Re in Σ_R centered at G. For $Re = 80$ the intersection is a point (figure 9b), meanwhile for $Re = 160$ and 240 it is a circle (figure 9c and 9d). This indicates that for $Re = 80$ the seed gravity centre is rotating about a fixed axis in the laboratory reference frame, as we anticipated from figure 9a. On the other hand, the *moving axoid* for $Re = 240$ and 160 resembles that of a cylinder with its mass centre at a position different from its geometric centre, rolling without slipping over a surface. The radius of the intersection corresponds to the radius of the cylinder, and the distance from the centre of the intersection to G is the offset between the gravity centre and the geometric centre of the cylinder.

Therefore, the moving axoids shown in figure 9c and 9d are consistent with a seed rotating about an axis (the geometric centre of the intersection) which in turn is displacing, as we hypothesized from figure 9a. In this fashion, we can define $\mathbf{r}_{GR}$ to be the vector from G to the mean position of the intersection during the last four periods (represented with the symbol $\times$ in figure 9b-d). It is interesting to note that the modulus of $\mathbf{r}_{GR}$ decreases with Re (see table 1), while the angle between $\mathbf{r}_{GR}$ and $\mathbf{j}_R$, γ, remains constant for all Re and close to 120° (particularly it ranges from 126.0° for $Re = 80$, to 120.1° for $Re = 240$). This means that the seed is rotating while skidding (i.e, oversteering), which in the helicopter nomenclature corresponds to a positive lead angle equal to $\pi - \gamma$. Nevertheless, it should be stressed that as shown in table 1, $\tilde{r}_{GR} \sim 0.01$. Hence, the seed is rotating about a vertical axis which practically coincides with G, as we anticipated from the visualization of figure 4.

In sight of the above, we could attempt to split $\mathbf{u}_G$ into a rotational component, $\mathbf{u}_{G,r}$, and a displacement component, $\mathbf{u}_{G,d}$. The former would be the velocity of G relative to the rotation axis, that is $\mathbf{u}_G$ if the axis of rotation is fixed. Hence, the latter would be the velocity at which the axis of rotation *moves*. To calculate $\mathbf{u}_{G,d}$ we apply a low pass filter to $\mathbf{u}_G$, removing the frequencies greater than 1/2 the rotation frequency, $\Omega/2\pi$. The filtered signal corresponds to $\mathbf{u}_{G,d}$. Then, we calculate the modulus of $\mathbf{u}_{G,d}$, yielding $u_{G,d}/w_d = 0.0014$, 0.0058 and 0.0213 for $Re = 80, 160$ and 240, respectively. Therefore, as Re increases the seed rotates about a vertical axis which tends to move faster.

The displacement velocity, $\mathbf{u}_{G,d}$, may explain the increasing oscillations of β and θ with Re. The motion of the seed is analogous to the motion of a helicopter's blade in forward flight. The aerodynamic forces produced by the blade depend on the relative velocity of the fluid with respect to the blade. Higher velocities produce higher aerodynamic forces (Seddon & Newman 2011). When the helicopter is fixed at a point, the relative velocity is radial and depends only on the angular velocity of the blade and the radial distance. In this fashion, the aerodynamic forces developed are constant throughout a cycle. However, when the helicopter is moving forward at a

	Forces			Moments		
Re	$\langle\tilde{F}_x^R\rangle$	$\langle\tilde{F}_y^R\rangle$	$\langle\tilde{F}_z^R\rangle$	$\langle\tilde{M}_x^R\rangle$	$\langle\tilde{M}_y^R\rangle$	$\langle\tilde{M}_z^R\rangle$
80	-0.46	-0.34	1.72	1.02	-0.25	$7\cdot10^{-4}$
160	-0.46	-0.30	2.48	1.70	-0.39	$7\cdot10^{-4}$
240	-0.43	-0.27	2.87	2.08	-0.46	$6\cdot10^{-4}$

TABLE 2: Average values of the forces and moments as a function of Re.

given velocity, $\mathbf{U}$ (or the flow surrounding it has a velocity $-\mathbf{U}$), the relative velocity of the blade depends also on its orientation with respect to the direction of the motion. Therefore, the aerodynamic forces would change depending on the azimuthal position of the blade.

For the case of the winged-seed, when it is moving with a velocity $\mathbf{u}_{G,d}$, a similar behaviour might be expected, with the addition that the seed is free to change its attitude. Hence, variations of the attitude could be expected due to the variation of the aerodynamic forces. In fact, the amplitude of the oscillations of the angles are in accordance to the amplitudes imposed to the helicopter's blades for the given advance ratios, $u_{G,d}/\Omega b$ (Seddon & Newman 2011).

3.2. *Dynamics and force equilibrium*

After the analysis of the kinematics of motion, we proceed with the analysis of the aerodynamic forces. Table 2 gathers the mean aerodynamic forces and moments about G averaged over the last four periods and expressed in Σ_R. The forces are non-dimensionalized with $\rho_f w_d^2 c^2$ and the moments are non-dimensionalized with $\rho_f w_d^2 c^3$, such that $\tilde{F} = F/\rho_f w_d^2 c^2$ and $\tilde{M} = M/\rho_f w_d^2 c^3$.

The data in table 2 show that the horizontal forces ($\langle\tilde{F}_x^R\rangle$ and $\langle\tilde{F}_y^R\rangle$) slightly decrease in magnitude with Re, whereas the vertical force $\langle\tilde{F}_z^R\rangle$ substantially increases. The latter means that the *allowed* weight of a given seed increases with Re. On the other hand, if G is rotating about a vertical axis, the projection of the aerodynamic forces onto the horizontal plane should counteract the centrifugal force, i.e. it should be $m_s\Omega^2\mathbf{r}_{GR}$. Indeed, the modulus of the horizontal component of $\tilde{\mathbf{F}}$ is $0.57, 0.55$ and 0.51 for $Re = 80, 160$ and 240, respectively. These values are within a 2% of the average non-dimensional centrifugal force, namely $m_s\langle\tilde{\Omega}\rangle^2\langle\tilde{r}_{GR}\rangle/\rho c^3$. It is also interesting to remark that even though r_{GR} is small, and one could presume the seed is rotating about G, this small distance is responsible for the slight decrease of $m_s\langle\tilde{\Omega}\rangle^2\langle\tilde{r}_{GR}\rangle/\rho c^3$ with Re (i.e., Ω increases with Re). Moreover, the centrifugal force is of the same order as the vertical force. Finally, as expected, the resultant aerodynamic force points towards the axis of rotation and the angle between the horizontal projection of $\mathbf{F}$ and the y_c axis ranges from 126.1° for $Re = 80$, to 122.4° for $Re = 240$, in agreement with the position of the *moving axoids* in figure 9.

The moments along x_R and y_R are higher for higher Re. Note that this trend is in accordance with the behaviour of the forces, i.e.: higher vertical force and relatively constant horizontal forces. Note also that the latter is necessary to compensate the acceleration terms due to the rotation of the seed around an axis which is not parallel

to a principal axis of inertia. On the other hand, the moment along z_R axis is nearly zero for all Re. This is a necessary consequence of having a constant angular velocity pointing along $\mathbf{k}_R$.

With the aim of explaining the previous trends, we analyse the force distribution on the seed with respect to Σ_c. We choose Σ_c because it is a body fixed reference frame whose vertical axis, z_c, is normal to the wing, which is the direction along which the aerodynamic force is largest.

Figure 10 shows the distribution of the three components of the aerodynamic force and the pitching moment with respect to the axis y_c (figure 10d). These quantities are non-dimensionalized using the descent speed, w_d, the chord, c, and the fluid density, ρ. The distributions are averaged over a time interval that corresponds to the last revolution of the seed. Note that the discretization of the wing is such that near the wing tip there are only a few lagrangian points per chord (see figure 3b), which leads to oscillations of the force distribution at this region.

As expected figure 10a shows that the largest contribution to F_z^c is produced by the wing. The contribution of the nut is also positive and it is likely more related to the drag experienced by the nut in a free-stream of velocity w_d, than to the fact that the seed is rotating. On the wing, the normal force distribution is roughly parabolic, with a peak value that increases and displaces towards the tip as Re increases. As a result, the integral of the normal force along the span increases as Re rises. This increase is likely a consequence of the larger angular velocity, yielding higher relative velocities.

On the contrary, the contribution of the force along the x_c direction, figure 10b, is very similar despite the different Ω among cases. In fact, the integral of F_x^c decreases with Re. This behaviour might be explained by the fact that these forces are associated to the skin friction (at least on the wing), rather than to the angular velocity. The nut and the sections of the wing closer to the nut are actually producing negative drag. Note that this region is close to the axis of rotation, and the flow pattern near the nut is complex (see figure 5). Therefore, the behaviour of the forces in this region cannot be easily explained.

The force distribution in the spanwise direction is shown in figure 10c. It is positive along the wing and relatively constant (slightly increasing with Re) meanwhile it becomes negative at the nut at $y_c \approx 0.15c$. Similarly to f_x^c, f_y^c is a tangential force, thus it is likely linked to skin friction rather than to pressure forces, as f_z^c. Hence, a positive spanwise force suggests the presence of a spanwise flow towards the tip, a hypothesis that is confirmed in Arranz *et al.* (2018).

The distribution of the pitching moment (figure 10d) along the span gives an indication of how the normal force is distributed along the chord at each spanwise section. Positive pitching moment means *nose up* moment about the y_c axis. For all Re the pitching moment is negative at every spanwise location. Therefore, there is a *nose down* moment about y_c for all Re along the span, which is consistent with $\langle \tilde{M}_y^R \rangle$. Note that the behaviour of the pitching moment with Re is similar to the one observed for f_z^c. This could be anticipated beforehand since the pitching is directly proportional to f_z^c.

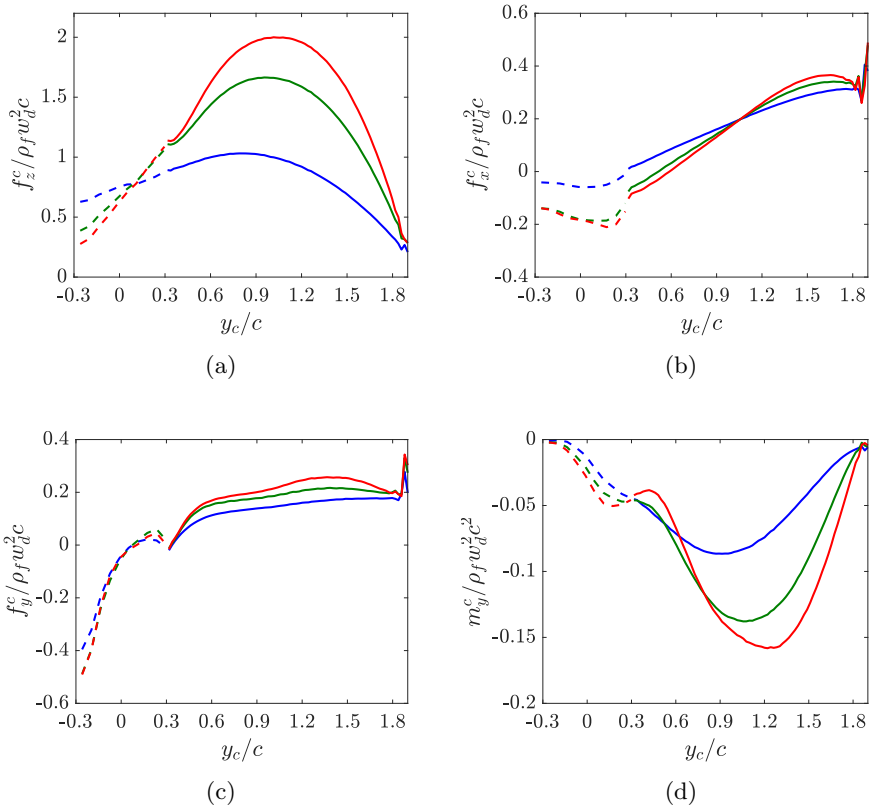

FIGURE 10: Forces and moment distribution over the seed in Σ_c reference frame for (——) $Re = 80$, (——) $Re = 160$ and (——) $Re = 240$. (a) Force distribution normal to the wing, f_z^c. (b) Force distribution tangential to the chordwise direction, $\mathbf{i}_c$, f_x^c. (c) Force distribution tangential to the spanwise direction, $\mathbf{j}_c$, f_y^c. (d) Pitching moment –i.e. moment along y_c axis–, m_y^c. Dashed lines correspond to the nut, continuous lines correspond to the wing.

The selection of the descent speed for the non-dimensionalization of the force in figure 10 is somewhat arbitrary. It could be argued that since the angular velocity changes with Re, this quantity should also enter in the non-dimensionalization of the aerodynamic forces. This idea is explored by defining the aerodynamic force and moment coefficients

$$C_f(y_c) = \frac{f^c}{\frac{1}{2}\rho_f U_e^2(y_c) c(y_c)}, \qquad C_m(y_c) = \frac{m^c}{\frac{1}{2}\rho_f U_e^2(y_c) c(y_c) c},$$

in terms of the modulus of the effective velocity at each wing section, $U_e(y_c) = \|\mathbf{u}_e(y_c)\|$, and the local chord, $c(y_c)$. Note that the effective velocity is a function of the descent speed, coning angle and angular velocity.

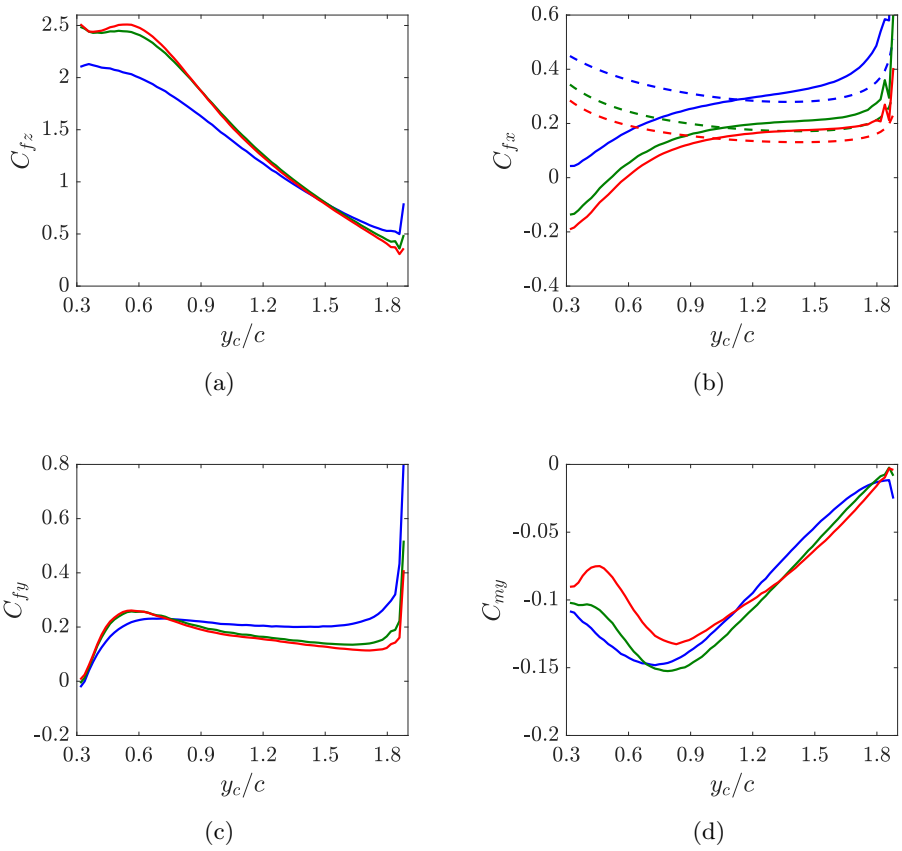

FIGURE 11: Forces and moment coefficients distribution over the seed in Σ_c reference frame for (——) $Re = 80$, (——) $Re = 160$ and (——) $Re = 240$. (a) Normal force coefficient, C_{fz}. (b) Tangential force coefficient, C_{fx}. Dashed lines are the friction coefficient calculated with the local chord $c(y_c)$ and the effective velocity $U_e(y_c)$. (c) Spanwise force coefficient C_{fy}. (d) Pitching moment coefficient C_{my}.

Figure 11 shows these aerodynamic force and moment coefficients along the span. Note that only the portion of the span corresponding to the wing is depicted in the figure since U_e has not been defined for the nut. In general, the force and moment coefficients tend to collapse better than in figure 10 (except possibly for C_{fx}), especially when only $Re = 160$ and 240 are considered. In figure 11a and figure 11d one can appreciate that C_{fz} and C_{my} tend to collapse for all Re for $y_c \geq 1.2c$. Thus, as we anticipated, f_z^c (and in turn, m_y^c) is highly linked to the relative velocity at each spanwise section, rather than to the Re. In other words, f_z^c is more related to pressure forces than to viscous forces. It is also noteworthy that C_{fz} along the span resembles the angle of attack distribution of figure 8b.

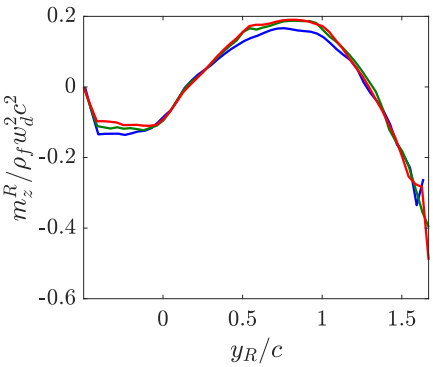

FIGURE 12: Vertical moment distribution, m_z^R along y_R direction. (——) $Re = 80$, (——) $Re = 160$ and (——) $Re = 240$.

As mentioned above, C_{fx} (figure 11b) seems to show a Re number dependency, decreasing as Re increases at any spanwise section. This behaviour is in agreement with the evolution of the skin friction coefficient of a flat plate with Re, which is included in figure figure 11b with dashed lines. Although the behaviour of the local friction coefficient is not the same as C_{fx} (in the calculation of the friction coefficient, it is assumed that the flow is aligned with the chord and three dimensional effects are not considered), it is observed that the offset among different Re coincides for both coefficients. Finally, the behaviour of C_{fy} (figure 11c) is more intricate, and it is probably linked to both viscous effects and centrifugal forces.

Integration of the previous forces yields $\mathbf{F}^R$. However, it is not clear *a priori* how these force distributions yield $\langle \tilde{M}_z^R \rangle \approx 0$. There are two possibilities: the distribution of the vertical moment is negligible at all spanwise sections (i.e., $m_z^R(y_R) \approx 0$ for all y_R), or the distribution is non-zero but it changes sign along y_R. Figure 12 depicts m_z^R as a function of y_R for the different Reynolds numbers, non-dimensionalized with the descent speed, w_d, the characteristic chord of the wing, c, and the fluid density ρ. Two facts are remarkable. First, the moment distribution is very similar for all Re despite the difference in the force distribution for the different cases. Second, the moment is negative near the nut and near the tip and positive elsewhere, which is very similar to the distribution of m_z^R in the blades of helicopters in auto-rotation (Cuerva *et al.* 2009). Moreover, the spanwise section of *proper* auto-rotation (i.e. the spanwise section near the tip where $m_z^R = 0$) is at approximately 70% of the total span of the seed's wing, which is the characteristic spanwise section of auto-rotation of helicopter's blades (Cuerva *et al.* 2006).

4. Conclusions

We present simulations of the auto-rotation of a model winged seed at various Reynolds numbers in the range $80 - 240$, keeping the seed's geometry and inertia constant. The calculations have been performed by solving the Navier-Stokes equations for the

flow surrounding the seed using an immersed boundary method, together with the Newton-Euler rigid-body equations for the motion of the seed. Within this Reynolds number range, the seed attains a stable auto-rotative state, with an approximately constant angular velocity about a vertical axis. The coning angle and the pitch angle present small oscillations about a mean value for all Re under study. Both the mean value and the amplitude of the oscillations decrease as the Reynolds number is increased. Thus, with increasing Re, the seed tends to rotate at higher speeds, with less inclination with respect to the horizontal plane. The kinematics of the seed is similar to that reported in the literature in experiments with real winged seeds.

Also with increasing Re, it has been found that the translation of seed on the horizontal plane seems to increase. By computing the *moving axoid* we have observed that the vertical axis of rotation displaces, while the distance from the gravity centre of the seed to the axis remains rather constant for a given Re. Therefore, the lateral motion of the seed can be described as a regular rotation with respect to an axis which is drifting. This drifting velocity seems to increase with Re, and seems to be connected to the oscillations in β and θ. Moreover, we have found that the seed rotates while skidding (oversteering), resulting in an angle between the spanwise axis of the seed and the centrifugal forces (pointing towards the center of the moving axoid) of about $\gamma \approx 120°$, irrespective of the Re. In the helicopter nomenclature, this corresponds to a positive lead angle of the blade.

We have analysed the aerodynamic forces and moments acting on the seed. Is is observed that, with increasing Reynolds number, the horizontal components decrease in magnitude while the vertical component increases. Thus, the allowed weight of a given seed increases with the Reynolds number. Despite the displacement of the seed on the horizontal plane, and the oscillations of the angles (which lead to small variations in the angular velocity), a simplified equilibrium of forces and moments was found. The horizontal force is directed towards the axis of rotation and with a magnitude roughly equal to the centrifugal force. The moment about the vertical direction vanishes (as expected if the seed rotates with constant angular velocity about a vertical axis). In this regard, we have analysed the vertical moment distribution along the span that results in a zero moment. It has been found that it is very similar to typical moment distributions on auto-rotating helicopter blades, and it seems to be independent of Re.

The force distribution along the wing span was characterized using both global and local characteristic speeds and chord lengths for the non dimensionalisation of the force coefficients. It was found that the vertical component does not depend on the Reynolds number when using local scaling, suggesting that this component is mainly due to pressure force. On the other hand, the components tangent to the wing do present variations with the Reynolds number, so that they seem to be related to viscous forces.

Acknowledgements

This work was supported by grants TRA2013-41103-P (Mineco/Feder UE) and DPI2016-76151-C2-2-R (AEI/Feder UE). MGV was partially supported by a grant of the BBVA Foundation. The code was partially developed during a stay of MM

Points/c	$\tilde{F}_z$	ε_z	$\tilde{F}_x$	ε_x
32	1.8989	5.2%	0.9421	2.3%
40	1.8592	2.9%	0.9326	1.3%
48	1.8342	1.6%	0.9263	0.6%
64	1.8060	–	0.9205	–

TABLE 3: Non-dimensional forces and relative errors, ε, as a function of the resolution.

(funded by BBVA) and MGV (funded by the Spanish Ministry of Education through the program José Castillejo) at the Karlsruhe Institute of Technology. The simulations were partially performed at the Steinbuch Centre for Computing (SCC), Karlsruhe. The computer resources, technical expertise and assistance provided by this center are thankfully acknowledged.

Appendix A. Grid refinement study

A grid refinement study was performed to determine the grid resolution to be employed in the simulations. The study was performed by externally imposing the attitude and angular velocity of the seed. The attitude of the seed and angular velocity were chosen corresponding to those obtained in a preliminary calculation of the auto-rotating seed at $Re = 75$ with high resolution. Therefore, the imposed motion of the seed is defined by $\langle\beta\rangle = 15.91°$, $\langle\theta\rangle = -25.48°$ and $\langle\tilde{\Omega}\rangle = 0.89$. We then performed several simulations varying the grid resolution at $Re = 240$, to study the convergence of the aerodynamic forces. These simulations were performed in a computational domain of dimensions $x_L/c \in [-2, 2]$, $y_L/c \in [-2, 2]$ and $z_L/c \in [-3, 5]$, with *free-slip* boundary conditions at the lateral walls, an inflow at the bottom wall and advective boundary condition at the top wall. Note that *free-slip* boundary conditions are imposed at the lateral walls because the gravity centre of the seed is fixed at the center of the horizontal plane $z_L = 0$. Therefore, the seed cannot cross the lateral boundaries, as it may occur when the seed is free to move on the horizontal plane.

Four grid resolutions were tested, 32, 40, 48 and 64 points per chord length, which correspond to domains of $128 \times 128 \times 256$ grid points, $160 \times 160 \times 320$ grid points, $256 \times 256 \times 512$ grid points, and $512 \times 512 \times 768$ grid points, respectively.

The variation of the vertical (F_z) and horizontal (F_x) aerodynamic forces non-dimensionalized with $\rho w_d^2 c^2$, as well as their relative error, ε, are gathered in table 3. The relative error is calculated using the forces obtained with 64 points/c, averaged over one period, as reference values:

$$\varepsilon_{z,x} = \frac{|\tilde{F}_{z,x} - \tilde{F}^{64}_{z,x}|}{\tilde{F}^{64}_{z,x}} \tag{12}$$

Figure 13 displays the variation of ε_z and ε_x with the resolution. There, one can appreciate that for resolutions higher than 32 points/c, ε_x is less than 2%. Likewise, for 48 points/c, ε_z is also less than 2%. Therefore, we choose a resolution of 48 points/c since both ε_x and ε_z are smaller than 2%. Although the grid refinement study was

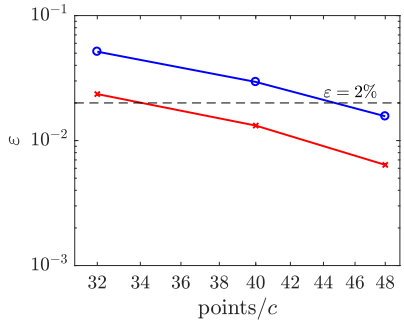

FIGURE 13: Variation of the relative error of the vertical force, (—•—) ε_z, and the horizontal force, (—×—) ε_x, with the resolution.

performed for $Re = 240$, the same grid was employed for the cases $Re = 80$ and $Re = 160$, for which the results are expected to be correspondingly more accurate.

REFERENCES

ARRANZ, G., GONZALO, A., UHLMANN, M., FLORES, O. & GARCÍA-VILLALBA, M. 2018 A numerical study of the flow around a model winged seed in auto-rotation. Submitted to *Flow Turbul. Combust.*

AZUMA, A. 1992 *The biokinetics of flying and swimming*. Springer-Verlag.

AZUMA, A. & YASUDA, K. 1989 Flight performance of rotary seeds. *J. Theor. Biol.* **138** (1), 23–53.

BEJU, I., SOÓS, E. & TEODORESCU, P. 1983 *Euclidean tensor calculus with applications*. CRC Press.

BURROWS, F. M. 1975 Wind-borne seed and fruit movement. *New Phytol.* **75** (2), 405–418.

CHRUST, M. 2012 Etude numérique de la chute libre d'objets axisymétriques dans un fluide newtonien. PhD thesis, Strasbourg.

CUERVA, A., ESPINO, J. L., LÓPEZ, O., MESEGUER, J. & SANZ, A. 2009 *Teoría de los helicópteros*. Madrid: ETSI Aeronáuticos, UPM.

CUERVA, A., SANZ-ANDRÉS, A., MESEGUER, J & ESPINO, J. L. 2006 An engineering modification of the blade element momentum equation for vertical descent: an autoration case study. *J. Am. Helicopter Soc.* **51** (4), 341–348.

ERN, P., RISSO, F., FABRE, D. & MAGNAUDET, J. 2012 Wake-induced oscillatory paths of bodies freely rising or falling in fluids. *Annu. Rev. Fluid Mech.* **44**, 97–121.

FREGENE, K. & BOLDEN, C. L. 2010 Dynamics and control of a biomimetic single-wing nano air vehicle. In *American Control Conference (ACC), 2010*, pp. 51–56. IEEE.

GREEN, D. S. 1980 The terminal velocity and dispersal of spinning samaras. *Am. J. Bot.* **67** (8), 1218–1224.

HUNT, J. C. R., WRAY, A. A. & MOIN, P. 1988 Eddies, stream, and convergence zones in turbulent flows **Report CTR-S88**.

LEE, INJAE & CHOI, HAECHEON 2017 Flight of a falling maple seed. *Phys. Rev. Fluids* **2**, 090511.

LENTINK, D., DICKSON, W. B., VAN LEEUWEN, J. L. & DICKINSON, M. H. 2009 Leading-edge vortices elevate lift of autorotating plant seeds. *Science* **324** (5933), 1438–1440.

Limacher, E. & Rival, D. E. 2015 On the distribution of leading-edge vortex circulation in samara-like flight. *J. Fluid Mech.* **776**, 316–333.

Miller, A., Muljadi, E. & Zinger, D. S. 1997 A variable speed wind turbine power control. *IEEE T. Energy Conver.* **12** (2), 181–186.

Minami, S. & Azuma, A. 2003 Various flying modes of wind-dispersal seeds. *J. Theor. Biol.* **225** (1), 1–14.

Moriche, M. 2017 A numerical study on the aerodynamic forces and the wake stability of flapping flight at low reynolds number. PhD thesis, Univ. Carlos III Madrid.

Moriche, M., Flores, O. & García-Villalba, M. 2016 Three-dimensional instabilities in the wake of a flapping wing at low Reynolds number. *Int. J. Heat Fluid Flow* **62A**, 44–55.

Moriche, M., Flores, O. & García-Villalba, M. 2017 On the aerodynamic forces on heaving and pitching airfoils at low Reynolds number. *J. Fluid Mech.* **828**, 395–423.

Nathan, R. 2006 Long-distance dispersal of plants. *Science* **313** (5788), 786–788.

Norberg, R. 1973 Autorotation, self-stability, and structure of single-winged fruits and seeds (samaras) with comparative remarks on animal flight. *Biol. Rev.* **48** (4), 561–596.

Obradovic, B., Ho, G., Barto, R., Fregene, K. & Sharp, D. 2012 A multi-scale simulation methodology for the samarai monocopter μUAV. In *AIAA Modeling and Simulation Technologies Conference*, p. 5012.

Ortega-Jiménez, V. M., Martín-Alcántara, A., Fernández-Feria, R. & Dudley, R. 2017 On the autorotation of animal wings. *J. R. Soc. Interface* **14** (126), 20160870.

Pedersen, C. B. & Żbikowski, R. 2006 *An indicial-Polhamus aerodynamic model of insect-like flapping wings in hover*, *Flow Phenomena in Nature*, vol. 2, pp. 606–666. Liebe, R.

Pounds, P. & Singh, S. 2015 Samara: Biologically inspired self-deploying sensor networks. *IEEE Potentials* **34** (2), 10–14.

Rosen, A. & Seter, D. 1991 Vertical autorotation of a single-winged samara. *J. App. Mech.* **58** (4), 1064–1071.

Salcedo, E., Treviño, C., Vargas, R. O. & Martínez-Suástegui, L. 2013 Stereoscopic particle image velocimetry measurements of the three-dimensional flow field of a descending autorotating mahogany seed (*Swietenia macrophylla*). *J. Exp. Biol.* **216** (11), 2017–2030.

Seddon, John M. & Newman, Simon 2011 *Basic helicopter aerodynamics*, 3rd edn. Chichester, West Sussex, UK: Wiley.

Seter, D. & Rosen, A. 1992*a* Stability of the vertical autorotation of a single-winged samara. *J. App. Mech.* **59** (4), 1000–1008.

Seter, D. & Rosen, A. 1992*b* Study of the vertical autorotation of a single-winged samara. *Biol. Rev.* **67** (2), 175–197.

Tewari, A. 2007 *Atmospheric and space flight dynamics*. Springer.

Uhlmann, M. 2005 An immersed boundary method with direct forcing for the simulation of particulate flows. *J. Comput. Phys.* **209** (2), 448–476.

Uhlmann, M. & Dušek, J. 2014 The motion of a single heavy sphere in ambient fluid: A benchmark for interface-resolved particulate flow simulations with significant relative velocities. *Int. J. Multiphas. Flow* **59**, 221–243.

Ulrich, E. & Pines, D. J. 2012 Effects of planform geometry on mechanical samara autorotation efficiency and rotational dynamics. *J. Am. Helicopter Soc.* **57** (1), 1–10.

Ulrich, E. R., Darryll, P. & Humbert, J. S. 2010 From falling to flying: the path to powered flight of a robotic samara nano air vehicle. *Bioinspir. Biomim.* **5** (4), 045009.

Varshney, K., Chang, S. & Wang, Z. J. 2012 The kinematics of falling maple seeds and the initial transition to a helical motion. *Nonlinearity* **25** (1), C1.

Yasuda, K. & Azuma, A. 1997 The autorotation boundary in the flight of samaras. *J. Theor. Biol.* **185** (3), 313–320.

Paper 3

3

A numerical study of the flow around a model winged seed in auto-rotation

G. Arranz[1], A. Gonzalo[1], M. Uhlmann[2], O. Flores[1], M. García-Villalba[1]

[1] Universidad Carlos III de Madrid, Spain
[2] Karlsruhe Institute of Technology, Germany

Flow, Turbulence & Combustion (2018), vol. **101** (2), 477–497

In this study the flow around a winged-seed in auto-rotation is characterized using direct numerical simulations (DNS) at Reynolds number in the range $80 - 240$, based on the descent speed and a characteristic chord length. In this range, the flow is approximately steady when observed from a reference frame fixed to the seed. For all cases, the flow structure consists of a wing tip vortex which describes a helical path, a vortex shed behind the nut of the seed and a stable leading edge vortex above the wing surface which merges with the tip vortex. With increasing Reynolds number, the leading edge vortex becomes more intense and gets closer to the wing surface. The simulation results also show the formation of a spanwise flow on the upper surface of the wing, moving fluid towards the wing tip in a region downstream and beneath the leading edge vortex. This spanwise flow is rather weak inside the core of the leading edge vortex, and the analysis of the streamlines show a very weak transport of vorticity along the vortex for the cases under consideration. The analysis of the flow suggests that the stabilization of the leading edge vortex is mainly due to non-inertial accelerations, although viscous effects may contribute, specially at lower Re. Furthermore, the leading edge vortex has been characterized by analysing the flow variables averaged along cross-sections of the vortex. While some quantities, like the spanwise velocity or the pressure inside the vortex, are rather insensitive to the threshold used to define the leading edge vortex, the same is not true for the circulation of the vortex or its averaged spanwise vorticity, due to the viscous nature of the vortex. Finally, it is observed that the spanwise vorticity scales with the angular rotation of the seed for the different Re.

Key words: direct numerical simulation, auto-rotation, leading edge vortex

1. Introduction

Geometric and inertia properties of certain bodies induce their rotation when falling through an ambient fluid at rest. Winged seeds, or samaras, are a clear example: when they fall from their tree, they start auto-rotating thanks to their structural pattern (Norberg 1973). The particular case of the samara is interesting among other auto-rotative bodies because, as it rotates, it creates a high lifting force, opposite to

the gravity force, which results in a decrease of its descent speed. This "parachuting effect" increases the chance of being transported by a lateral gust wind, thus allowing the seed to spread over a wider area (Green 1980).

The auto-rotation of winged-seeds has received some attention in the literature over the last decades. Probably one of the first detailed studies on the dynamics of auto-rotation of winged-seeds is due to Norberg (1973), who studied this phenomenon theoretically. Later, Azuma & Yasuda (1989) report kinematic and aerodynamic parameters for different winged-seeds species, based on experimental measurements. More recent studies focus on the characterization of the parametric space where winged-seeds auto-rotate, in terms of their geometry and their mass distribution. For instance, Yasuda & Azuma (1997) analyse the influence of the position of the gravity centre and the geometry of the wing, performing experiments with both real seeds and models with simplified geometries. Similarly, Varshney *et al.* (2012) present a series of experiments on winged-seeds, in which sections of the wing are systematically removed until the wing surface is reduced to 30% of the original value. They report that the seed is still able to enter into auto-rotation, despite these drastic structural changes. Seter & Rosen (1992) conducted a stability analysis, using a numerical model, to analyse the effect of the mass distribution of the seed on its auto-rotation. Their results show that stability is highly dependent on the chordwise distribution, being a concentrated mass towards the leading edge a necessary condition for auto-rotation. More recently, Lee & Choi (2017) performed direct numerical simulations to analyse the effect of lateral wind disturbances on the trajectory of the seed. They show that in the presence of moderately strong wind (of the order of the descent velocity) the autorotation is maintained, and the seed falls at roughly the same velocity.

On the other hand, the autorotation of winged seeds has motivated the development of some bio-inspired aerial vehicles (Obradovic *et al.* 2012; Fregene & Bolden 2010; Ulrich *et al.* 2010; Pounds & Singh 2015). Lentink and co-workers found that a stable leading edge vortex (LEV), similar to the one produced in flapping wings (Ellington *et al.* 1996), is created on the upper surface of winged seeds as they auto-rotate (Lentink *et al.* 2009). The presence of a stable LEV was later confirmed Salcedo *et al.* (2013) and Lee *et al.* (2014) in winged-seeds of different size and shape, suggesting that leading edge vortex formation is a common mechanism in auto-rotating seeds. Due to the interest in the development of bio-inspired micro air vehicles (MAV) and the role that the LEV plays in the aerodynamic performance of flapping wings, the relevance of this discovery can be easily understood: the flow around a steadily falling seed is simpler than the fully unsteady flow over the flapping wings of animals. In the former, the LEV remains always attached, reaching a quasi-steady state. In flapping wings, a new LEV is generated in every stroke, to be shed into the wake at the stroke reversal.

In fact, the study of LEV stability on revolving and flapping wings is a topic of active research. There is a broad literature (including both experimental and numerical studies) discussing the stabilization mechanisms of the LEV in revolving and hovering wings (Garmann & Visbal 2014; Harbig *et al.* 2013; Jardin & David 2014; Jardin 2017; Lentink & Dickinson 2009; Limacher & Rival 2015; Birch & Dickinson 2001; Birch *et al.* 2004; Poelma *et al.* 2006). Although the understanding of the phenomenon is

far from complete, several mechanisms have been already identified. The existence of a spanwise flow inside the LEV, which drains vorticity towards the tip, is widely accepted as a stabilization mechanism for revolving wings at $Re \gtrsim 1000$ (van den Berg & Ellington 1997; Birch *et al.* 2004; Jardin & David 2014). At lower Re, the spanwise flow is weaker; thus, although vorticity transport could still balance production at the leading edge (see Poelma *et al.* (2006)), other mechanisms may play an important role, such as a centrifugal pumping (Lentink & Dickinson 2009), or viscous effects (Jardin 2017).

It is also interesting to note that, in the references of the previous paragraph, the simulations and the experiments are conducted on wings which are impulsively started and they revolve with a certain amplitude while the LEV develops. This angular amplitude is always restricted to be less than 360° to avoid the wing encountering its own wake. In the case of the winged-seed falling in ambient fluid, the seed never encounters its own wake. This, together with the low Reynolds number under consideration, means that the LEV remains always attached and steady.

Besides its advantages for the study of the dynamics of the LEV, the study of samara's auto-rotation entails several challenges. Auto-rotation is the result of the coupling between inertia and aerodynamic force, thus it is inherently a non-linear phenomenon (Lugt 1983). As a consequence, the motion and attitude of the seed are not known *a priori* so that it is necessary to solve the Newton-Euler equations of the seed coupled with the Navier-Stokes equations, which provide the aerodynamic force. Therefore, the resulting motion will largely depend on the seed's shape, its mass distribution, and the fluid properties, leading to a large parametric space.

The purpose of the present paper is to characterize the flow and the LEV around a model winged-seed (with fixed shape and inertia properties) in auto-rotation, varying the Reynolds number ($Re = w_d c/\nu$, where w_d is the descent speed, c is the characteristic chord of the seed, and ν is the kinematic viscosity of the fluid). To that end, direct numerical simulations of a falling winged seed in auto-rotation are performed at Re ranging from 80 to 240. Note that, by fixing the geometry and the inertia of the seed while changing Re, it is possible to isolate its effect on the auto-rotation of the seed, both in terms of the dynamics (which will vary due to the aforementioned coupling) and in terms of the flow around the seed. The present paper focus on the analysis of the latter. Although we also briefly discuss the motion of the winged seed (since it affects the flow), the detailed analysis of the kinematics and dynamics of the seed is reported elsewhere (Arranz *et al.* 2018).

The paper is structured as follows: section 2 details the numerical model used to perform the simulations, as well as the seed model and the set-up of the simulations; the analysis of the flow is presented in section 3; and finally, several conclusions are drawn in section 4.

2. Methodology

2.1. *Numerical model*

In the present study the descent of a model winged-seed at a constant speed w_d is considered. The seed is free to rotate along any direction and its gravity centre, G, can displace within the horizontal plane.

To simulate the motion of the seed, it is treated as a rigid body. Hence, we solve the equations of motion of the seed,

$$m_s \dot{\mathbf{v}}_G = \mathbf{F}_{ext}, \tag{1}$$

$$\mathsf{I}_G \dot{\boldsymbol{\Omega}} + \boldsymbol{\Omega} \times \mathsf{I}_G \boldsymbol{\Omega} = \mathbf{M}_G. \tag{2}$$

In these equations, a dot on a variable denotes its time derivative. In eq. (1), m_s is the mass of the seed, $\mathbf{v}_G$ is the velocity of the seed's gravity centre and $\mathbf{F}_{ext}$ is the external force acting upon the seed (sum of aerodynamic force, gravity force and buoyant force). In eq. (2), I_G is the inertia tensor of the seed with respect to G, $\boldsymbol{\Omega}$ is the angular velocity, and $\mathbf{M}_G$ are the external moments about G. Note that eq. (2) holds when expressed in a body fixed reference frame, where I_G is time independent. Moreover, $\mathbf{M}_G$ is due only to aerodynamic forces, which is strictly true for a seed of uniform density.

In order to obtain the aerodynamic force acting upon the seed, the equations of motion are solved together with the incompressible Navier-Stokes equations. This is done with TUCAN, an in-house DNS code that solves the incompressible Navier-Stokes equations. TUCAN uses a fractional step method on a staggered grid. Spatial derivatives are discretized with centered, second-order finite differences, and a semi-implicit low-storage three-stage Runge-Kutta method is used for time integration. The presence of the body is modelled using the immersed boundary method (IBM) proposed by Uhlmann (2005). More details on the flow solver can be found in Moriche (2017), which has been validated with a collection of 2D (Poiseuille flow, Taylor-Green vortices, stationary and moving cylinders and heaving and pitching airfoils (Moriche *et al.* 2017)), and 3D flows (fully-developed turbulent channel flow, laminar flow around a sphere and heaving and pitching wings (Moriche *et al.* 2016)).

The coupling between the Navier-Stokes equations and the equations of motion also follows the algorithm proposed by Uhlmann (2005). The coupling between the rigid-body equations for the seed and the fluid equations is weak: at each Runge-Kutta stage the aerodynamic force on the seed is computed from the flow solver, then this force is used in the rigid-body equations to update the state of the seed. The most important difference between the present code and the algorithm proposed by Uhlmann (2005) is that the latter is designed to deal with spheres, where only their angular velocity and acceleration is needed (i.e., not their angular orientation). In the present simulations it is necessary to track the orientation of the seed, which is accomplished with the quaternion formulation described in Arranz *et al.* (2018). The present algorithm has been validated by computing the motion of an oblate spheroid of aspect ratio 1.5 and density ratio $\rho_s/\rho_f = 2.14$ (where ρ_s and ρ_f are the spheroid and fluid density, respectively) settling under gravity in ambient fluid, a configuration for which high-fidelity data from a boundary-conforming spectral-element method is available (Chrust 2012). Using a grid resolution of 24 points per major axis, we have reproduced the instability regimes described in Chrust (2012), and their transitions with increasing the Galileo number, $Ga = \sqrt{(\rho_s/\rho_f - 1)gV}/\nu$, where g is the gravity acceleration and V is the volume of the spheroid. In particular our validation runs show a steady vertical trajectory for $Ga = 96$, steady oblique for $Ga = 110$, oscillating oblique for $Ga = 122$ and vertical with lateral oscillations for $Ga = 150$.

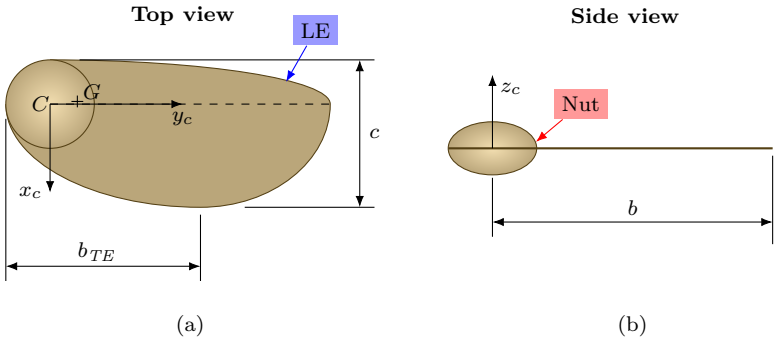

FIGURE 1: Sketch of the modelled seed used in the simulations. (a) Top view, and (b) side view. Besides the characteristic dimensions of the seed, the body fixed reference frame, Σ_c (x_c, y_c, z_c), the geometric centre of the nut, C, the gravity centre, G, and the position of the leading edge (LE) are shown.

The model of the seed has been inspired by an actual *Tipuana Tipu* seed. A sketch of the model is shown in figure 1. It consists of a nut, modelled as an oblate spheroid, and a flat wing, modelled with quarters of ellipses, which are tangent to each other, as proposed by Pedersen & Żbikowski (2006). We define the characteristic chord of the seed to be equal to the maximum chord, denoted c. Thus, the dimensions of the wing are given by $b = 1.9c$ and $b_{TE} = 1.32c$. The semi-major axis of the nut is $0.3c$ and the semi-minor axis is $0.18c$. Figure 1 depicts also the body fixed reference frame Σ_c, whose origin is located at the geometric centre of the nut (point C). The axes of Σ_c are defined such that z_c is perpendicular to the wing's surface, y_c is the spanwise direction (pointing towards the wing tip), and x_c is the chordwise direction (fulfilling the right hand rule).

We prescribe the inertia of the seed in order to take into account the uneven mass distribution along the wing of the seed (Norberg 1973). Thus, the gravity centre of the seed is at $\mathbf{CG} = -0.018c\mathbf{i}_c + 0.185c\mathbf{j}_c$ (where $\mathbf{CG}$ is the vector from C to G and $\mathbf{i}_c$ and $\mathbf{j}_c$ are the unitary vectors of x_c and y_c, respectively); and the inertia tensor of the seed about C expressed in Σ_c is:

$$\mathsf{I}_C = \begin{bmatrix} 19.26 & -0.99 & 0 \\ -0.99 & 3.20 & 0 \\ 0 & 0 & 21.57 \end{bmatrix} \cdot 10^{-3} \rho_s c^5,$$

where ρ_s is the density of the seed. A more complete description of the geometric and inertial model of the seed can be found in Arranz *et al.* (2018).

2.2. *Computational set-up*

The fluid domain employed for the simulations is a cube of length $L = 10.66c$ in which the seed is placed. Periodic boundary conditions are imposed at the lateral walls, a uniform inflow of velocity w_d is imposed at the bottom wall, and an advective boundary condition is imposed at the top boundary. The value of L has been selected

after performing several simulations to ensure that the dynamics of the seed is not affected by the horizontal size of the computational domain. The grid resolution consists of 512^3 grid points, which is equivalent to 48 points per chord length. The resolution was selected after performing a grid refinement study presented in Arranz *et al.* (2018). In addition to the grid for the fluid domain, a Lagrangian grid for the seed needs to be defined. In the IBM of Uhlmann (2005), the area associated to each Lagrangian point has to be roughly the same as the square of the grid spacing for the fluid domain. In the present configuration, this leads to a total number of 5674 Lagrangian points. The time step, Δt, for the temporal evolution is chosen to ensure that $CFL = u_{max}\Delta t/\Delta \leq 0.2$, where u_{max} is the maximum fluid velocity in the whole domain and $\Delta = c/48$ is the grid spacing.

To perform the simulations, the vertical position of the seed's gravity centre is fixed at $3.66c$ from the bottom boundary of the domain (i.e., inflow boundary condition). This means that the seed gravity centre can move within a horizontal plane and the seed can rotate freely about any direction. Therefore, the configuration is equivalent to a seed descending at a constant speed w_d. Consequently, for a given seed geometry and inertia, the Reynolds number, Re, and the density ratio, $\varrho = \rho_s/\rho_f$ (where ρ_f is the fluid density), univocally define the problem. For the present simulations, the density ratio is set to $\varrho = 300$, a value close to the one of real seeds falling in air (according to data extracted from Azuma & Yasuda (1989)).

3. Results

Although the aim of this work is to characterize the flow, we start by summarizing the resulting motion of the seed and its variation with Re. More details can be found in Arranz *et al.* (2018).

For all Reynolds number investigated in this study, the seed auto-rotates at an approximately constant angular velocity about an approximately vertical axis (except for small deviations which never exceed 2° with respect to the vertical). It is interesting to recall that the problem presents hysteresis: the seed auto-rotates at $Re = 80$ if the simulation is started from a flow field obtained from a higher Re calculation, whereas it fails to auto-rotate if the simulation is initialized with a uniform flow field and an impulsive rotation of the seed. Decreasing further Re, the wing of the seed aligns with the free stream and auto-rotation stops, even for the simulations started from initial flow fields obtained from higher Re calculations.

The angular velocity and the attitude of the seed change with Re. The latter is defined by two angles: the coning angle, β, and the pitch angle, θ. The coning angle is the angle between the spanwise axis, y_c, and its projection onto the horizontal plane. The pitch angle is a geometric angle of attack: it is the angle between the chordwise axis, x_c, and the horizontal line contained in a plane perpendicular to y_c. Both angles are depicted in figure 2a.

Figure 2b shows the variation with Re of β, θ and the tip speed ratio, defined as $\lambda = \Omega b/w_d$, being Ω the average angular velocity. It should be noted that the motion of the seed is such that both the coning angle and the pitch angle present small oscillations about a mean value. Therefore, figure 2b shows the mean value of β and θ, together with their standard deviation, depicted as vertical bars. From figure 2b it

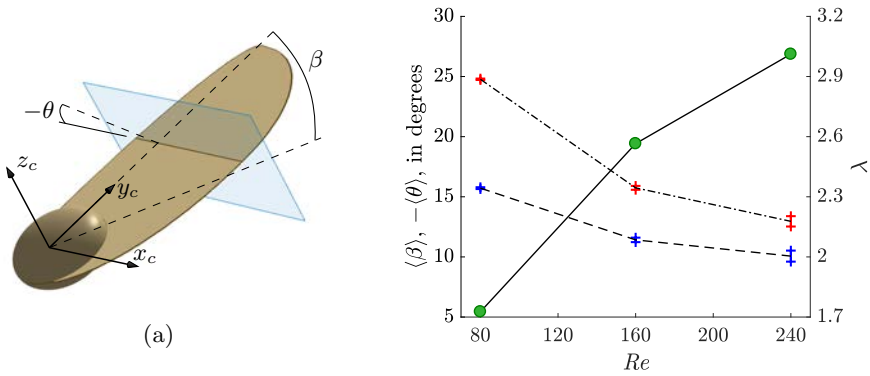

FIGURE 2: (a) Definition of the seed reference frame Σ_c, and the coning (β) and pitch (θ) angles. (b) Evolution of the angles β (- - -), and θ (-·-·-), and the tip speed ratio, λ, (–●–) as a function of the Reynolds number.

is observed that while λ increases with Re (i.e., the seed spins faster with Re), both the coning angle and the pitch angle decrease in magnitude. This means that, with increasing Re, the seed's wing becomes more aligned with the horizontal plane.

The changes in the kinematics of the seed have an impact on the flow around the seed. This is illustrated in figure 3, that displays iso-surfaces of the second invariant of the velocity-gradient tensor, Q (Hunt *et al.* 1988), for $Re = 80$, $Re = 160$ and $Re = 240$. Since the angular velocity changes with Re and the descent velocity is constant for all the cases, we choose Ω^2 to non-dimensionalize Q in order to facilitate the comparison between the various cases. Three main vortical structures can be identified for all Re: a wing tip vortex, a vortex shed behind the nut, and an LEV which is formed above the wing and corresponds to the darker grey surface in figure 3. The wing tip vortex wraps around a vertical axis yielding a helical structure, whose pitch decreases with increasing Re, indicating a faster rotation. The vortex shed behind the nut also forms an helix with the same sense of rotation but smaller radius than the wing tip vortex. This suggests that the axis of rotation is close to the nut (indeed it is found approximately at the gravity centre (Arranz *et al.* 2018)). Finally, the LEV seems to become more intense with increasing Re, especially when comparing the cases $Re = 80$ and 160. Note that the intensity of the LEV is usually related to the lift, so that a more intense LEV results in a larger lift on the wing (Arranz *et al.* 2018).

As discussed above, the coning angle, β, the pitch angle, θ, and the angular velocity remain approximately constant as the seed falls, for a given Reynolds number. As a consequence, and due to the low Reynolds number, the flow around the seed is approximately steady when observed from a reference frame fixed to the seed.

(a) (b) (c)

FIGURE 3: Iso-surfaces of the second invariant of the velocity gradient tensor, Q, for (a) $Re = 80$, (b) $Re = 160$, and (c) $Re = 240$. Light grey surface corresponds to $Q = 0.75\Omega^2$ and dark grey surface corresponds to $Q = 12\Omega^2$ for each case.

Therefore, it seems appropriate to study the flow variables with respect to the seed's reference frame Σ_c. Thus, the time-averaged relative velocity of a given point, $\mathbf{x}$, is

$$\mathbf{u}(\mathbf{x}) = \frac{1}{T}\int_0^T (\mathbf{U} - \mathbf{v}_G - \boldsymbol{\Omega} \times \mathbf{r})\, dt, \tag{3}$$

where $\mathbf{U}$ is the instantaneous absolute velocity, $\mathbf{v}_G$ is the velocity of the seed's gravity centre, $\boldsymbol{\Omega}$ is the instantaneous angular velocity and $\mathbf{r}$ is the vector position from G to $\mathbf{x}$. Note that all the vectors in eq. (3) need to be expressed in Σ_c. For the present cases, the time average is performed over the last 2 revolutions run in the simulation, discarding an initial transient whose duration varies with the Reynolds number from about 10 revolutions for $Re = 80$ to 30 revolutions for $Re = 240$ (see Arranz *et al.* (2018)). Thus, $T \approx 4\pi/\Omega$, where Ω is the averaged angular velocity of the seed. Similarly, the time-averaged relative vorticity is defined as $\omega = \nabla \times \mathbf{u}$, where again the curl is taken in the seed's reference frame Σ_c. From now on, all relative flow variables are implicitly assumed to be averaged in time.

The second invariant of the time-averaged relative-velocity-gradient tensor, q, can also be expressed in terms of the time averaged value of Q, the mean angular velocity, $\Omega\,\mathbf{k}$ (being $\mathbf{k}$ the unit vector parallel to the rotation axis), and ω,

$$q = \frac{1}{T}\int_0^T Q dt - \Omega^2 - \Omega\,\mathbf{k}\cdot\omega. \tag{4}$$

Surfaces of constant q will be used in the following sections to identify and characterize the LEV. Relevant quantities like the circulation of the LEV will be shown to depend on the particular threshold value of q chosen to identify the vortex, henceforth denoted as q_{th}. Note that the range of q_{th} to be employed is implicitly limited by eq. (4). At the inflow, Q and the absolute vorticity are zero, so that $\omega = -2\Omega\,\mathbf{k}$ and $q = \Omega^2$. Therefore, the threshold, q_{th}, to be used to identify the LEV has to be several times larger than q at the inflow.

3.1. *Flow characterization*

The flow around the winged seed, even when observed from Σ_c, is 3D and rather complex, as it can be appreciated in figure 3. Hence, in order to characterize the flow, we analyze it first in spanwise cross-sections. Three planes are selected, namely $y_c = 0.25b$, $y_c = 0.5b$ and $y_c = 0.75b$, as sketched on top of figures 4-6.

First, we analyze the relative spanwise vorticity in figure 4 since this is the main component of the vorticity in the LEV. In the figure, contours of ω_y, are shown for the three cases, at the three spanwise locations mentioned above. In addition to the vorticity contours, contours of q for the thresholds $6\Omega^2$ and $12\Omega^2$ are also displayed in the figure. This gives an indication of the position of the LEV along the span for the different Re. Note that the contours are normalized with the maximum spanwise vorticity (computed in the fluid domain defined by $y_c = [0.3c, 1.9c]$ and the limits shown in figure 4), $\omega_{y,\max}c/w_d = [46, 85, 107]$, for $Re = 80, 160$ and 240, respectively. Therefore, it should be borne in mind that the intensity of the vorticity field shown in figure 4 increases with the Reynolds number. For all spanwise positions, the contours of ω_y and the contours of q look qualitatively similar, and, as expected, the maximum of ω_y is found inside the LEV. The main difference between the three cases is that with increasing Re the LEV gets closer to the wing surface, all along the span.

In the literature, the presence of an LEV near the wing surface is associated with lift augmentation as a result of the low-pressure region developed in the core of the LEV (Lentink *et al.* 2009). Figure 5 shows the contours of the pressure (relative to the pressure at the inflow) normalized with the absolute value of the minimum pressure for each Reynolds number, $p_{\min}/(\rho_f w_d^2) = [1.3, 2.4, 3.0]$ for $Re = 80$, 160 and 240, respectively. Regardless of Re and the spanwise section, there is a low pressure region above the wing whose peak is located near the LEV. This low pressure region seems to be narrower near the wing root (see left panels of figure 5, $y_c = 0.25b$) and it widens towards the wing tip (see right panels of figure 5, $y_c = 0.75b$). Note that, as a result of larger pressure difference with Re (recall that the values are normalized with $p_{\min}$, which is larger for higher Re), larger lifting forces are developed for the higher Reynolds numbers (Arranz *et al.* 2018).

As discussed in the introduction, the stability of the LEV in revolving wings has been widely studied in the literature. Several authors suggest that the stabilization may be linked to the development of a spanwise flow over the wing surface (van den Berg & Ellington 1997; Birch *et al.* 2004; Poelma *et al.* 2006; Lentink *et al.* 2009). Therefore, it is interesting to analyze the relative spanwise velocity, u_y, for the present cases. This velocity is shown in figure 6 at the same spanwise locations studied above. As before, u_y is normalized with the maximum spanwise velocity for each Re,

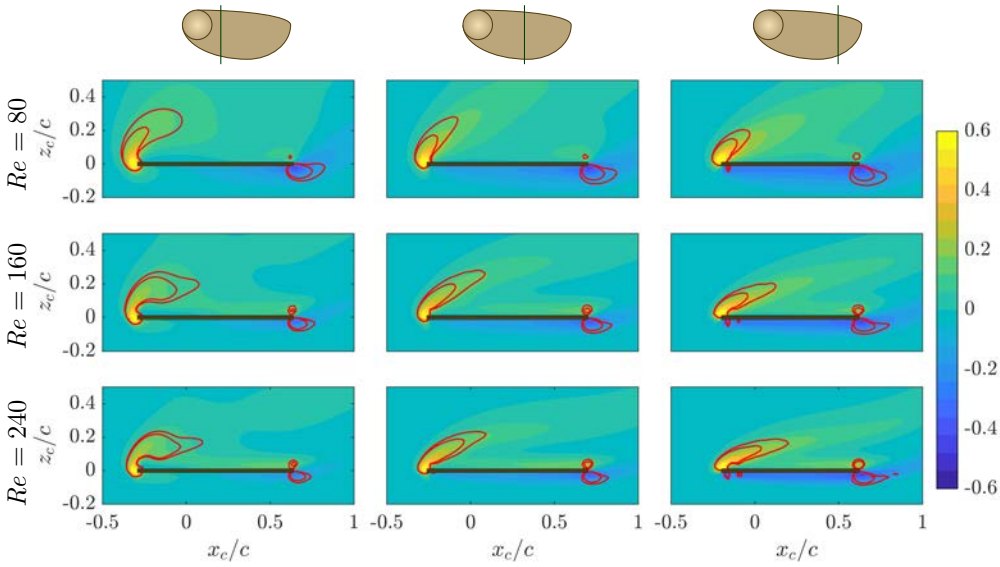

FIGURE 4: Contours of the spanwise vorticity, ω_y, normalized with the maximum spanwise vorticity for each Re. Each row corresponds to a different Reynolds number. The columns correspond (from left to right) to spanwise positions at 25%, 50% and 75% of the span. For a visualization, the corresponding spanwise plane is sketched above the column. Red contours correspond to the intersection of the iso-surfaces of $q = 6\Omega^2$ and $q = 12\Omega^2$ with the plane.

$u_{y,\max}/w_d = [0.89, 1.10, 1.44]$. First of all, a chordwise gradient of u_y is observed for all cases. This velocity gradient, which yields a positive u_y upstream and a negative u_y downstream is due to the wing rotation, i.e. the last term of eq. (3). Besides this linear variation, a region of positive spanwise velocity is found above the wing, for all cases. This spanwise flow (except near the nut) is behind and below the LEV, and the peak of maximum u_y never coincides with the core of the LEV but it is downstream and beneath it. Its intensity decreases towards the tip and with decreasing Re. Particularly, it is barely appreciable for $Re = 80$, whereas it reaches a maximum at $y_c = 0.25b$ for $Re = 240$ (left panel of figure 6), being approximately equal to 40% of the tip velocity.

The increase of the intensity of this spanwise flow with Re may be linked to the centrifugal and Coriolis accelerations, as reported in previous works (Sun & Wu 2004; Aono *et al.* 2008). figure 7 displays the contribution of these terms to the spanwise momentum equation (namely, $-[\mathbf{\Omega}\times\mathbf{\Omega}\times\mathbf{r}+2\mathbf{\Omega}\times\mathbf{u}]\cdot\mathbf{j}_c$), normalized with its maximum value for each Re, namely, $1.76w_d^2/c$, $4.53w_d^2/c$ and $6.51w_d^2/c$ for $Re = 80$, 160 and 240, respectively. These fictitious accelerations are positive in the region where the spanwise flow is present, and they increase with Re, in agreement with the spanwise flow behind the LEV shown in figure 6.

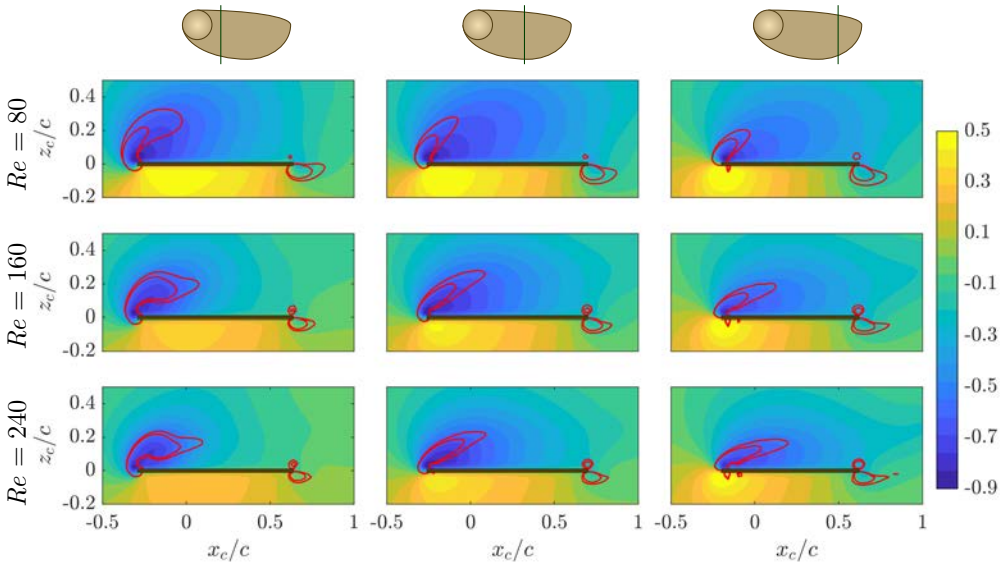

FIGURE 5: Contours of the pressure normalized with the absolute value of the minimum pressure for each Re. Each row correspond to a different Reynolds number. The columns correspond (from left to right) to spanwise positions at 25%, 50% and 75% of the span. For a visualization, the corresponding spanwise plane is sketched above the column. Red contours correspond to the intersection of the iso-surfaces of $q = 6\Omega^2$ and $q = 12\Omega^2$ with the plane.

The spanwise velocity and vorticity contours shown in figure 4 and 6 are qualitatively similar to those observed in the flow around revolving and flapping wings at similar Re (Birch & Dickinson 2001; Birch *et al.* 2004; Poelma *et al.* 2006; Lentink & Dickinson 2009; Harbig *et al.* 2013). It should be noted that, in these references the Reynolds number is expressed in terms of the mean chord and the velocity of the wing tip, which yields Reynolds numbers equal to $[121, 337, 584]$ in the present case.

3.2. *Spanwise flow and stabilization of the LEV*

The fact that the maximum u_y in figure 6 does not occur inside the LEV seems to suggest that, at least for the geometry, kinematics and Reynolds numbers considered here, the stability of the LEV (i.e., the fact that it is not shed into the wake) is not linked to a spanwise flow inside the vortex. Recall that, as mentioned in the introduction, several authors argue that the vorticity transport along the LEV produced by the spanwise flow contributes to the stability of the LEV for $Re \gtrsim 1000$ (van den Berg & Ellington 1997; Birch *et al.* 2004; Poelma *et al.* 2006). However, while figure 6 shows that the maximum of u_y is registered outside of the LEV, it does not show whether the weaker u_y inside the LEV is strong enough to produce vorticity transport along the LEV. To test this hypothesis, we compute the streamlines of the relative velocity

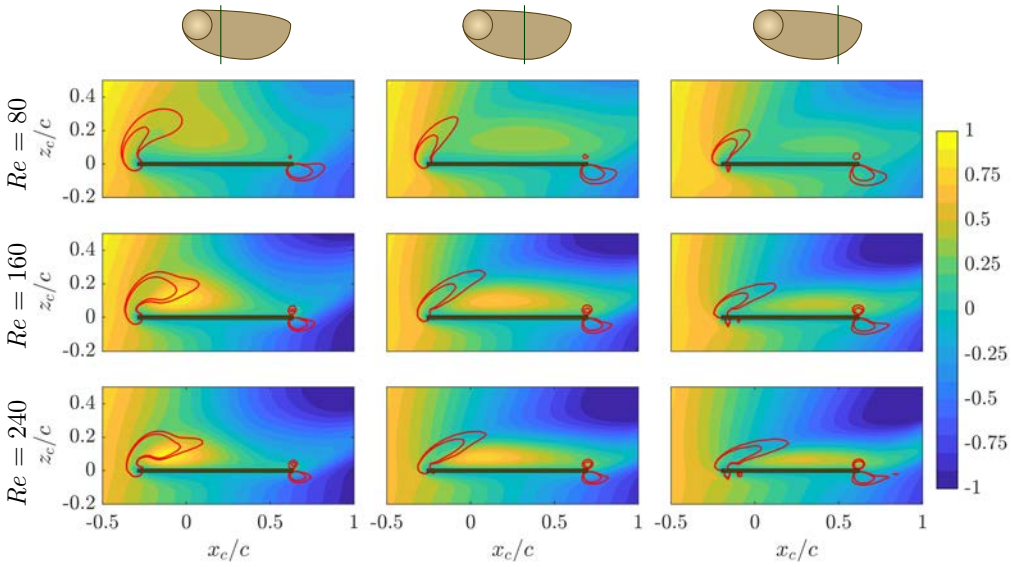

FIGURE 6: Contours of the spanwise velocity, u_y, normalized with the maximum spanwise velocity for each Re. Each row correspond to a different Reynolds number. The columns correspond (from left to right) to spanwise positions at 25%, 50% and 75% of the span. For a visualization, the corresponding spanwise plane is sketched above the column. Red contours correspond to the intersection of the iso-surfaces of $q = 6\Omega^2$ and $q = 12\Omega^2$ with the plane.

field. Note that, since the flow is steady with respect to Σ_c, the streamlines of the relative velocity correspond to the path lines followed by the fluid particles as they move past the rotating seed. These streamlines are shown in figure 8, for the three Re under study.

Particularly, figure 8 shows the streamlines crossing the plane $y_c = 0.5b$ above the wing surface at prescribed seeding points uniformly spaced in the plane. Streamlines crossing the plane $y_c = 0.5b$ inside the LEV (defined as the iso-surface of $q_{th} = 6\Omega^2$) are colored with the velocity magnitude, while streamlines crossing $y_c = 0.5b$ between the LEV and the wing surface are colored in blue. The rationale between this differentiation is to compare the behaviour of the fluid particles inside the LEV to those moving outward through the region of maximum u_y.

Figure 8 shows that the fluid particles that enter the LEV come from the pressure side (lower surface of the wing): they are accelerated as they turn around the leading edge of the seed, and they leave the LEV without travelling inside it along its longitudinal axis. On the contrary, fluid particles beneath the leading edge vortex do not seem to come from the leading edge but from the vortex at the nut, and they travel longer distances along the wing span before leaving the wing. The same behaviour is observed for the streamlines in the three Reynolds numbers under study, although the

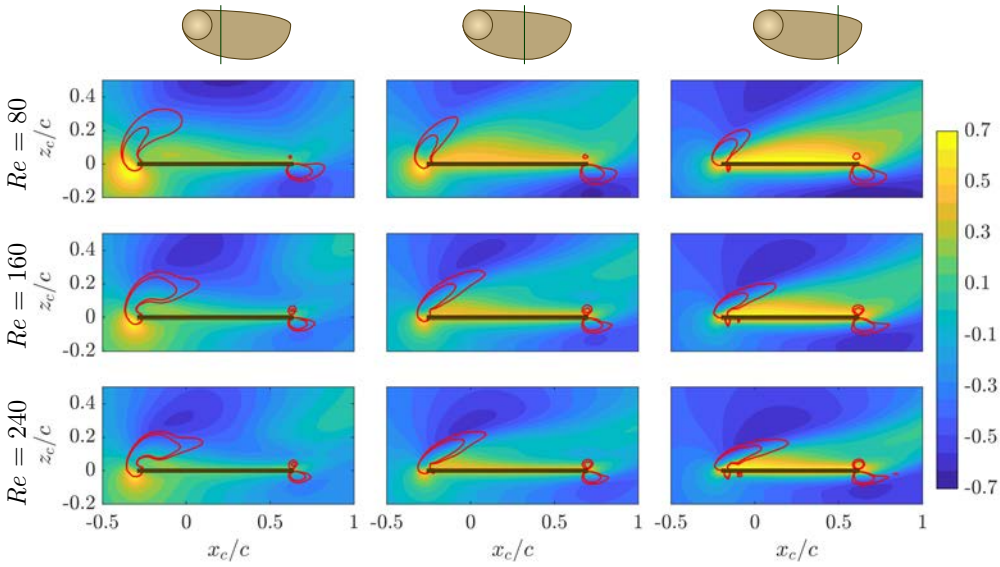

FIGURE 7: Contours of the spanwise component of the centrifugal and Coriolis accelerations normalized with its maximum for each Re. Each row correspond to a different Reynolds number. The columns correspond (from left to right) to spanwise positions at 25%, 50% and 75% of the span. For a visualization, the corresponding spanwise plane is sketched above the column. Red contours correspond to the intersection of the iso-surfaces of $q = 6\Omega^2$ and $q = 12\Omega^2$ with the plane.

spanwise distance travelled by the streamlines beneath the LEV (blue lines in figure 8) becomes larger as Re increases, as it may be expected from the larger spanwise velocity observed in figure 6.

Note that the same behaviour is observed for streamlines defined at different y_c planes, and for different q_{th} in the definition of the LEV. To demonstrate this, we compute streamlines passing through seeding points uniformly distributed in the volume of the LEV, defined as the region with $q \geq 6\Omega^2$. We compute approximately 4.5×10^4 streamlines for each Re, storing the y_c coordinate of the point where each streamline enters and exits the LEV, y_0 and y_f, respectively. These data is used to compute the joint probability density functions (JPDFs) shown in figure 9.

Figure 9a shows an iso-contour containing 95% of the JPDF of y_0 and y_f. It can be observed that the JPDF is very similar for all Re. It mostly lies on the region $y_f > y_0$, corresponding to fluid particles travelling along the wing span inside the LEV towards the wing tip. For $y_0/c \lesssim 0.6$ the effect of increasing the Re is to have shorter displacements along the wing span (i.e., the contour gets closer to the line $y_0 = y_f$). A similar behaviour is observed near the wing tip, where the JPDF of case $Re = 240$ shows values $y_f < y_0$ (i.e., fluid particles travelling inward). This is better observed in figure 9b, where an iso-contour of the JPDF of $y_f - y_0$ and y_0 is shown

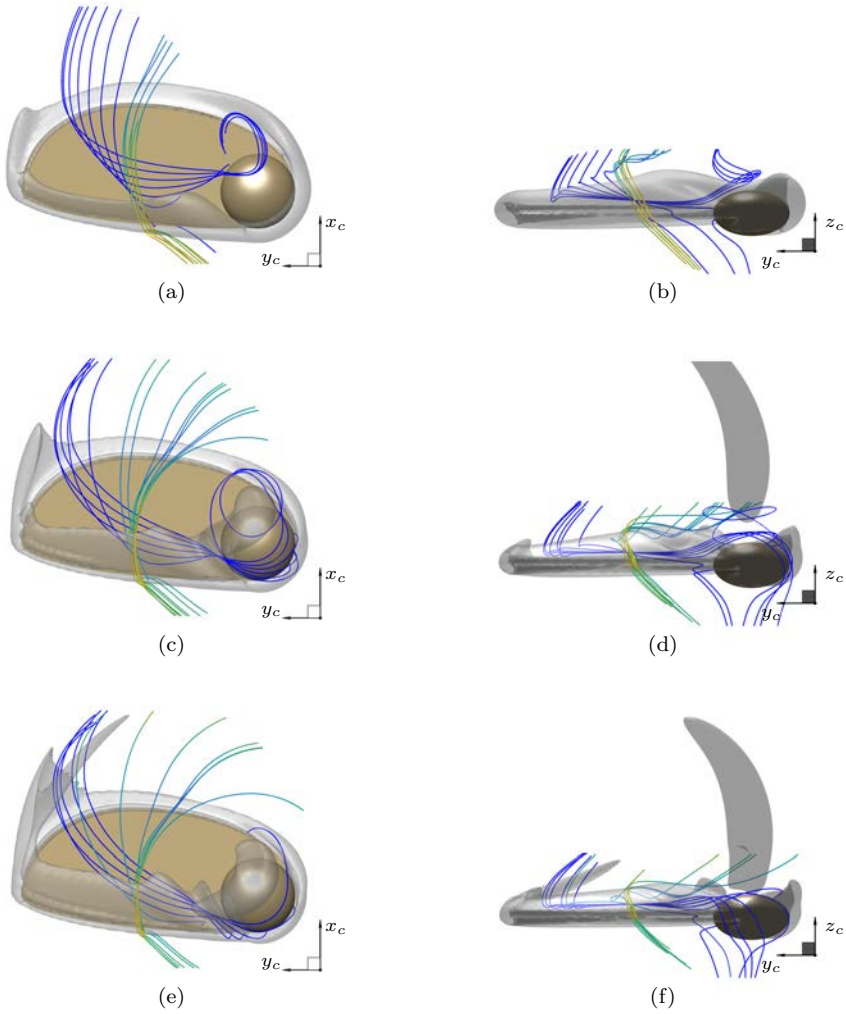

FIGURE 8: Streamlines at plane $y_c = 0.5b$. Streamlines whose intersection with $y_c = 0.5b$ lies inside the LEV (for $q = 6\Omega^2$, also shown) are colored by its velocity intensity. Blue streamlines beneath and downstream the LEV. (a) Top view and (b) side view for $Re = 80$. (c) Top view and (d) side view for $Re = 160$. (e) Top view and (f) side view for $Re = 240$.

(containing 20% of the JPDF). Note that this iso-contour roughly shows the mode of the JPDF (i.e. the most probable values of the JPDF at each y_0). The spanwise distance travelled by the fluid particles inside the LEV decreases as Re increases for all spanwise sections, in agreement with the visualizations in figure 8. Also, as streamlines closer to the wing tip are considered, the travelled distance $(y_f - y_0)$ becomes smaller,

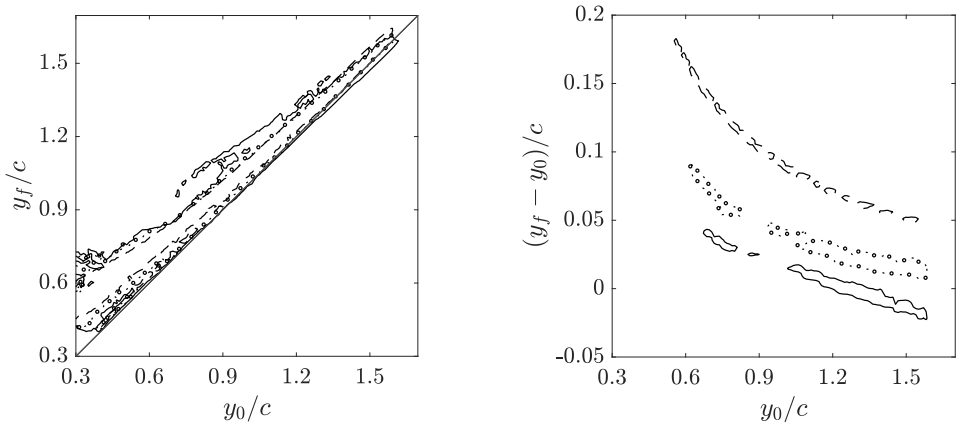

FIGURE 9: (a) JPDF of y_0 and y_f. The iso-contour contains 95% of the JPDF. (b) JPDF of y_0 and the spanwise travelled distance $y_f - y_0$. The iso-contour contains 20% of the JPDF, which provides an approximation to the mode of the JPDF. Note the different scale of the abscissa and the ordinate in (b). In both panels, line styles correspond to a different Re: (- - -) $Re = 80$, (-∘-) $Re = 160$ and, (——) $Re = 240$.

changing sign for $Re = 240$ for $y_0/c \approx 1.2 - 1.3$. This decrease of the travelled distance may be a combination of two factors. On the one hand, as it can be inferred from figure 6, the spanwise velocity in the LEV decreases from the nut to the wing tip. On the other hand, the chordwise velocity increases with y_0 (being roughly proportional to $\Omega y_0 \cos\beta$), and with Re (due to the larger rotational velocity and the decrease in the coning angle). The change of sign (i.e., change of direction) of the travelled distance is probably due to the wing tip vortex, i.e. an effect of the flow around the tip from the lower surface to the upper surface of the wing. This effect becomes more noticeable for larger Re, since β decreases. Moreover, figure 9b shows that for $y_0 > c$ the difference in $(y_f - y_0)$ for the different Reynolds number becomes of the same order as the change of $w_d \sin\beta$ with Re. This fact might suggest that the spanwise flow inside the LEV is mainly due to β (i.e., the projection of the descent speed along the spanwise direction), rather than to rotational accelerations. This is supported by figure 7, where it is observed that the magnitude of these accelerations is small inside the LEV.

Overall, the analysis of the streamlines shows a spanwise flow inside the LEV that becomes less dominant as Re increases. On the other hand, the spanwise flow increases with Re outside of the LEV, as it has been discussed in figure 6. From this point of view, our results do not seem to be consistent with a scenario where the LEV is stabilized by vorticity transport within the LEV itself.

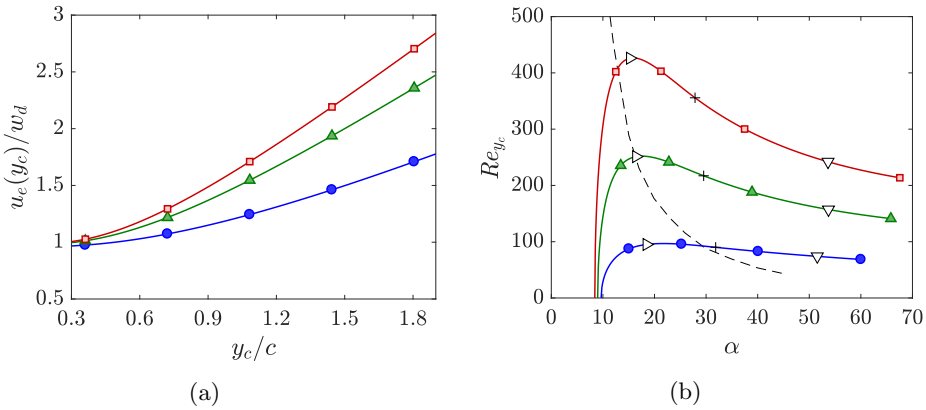

FIGURE 10: (a) Variation of the modulus of the effective velocity along y_c. (b) Effective Reynolds number at y_c versus the effective angle of attack at the same spanwise location. Characteristic spanwise sections are marked at 25% (▽), 50% (+), and 75% (▷) of the span. Dashed line in (b) correspond to the theoretical 2D-viscous stability limit (extracted from Zhang *et al.* (2009)). In both panels, (–●–)$Re = 80$, (–▲–)$Re = 160$, and (–□–)$Re = 240$.

At the present range of Reynolds number, LEV stability could be due to viscous effects. For a sufficiently low Re, Jardin (2017) argues that the stability of the LEV at a given spanwise section is solely determined by its local Re and its effective angle of attack, as in a 2D wing. Hence, in order to evaluate the stabilization of the LEV due to viscous effects, we compute the local Reynolds number, Re_{y_c}, and the effective angle of attack, α, at each spanwise section. The local Reynolds number is based on the local chord, $c(y_c)$, and the local effective velocity, $\mathbf{u}_e(y_c)$. This velocity is the projection of the rigid body velocity along the y_c axis (dashed line in figure 1) onto the plane perpendicular to this axis. Mathematically, its modulus is

$$u_e(y_c) = \sqrt{(\mathbf{v}(y_c)\cdot\mathbf{i}_c)^2 + (\mathbf{v}(y_c)\cdot\mathbf{k}_c)^2}, \tag{5}$$

where $\mathbf{v}(y_c) = \mathbf{v}_G + \boldsymbol{\Omega}\times(y_c\mathbf{j}_c - \mathbf{CG})$. The modulus of the effective velocity is depicted in figure 10a for each Re. On the other hand, the effective angle of attack, $\alpha(y_c)$, is the angle between $\mathbf{u}_e(y_c)$ and the wing chordwise direction.

Figure 10b shows, for each case, the effective Reynolds number, Re_{y_c}, as a function of the effective angle of attack. For reference, several characteristic spanwise sections have been marked. It can be observed that α is high near the nut (between $60^\circ - 70^\circ$) and decreases towards the tip (until $\sim 10^\circ$). The effective Re increases towards the tip due to the higher u_e until $y_c \approx 0.75b$, dropping to zero for spanwise sections beyond 75% of the span because of the sharp decrease of $c(y_c)$ near the wing tip. The region below the dashed line in figure 10b would correspond to the spanwise sections whose LEV might be stabilized by viscous effects. Hence, for $Re = 160$ and 240, only for $y_c \geq 0.75b$ the LEV might be stabilized due to this phenomenon. Meanwhile for

$Re = 80$, this threshold would extend up to $y_c \geq 0.5b$. Therefore, viscosity does not seem to be a plausible candidate to explain LEV stability, specially for $Re = 160$ and 240, since it would only be dominant near the tip, where the LEV has tilted and merged with the wing tip vortex.

Having discarded vorticity transport along the spanwise direction and having analysed the importance of viscous effects, Coriolis and centrifugal effects (referred to as centrifugal pumping in the present paper) may play a role in the attachment of the LEV. The importance of non-inertial effects have been already recognised in the development of an spanwise flow behind the LEV for the present cases. According to several authors (Lentink & Dickinson 2009; Harbig *et al.* 2013; Jardin 2017), fictitious forces would contribute to the attachment of the LEV for Rossby numbers, Ro, of order unity. Defining Ro as in Hargib *et al.* Harbig *et al.* (2013), namely $Ro = u_{tip}/\Omega b$, where $u_{tip} = \sqrt{w_d^2 + \Omega b}$, it is found that $Ro = \sqrt{\lambda^2 + 1}/\lambda$, which, in the cases presented here, ranges from 1.2 to 1. Consequently, centrifugal pumping would be a feasible candidate for the stabilization of the LEV in the cases analysed here. Nevertheless, the exact mechanisms by which fictitious forces stabilize the LEV in the present case are still not clear.

3.3. *Leading edge vortex characterization*

We now proceed to a more detailed characterization of the LEV. To that end we average the relative velocity ($\langle u_y \rangle$), relative vorticity ($\langle \omega_y \rangle$) and pressure ($\langle p \rangle$) inside the LEV (regions where $q > q_{th}$) in planes of constant y_c. These averages are performed for different values of q_{th}, in order to assess the dependence of the averaged values upon the particular threshold used in the identification of the LEV. Figure 11 depicts the three variables along the LEV for each Re and for q_{th}/Ω^2 in the range $6 - 12$. They are normalized with the descent speed, w_d, the characteristic chord, c, and ρ_f.

Figure 11a-c shows $\langle \omega_y \rangle$ for the different Re and q_{th}. Regardless of q_{th} and Re, $\langle \omega_y \rangle$ slightly decreases from the nut to 25% of the span, and then it increases until reaching a plateau. This increase becomes steeper as Re increases. At the wing tip, $\langle \omega_y \rangle$ abruptly decreases, due to the merging of the LEV into the wing tip vortex, with the consequent change of direction of the vorticity. At a given spanwise section and q_{th}, $\langle \omega_y \rangle$ increases with Re. On the other hand, $\langle \omega_y \rangle$ increases with q_{th} for all Re analyzed., This indicates that ω_y is not constant inside the cross sections of the LEV, as it corresponds to a viscous vortex.

The relative spanwise velocity averaged over the LEV is displayed in figure 11d-f. Note that, contrary to $\langle \omega_y \rangle$, $\langle u_y \rangle$ is fairly independent of q_{th} for a given Re. Therefore, we can focus the discussion on the evolution of $\langle u_y \rangle$ along the LEV and the effect of the Reynolds number. For all cases we observe that $\langle u_y \rangle$ decreases towards the tip, although the profiles for $Re = 160$ and 240 differ considerably from the profile for $Re = 80$. In particular, the negative gradient of $\langle u_y \rangle$ along the span is much less pronounced for $Re = 80$ than for the higher Re. The latter profiles present a steep gradient up to $y_c \approx 0.7$ and a milder one beyond that location. This higher spanwise velocity near the nut is due to the spanwise flow, developed presumably due to non-inertial forces, which partially coincides with the LEV for $Re = 160$ and 240 and

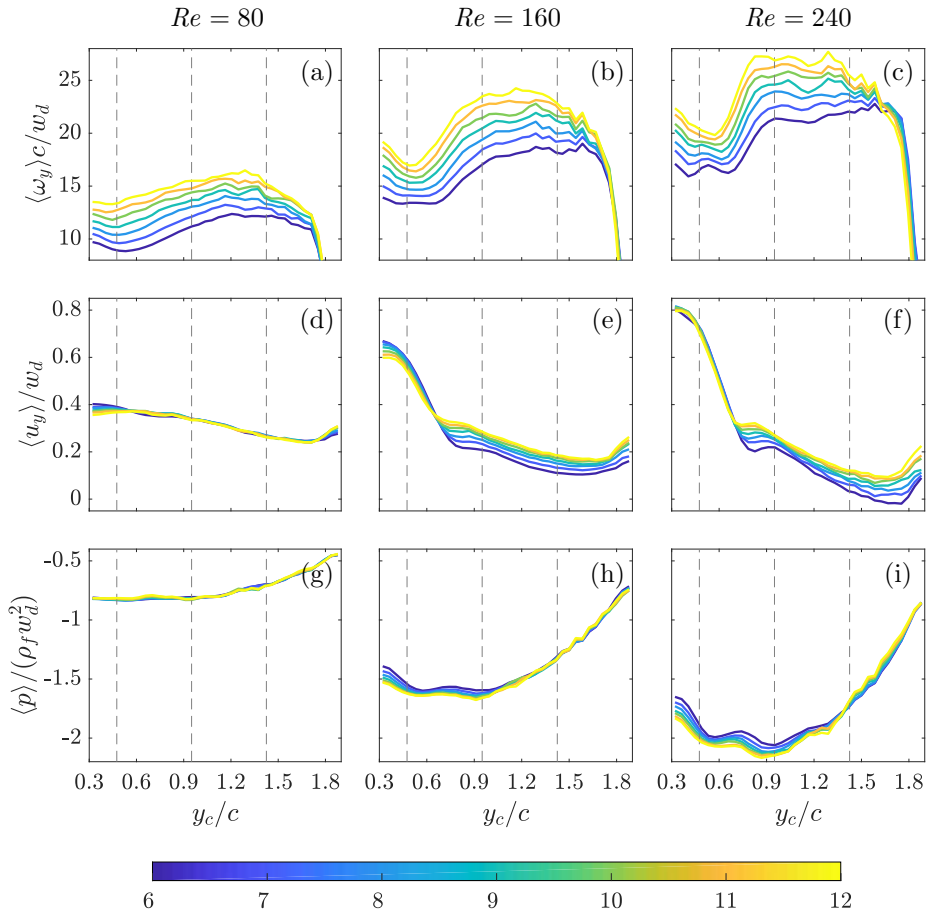

FIGURE 11: Relative spanwise vorticity averaged over the LEV cross-sections, $\langle\omega_y\rangle c/w_d$, as a function of y_c for (a) $Re = 80$, (b) $Re = 160$, and (c) $Re = 240$. Relative spanwise velocity averaged over the LEV cross-sections, $\langle u_y\rangle c/w_d$, as a function of y_c for (d) $Re = 80$, (e) $Re = 160$, and (f) $Re = 240$. Pressure averaged over the LEV cross-sections, $\langle p\rangle/(\rho w_d^2)$, as a function of y_c for (g) $Re = 80$, (h) $Re = 160$, and (i) $Re = 240$. Different q_{th}/Ω^2 values have different color intensity, as shown in the colorbar. Dashed lines correspond to the 25%, 50% and 75% spanwise sections (figure 4-6).

it is not present for $Re = 80$ (see figure 6). Except in this region, $\langle u_y\rangle$ decreases with Re, in agreement with the behaviour of the streamlines (see discussion of figure 9b).

As commented before, the decrease of spanwise flow in the LEV with increasing Re seems to be related to the attitude of the seed: the coning angle is larger at lower

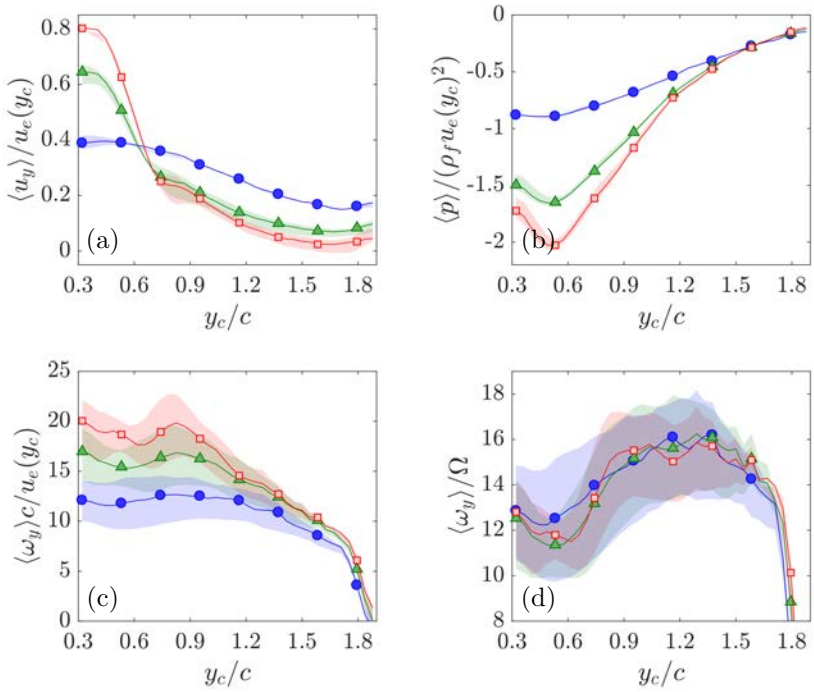

FIGURE 12: (a) Relative spanwise velocity averaged over the LEV cross-sections normalized with $u_e(y_c)$. (b) Relative pressure averaged over the LEV cross-sections normalized with $\rho_f c u_e(y_c)$. (c) Relative spanwise vorticity normalized with $c/u_e(y_c)$, and (d) with Ω. (—●—)$Re = 80$, (—▲—)$Re = 160$ and (—□—)$Re = 240$. Shaded regions correspond to the variation with $q_{th} = [6 - 12]$.

Re, which implies a larger projection of the descent velocity w_d along the spanwise direction of the wing, y_c.

The pressure averaged over the LEV cross-sections, $\langle p \rangle$, is depicted in figure 11g-i for the different Re. Similarly to $\langle u_y \rangle$, the averaged pressure is also largely independent of q_{th}. Throughout the span, lower pressures are found for increasing Re, which suggests that the lift force of the winged seed increases with Re (as confirmed in Arranz *et al.* (2018)). For all Re, the pressure increases towards the tip for $y_c \gtrsim 0.9c$, producing and adverse pressure gradient which becomes stronger as Re increases. Note that, while the projection of w_d along the spanwise direction of the seed could explain the intensity of $\langle u_y \rangle$, the presence of an adverse pressure gradient might explain why $\langle u_y \rangle$ decreases towards the wing tip.

Note that the variables shown in figure 11 are normalized with magnitudes which remain constant regardless of Re. Hence, it is interesting to use a normalization in which the effect of the Reynolds number is somehow involved. Figure 12a-d depicts $\langle u_y \rangle$, $\langle p \rangle$ and $\langle \omega_y \rangle$ normalized with c, ρ_f and the effective velocity at y_c. Note that

by employing $u_e(y_c)$ as the characteristic velocity, we are accounting for the change in the angular speed and for the change in the seed's attitude. Figure 12 shows $\langle u_y \rangle$, $\langle p \rangle$ and $\langle \omega_y \rangle$ for $q_{th} = 9$. Additionally, the shaded regions correspond to the variation with the threshold, $q_{th} = [6 - 12]$ for each variable and Re. Figure 12a and figure 12b reveal that, upon this normalization, the cases $Re = 160$ and 240 tend to collapse, contrary to the case $Re = 80$. This behaviour is also observed in the aerodynamic forces (Arranz *et al.* 2018), and seems to suggest that auto-rotation at $Re = 80$ differs from auto-rotation at higher Re (within the range of study). Nonetheless, it has been already mentioned that the case with $Re = 80$ is somewhat anomalous since for example its auto-rotation depends on the initial conditions (hysteresis).

Regarding $\langle \omega_y \rangle$, it is interesting to recall that, although using $u_e(y_c)$ as the characteristic velocity (figure 12c) yields a result similar to figure 12a-b, using Ωc instead, results in a collapse of the profiles of $\langle \omega_y \rangle$ for all Re, except close to the nut ($y_c < 0.8c$), where the case $Re = 80$ differs from the other two cases. This can be appreciated in figure 12d, and it is also true for other q_{th}. This suggests that the characteristic velocity for chordwise and vertical velocities is Ωc, even if the precise cause for this scaling is not clear at the present time.

Finally, we conclude the characterization of the LEV by computing the spanwise circulation inside the LEV, Γ, since it is usually employed to relate the intensity of the LEV to the aerodynamic force. We compute Γ as the integral of ω_y over the LEV cross-sections. This circulation is shown in figure 13 for different thresholds q_{th}, and for the three Reynolds numbers considered here. Note that, if ω_y were concentrated in a finite surface (i.e., a vortex tube), then Γ would become independent of q_{th} for a sufficiently low value of the threshold. However, figure 13 shows Γ increasing monotonously as q_{th} decreases, with no sign of a plateau. This is the expected behaviour for a viscous vortex, as it corresponds to a low-Reynolds number flow. An important consequence of the lack of collapse of Γ with q_{th} in figure 13 is that Γ can hardly be used to characterize the aerodynamic force on the wing at the present Re. Note that this approach is usually found in the literature for winged seeds at higher Re (Lentink *et al.* 2009; Poelma *et al.* 2006).

4. Conclusions

Numerical simulations of the auto-rotation of a winged-seed at Re in the range $80-240$ have been performed. The seed, for all cases under study, reaches a state of stable auto-rotation with approximately constant angular velocity and attitude, which vary with Re. Due to this, and to the low Reynolds number, the flow is approximately steady when observed from a reference frame fixed to the seed, so that this perspective has been employed in the flow characterization. Three vortical structures are formed near the seed: a wing tip vortex which describes a helical path; a vortex shed behind the nut; and a stable LEV above the wing surface which merges with the tip vortex.

We have characterized the flow over the wing surface by analyzing the relative spanwise vorticity, the relative spanwise velocity and the pressure at various spanwise sections. With increasing Reynolds number, the flow visualizations show that the LEV becomes more intense and gets closer to the wing surface. For all cases the low pressure peak on the wing surface is located in the neighbourhood of the LEV. We

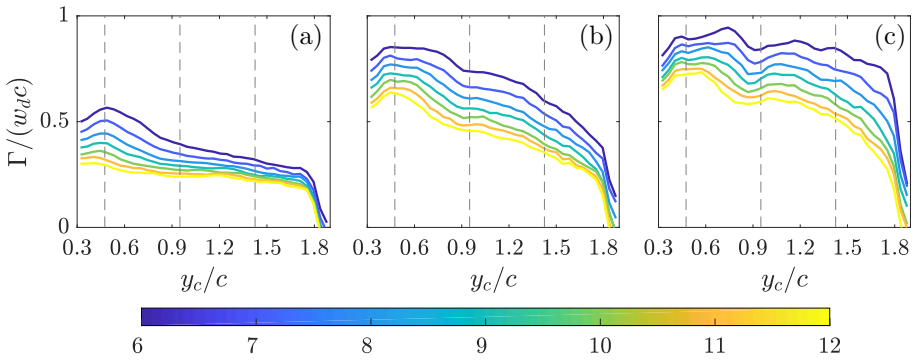

FIGURE 13: Circulation averaged over the LEV cross-sections, $\Gamma/(w_d c)$, as a function of y_c. (a) $Re = 80$, (b) $Re = 160$, and (c) $Re = 240$. Different q_{th}/Ω^2 values have different color intensity, as shown in the colorbar.

have also identified the formation of a spanwise flow on the wing surface, which is more intense downstream and beneath the LEV. This flow topology is directly linked to Coriolis and centripetal accelerations and is in agreement with flows around revolving wings found in the literature.

We have explored the three possible mechanisms for the stabilization of the LEV reported in the literature, namely, the vorticity transport within the LEV, viscous effects and centrifugal pumping. The first mechanism has been evaluated via a statistical analysis of fluid particle trajectories along the LEV. We have found no evidence of significant vorticity transport along the LEV for the flow under consideration. The evaluation of the viscous stabilization of the LEV has been performed in terms of the local Re and local angle of attack of the corresponding wing section. The results suggest that this mechanism can only be important near the tips, but the 3D character of the flow in this region makes it unlikely. Finally, the stabilization via non-inertial accelerations seems to be a potential candidate, since the Rossby number is of order unity in the present study.

To conclude, the flow inside the LEV has been characterized, studying the variation of average flow magnitudes inside the LEV with different q thresholds. The average spanwise velocity and the pressure inside the LEV do not seem to depend on the q value. We also found that $\langle u_y \rangle$ decreases for increasing Re, contrary to the behaviour of the spanwise flow outside the LEV.

The average spanwise vorticity inside the LEV, $\langle \omega_y \rangle$, for a given Re depends on the value of q. On the contrary, for a given q, $\langle \omega_y \rangle$ is quantitatively similar for the different Re when scaled with Ω, suggesting that both the chordwise and vertical velocity components scale with the angular speed. The multiplication of $\langle \omega_y \rangle$ by the cross-sectional area of the LEV to compute its spanwise circulation, Γ, yielded that it largely depends on the q value, as it should be expected for a low-Reynolds flow.

Hence, the aerodynamic forces cannot be inferred from Γ, contrary to what can be done with reasonable accuracy at higher Re.

Overall, we observe that the flow around the auto-rotating seed for $Re = 160$ and 240 is qualitatively different compared to $Re = 80$. This result may be explained by the fact that $Re = 80$ seems to be close to the lower limit where auto-rotation is possible (for the seed considered here).

Acknowledgements

This work was supported by grants TRA2013-41103-P (Mineco/Feder UE) and DPI2016-76151-C2-2-R (AEI/ Feder UE). MGV was partially supported by a grant of the BBVA Foundation. The code was partially developed during a stay of MGV (funded by the Spanish Ministry of Education through the program José Castillejo) at the Karlsruhe Institute of Technology. The simulations were partially performed at the Steinbuch Centre for Computing (SCC), Karlsruhe. The computer resources, technical expertise and assistance provided by this center are thankfully acknowledged.

References

Aono, H., Liang, F. & Liu, H. 2008 Near- and far-field aerodynamics in insect hovering flight: an integrated computational study. *J. Exp. Biol.* **211** (2), 239–257.

Arranz, G., Moriche, M., Uhlmann, M., Flores, O. & García-Villalba, M. 2018 Kinematics and dynamics of the auto-rotation of a model winged seed. *Bioinspir. Biomim.* **13** (3), 036011.

Azuma, A. & Yasuda, K. 1989 Flight performance of rotary seeds. *J. Theor. Biol.* **138** (1), 23–53.

van den Berg, C. & Ellington, C. P. 1997 The vortex wake of a 'hovering' model hawkmoth. *Phil. Trans. R. Soc. Lond. B* **352** (1351), 317–328, arXiv: http://rstb.royalsocietypublishing.org/content/352/1351/317.full.pdf.

Birch, J. M. & Dickinson, M. H. 2001 Spanwise flow and the attachment of the leading-edge vortex on insect wings. *Nature* **412** (6848), 729–33.

Birch, J. M., Dickson, W. B. & Dickinson, M. H. 2004 Force production and flow structure of the leading edge vortex on flapping wings at high and low Reynolds numbers. *J. Exp. Biol.* **207** (7), 1063–1072.

Chrust, M. 2012 Etude numérique de la chute libre d'objets axisymétriques dans un fluide newtonien. PhD thesis, Strasbourg.

Ellington, C. P., Van Den Berg, C., Willmott, A. P. & Thomas, A. 1996 Leading-edge vortices in insect flight. *Nature* **384** (6610), 626.

Fregene, K. & Bolden, C. L. 2010 Dynamics and control of a biomimetic single-wing nano air vehicle. In *American Control Conference (ACC), 2010*, pp. 51–56. IEEE.

Garmann, D. J. & Visbal, M. R. 2014 Dynamics of revolving wings for various aspect ratios. *J. Fluid Mech.* **748**, 932–956.

Green, D. S. 1980 The terminal velocity and dispersal of spinning samaras. *Am. J. Bot.* **67** (8), 1218–1224.

Harbig, R. R., Sheridan, J. & Thompson, M. C. 2013 Reynolds number and aspect ratio effects on the leading-edge vortex for rotating insect wing planforms. *J. Fluid Mech.* **717**, 166–192.

Hunt, J. C. R., Wray, A. A. & Moin, P. 1988 Eddies, stream, and convergence zones in turbulent flows. *Center For Turbulence Research* **Report CTR-S88**.

Jardin, T. 2017 Coriolis effect and the attachment of the leading edge vortex. *J. Fluid Mech.* **820**, 312–340.

Jardin, T. & David, L. 2014 Spanwise gradients in flow speed help stabilize leading-edge vortices on revolving wings. *Phys. Rev. E* **90** (1), 013011.

Lee, Injae & Choi, Haecheon 2017 Flight of a falling maple seed. *Phys. Rev. Fluids* **2**, 090511.

Lee, S. J., Lee, E. J. & Sohn, M. H. 2014 Mechanism of autorotation flight of maple samaras (*Acer palmatum*). *Exp. Fluids* **55** (4), 1–9.

Lentink, D. & Dickinson, M. H. 2009 Rotational accelerations stabilize leading edge vortices on revolving fly wings. *J. Exp. Biol.* **212** (16), 2705–2719, arXiv: http://jeb.biologists.org/content/212/16/2705.full.pdf.

Lentink, D., Dickson, W. B., van Leeuwen, J. L. & Dickinson, M. H. 2009 Leading-edge vortices elevate lift of autorotating plant seeds. *Science* **324** (5933), 1438–1440.

Limacher, E. & Rival, D. E. 2015 On the distribution of leading-edge vortex circulation in samara-like flight. *J. Fluid Mech.* **776**, 316–333.

Lugt, Hans J 1983 Autorotation. *Ann. Rev. Fluid Mech.* **15** (1), 123–147.

Moriche, M. 2017 A numerical study on the aerodynamic forces and the wake stability of flapping flight at low Reynolds number. PhD thesis, Univ. Carlos III Madrid.

Moriche, M., Flores, O. & García-Villalba, M. 2016 Three-dimensional instabilities in the wake of a flapping wing at low Reynolds number. *Int. J. Heat Fluid Flow* **62A**, 44–55.

Moriche, M., Flores, O. & García-Villalba, M. 2017 On the aerodynamic forces on heaving and pitching airfoils at low Reynolds number. *J. Fluid Mech.* **828**, 395–423.

Norberg, R. 1973 Autorotation, self-stability, and structure of single-winged fruits and seeds (samaras) with comparative remarks on animal flight. *Biol. Rev.* **48** (4), 561–596.

Obradovic, B., Ho, G., Barto, R., Fregene, K. & Sharp, D. 2012 A multi-scale simulation methodology for the samarai monocopter μUAV. In *AIAA Modeling and Simulation Technologies Conference*, p. 5012.

Pedersen, C. B. & Żbikowski, R. 2006 *An indicial-Polhamus aerodynamic model of insect-like flapping wings in hover*, *Flow Phenomena in Nature*, vol. 2, pp. 606–666. Liebe, R.

Poelma, C., Dickson, W. B. & Dickinson, M. H. 2006 Time-resolved reconstruction of the full velocity field around a dynamically-scaled flapping wing. *Exp. Fluids* **41** (2), 213–225.

Pounds, P. & Singh, S. 2015 Samara: Biologically inspired self-deploying sensor networks. *IEEE Potentials* **34** (2), 10–14.

Salcedo, E., Treviño, C., Vargas, R. O. & Martínez-Suástegui, L. 2013 Stereoscopic particle image velocimetry measurements of the three-dimensional flow field of a descending autorotating mahogany seed (*Swietenia macrophylla*). *J. Exp. Biol.* **216** (11), 2017–2030, arXiv: http://jeb.biologists.org/content/216/11/2017.full.pdf.

Seter, D. & Rosen, A. 1992 Stability of the vertical autorotation of a single-winged samara. *J. App. Mech.* **59** (4), 1000–1008.

Sun, M. & Wu, J. 2004 Large aerodynamic forces on a sweeping wing at low reynolds number. *Acta Mechanica Sinica* **20** (1), 24–31.

Uhlmann, M. 2005 An immersed boundary method with direct forcing for the simulation of particulate flows. *J. Comput. Phys.* **209** (2), 448–476.

Ulrich, E. R., Darryll, P. & Humbert, J. S. 2010 From falling to flying: the path to powered flight of a robotic samara nano air vehicle. *Bioinspir. Biomim.* **5** (4), 045009.

Varshney, K., Chang, S. & Wang, Z. J. 2012 The kinematics of falling maple seeds and the initial transition to a helical motion. *Nonlinearity* **25** (1), C1.

Yasuda, K. & Azuma, A. 1997 The autorotation boundary in the flight of samaras. *J. Theor. Biol.* **185** (3), 313–320.

Zhang, J., Liu, N. & Lu, X. 2009 Route to a chaotic state in fluid flow past an inclined flat plate. *Phys. Rev. E* **79**, 045306.

Paper 4

4

Three-dimensional effects on the aerodynamic performance of flapping wings in tandem configuration

G. Arranz[1], **O. Flores**[1], **M. García-Villalba**[1]

[1] Universidad Carlos III de Madrid, Spain
[2] Karlsruhe Institute of Technology, Germany

Journal of Fluids and Structures (2020), vol. **94**, 102893

Direct numerical simulations have been performed to analyse how three-dimensional effects influence the performance of wings in tandem configuration undergoing a two-dimensional optimal kinematics. This optimal motion is a combination of heaving and pitching of the airfoils in a uniform free-stream at a Reynolds number $Re = 1000$ and Strouhal number $St_c = 0.7$. Wings of two different aspect ratios, $\mathit{AR} = 2$ and 4, undergoing the 2D motion have been considered. It has been found that the interactions between the vortical structures of the fore- and the hind-wings are qualitatively similar to the two-dimensional case for both AR. However, the ratio between the mean thrust of the hind-wing and the fore-wing decreases from 80% in 2D to 70% in 3D, implying that the 3D effects are detrimental for the vortical interactions between the wings in terms of thrust production. Nonetheless, the propulsive efficiency remains constant both in 2D and 3D, for both AR. A more realistic flapping motion has also been analysed and compared to the heaving motion. It has been found that the aerodynamic forces decrease when the wings are in flapping motion. This detrimental behaviour has been linked to a sub-optimal motion of the inboard region of the wings. This sub-optimal region of the wings entails a decrease of the mean thrust and of the propulsive efficiency compared to the heaving case, which are more pronounced for the $\mathit{AR} = 4$ wings.

1. Introduction

In contrast to birds, bats and most insects, dragonflies have two pairs of wings which can be controlled independently (Norberg 1975; Thomas *et al.* 2004). By modifying the kinematics and the phase relationship between the fore and hind pair of wings, dragonflies are capable of performing rapid manoeuvres, accelerate, or cruising efficiently (Alexander 1984; Wakeling & Ellington 1997). This versatility, and the recent interest in the development of micro air vehicles (MAVs), have fostered the scientific community to understand which are the mechanisms that govern the flight of these insects. Thanks to this interest, it has been discovered, and now it is widely accepted, that one of the most important mechanisms dragonflies take advantage of is the wake interaction between their wings (Wang & Russell 2007; Lehmann 2007; Usherwood & Lehmann 2008).

In hovering flight, the wake interaction between the fore- and the hind-wing has a negative effect in terms of lift generation. This was shown by Maybury & Lehmann (2004). They conducted experiments on two robotic flapping wings vertically stacked, showing that the total vertical force obtained was reduced due to the interaction between the wings, regardless of the phase shift of the wings. Likewise, Wang & Sun (2005) performed numerical simulations of two wings in tandem configuration with a motion close to the actual motion of dragonfly's wings. By modifying the phase shift between the wings, they showed that the vertical force developed by each wing is always lower than the force developed by the same wing when isolated. Similar results were obtained by Rival *et al.* (2011) for two-dimensional pitching and heaving plates. Nonetheless, they found that for an optimal phase shift, similar values of mean lift than the foils when isolated were achieved, but with more constant force production over the cycle. Likewise, Wang & Russell (2007) performed numerical simulations of the two-dimensional wings' motion of a dragonfly, revealing that counter-stroking of the wings minimizes the aerodynamic power. Later, Usherwood & Lehmann (2008) found that adequate wing phasing during hovering can lead to a power reduction up to 22% compared with a single pair of wings.

Contrary to hovering, airfoil tandem configurations in forward flight can outperform isolated airfoils in terms of aerodynamic force production or propulsive efficiency. By modifying only the phase lag between two airfoils in tandem under a simplified pitching/heaving motion, Broering & Lian (2015) were able to obtain higher lift or propulsive efficiency compared to a single airfoil. Likewise, Boschitsch *et al.* (2014) performed a parametric study of the phase lag and spacing between two pure pitching foils. They observed a banded pattern of the thrust and propulsive efficiency in the phase-spacing diagram, revealing a linear dependency between both parameters. This dependency was later observed for combined pitching/heaving foils (Lua *et al.* 2016; Muscutt *et al.* 2017), and it was also mentioned by Maybury & Lehmann (2004) for 3D wings in hovering configuration. Kamisawa & Isogai (2008) performed numerical simulations to find the flapping kinematics of two pairs of flapping tandem wings of minimum required power for forward flight. They found that, for the range of velocities studied, the required power was lower than the maximum available power. More recently, Nagai *et al.* (2019) studied the effect of phasing of tandem flapping wings in forward flight. Their results suggest that actual dragonfly might not select the phase differences in term of aerodynamic efficiency but also in terms of other factors such as longitudinal manoeuvrability or flight stability.

Other studies have focused on finding optimal tandem kinematics in two dimensions (Ortega-Casanova & Fernandez-Feria 2016; Ortega-Casanova & Fernández-Feria 2019; Huera-Huarte 2018). However, there are fewer studies addressing the aerodynamic performance of optimal kinematics in 3D wings, specially in terms of comparison with their corresponding 2D configurations. There are only a few works that compare 2D and 3D configurations with the same kinematics, which are briefly reviewed next.

Zheng *et al.* (2016) analysed the forewing-hindwing interaction of finite aspect ratio wings in heaving and pitching motion. Their results revealed discrepancies with past 2D studies undergoing similar kinematics, which might be attributed to 3D effects. However, flow visualization was limited by phase-locked 2D measurements at a single

spanwise location, leaving as an open question if three dimensional effects significantly affect the forewing-hindwing interaction. Kurt & Moored (2018) experimentally analysed the effect of the wing tip vortices of two tandem wings of $\mathcal{AR} = 2$ in pure pitching motion on the propulsive efficiency and thrust. To do so, they measured the forces on the wings for a range of different phasing and spacing, and repeated the experiments placing a splitter plate and a surface plate at the wing tips to minimize 3D effects. Their results show many broad similarities between both configurations; however, they found that, for the 3D configuration, increasing the spacing while keeping the phase lag constant, always results in a decrease of the propulsive efficiency due to the breakdown of the vortices. On the contrary, when 3D effects were minimized, optimal configurations were found for larger spacing between the wings. A comparison between two tandem airfoils in heaving and pitching motion and two wings of $\mathcal{AR} = 2$ under the same kinematics and spacing was performed by Broering & Lian (2015) by means of numerical simulations. They compared the 2D and 3D simulations for 3 different phases. Generally, three dimensional effects led to a force reduction; nonetheless, collective propulsive efficiencies for the three-dimensional cases were very similar or even slightly higher than their two-dimensional counterparts. Overall, these works show a discrepancy on the extent of the influence that the 3D effects have on the aerodynamic performance of a two-dimensional (2D) configuration.

Moreover, it should be noted that previous comparisons between 2D and 3D configurations, Broering & Lian (2015),Zheng *et al.* (2016) and Kurt & Moored (2018), consider the motion of the finite wings to be two-dimensional (i.e., heaving). However, actual motion of dragonfly's wings is a flapping motion in which each section of the wing has a different velocity. Practically no studies are found in the literature which compare flapping kinematics with a 2D motion. Sun & Lan (2004) performed a numerical simulation of a pair of dragonfly tandem undergoing a realistic hovering motion, and compared the obtained aerodynamic forces with those of a 2D computation based on similar wing kinematics; They observed that, for the particular configuration, 3D fore-hind wing interaction is weaker than 2D interaction in terms of force generation. Nonetheless, we have not found in the literature other studies which assessed the effect of implementing a 2D optimal kinematics in a 3D configuration with flapping motion. Therefore, the objective of the present study is to analyse how three dimensional effects influence the aerodynamic forces and flow structures of tandem wings with a flapping motion. To that end, we perform direct numerical simulations (DNS) of tandem wings in flapping motion, tandem wings in heaving motion and tandem airfoils (2D) in heaving motion. Moreover, in this study we analyse the effect of the $\mathcal{AR}$ by considering wings of $AR = 2$ and 4, extending the results from Broering & Lian (2015), Zheng *et al.* (2016) and Kurt & Moored (2018), which only considered a single $\mathcal{AR}$.

The structure of the paper is as follows: the description of the problem and computational set-up is provided in section 2; the discussion of the results from the simulations is given in section 3; and section 4 gathers the main conclusions extracted from this study.

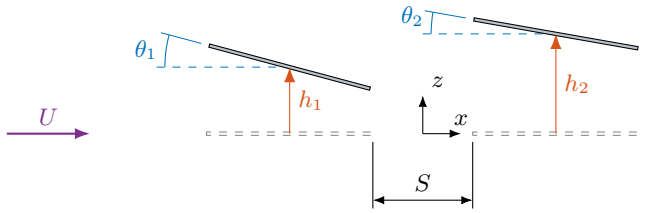

FIGURE 1: Sketch of the 2D-kinematics with the definition of θ_i and h_i. The inertial reference frame is also depicted for reference.

i	$\varphi_{h,i}$	$\varphi_{\theta,i}$	θ_0	St_c	St_a
1	0	$3\pi/4$	$25°$	0.7	0.17
2	π	$-\pi/4$			

TABLE 1: Kinematic parameters of the two-dimensional configuration.

2. Methodology

2.1. *Problem description*

Two equal, finite wings in an in-line tandem arrangement and immersed in a uniform and constant free-stream of magnitude U, are considered. Both wings move with a kinematics based on the optimal, two-dimensional configuration of Ortega-Casanova & Fernández-Feria Ortega-Casanova & Fernández-Feria (2019). The motion corresponds to a combination of heaving and pitching about the mid chord. The pitching angle, θ, and heaving amplitude, h, are described by the sinusoidal functions:

$$h_i(t) = h_0 \cos(2\pi f t + \varphi_{h,i}), \tag{1}$$

$$\theta_i(t) = \theta_0 \cos(2\pi f t + \varphi_{\theta,i}), \tag{2}$$

where the subscript i indicates the wing ($i = 1$ fore-wing, $i = 2$ hind-wing) as shown in figure 1. In eqs. (1) and (2), h_0 is the maximum heaving amplitude, θ_0 is the pitching amplitude, f is the frequency, $\varphi_{h,i}$ is the heaving phase shift and $\varphi_{\theta,i}$ is the pitching phase shift. The frequency and heaving amplitude are fixed by the non-dimensional numbers, $St_c = fc/U$ and $St_a = h_0 f/U$. All the parameters that define the motion are gathered in table 1. Note that, according to the values of $\varphi_{h,i}$ and $\varphi_{\theta,i}$ in table 1, pitching is advanced $3\pi/4$ with respect to heaving for both foils. Consequently, the motion of both foils is identical with a phase shift equal to π. Moreover, since the pitch angle averaged over a cycle is zero, the motion is symmetric with respect to the horizontal plane.

The airfoil sections correspond to a flat plate with chord, c. The distance between the trailing edge of the fore-wing and the leading edge of the hind-wing when they lay onto a horizontal plane is $S/c = 0.5$ (see figure 1). The Reynolds number based on the chord and the free-stream velocity is $Re = Uc/\nu = 1000$ for all the cases.

For the three-dimensional simulations, wings of rectangular planform with span, b, and the same cross-section as the 2D airfoils are considered. We study two aspect ratios, $\mathit{AR} = b/c = 2$ and 4, and two kind of motions: heaving and flapping (i.e., rotation about an axis parallel to the free-stream velocity). Kinematics of the finite span wings in the heaving case is straightforward: all chordwise sections of the wings move according to eqs. (1) and (2), exactly as in the 2D case. On the contrary, in flapping motion, only one chordwise section has the same vertical amplitude, h_0, as in the 2D case. We denote this section as the *characteristic section*, and set it to be at $0.65b$ from the inboard wing tip. Moreover, the axis of rotation for the flapping motion is located at a fixed distance to the inboard wing tip, set to $\Delta\xi = c$ for all flapping cases. For clarity, figures 2a and 2b show a sketch of the wings in flapping motion, the position of the characteristic section, and the position an orientation of the flapping axis. The figures also include the wing-fixed reference frames, Σ_i. For the i-wing, the origin of Σ_i is located at the mid-chord of the inboard wing tip, the ξ_i-axis is oriented along the spanwise direction and coincides with the pitching axis, the η_i-axis is perpendicular to the wing surface, and τ_i-axis correspond to the chordwise direction.

As shown in figure 2b, the flapping motion of the wings depends on the vertical amplitude of the characteristic section, h_0, the distance of this section to the inboard wing tip, ξ_C, and the root offset, $\Delta\xi$. Hence, the flapping angle (see figure 2a) is:

$$\phi_i(t) = \phi_0 \cos\left(2\pi f t + \varphi_{h,i}\right), \tag{3}$$

where $\phi_0 = \sin^{-1}\left(h_0/\left(\Delta\xi + \xi_C\right)\right)$ is the flapping amplitude. For the aspect ratios considered here, $\phi_0 \approx 6.1^\circ$ and 3.9° for $\mathit{AR} = 2$ and 4, respectively. On the other hand, the pitching axis coincides with the longitudinal symmetry axis of the wing, as shown in figure 2a. Finally, it should be pointed out that the wing reference frames defined in figure 2a are also used when the wings are in heaving motion to ease the comparison between the cases.

In the subsequent sections, the aerodynamic forces at certain chordwise sections are analysed. These sections are sketched in figures 2c and 2d: section m corresponds to the wing section at the midspan; sections I and O are located at $0.5c$ from the inboard and outboard wing tips, respectively (note that, in the heaving case, the forces at both sections will be the same owing to symmetry); and section C corresponds to the characteristic section defined above.

2.2. *Computational set-up*

Direct numerical simulations (DNS) are performed with the in-house code TUCAN, which solves the Navier-Stokes equations of the incompressible flow. TUCAN uses second-order finite differences for the spatial discretization in a staggered grid and a 3-stage, low-storage Runge-Kutta scheme for time integration. The time step is always selected so that the Courant–Friedrichs–Lewy number is smaller than 0.2. The presence of the bodies is modelled by means of the immersed boundary method proposed by Uhlmann (2005). The present algorithm has been successfully used for the simulation of aerodynamic flows, both in two- (Moriche *et al.* 2017, 2020) and three-dimensions (Moriche *et al.* 2016; Gonzalo *et al.* 2018; Arranz *et al.* 2018*b*,*a*; Moriche *et al.* 2019).

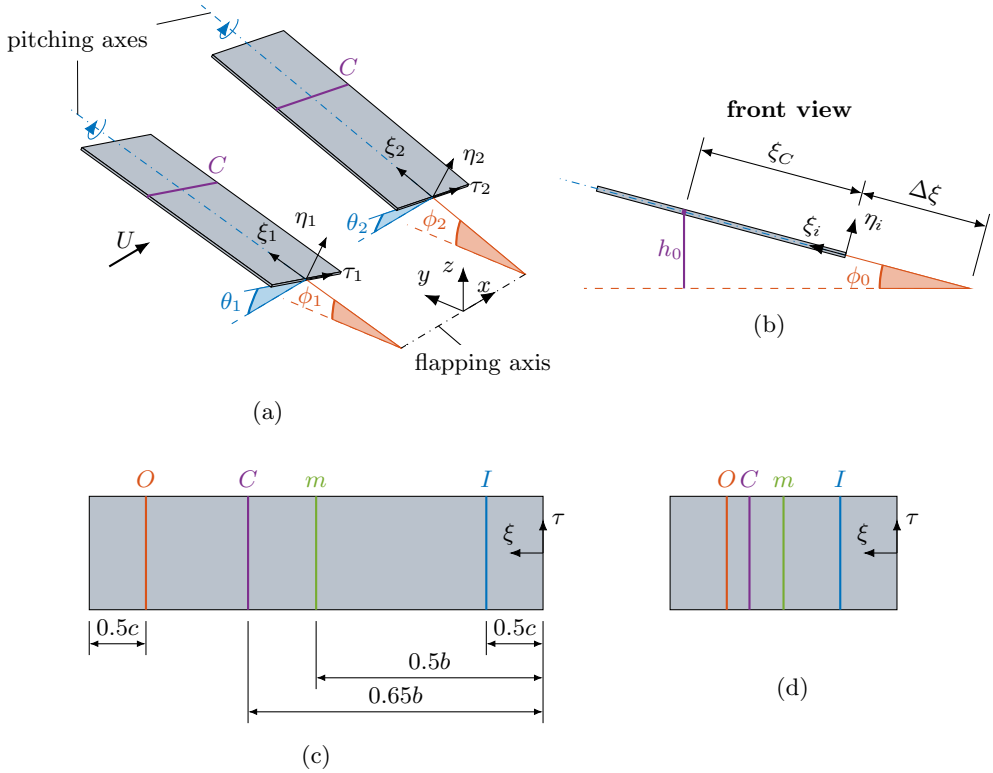

FIGURE 2: (a) Sketch of the flapping motion. The sections whose heaving amplitude is h_0 are highlighted in purple. The inertial reference frame $\Sigma \equiv (x, y, z)$ and the body reference frames $\Sigma_i \equiv (\tau_i, \xi_i, \eta_i)$ are also shown. (b) Front view of a single wing with the definition of $\Delta\xi$ and ξ_C. (c) Illustration of the chordwise sections where the sectional forces are computed for $\mathit{AR} = 4$ and (d) $\mathit{AR} = 2$.

The computational domain is a rectangular prism, displayed in figure 3. The wings are centered in a refined region ($3.5c \times L_{y_r} \times L_{z_r}$ in figure 3) with a uniform grid spacing in all directions, $\Delta r = c/96$. Outside this region, a constant stretching of 1% is applied to the grid in all directions. The dimensions of the refined region depend on the AR and on the motion of the wings. For the heaving motion, $L_{y_r}/c = 1 + \mathit{AR}$ and $L_{z_r}/c = 1$. For the flapping motion, $L_{y_r}/c = 1 + \mathit{AR}$ and $L_{z_r}/c = 1.6$ and 2, for $\mathit{AR} = 2$ and 4, respectively. Finally, $L_{y_i} = 3c$ in the heaving case and $L_{y_i} = 0.5c$ in the flapping cases. Thus, in flapping motion the plane $Y = 0$ contains the flapping axis. As a result, the 3D simulations consists of around 2×10^8 grid points, depending on the particular case. The computational domain for the 2D simulation corresponds to a $Y = const.$ plane of the 3D computational domain with a uniform grid spacing $\Delta r = c/96$, leading to a grid with 9×10^5 points.

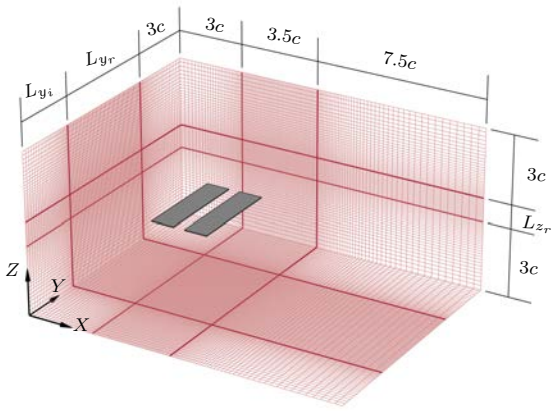

FIGURE 3: Sketch of the 3D computational domain. Solid lines delimit the uniform grid and the stretched grid. Only one of each five grid lines is represented.

In terms of boundary conditions, a uniform free-stream velocity, U, is imposed at the inflow plane ($X = 0$). A convective boundary condition is imposed at the outflow plane ($X = 14c$). Free-slip boundary conditions are imposed at the lateral boundaries.

TUCAN uses and immersed boundary method, which requires the specification of a Lagrangian mesh for the wings. Since the wings are flat plates, two flat surfaces are employed to discretize each wing. A uniform grid is used in each surface, with a grid spacing $\Delta r = c/96$ in both spanwinse and chordwise directions. The two surfaces discretizing each wing are separated a distance Δr, leading to a thickness $e/c \approx 0.01$.

The grid resolution reported in the previous paragraphs was selected after performing a grid sensitivity study for the 2D configuration, for $\Delta r = c/48$, $\Delta r = c/96$ and $\Delta r = c/192$. Figure 4 displays the temporal evolution of the aerodynamic force coefficients for the hind airfoil, which are more affected by the vortical interactions. Although not shown here, similar results are obtained for the fore airfoil. It can be appreciated that the temporal history of the forces with $\Delta r = c/96$ is very similar to that of $\Delta r = c/192$, while with $\Delta r = c/48$ the peaks in the forces are clearly different. Moreover, the differences in the propulsive efficiency computed for $\Delta r = c/96$ and $c/192$ are about 3%. Therefore, as a compromise between accuracy and computational cost, all simulations are performed with a grid spacing of $\Delta r = c/96$ in the refined region.

The simulations are started in a grid with a lower resolution ($\Delta r = c/56$ in the refined region) during the first 3 cycles, then the flow field is interpolated on the finer grid and the simulation is restarted and run until convergence is achieved. This entails about $3 - 4$ additional cycles. For the present cases, convergence means that periodic flow conditions are obtained for all cases, with the same period of oscillation of the forcing motion. Consequently, the aerodynamic forces and the flow in the region of

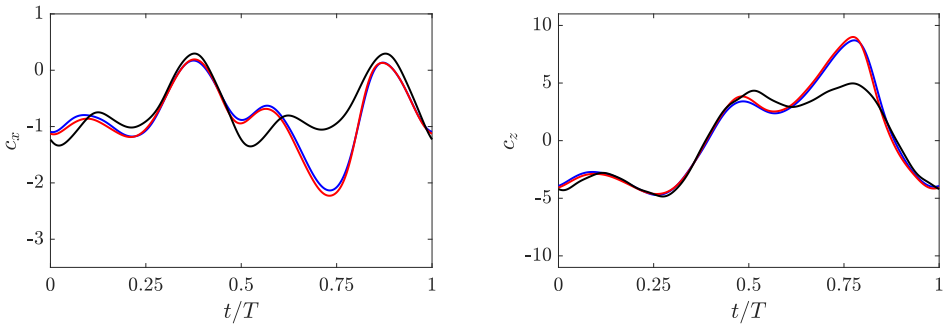

(a) (b)

FIGURE 4: Temporal evolution of the (a) horizontal and (b) vertical force coefficients of the hind airfoil. (——) $\Delta r = c/48$; (——) $\Delta r = c/96$; and (——) $\Delta r = c/192$.

interest are periodic, and the discussion of the results is based on the last computed cycle without any loss of generality.

2.3. *Definition of aerodynamic coefficients*

The aerodynamic force coefficients are defined as

$$C_{k,i} = \frac{2\mathbf{F}_i \cdot \mathbf{e}_k}{\rho U^2 bc}, \tag{4}$$

where $\mathbf{F}_i$ is the total aerodynamic force on the i-wing, $\mathbf{e}_k$ is the unitary vector parallel to the k-axis and ρ is the fluid density. On the other hand, we also analyse sectional forces at a given spanwise position. To that end, we define the sectional force coefficients as

$$c_{k,i}(\xi) = \frac{2\mathbf{f}_i(\xi) \cdot \mathbf{e}_k}{\rho U^2 c}, \tag{5}$$

where $\mathbf{f}_i(\xi)$ is the sectional force at the spanwise position ξ of the i-wing. Note that eq. (5) also corresponds to the aerodynamic force coefficient for the 2D case.

As reported by Lee *et al.* (2011), immersed boundary methods generate low amplitude, high frequency spurious oscillations on the forces when the bodies are moving. These oscillations do not affect the statistics of the forces during a cycle, and, since they do not represent a physical phenomenon, are removed in the present analysis using a sharp cut-off low-pass filter. The cutoff frequency is $f_c = (84\Delta t)^{-1} = 50f$, ensuring that only the spurious oscillations are supressed.

Finally, the performance of the wings is assessed by means of the individual propulsive efficiency and the global propulsive efficiency, computed as:

$$\eta_{p,i} = \frac{\overline{C}_{T,i}}{\overline{P}_i}, \qquad \eta_p = \frac{\sum_{i=1,2} \overline{C}_{T,i}}{\sum_{i=1,2} \overline{P}_i},$$

respectively, where $\overline{C}_{T,i}$ is the average thrust coefficient (computed as the average of $-C_{x,i}$ over a cycle), and $\overline{P}_i$ is the averaged non-dimensional input power of the i wing over a cycle. The instantaneous power is computed as:

$$P_i(t) = C_{z,i}\frac{\dot{h}_i(t)}{U} + \frac{2\mathbf{M}_i \cdot \boldsymbol{\varpi}(t)}{\rho U^3 b c^2}, \tag{6}$$

where $\boldsymbol{\varpi}(t) = \dot{\phi}(t)\mathbf{e}_x + \dot{\theta}(t)\mathbf{e}_\xi$ is the angular frequency. In heaving, $\mathbf{M}_i$ is the aerodynamic moment computed at any point along the ξ_i axis and $\dot{\phi} = 0$. In flapping, $\mathbf{M}_i$ is computed at the intersection of the ξ_i axis with the flapping axis, where $\dot{h} = 0$, so that the first term of eq. (6) is dropped.

3. Results

3.1. *2D simulation: reference case*

As a reference case we have selected a flow configuration with optimal kinematics as reported in previous works (Ortega-Casanova & Fernández-Feria 2019). The temporal evolution of the force coefficients of the 2D reference case is displayed in figure 5. These results are discussed below together with the results of the 3D simulations. Note that, the force coefficients obtained in the present simulations are in good agreement with the force reported in Ortega-Casanova & Fernández-Feria (2019) (not shown). Table 2 gathers the thrust and propulsive efficiencies of each airfoil averaged over a cycle. The motion of the airfoils results in a net production of thrust, with an overall propulsive efficiency slightly larger than the corresponding efficiency of an isolated airfoil oscillating as the fore-airfoil. The average thrust of the hind-wing ($\overline{c}_{T,2}$) is reduced compared to the average thrust of the fore-wing ($\overline{c}_{T,1}$) by approximately 20%. Despite this thrust reduction, the propulsive efficiency of the hind-foil ($\eta_{p,2}$) is very similar to the propulsive efficiency of the fore-wing ($\eta_{p,1}$), as shown in table 2. Hence, the thrust reduction is accompanied by a reduction of the required power, leading to a relatively constant propulsive efficiency for both airfoils.

Although the motion of the airfoils is symmetric with respect to the horizontal plane, a net lift ($\overline{c}_z = 0.51$) is obtained in the tandem configuration as a result of wake deflection (see figure 6a below). This phenomenon does not occur for the isolated airfoil with the present kinematics (Ortega-Casanova & Fernández-Feria 2019), although it has been observed on isolated airfoils with different motions (Lewin & Haj-Hariri 2003).

$\overline{c}_{T,1}$	$\overline{c}_{T,2}$	$\eta_{p,1}$	$\eta_{p,2}$	η_p
1.02	0.81	0.24	0.23	0.23

TABLE 2: Averaged results of the 2D simulations. Mean thrust ($\overline{c}_{T,i}$), individual propulsive efficiencies ($\eta_{p,i}$) and global propulsive efficiency (η_p).

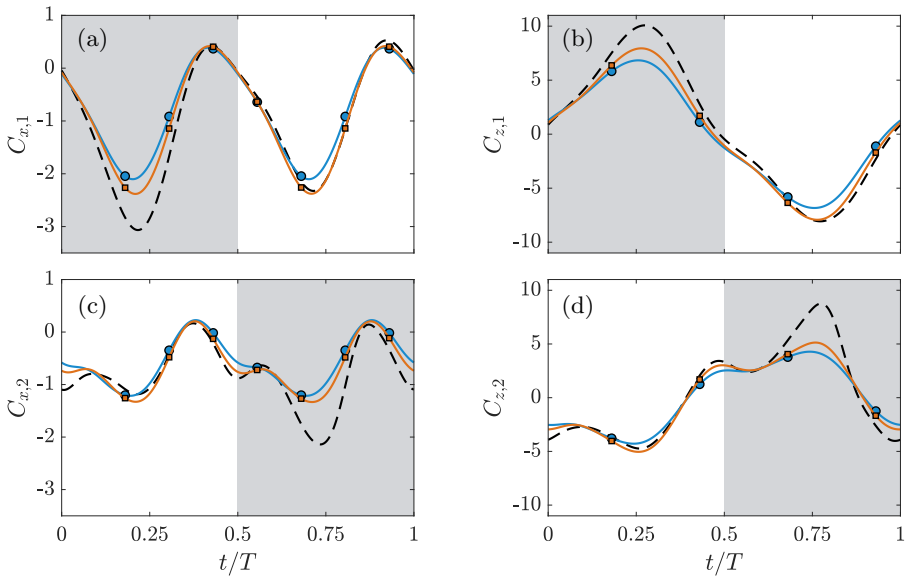

FIGURE 5: Temporal evolution of the force coefficients. (a-b) Fore-wing, (c-d) hind-wing. (a) and (c) horizontal force coefficient; (b) and (d) vertical force coefficient. (- - -) 2D reference case; (—●—) $\mathit{AR} = 2$; (—■—) $\mathit{AR} = 4$. In all plots, the shaded region corresponds to the downstroke of each wing.

3.2. *3D simulations: Aspect ratio effects*

In order to assess the three dimensional effects due to the finite aspect ratio of the wings, the 2D and the 3D heaving cases are compared first.

Figure 5 depicts the aerodynamic force coefficients ($C_{x,i}$ and $C_{z,i}$) in heaving motion for both AR, together with the forces of the 2D reference case. Qualitatively, the aerodynamic forces of the finite wings are similar to those of the 2D case. Both the fore and the hind-wing produce thrust (i.e., negative horizontal force) during most of the cycle. Figure 5a shows two thrust peaks for the fore-wing at mid-downstroke and mid-upstroke; these peaks are also present for the hind-wing (figure 5c) but less intense, due to flow interaction, as it will be discussed below. On the other hand, the vertical force for both airfoils is mostly positive during the downstroke and negative during the upstroke (figures 5b and 5d). These forces yield a zero mean lift, contrary to the non-zero mean lift observed in the 2D case. This difference on the mean lift is clearly observable in the structure of the far wake of these cases. To illustrate this, figure 6 shows the vertical velocity component time-averaged over a cycle. In the 2D case, figure 6a, the deflection of the wake with respect to the horizontal plane is clearly visible. In the 3D heaving case with $\mathit{AR} = 4$, no significant deviation from anti-symmetry is observed in the wake, figure 6b. A similar observation was reported by Dong *et al.* (2006) on single plunging foils and wings at similar reduced frequencies.

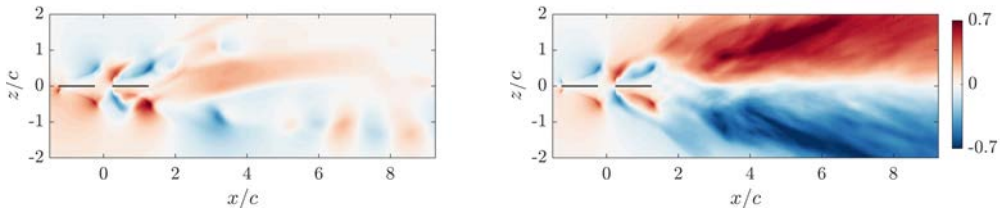

(a) (b)

FIGURE 6: Vertical velocity time-averaged over a cycle. (a) 2D reference case, (b) midspan plane of $AR = 4$ heaving case. Contours are normalized with the freestream velocity, U.

	$\mathcal{AR}$	$\overline{C}_{T,1}$	$\overline{C}_{T,2}$	$\overline{C}_{z,1}$	$\overline{C}_{z,2}$	$\eta_{p,1}$	$\eta_{p,2}$	η_p
Heaving	**2**	0.81	0.57	3.83	2.05	0.23	0.21	0.23
	4	0.91	0.65	4.39	2.24	0.23	0.22	0.23
Flapping	**2**	0.62	0.45	3.42	1.90	0.22	0.19	0.21
	4	0.66	0.49	3.78	2.04	0.21	0.19	0.20

TABLE 3: Average forces during half-stroke and propulsive efficiencies for the finite span cases.

Regarding the effect of the aspect ratio on the forces, figures 5a and 5b show that, on the fore-wing, larger $\mathcal{AR}$ leads to higher forces during the mid-upstroke and mid-downstroke. On the hind-wing (figures 5c and 5d), the temporal evolution of the force coefficients presents more oscillations due to the interaction with the wake of the fore-wing, like in the 2D configuration (Ortega-Casanova & Fernández-Feria 2019). Despite this, a qualitatively similar increase in the peak forces of the hind-wing with $\mathcal{AR}$ is also observed. In fact, the average forces over half cycle of each wing decrease roughly 10% from $\mathcal{AR} = 4$ to 2. This is reported in table 3 that gathers the thrust and lift coefficients averaged over half a cycle and the propulsive efficiencies of each wing.

Figure 7 shows visualizations of the three-dimensional simulations for the cases $\mathcal{AR} = 2$ and $\mathcal{AR} = 4$ at various time instants during the cycle. The vortical structures depicted in the figure correspond to iso-surfaces of the second invariant of the velocity gradient tensor, Q (Hunt *et al.* 1988). The iso-surfaces of $Q = 6\Omega_0^2$ are coloured with the spanwise vorticity, ω_y, where $\Omega_0 = 2\pi f$ is the maximum angular velocity. On the other hand, semi-transparent iso-surfaces correspond to $Q = 3\Omega_0^2$ and are associated to less intense vortical structures. Figure 7a depicts the flow structures at the end of the fore-wing's downstroke. For both $\mathcal{AR}$ one can appreciate the two main vortical structures developed during the motion, namely: the trailing edge vortex developed by the fore-wing (TV), and a leading edge vortex on the hind-wing. The latter is denoted

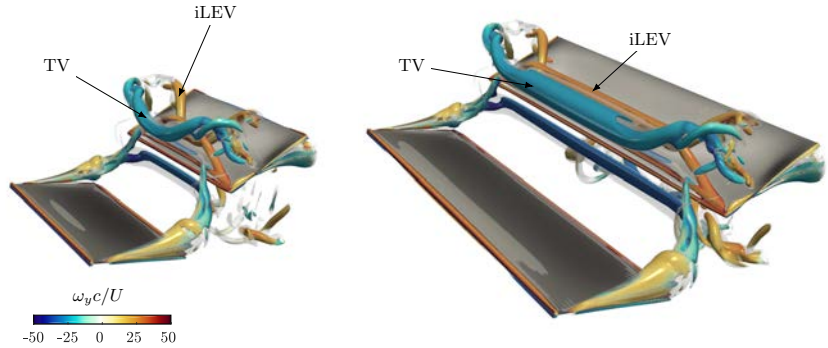

(a) $t/T = 0.5$

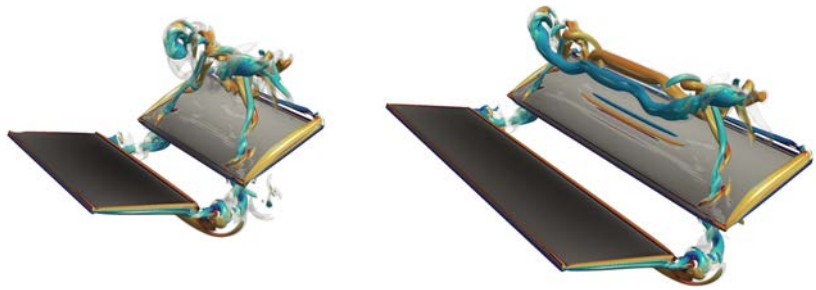

(b) $t/T = 0.75$

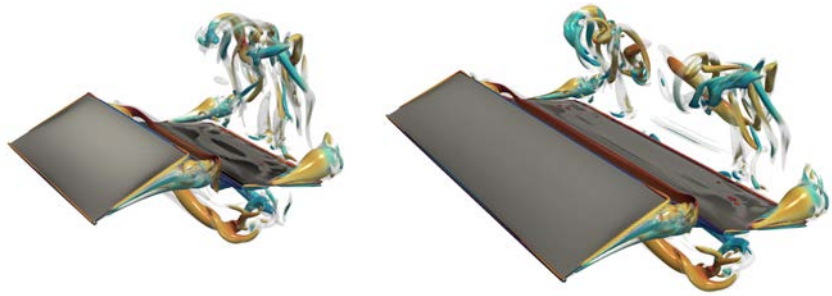

(c) $t/T = 1$

FIGURE 7: Flow visualization of the cases in heaving motion at various time instants: (a) end of the fore-wing downstroke; (b) fore-wing mid-upstroke; and (c) end of the fore-wing upstroke. (left) $\mathcal{AR} = 2$, and (right) $\mathcal{AR} = 4$. Vortices are represented by means of the Q-criterion Hunt *et al.* (1988). Semi-transparent iso-surface correspond to $Q = 3\Omega_0^2$; iso-surface coloured with the spanwise vorticity, ω_y, correspond to $Q = 6\Omega_0^2$.

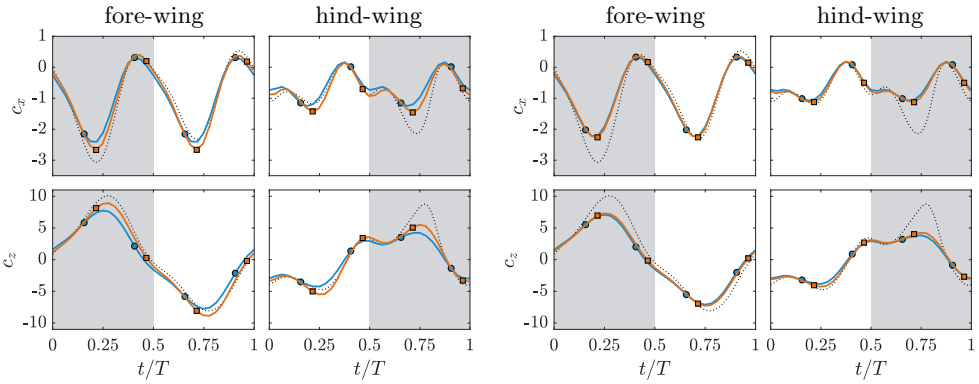

(a) section m (b) section I (O)

FIGURE 8: Temporal evolution of sectional force coefficients at chordwise sections (a) $\xi = \xi_m$ and (b) $\xi = \xi_I$. (–●–) $\mathit{AR} = 2$, (–■–) $\mathit{AR} = 4$ and (·····) 2D force coefficient. As in figure 5, the shaded region correspond to the downstroke of each wing.

as the induced leading edge vortex (iLEV), since it is induced by the wake shed by the fore-wing. For both AR, the TV and the iLEV tilt upwards and break near the tips of the hind-wing. However, for $\mathit{AR} = 4$, there is a region at the midspan where both vortices resemble two-dimensional vortices. This breakdown observed near the wing tips progresses towards mid section, as observed at later time instants in figures 7b and 7c. The progression of the breakdown seems to occur at the same velocity for both AR. As a consequence, the dipole in the midspan section of the $\mathit{AR} = 2$ case breaks down earlier than in the $\mathit{AR} = 4$ case. This breakdown of the vortices at the midspan is in accordance with observations on pitching tandem wings of $\mathit{AR} = 2$ (Kurt & Moored 2018). Finally, it is interesting to note that the vortex structures near the tips of both wings are very similar for both AR at all times depicted in figure 7.

It is interesting to analyse if the differences between the flow structures observed in figure 7 for each AR have a direct impact on the forces. Hence, we compute the sectional forces at the mid-span section, $\xi = \xi_m$ (see figures 2c and 2d) and at the inboard (or equivalently, outboard) sections, $\xi = \xi_I$ (ξ_O). These sectional force coefficients are shown in figure 8. The sectional force coefficients differ at the mid-span (figure 8a), where figure 7a shows differences in the vortical structures of cases $\mathit{AR} = 2$ and 4. In particular, figure 8a shows that the peak sectional forces of both wing at midspan decrease with decreasing AR. On the other hand, figure 8b shows that the sectional forces at spanwise positions which are influenced by the wing-tip vortices are very similar for both AR, provided that sections at the same distance to the wing tip are considered. Comparison of sectional forces at different chordwise sections reveals that, for the present case, this similarity is extended up to $0.75c$ from the wing tips for both the fore-wing and the hind-wing (not shown).

In order to analyse the origin of the discrepances in the forces at the midspan section, Figures 9 and 10 depict the spanwise vorticity of the 2D case, and of the 3D simulations at $\xi = \xi_m$, respectively. Figure 9 shows a complete cycle of the 2D case. It is interesting to compare the first half (figures 9a-9d), which corresponds to the downstroke of the fore-wing, and the second half of the cycle (figures 9e-9h). One can appreciate that the dipole that is formed by the TV and the iLEV on the lower surface of the hind-airfoil during its upstroke (figures 9a-9d) remains close to the hind-airfoil during its downstroke (figures 9e-9h). The same does not happen to the dipole that develops on the upper surface (figures 9e and 9f), which detaches from the foil and travels downstream (figures 9g and 9h). This difference is clearly appreciated by analysing the position of the vortices in figures 9a and 9e. The relative attachment of the dipole during the hind-wing downstroke explains the larger peak forces near $t/T = 0.75$ (figure 9f) compared to those at $t/T = 0.25$ (figure 9b), during the upstroke of the hind-wing, as shown in figure 5. Likewise, the development of a leading edge vortex on the suction surface of the fore-wing at the end of its downstroke (figure 9d) explains the force reduction during its upstroke. In particular, this vortex lowers the pressure on the upper surface, leading to an increase in the force normal to the airfoil whose projection on the x- and z-axes leads to an increase of both c_x (thrust reduction) and c_z (negative force reduction), respectively.

Figure 10 displays only the first half of the cycle for the finite aspect ratio wings, since the flow is symmetric with respect to the $z = 0$ plane on the other half of the cycle. The spanwise vorticity contours at the mid-span show that the iLEV development from the shear layer of the fore-wing, as well as its first interaction with the TV, are qualitatively similar to the 2D case (figures 9a-9d) for both $\mathcal{AR}$. The subsequent evolution of the dipole can be observed on the lower surface of the hind-wing, which corresponds to the vortices shed during the previous cycle. Specifically, the vortical structures on the lower hind-wing surface would correspond to the iLEV and TV at $t = t_0 + 0.5T$ (being t_0 the time specified in figure 10) with the opposite vorticity. It is observed that, as the vortices interact and travel downstream, the differences between the cases become more evident. For $\mathcal{AR} = 4$ (figures 10e-10h), the dipole travels downstream and detaches from the hind-wing, like during the downstroke of the 2D hind-airfoil (figures 9e-9h). On the contrary, the vorticity intensity of the dipole for $\mathcal{AR} = 4$ diminishes faster than its 2D counterpart. This effect is due to the *spanwise compression* of the wake, also observed for single pitching/heaving wings (Dong *et al.* 2006; Buchholz & Smits 2006; Green *et al.* 2011; Buchholz & Smits 2008). On the other hand, a proper dipole is not formed between the TV and the iLEV over the $\mathcal{AR} = 2$ hind-wing (figures 10a-10d); instead, vortex breakdown from the tips reach the midspan section before, as shown in figure 7b.

Although vortical interaction is clearly different at midspan of the hind-wing for $\mathcal{AR} = 2$ and 4, it does not explain the differences of the sectional forces on the fore-wing (figure 8a), since no vortices are found at the midspan of the fore-wing. Hence, the reduction of the sectional forces at $\xi = \xi_m$ on the fore-wing with lower $\mathcal{AR}$ seems more likely explained by finite-wing effects, namely, downwash induced velocity as in steady aerodynamics. Moreover, since the difference of the sectional force of the hind-wing with $\mathcal{AR}$ is similar to that of the fore-wing, it can be concluded that finite-wing effects

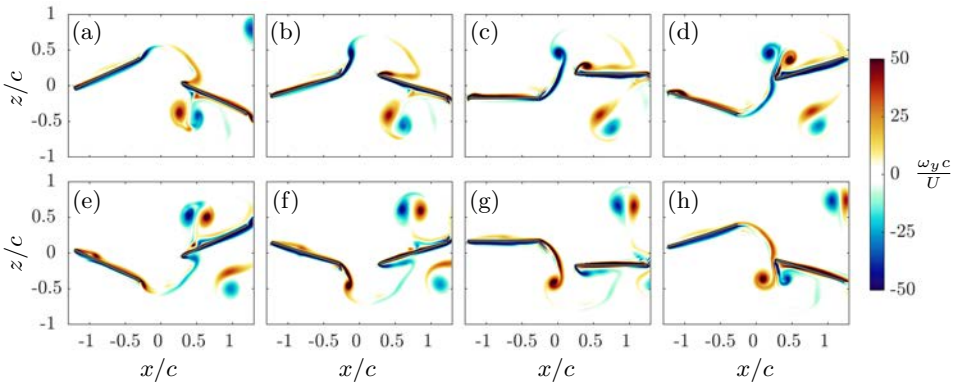

FIGURE 9: Spanwise vorticity contours of the 2D simulation during a full period. Pictures correspond to different equidistant time instants. (a-d) from $t/T = 0.125$ to $t/T = 0.5$; (e-h): from $t/T = 0.625$ to $t/T = 1$.

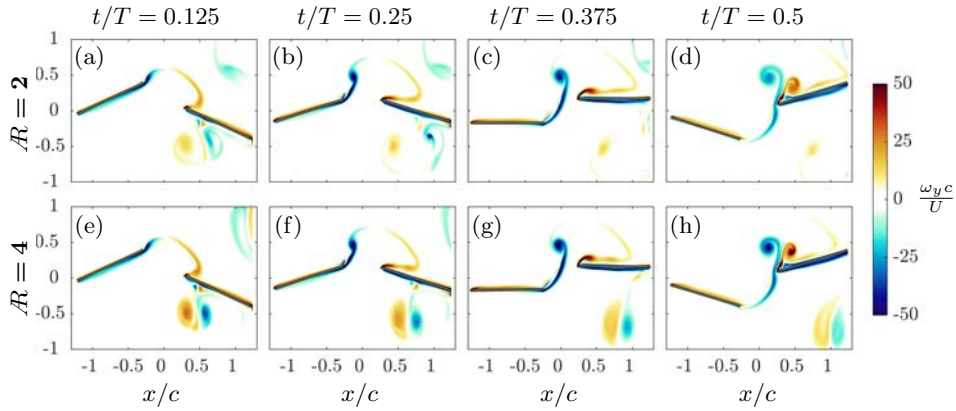

FIGURE 10: Spanwise vorticity contours at section $\xi = \xi_m$ during the downstroke of the fore-wing. From left to right, $t/T = 0.125$, 0.25, 0.375 and 0.5. The upper row corresponds to $\mathcal{AR} = 2$ and the lower row to $\mathcal{AR} = 4$.

are also the main responsible for force reduction on the hind-wing when $\mathcal{AR}$ decreases. Consequently, vortex breakdown at the midspan has a secondary effect on the forces since it does not occur close to the wing surface (Moriche *et al.* 2017).

To summarize, table 3 gathers, for each wing, the thrust and lift coefficients averaged over half a cycle, as well as the individual and global propulsive efficiencies. The averaged force coefficients are found to be smaller for $\mathcal{AR} = 2$ compared to $\mathcal{AR} = 4$, both for the fore-wing and the hind-wing. If the mean thrust of each wing is

compared to its two-dimensional counterpart (table 2), a reduction of approximately 21% and 11% is obtained for the fore-wing of $\mathcal{AR} = 2$ and 4, respectively. Preliminary simulations of isolated wings (not shown here) have shown that the thrust generated by the fore-wing is independent of the vortical interaction between the fore- and hind-wings, in agreement with previous works (Maybury & Lehmann 2004; Nagai *et al.* 2019). This suggests that the aforementioned thrust reduction is mainly due to wing-tip effects, namely, induced downwash velocity. For the hind-wing, the thrust reduction from 2D to 3D is larger, from 29% for $\mathcal{AR} = 2$ to 20% for $\mathcal{AR} = 4$ wings. Consequently, three-dimensional vortical mechanisms which are not present in the 2D case (i.e., wing-tip vortices and vortex breakdown) influence the hind-wing's thrust generation. Indeed, the thrust reduction of the hind-wing with respect to the fore-wing ($1 - \overline{C}_{T,2}/\overline{C}_{T,1}$) is very similar for both aspect ratios (30% and 28% for $\mathcal{AR} = 2$ and 4, respectively), and higher than for the two-dimensional case, which is close to 20%. This leads to the conclusion that 3D vortex interaction, for the $\mathcal{AR}$ considered in this study, has a non-negligible impact on the aerodynamic forces. Despite the detriment in thrust generation, the propulsive efficiency of the hind-wing ($\eta_{p,2}$) is very similar to the propulsive efficiency of the fore-wing ($\eta_{p,1}$) and only slightly lower than the individual propulsive efficiencies of the two-dimensional case. Consequently, the overall propulsive efficiency, η_p is virtually the same. The low dependency of η_p on $\mathcal{AR}$ was reported by Dong *et al.* (2006) for single wings in pitching and heaving motion, and later by Buchholz & Smits (2008) for a low-$\mathcal{AR}$ pitching wing. In both cases, the Strouhal number was in the same range as the one considered in the present study.

3.3. *3D simulations: Heaving vs. flapping*

From a mechanical point of view, heaving is not a realistic motion for either MAVs or flying animals. Therefore, in the present section we analyse the differences between a pair of tandem finite wings in heaving (section 3.2) and the same wings performing a flapping motion about a fixed axis, as described in section 2.

Figure 11 shows the temporal evolution of the aerodynamic force coefficients in the heaving and flapping configurations, for both $\mathcal{AR} = 2$ and 4. In the flapping case, for both the fore- and the hind-wing, a decrease of the thrust peaks is observed compared to to the heaving case (figures 11a and 11c), while drag peaks (at $t/T \approx 0.35$ and 0.85) remain virtually equal. This decrease is more pronounced for $\mathcal{AR} = 4$ than for $\mathcal{AR} = 2$. As a consequence, the average thrust of both wings is reduced in flapping motion when compared to heaving motion (see table 3). Regarding the effect on the vertical force, figures 11b and 11d reveal an amplitude decrease for both wings in the flapping case. Moreover, from heaving to flapping, there is a shift in the time at which forces are maximum.

Top row of figure 12 shows the sectional aerodynamic forces at the characteristic section, ξ_C (viz., the section which moves like the 2D-configuration in flapping motion) for both $\mathcal{AR}$ and for the heaving and flapping motion. One can appreciate that, for a given $\mathcal{AR}$, the sectional forces at ξ_C are very similar both in heaving and flapping. This observation holds for the fore and the hind-wing and for the horizontal and vertical components of the forces. However, the sectional force coefficients vary with $\mathcal{AR}$. In particular, the peak forces are diminished for the lower aspect ratio. Since the

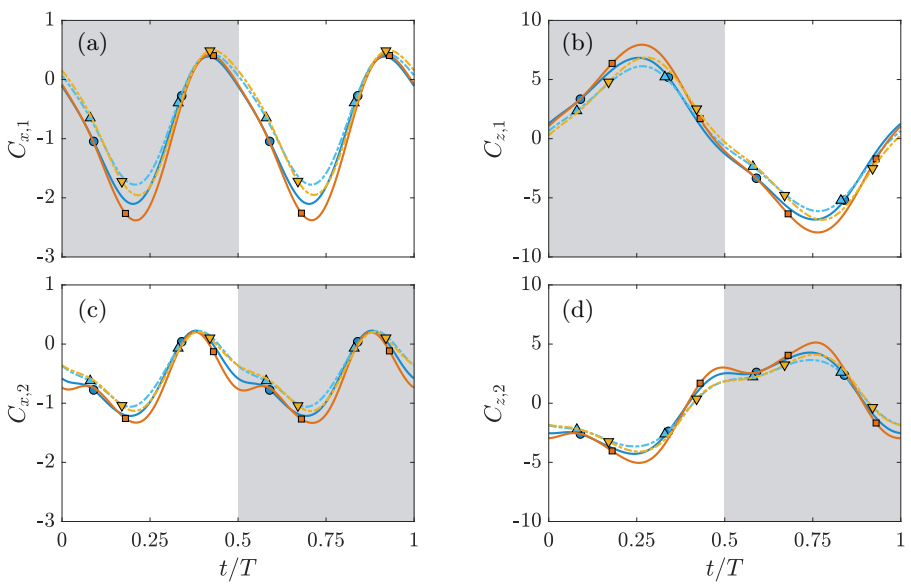

FIGURE 11: Temporal evolution of the force coefficients. (a-b) Fore-wing, (c-d) hind-wing. (a) and (c) horizontal force coefficient; (b) and (d) vertical force coefficient. $\mathcal{AR} = 2$: (—●—) heaving, (- -▲- -) flapping; and $\mathcal{AR} = 4$ (—■—) heaving, (- -▼- -) flapping.

characteristic section, ξ_C, changes with $\mathcal{AR}$ ($\xi_C = 1.3c$ for $\mathcal{AR} = 2$, and $\xi_C = 2.6$ for $\mathcal{AR} = 4$), the fact that the sectional forces at ξ_C vary with $\mathcal{AR}$ but not with the motion seems to suggest that the sectional forces do not depend only on the sectional motion but also on the vortical structures.

Since the amplitude of the aerodynamic forces is lower in flapping motion, there must be wing sections with lower sectional forces than at ξ_C. To show this, figure 12 (bottom row) displays the sectional forces at ξ_I and ξ_O for the flapping motion of the $\mathcal{AR} = 2$ and 4 wings. As expected, the amplitude of the vertical force is decreased at the inboard sections of the wings; the same happens for the peak thrust. The opposite behaviour is observed at outboard wing section. Moreover, it is interesting to note that, in addition to a reduction of the peak thrust at inboard sections, there is an increase of positive horizontal force (drag), at the end of the downstroke. This effect is more pronounced for the $\mathcal{AR} = 4$ wing. Additionally, the peak of the forces shifts forward in time from outboard to inboard wing sections. This shift is related to the spanwise variation of the *effective angle of attack*, $\alpha_i(\xi)$, which is the angle between the chordwise direction (τ_i in figure 2) and the flow velocity at the mid-chord of the ξ_i-section. Particularly,

$$\alpha_i(\xi) = \theta_i - \tan^{-1}\left(\frac{\dot{\phi}_i(\Delta\xi + \xi)}{U}\right) \tag{7}$$

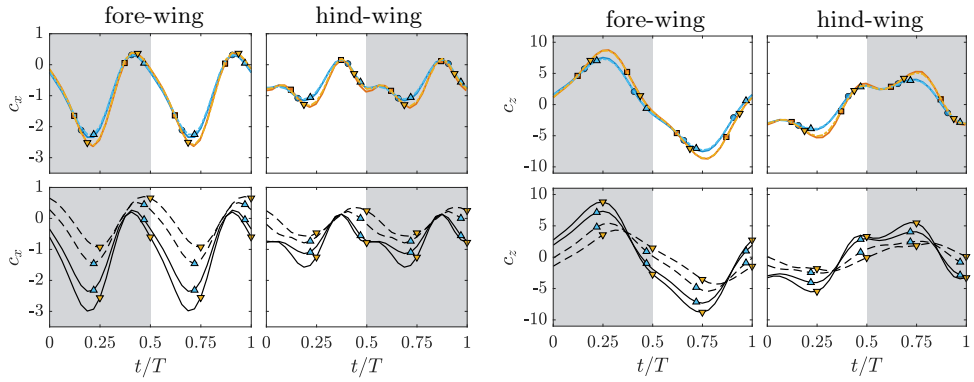

FIGURE 12: Temporal evolution of the sectional (a) horizontal and (b) vertical force coefficients. For both figures, top row displays the sectional forces at the characteristic section, $\xi_C = 0.65b$: $\mathcal{AR} = 2$: (–●–) heaving, (-▲-) flapping; $\mathcal{AR} = 4$: (–■–) heaving, (-▼-) flapping. Bottom row displays the sectional forces near the wing tips during flapping motion: (- - -) inboard section, ξ_I, and (——) outboard section, ξ_O. (▲) $\mathcal{AR} = 2$ and (▼) $\mathcal{AR} = 4$.

where $\dot{\phi}$ is the time derivative of ϕ. The peak of α_i occurs earlier at outboard sections than at inboard sections of the wing, in accordance to peak of the forces.

The spanwise variation of the forces for both wings can be understood by looking at the spanwise vorticity (figure 13). The results correspond to $\mathcal{AR} = 4$, since for this case the differences between the outboard and the inboard sections are more noticeable. Figure 13 depicts, for the inboard (ξ_I), midspan (ξ_m) and outboard (ξ_O) wing sections, the vorticity normal to the cylindrical surface whose axis of revolution coincides with the flapping axis and with radii equal to $\Delta\xi + \xi_I$, $\Delta\xi + \xi_m$ and $\Delta\xi + \xi_O$, respectively. These surfaces are also illustrated in figure 14a. It is noticeable that the vorticity at the midspan (second row in figure 13) is very similar to that in heaving motion at the same section, figure 10. This is not true for the inboard and outboard wing sections. If we focus on the fore-wing at $\xi = \xi_I$, a vortex is developed on the lower surface of the fore-wing, due to the pitch-up rotation of the wing, $t/T = 0.375$. This vortex is labelled 1 in the figure. During the cycle, this vortex travels downstream until it merges with the shear layer shed at the hind-wing's trailing edge. The vortex motion is chronologically indicated by the numbers in figure 13 (top row). Note that, since only half a cycle is shown, the vortex flips side from 2 to 3 and from 6 to 7 in the present representation. On the contrary, if we compare the vorticity contour at the inboard (top row of figure 13) and outboard (bottom row) wing sections, it is appreciated that no vortex is shed at $\xi = \xi_O$. Instead, the shear layer on the upper surface detaches at the leading edge ($t/T = 0.5$).

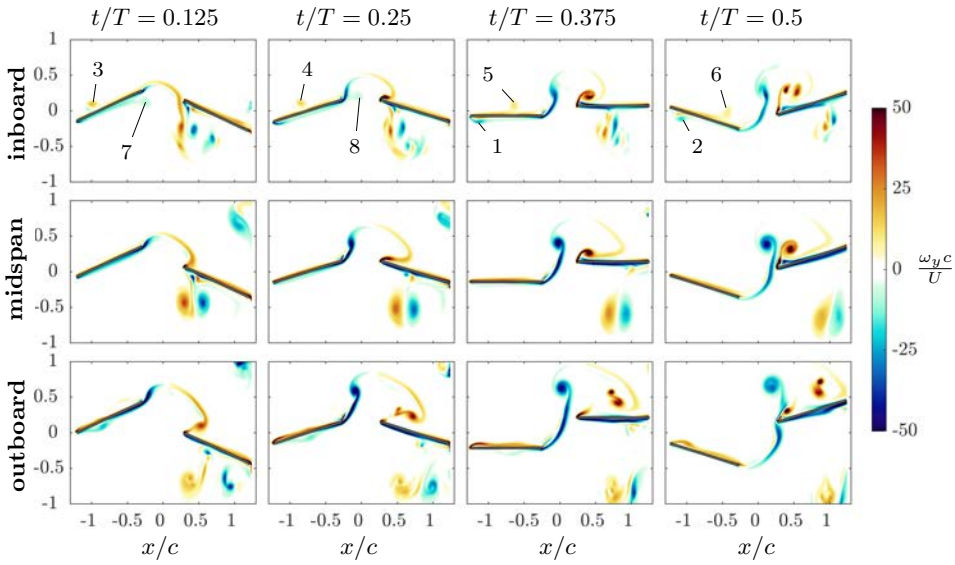

FIGURE 13: Spanwise vorticity contours during the downstroke (upstroke) of the fore-(hind-)wing at different chordwise sections of $\mathcal{AR} = 4$ wings in flapping motion. Each column correspond to a given time: from left to right, $t/T = 0.125$, 0.25, 0.375 and 0.5. Upper row correspond to the inboard wing tip ($\xi = \xi_I$), middle row correspond to the midspan section ($\xi = \xi_m$), and lower row correspond to the outboard wing tip ($\xi = \xi_O$).

The spanwise variation of the vorticity can be explained by the spanwise variation of the *effective angle of attack* (see eq. (7)). Near the inboard wing tip, the contribution of the vertical velocity to α_1 is small, and inboard sections behave like an airfoil in pure pitching. Specifically, the shedding and travelling of the vortices at the fore-wing leading edge at ξ_I is similar to that observed in pure pitching foils for $\theta_0 \geq 8°$ (and similar St_c and Re) (Das *et al.* 2016). Outboard fore-wing sections have larger *heaving* amplitudes. As a consequence, an LEV starts developing after the mid-downstroke ($t/T = 0.375$ in figure 13) at outboard spanwise locations, in a similar fashion as wings in flapping without pitching motion (Gonzalo *et al.* 2018). However, pitch-up rotation inhibits its later development and shedding as for flapping wings without pitching (Gonzalo *et al.* 2018) or heaving airfoils (Lewin & Haj-Hariri 2003).

The spanwise variation of the fore-wing wake flow affects the hind-wing. Figure 13 shows that, for a given time instant, the trailing edge vortex is located further upwards and downstream at outboard spanwise positions. As a consequence, the shear layer of the TV impinges earlier on the leading edge at outboard wing sections and the iLEV starts developing earlier at outboard wing sections. This is illustrated in the last column of figure 13 ($t/T = 0.5$), where it is observed that the shear layer shed during the downstroke of the fore-wing have just impinged on the leading edge of outboard

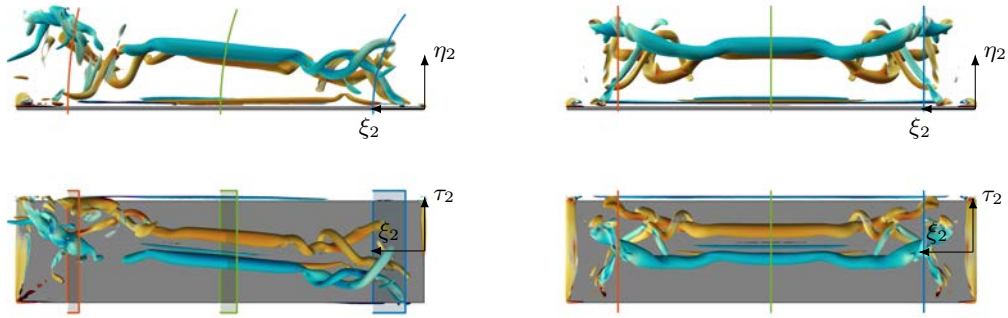

(a) Flapping **(b)** Heaving

FIGURE 14: Vortical structures on the $\mathcal{AR} = 4$ hind-wing at $t/T = 0.75$ for the (a) flapping and (b) heaving case. The vortical structures correspond to $Q = 6\Omega_0^2$ and are coloured with ω_y (legend as in figure 7). The planes sketched in (a) and (b) are the ones used to display the vorticity contours in figures 13 and 10, respectively (note that in the latter, inboard and outboard planes are equivalent).

wing sections (bottom row); meanwhile at the inboard wing sections the shear layer has not yet reached the leading edge of the hind-wing.

Figure 14 shows that, even with the spanwise variation of TV and iLEV, the overall vortical interactions on the hind-wing for the flapping case are similar to the heaving case. Nonetheless, it is observed that, as a consequence of the varying intensity of the vortices along the spanwise direction, both the TV and iLEV are found more downstream and upwards on the outboard regions when compared to the heaving case. At longer times, there is a vortex breakdown similar to the heaving case (figure 15).

Regarding averaged forces, table 3 shows that the mean thrust of each wing decreases in the flapping case compared to the heaving case. The reduction is more pronounced for $\mathcal{AR} = 4$ (27% and 26% for the fore- and hind-wing, respectively) than for $\mathcal{AR} = 2$ (23% and 20% for the fore- and hind-wing, respectively). On the other hand, the thrust reduction of the hind-wing compared to the fore-wing is 27% for both $\mathcal{AR}$, being very similar to the results observed in heaving. This entails that, as shown before, the interaction between both wings is rather similar both in heaving and flapping motions. Finally, a reduction in the propulsive efficiency, η_p, is also observed in the flapping case compared to the heaving case. Contrary to heaving, η_p slightly decreases with $\mathcal{AR}$ in the flapping case. This adverse effect of $\mathcal{AR}$ can be attributed to the fact that, as $\mathcal{AR}$ increases, there is a larger region of the wing which has a *suboptimal* motion, particularly close to the inboard wing tip, whose sectional propulsive efficiency is lower. This is true for both the fore- and the hind-wing.

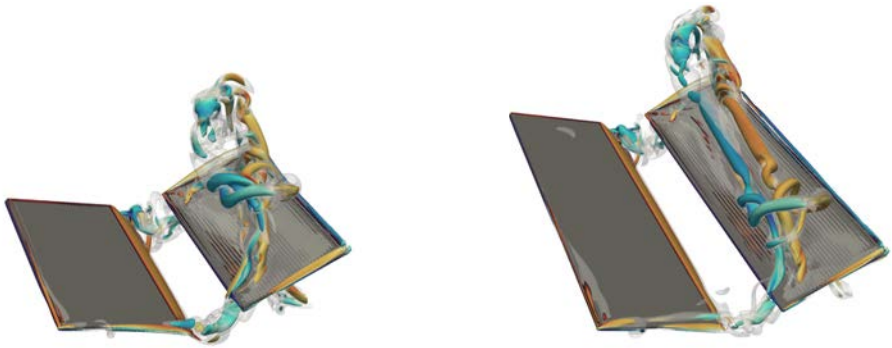

(a) $t/T = 0.75$

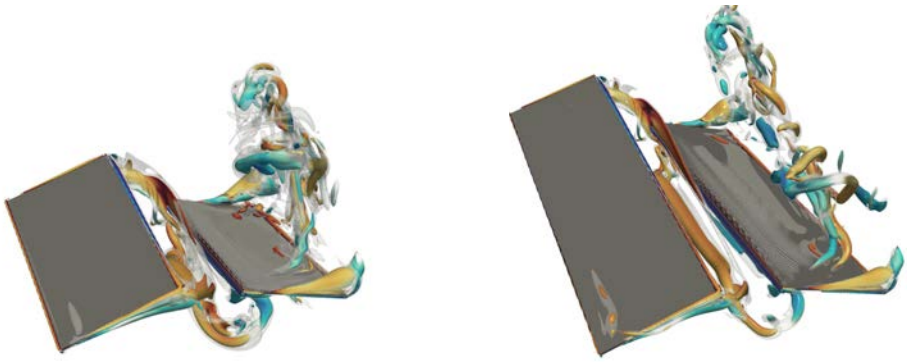

(b) $t/T = 1$

FIGURE 15: Visualization of the cases in flapping motion. (a) $t/T = 0.75$ and (b) $t/T = 1$. The closer tips correspond to the inboard wingtips. Iso-surfaces of the Q-criterion are equal to those on figure 7.

4. Conclusions

The objective of this study was to analyse how three dimensional effects influence the performance of wings in tandem configuration undergoing a two-dimensional optimal kinematics. To do so, direct numerical simulations, both in 2D and 3D, have been performed.

First, finite aspect ratio effects have been studied by considering wings of two different aspect ratios, 2 and 4, undergoing a heaving and pitching motion corresponding to the 2D optimal kinematics (Ortega-Casanova & Fernández-Feria 2019). The analysis has been based on comparisons of the flow structure and of the aerodynamic forces on the wings. For both $\mathcal{AR}$, the interaction mechanisms between the fore- and the hind-wing vortical structures are qualitatively similar to the two-dimensional case.

Namely, the shear layer shed by the fore-wing induces a leading edge vortex on the hind-wing surface which interacts with the trailing vortex of the fore-wing. However, in 3D, there is a breakdown of both vortices starting at the wing tips of the hind-wing and progressing towards the midspan, leading to somewhat different vortex organisation surrounding the wings. The mean thrust of the finite wings is lower than in the 2D case. This reduction is larger with decreasing AR. Moreover, it is found that the thrust reduction is more pronounced on the hind-wing. This entails that 3D vortical mechanisms, not present in 2D, have a non-negligible impact on the aerodynamic forces of the hind-wing. Nonetheless, the propulsive efficiency (η_p) remains approximately constant for both AR and for the 2D dimensional case. Our results are consistent with the observations of Dong *et al.* (2006) for single heaving/pitching wings, as well as those of Broering & Lian (2015) for tandem wings at a significantly lower Reynolds number than the one considered here.

The results of the tandem wings in heaving motion have been compared to those obtained for a flapping motion. The objective was to analyse the effects of having a more realistic, three-dimensional motion. The results show that, for a given AR, the aerodynamic forces decrease when the wings are in flapping motion. A comparison of the sectional forces along the span reveals that the forces are nearly identical for the heaving motion at midspan and for the flapping motion at the characteristic section (i.e. the section whose motion corresponds to the 2D airfoil motion). On the contrary, the amplitude of the vertical force decreases at inboard wing sections in flapping motion; likewise, both the amplitude and the mean value of the thrust force decrease. This detrimental behaviour has been linked to a sub-optimal motion of the inboard region, which is close to a pure pitching motion of low efficiency (Das *et al.* 2016). It should be noted that this behaviour is found both on the fore-wing and on the hind-wing. This sub-optimal region of the wings entails not only a decrease of the mean thrust, but also a decrease of the propulsive efficiency compared to the heaving case, which is more noticeable for $\mathit{AR} = 4$, since the extension of this region is larger in this case.

The present results also suggest that for 3D configurations, a moderate spacing between the wings (i.e, $s \lesssim c$) is probably desirable to avoid the full breakdown of the TEV before it reaches the hind-wing. This is not the case for 2D airfoils in tandem configuration, where the vortices shed by the fore-wing dissipate very slowly, allowing basically the same vortical interactions when the distance between the airfoils is increased by λ (where λ is the wavelength of wake shed by the fore-wing) (Zhu *et al.* 2014; Kurt & Moored 2018).

To summarise, it has been found that 2D tandem simulations provide reasonable predictions of the propulsive efficiency of finite aspect ratio wings, in the range of Reynolds and Strouhal numbers studied here. On the other hand, mean thrust production of the hind-wing is not properly estimated in 2D simulations, due to differences between 2D and 3D vortical interactions. Concerning the mean lift, it has been observed that a non-zero value is obtained in 2D that can be attributed to the well-known phenomenon of wake deflection. On the contrary, in the 3D simulations the mean lift is zero for all cases. This is consistent with the observations of Dong *et al.* (2006) for single heaving/pitching wings and hints that, for finite-aspect ratio

tandem wings, the practical relevance of the wake deflection phenomenon might be limited. Finally, it has been found that the aerodynamic performance of the tandem wings is deteriorated when a realistic, three-dimensional flapping motion is considered.

Acknowledgements

This work was supported by grant DPI2016-76151-C2-2-R (AEI/FEDER, UE). The computations were partially performed at the supercomputer Tirant from the *Red Española de Supercomputación* in activity FI-2018-2-0025. We thank Dr. J. Ortega-Casanova for fruitful discussions.

References

Alexander, D. 1984 Unusual phase relationships between the forewings and hindwings in flying dragonflies. *J. Exp. Biol.* **109** (1), 379–383.

Arranz, G., Gonzalo, A., Uhlmann, M., Flores, O. & García-Villalba, M. 2018*a* A numerical study of the flow around a model winged seed in auto-rotation. *Flow Turbul. Combust.* **101** (2), 477–497.

Arranz, G., Moriche, M., Uhlmann, M., Flores, O. & García-Villalba, M. 2018*b* Kinematics and dynamics of the auto-rotation of a model winged seed. *Bioinspir. Biomim.* **13**, 036011.

Boschitsch, B., Dewey, P. & Smits, A. 2014 Propulsive performance of unsteady tandem hydrofoils in an in-line configuration. *Phys. Fluids* **26** (5), 051901.

Broering, T. & Lian, Y. 2015 Numerical study of tandem flapping wing aerodynamics in both two and three dimensions. *Comput. Fluids* **115**, 124–139.

Buchholz, J. & Smits, A. 2008 The wake structure and thrust performance of a rigid low-aspect-ratio pitching panel. *J. Fluid Mech.* **603**, 331–365.

Buchholz, J. & Smits, A. J. 2006 On the evolution of the wake structure produced by a low-aspect-ratio pitching panel. *J. Fluid Mech.* **546**, 433–443.

Das, A., Shukla, R. & Govardhan, R. 2016 Existence of a sharp transition in the peak propulsive efficiency of a low-*Re* pitching foil. *J. Fluid Mech.* **800**, 307–326.

Dong, H., Mittal, R. & Najjar, F. M. 2006 Wake topology and hydrodynamic performance of low-aspect-ratio flapping foils. *J. Fluid Mech.* **566**, 309–343.

Gonzalo, A., Arranz, G., Moriche, M., García-Villalba, M. & Flores, O. 2018 From flapping to heaving: A numerical study of wings in forward flight. *J. Fluids Struct.* **83**, 293–309.

Green, M., Rowley, C. & Smits, A. 2011 The unsteady three-dimensional wake produced by a trapezoidal pitching panel. *J. Fluid Mech.* **685**, 117–145.

Huera-Huarte, F. 2018 Propulsive performance of a pair of pitching foils in staggered configurations. *J. Fluids Struct.* **81**, 1–13.

Hunt, J. C. R., Wray, A. A. & Moin, P. 1988 Eddies, stream, and convergence zones in turbulent flows. *Center For Turbulence Research* **Report CTR-S88**.

Kamisawa, Y. & Isogai, K. 2008 Optimum flapping wing motions of dragonfly. *Trans. Japan Soc. Aero. Space Sci.* **51** (172), 114–123.

Kurt, M. & Moored, K. 2018 Flow interactions of two- and three-dimensional networked bio-inspired control elements in an in-line arrangement. *Bioinspir. Biomim.* **13** (4), 045002.

Lee, J., Kim, J., H., Choi & Yang, K. 2011 Sources of spurious force oscillations from

an immersed boundary method for moving-body problems. *J. Comput. Phys.* **230** (7), 2677–2695.

Lehmann, F. 2007 When wings touch wakes: understanding locomotor force control by wake wing interference in insect wings. *J. Exp. Biol.* **211** (2), 224–233.

Lewin, G. C. & Haj-Hariri, H. 2003 Modelling thrust generation of a two-dimensional heaving airfoil in a viscous flow. *J. Fluid Mech.* **492**, 339–362.

Lua, K., Lu, H., Zhang, X., Lim, T. & Yeo, K. 2016 Aerodynamics of two-dimensional flapping wings in tandem configuration. *Phys. Fluids* **28** (12).

Maybury, W. & Lehmann, F. 2004 The fluid dynamics of flight control by kinematic phase lag variation between two robotic insect wings. *J. Exp. Biol.* **207** (26), 4707–4726.

Moriche, M., Flores, O. & García-Villalba, M. 2016 Three-dimensional instabilities in the wake of a flapping wing at low Reynolds number. *Int. J. Heat Fluid Flow* **62A**, 44–55.

Moriche, M., Flores, O. & García-Villalba, M. 2017 On the aerodynamic forces on heaving and pitching airfoils at low Reynolds number. *J. Fluid Mech.* **828**, 395–423.

Moriche, M., Gonzalo, A., Flores, O. & García-Villalba, M. 2019 Fast transverse maneuvers at low Reynolds numbers. AIAA 2019-0640.

Moriche, M., Raiola, M., Discetti, S., Ianiro, A., Flores, O. & García-Villalba, M. 2020 Assessing aerodynamic force estimation with experiments and simulations of flapping-airfoil flows on the verge of three-dimensionality. *Proc. Inst. Mech. Eng. G J. Aerospace Eng.* **234** (2), 428–444.

Muscutt, L., Weymouth, G. & Ganapathisubramani, B. 2017 Performance augmentation mechanism of in-line tandem flapping foils. *J. Fluid Mech.* **827**, 484–505.

Nagai, H., Fujita, K. & Murozono, M. 2019 Experimental study on forewing–hindwing phasing in hovering and forward flapping flight. *AIAA J.* **57** (9), 3779–3790.

Norberg, R. 1975 *Hovering Flight of the Dragonfly Aeschna Juncea L., Kinematics and Aerodynamics*, pp. 763–781. Springer US.

Ortega-Casanova, J. & Fernandez-Feria, R. 2016 Analysis of the aerodynamic interaction between two plunging plates in tandem at low Reynolds number for maximum propulsive efficiency. *J. Fluids Struct.* **63**, 351–373.

Ortega-Casanova, J. & Fernández-Feria, R. 2019 Maximum propulsive efficiency of two pitching and plunging plates in tandem at low Reynolds number: A numerical analysis. *Int. J. Numer. Method. Heat Fluid Flow* **29**, 4013–4033.

Rival, D., D., Schönweitz & Tropea, C. 2011 Vortex interaction of tandem pitching and plunging plates: a two-dimensional model of hovering dragonfly-like flight. *Bioinspir. Biomim.* **6** (1), 016008.

Sun, M. & Lan, S. 2004 A computational study of the aerodynamic forces and power requirements of dragonfly (Aeschna juncea) hovering. *J. Exp. Biol.* **207** (11), 1887–1901.

Thomas, A., Taylor, G., Srygley, R., Nudds, R. & Bomphrey, R. 2004 Dragonfly flight: free-flight and tethered flow visualizations reveal a diverse array of unsteady lift-generating mechanisms, controlled primarily via angle of attack. *J. Exp. Biol.* **207** (24), 4299–4323.

Uhlmann, M. 2005 An immersed boundary method with direct forcing for the simulation of particulate flows. *J. Comput. Phys.* **209** (2), 448–476.

Usherwood, J. & Lehmann, F. 2008 Phasing of dragonfly wings can improve aerodynamic efficiency by removing swirl. *J. R. Soc. Interface* **5** (28), 1303–1307.

Wakeling, J. & Ellington, C. 1997 Dragonfly flight. II. Velocities, accelerations and kinematics of flapping flight. *J. Exp. Biol.* **200** (3), 557–582.

Wang, J. K. & Sun, M. 2005 A computational study of the aerodynamics and forewing-hindwing interaction of a model dragonfly in forward flight. *J. Exp. Biol.* **208** (19), 3785–3804.

Wang, Z. & Russell, D. 2007 Effect of forewing and hindwing interactions on aerodynamic forces and power in hovering dragonfly flight. *Phys. Rev. Lett.* **99**, 148101.

Zheng, Y., Wu, Y. & Tang, H. 2016 An experimental study on the forewing–hindwing interactions in hovering and forward flights. *Int. J. Heat Fluid Flow* **59**, 62–73.

Zhu, X., He, G. & Zhang, X. 2014 Flow-mediated interactions between two self-propelled flapping filaments in tandem configuration. *Phys. Rev. Lett.* **113**, 238105.

Paper 5

5

Flow interaction of three-dimensional self-propelled flexible plates in tandem

G. Arranz[1], **O. Flores**[1], **M. García-Villalba**[1]

[1] Universidad Carlos III de Madrid, Spain

Journal of Fluid Mechanics (Under review) (2021)

Tandem configurations of two self-propelled flexible flappers of finite span are explored by means of numerical simulations. A sinusoidal vertical motion of the leading edge of both flappers with the same frequency and amplitude, but different phase, ϕ, is prescribed. In addition, a vertical offset, H, between the flappers is imposed. The configurations that emerge in the parametric space $H - \phi$ are characterized in terms of their hydrodynamic performance and topology. After an initial transient, the flappers reach a stable configuration with a constant mean propulsive speed and a mean equilibrium horizontal distance. Depending on the values of H and ϕ, two different tandem configurations are observed, namely *compact* and *regular* configurations. The performance of the upstream flapper (i.e., the leader) is virtually equal to the performance of an isolated flapper, except in the *compact* configurations, where the close interaction with the downstream flapper (i.e., the follower) results in higher power requirements and propulsive speed than the isolated flapper. On the contrary, the performance of the follower is significantly affected by the wake of the leader in both *regular* and *compact* configurations. The analysis of the flow shows that the performance of the follower is influenced by the interaction with the vertical jet induced by the vortex rings shed by the leader. This interaction can be beneficial or detrimental for the follower's performance, depending on the alignment of the jet velocity with the vertical motion of the follower. Finally, a qualitative prediction of the performance of a hypothetical follower is presented. The proposed model is semi-empirical, and it uses the flow field of the wake of an isolated flapper, exploiting the small effect of the follower on the leader's wake.

Key words: swimming/flying, flow-structure interaction, numerial simulation

1. Introduction

Nature provides a host of examples of interacting bodies through a fluid with surprising behaviours. These range from a single, passive body like an auto-rotating maple seed (Lentink *et al.* 2009), to a large number of synchronised, active bodies which interact with the surrounding fluid, like fish schooling or bird flocks (Weihs 1973; Mora *et al.* 2016). The latter is particularly interesting since, due to the presence of more than one body, each individual has to interact with an ambient fluid which is disturbed by the surrounding individuals. These interactions can be exploited by the individual

to extract energy from the fluid and move in a more efficient manner than if it were in isolation. Although the main reason why animals form schools or flocks may not be entirely clear yet, it is well known that animals benefit from collective motion in terms of flow interaction (Weimerskirch *et al.* 2001; Becker *et al.* 2015).

This beneficial interaction is not restricted to a large number of bodies, but it is also observed into its minimal expression for two body configurations. For example, Liao *et al.* (2003) observed that a trout behind the wake of a cylinder adapted its body kinematics to extract energy from the vortices of the cylinder's wake. They attributed this phenomenon to a beneficial interaction with the oncoming vortices, which they denoted as Kármán gait. Even more stunning are the results from Beal *et al.* (2006), who observed that a dead fish can overcome its own drag in the wake of a cylinder provided its resonant frequency matches that of the von Kármán vortex sheet. It can be argued that the beneficial flow interaction in the previous examples is merely due to the lower average streamwise velocity of the von Kármán vortex sheet wake. However, several studies have shown that swimmers are less efficient isolated (i.e., in a clean free-stream) than when swimming in reverse von Kármán streets, like those produced by thrust-producing, oscillating foils in a free-stream (Platzer *et al.* 2008) or self-propelling oscillating bodies (Alben & Shelley 2005). In particular, Boschitsch *et al.* (2014); Muscutt *et al.* (2017) and Kurt & Moored (2018) found that, for an *inline* tandem configuration of two oscillating foils, the distance and phase shift between the motion of the foils can always be adjusted such that the follower foil interacts with the on-coming vortices extracting energy from the flow; thus, confirming the Kármán gait hypothesis proposed in Liao *et al.* (2003) and Streitlien *et al.* (1996).

However, in the aforementioned examples the bodies were immersed in a free-stream with their horizontal position held fixed. Consequently, the configuration of the collective motion is not determined by the fluid interaction. On the contrary, when the bodies self-propel, the configuration cannot be imposed but is the one that results from the equilibrium of the hydrodynamic forces due to flow mediated interactions. Ramananarivo *et al.* (2016) and Newbolt *et al.* (2019) experimentally studied the case two airfoils in *inline* tandem configuration which self propelled due to an imposed heaving motion with a varying phase shift. They found that, for a given phase shift, stable configurations emerged at quantized equilibrium distances; and that this distance was linearly proportional to the phase shift. However, no measurement of the efficiency were provided, leaving open-ended the question of whether tandem configurations of self-propelled bodies can benefit from flow interactions. In this regard, numerical simulations have proven to be very useful, since they can provide quantitative data of the flow field, but also of the forces and moments acting on the bodies. Lin *et al.* (2019*b*) numerically simulated two self-propelling 2D foils undergoing a heaving and pitching motion, finding that the follower always benefits from the flow interaction, whereas the lead foil can benefit only if both foils are close. Similar studies are found in the literature where the bodies are modelled as flexible foils and self-propulsion is achieved thanks to a passive flexion of the body (Zhu *et al.* 2014; Peng *et al.* 2018*a*; Ryu *et al.* 2020), or where the deflection of the body is fully prescribed (Maertens *et al.* 2017). In all these cases, similar qualitative conclusions are extracted from these

works, suggesting that the same main flow mechanism interaction is present in all these examples of self-propelled collective locomotion.

Additional studies have focused on the effect of the size of the bodies (Peng *et al.* 2018*b*); or the stable schooling configurations with multiple individuals (Peng *et al.* 2018*c*; Park & Sung 2018; Dai *et al.* 2018; Lin *et al.* 2020). However, very few works are found in the literature which consider a three dimensional flow, being all the previous examples restricted to 2D configurations. For example, Daghooghi & Borazjani (2015) numerically investigated the performance of an "infinite" school of mackerels with a rectangular pattern; and Li *et al.* (2019) analysed the energetics benefit of a two fish school configuration where the kinematics of both fish where that of self-propulsion, but their relative distance where fixed. However –to our knowledge– the only 3D study where the bodies self-propel and their dynamics are determined from the fluid structure interaction is that of Verma *et al.* (2018), who used reinforcement learning to find the efficient optimal schooling configuration for a system of 2 and 3 self-propelled fish-like bodies.

This lack of 3D studies may be explained by the computational cost. However, it is known that the wake pattern of a self-propelled body significantly differs from 2D to 3D (Gazzola *et al.* 2011): from a reverse von Kármán vortex street in 2D to a diverging wake of vortex rings in 3D. This could lead to significant differences of 3D stable positions of the collective and on their associated performance when compared to its 2D counterparts. First of all, the stable *quantized positions* observed by Ramananarivo *et al.* (2016); Newbolt *et al.* (2019) on a von Kármán vortex street may not longer emerge on a 3D bifurcating wake. Secondly, on a 2D vortex street the only dissipation mechanism is viscosity; however, three-dimensional mechanisms can lead to vortex breakdown at much shorter distances. Hence, different vortical interactions might be expected from 2D to 3D which could alter the performance of the bodies. In summary, it is not clear if the main conclusions of tandem self-propelled bodies obtained from 2D studies are applicable to a 3D scenario.

In the present study, we analyse the problem of two self-propelled finite aspect ratio plates in tandem configuration. The main focus of the study is to identify which are the equilibrium positions and their associated performance, as well as to highlight the similarities/differences with the 2D configurations found in the literature. Particularly, the plates have chordwise flexibility (similarly to Yeh & Alexeev (2014); Quinn *et al.* (2014, 2015); Hoover *et al.* (2018)) and self propel due to an imposed heaving motion of their leading edge.

The paper is structured as follows: section 2 describes the problem and the numerical methodology; in section 3 the main results are discussed; and, finally the main conclusions of the study are gathered in section 4.

2. Methodology

2.1. *Problem description*

Two self-propelling plates in tandem configuration immersed in an otherwise undisturbed fluid are considered. The plates have a rectangular planform of chord C and span b; thickness, e; uniform density, ρ_s; and they are flexible along the chordwise direction. Under the tandem arrangements considered, one of the flappers *swims*

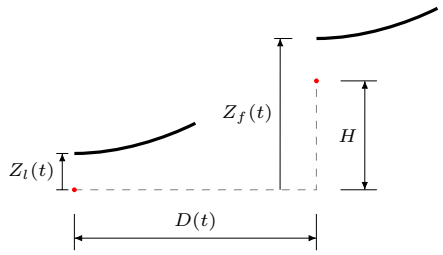

FIGURE 1: Side view of the schooling configuration. Each flapper has a prescribed heaving motion about a fixed vertical pivoting position (represented as a red dot in the figure). The vertical offset between the follower's and leader's pivoting position is denoted as H. $D(t)$ is the instantaneous horizontal distance between the flappers' leading edge.

downstream of the other. We denote the flapper swimming downstream as follower, and the upstream flapper as leader. Hence, variables related to the follower and leader are indicated hereafter with the subindexes f and l, respectively.

The vertical motion of the leading edge of the flappers is prescribed as sinusoidal functions, namely

$$Z_l(t) = A_l \cos(2\pi f t), \qquad Z_f(t) = H + A_f \cos(2\pi f t - \phi), \tag{1}$$

where A_i is the heaving amplitude of the i flapper, f is the frequency of oscillation, ϕ is the phase offset, and H is the mean vertical offset between the flappers. These magnitudes are sketched in figure 1, alongside the instantaneous horizontal distance, $D(t) = X_f(t) - X_l(t)$, where X_i is the horizontal position of the leading edge of the i flapper.

The flappers share the same fixed plane of symmetry along the spanwise (y) direction (i.e., they are aligned), and their leading edge is always parallel to the y-axis. Likewise, note that while the vertical motion of the leading edge of the flappers is prescribed, its horizontal motion results from the fluid structure interaction.

The fluid surrounding the flappers is governed by the Navier-Stokes equations of the incompressible flow for a Newtonian fluid, namely,

$$\nabla \cdot \mathbf{u} = 0, \tag{2a}$$

$$\frac{\partial \mathbf{u}}{\partial t} + (\mathbf{u} \cdot \nabla)\,\mathbf{u} = -\frac{1}{\rho}\nabla p + \nu \nabla^2 \mathbf{u}, \tag{2b}$$

where $\mathbf{u}$ is the flow velocity, p is the fluid pressure, ρ is the fluid density, and ν is the fluid kinematic viscosity.

One of the objectives of the present study is to find stable equilibrium positions of the flappers in the $H - \phi$ plane. The rest of parameters that define the problem are kept fixed, namely: the aspect ratio of the flappers, b/C, and their non-dimensional thickness, e/C; the heaving amplitude is set equal for both flappers, $A_l \equiv A_f = A$; the Reynolds number, $Re = VC/\nu$, where $V = 2\pi A f$ is the maximum vertical velocity of the leading edge of the flappers; the density ratio, $\varrho = \rho_s/\rho$; and the non-dimensional

Heaving offset, H	$[0, 0.3, 0.6]C$
Phase offset, ϕ	$[0° - 360°]$
Flappers' span, b	$0.5C$
Flappers' thickness, e	$0.02C$
Heaving amplitude, A	$0.5C$
Reynolds number, Re	200
Density ratio, ϱ	10
Natural frequency, ω^*	2.17

TABLE 1: Parameters of the problem under study.

natural frequency, $\omega^* = \omega_n/(2\pi f)$, where ω_n is the first natural frequency of the flapper's elastic response in vacuum. The value of these parameters is presented in Table 1.

To select the elastic properties of the flapper (i.e., its natural frequency), two different simulations of self-propelled isolated flappers with finite aspect ratio (i.e., 3D simulations) were performed with $\omega^* = 2.17$ and 4.59, choosing for the present study the case yielding maximum propulsive speed. The range for values of ω^* used in the prospective 3D simulations was selected after performing a finer parametric study of the equivalent 2D problem, similar to that presented in Arora *et al.* (2018).

2.2. *Computational set-up*

To simulate the flexibility of a flapper the lumped-torsional flexibility model of Arora *et al.* (2018) is used. Under this approach, a flapper is discretized into N_B rigid bodies linked to each other by means of torsional springs. The stiffness of these torsional springs is computed to match ω^*. A sketch of the multi-body model of a flapper is provided in Figure 2. For a given flapper, its rigid bodies are labelled as $j = 1, \ldots, N_B$. Each body is a rectangular prism of span b, length c and thickness e, separated a distance $d = e/2$ from the torsional spring that connects it to the consecutive body. Consequently, the relative attitude of body j with respect to its predecessor, $j - 1$ is given by the angle θ_j (see Figure 2b).

Under the previous model, each flapper has $2 + N_B$ degrees of freedom (*dof*s), namely: horizontal (X) and vertical (Z) translation of the leading edge, and N_B relative rotations of the bodies. Therefore, it is possible to express the equations that govern the dynamics of the flappers in the general form (Featherstone 2014):

$$\mathsf{H}(\mathbf{q})\ddot{\mathbf{q}} = \boldsymbol{\xi} - \mathsf{c}(\mathbf{q}, \dot{\mathbf{q}}) + \boldsymbol{\xi}_h, \tag{3}$$

where $\mathbf{q}$ is the vector of generalized coordinates (i.e., the *dof*s of the system), H is the generalized inertia matrix, c is the generalized bias force vector, $\boldsymbol{\xi}$ is the vector of the generalized forces (accounting for the torsional springs), and $\boldsymbol{\xi}_h$ is the vector of the generalized forces due to the flow. Although in eq. (3) only the dependence on $\mathbf{q}$ and $(\mathbf{q}, \dot{\mathbf{q}})$ is made explicit for H and c, respectively, they both implicitly depend on the geometric and inertia properties of the flappers.

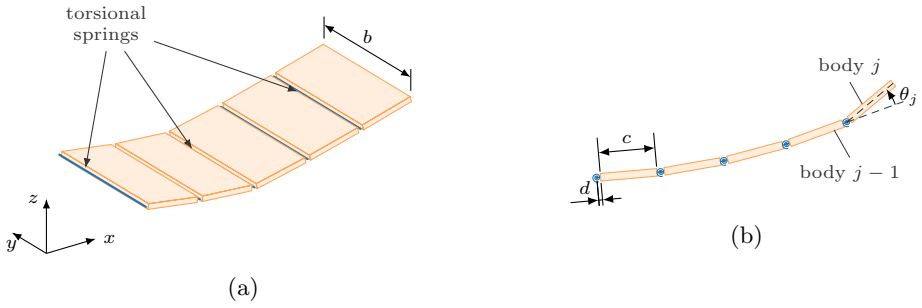

FIGURE 2: (a) 3D representation of the multi-body model of a flapper. (b) Side view ($x-z$ plane) of the multi-body model. Blue spirals are the torsional springs, and θ_j is the relative deflection angle of body j with respect to body $j-1$, similarly to Arora *et al.* (2018).

The vector of generalized coordinates is defined as $\mathbf{q} = [\mathbf{q}_u, \mathbf{q}_p]^\top$, where $\mathbf{q}_u = [X_l, \theta_{l,1}, ..., \theta_{l,N_B}, X_f, \theta_{f,1}, ..., \theta_{f,N_B}]^\top$ is the vector of unknown generalized positions, and $\mathbf{q}_p = [Z_l, Z_f]^\top$ is the vector which contains the prescribed generalized positions, given by eq. (1). Likewise, $\boldsymbol{\xi} = [\boldsymbol{\xi}_u, \boldsymbol{\xi}_p]$, where $\boldsymbol{\xi}_u = -K[0, \theta_{l,1}, ..., \theta_{l,N_B}, 0, \theta_{f,1}, ..., \theta_{f,N_B}]^\top$, and $\boldsymbol{\xi}_p = [F_{p,l}, F_{p,f}]^\top$ contains the unknown reaction vertical forces acting on the leading edge. In the present implementation, a reduced system of eq. (3) is solved to compute $\mathbf{q}_u$, $\dot{\mathbf{q}}_u$, and $\ddot{\mathbf{q}}_u$, as detailed in Arranz *et al.* (2021). After that, one can solve for the reactive forces acting on the leading edge. For the present study, $N_B = 5$, based on the work of Arora *et al.* (2018).

Equations (2) and (3) are solved together using an in-house code, TUCANMB (Arranz *et al.* 2021). In particular, the flow is solved by means of direct numerical simulations (DNS), where the presence of the body in the fluid is modelled using the immersed boundary method (IBM) proposed by Uhlmann (2005). On the other hand, H and c of eq. (3) are computed using the robotic algorithm presented in Felis (2017). The coupling between the fluid and the dynamic equations along time is done in an staggered way, usually referred to as *weak coupling*. Interested readers can find more details about the algorithm in Arranz *et al.* (2021).

The computational fluid domain is a rectangular prism of size $16C \times 6C \times 8C$ along the streamwise, spanwise and vertical directions, respectively. Note that, the same computational fluid domain was used in Yeh & Alexeev (2014) for similar simulations of an isolated 3D self-propelled flexible plate. The flappers are located inside a refined region with uniform grid size, Δr, extended from $[-0.5C, 0.5C]$ along the y-axis, $[-C, C + H]$ along the z-axis, and $[-6.5C, L_x]$ (where L_x ranged from $-2C$ to $4C$, depending on $\overline{D}$) along the x-axis. Note that, previous distances are given with respect to the cuboid centroid. Moreover, for cases with $H = 0.6C$ the total domain is also enlarged $0.6C$ in the positive z direction. Outside this uniformly refined region, the mesh has a constant stretching of 0.8% in all directions.

The grid size, Δr, is determined after performing a grid sensitivity analysis, leading to the conclusion that $\Delta r = C/50$ accurately captures the dynamics of the problem, whereas with $\Delta r = C/80$ the flow details and temporal evolution of the forces are accurately represented. Likewise, the time step is selected to be $\Delta tf = 5 \cdot 10^{-4}$ and $4 \cdot 10^{-4}$, for $\Delta r = C/50$ and $C/80$, respectively, ensuring $CFL = U_{\max}\Delta t/\Delta r < 0.2$ (where $U_{\max}$ is the maximum flow velocity in the domain). Interested readers can find more details of the grid sensitivity analysis in appendix Appendix A.

A constant horizontal velocity, U_∞, is imposed at the inflow boundary; an advective boundary condition is imposed at the outflow boundary; and free-slip boundary conditions are imposed at the lateral boundaries. With the present set-up, the flappers could reach the inflow or outflow boundaries if their mean advance velocity (denoted as *propulsive speed*, $\overline{U}_p$ in the following sections) is higher or lower than U_∞, respectively. Therefore, the inflow velocity must be set equal to $U_\infty \equiv \overline{U}_p$ so that the flappers remain in the refined region of the computational domain. Since $\overline{U}_p$ is unknown *a priori*, simulations are started with an initial guess of U_∞, denoted as U_i^0, which is updated every kth time step, by means of the relaxation equation:

$$U_i^k = (1-\beta)U_i^{k-1} + \beta \dot{X}_l^{k-1}, \tag{4}$$

where β is a small parameter set to Δtf, and superscripts indicate the time step where the variable is evaluated. After a transient, the horizontal position of the flappers oscillates around a fixed value, as well as U_i. It turns out that the average value of U_i over a complete oscillation, is a good estimate of the mean propulsive velocity. Therefore, U_∞ is set to this average value, and the simulation is continued with this constant inflow velocity. Only the results of this last phase of the simulations are reported in this manuscript, after discarding the initial transient.

2.3. *Performance indicators*

After an initial transient, the flappers self arrange into an stable configuration, with a constant mean separation distance, $\overline{D}$, and mean propulsive speed, $\overline{U}_p$, over a cycle. These magnitudes are computed as:

$$\overline{D} = \frac{1}{T}\int_{T_*-1}^{T_*} D(t)\,dt, \qquad \overline{U}_p = U_\infty - \frac{1}{T}\int_{T_*-1}^{T_*} \dot{X}_l\,dt, \tag{5}$$

where $T = 1/f$ is the flapping period, and T_* is the last computed full cycle of the simulation.

The performance of a self-propelled flapper is computed in terms of its average power consumption over a flapping cycle, namely:

$$\overline{P}_i = \frac{1}{T}\int_{T_*-1}^{T_*} \max\left(P_i, 0\right)dt, \tag{6}$$

where $P_i = F_{p,i} \cdot \dot{Z}_i$, being $F_{p,i}$ is the vertical component of the reaction force acting on the leading edge of the i flapper. Neglecting negative power contribution in (6) entails that elastic storage of power is not considered. This approach is similar to the one adopted in Berman & Wang (2007); Vejdani *et al.* (2018). In the following discussion the performance of a given flapper in tandem configuration will be assessed in terms of the comparison with the same flapper in isolation. To that purpose the

power ratio of the i flapper is defined as $\Pi_i = \overline{P}_i/\overline{P}_s$, where $\overline{P}_s$ is the averaged power of the isolated flapper.

As an additional measure of performance, the propulsive efficiency η is defined as the ratio between the total useful kinetic energy and the total power consumption,

$$\eta = \frac{m\overline{U}_p^2}{\overline{P}_l + \overline{P}_f}, \tag{7}$$

where m is the mass of each flapper. The equivalent propulsive efficiency that the tandem system would have if no interaction between flappers occurred is also defined,

$$\eta_s = \frac{m\overline{U}_{p,s}^2}{2\overline{P}_s}. \tag{8}$$

3. Results

3.1. *Emergent patterns and overall dynamics*

For reference, the case of the isolated flapper is presented first. The flapper self-propels at a mean speed, $\overline{U}_{p,s} = 0.88V$, shedding a vortex ring during each stroke. The vortex rings move away from the flapper with an oblique trajectory due to their own induced velocity, leading to a bifurcating wake (Kurt *et al.* 2020). These vortices are visible in figure 3a, which shows a visualization of the flow around the isolated flapper at mid-downstroke. The deflection of the flapper during a cycle is depicted in Figure 3b. Note that, the upstroke and the downstroke deflection patterns are symmetric. At the beginning of a stroke, the flapper is almost horizontal, whereas the largest deflection occurs at mid-stroke. Consequently, there is a phase offset of $\sim \pi/2$ between the heaving motion and the deflection. Such a phase offset is characteristic of flexible heaving foils when aerodynamic effects are more important than inertia effects (Arora *et al.* 2018), and is commonly associated to high propulsive efficiency both for passive flexion (Heathcote & Gursul 2007; Zhang *et al.* 2010) and prescribed pitching kinematics (Moriche *et al.* 2017).

Figure 4 depicts the streamwise, $\langle u \rangle$, and vertical, $\langle w \rangle$, velocities of the fluid averaged over a cycle and along the flapper's span $y/C = [-0.25, 0.25]$. Note that, for the averaging, a Galilean reference frame moving at a constant horizontal speed, $\overline{U}_{p,s}$, was used. The averaged wake left by the vortex rings results in a bifurcating momentum jet. Note that this wake pattern is not restricted to flexible, 3D self-propelling flappers, but is is general to oscillating bodies, like rigid wings, immersed in a free-stream within the typical range of Strouhal for propulsion, namely, $0.15 \leq St \leq 0.5$ (Taylor *et al.* 2003). In particular, the diverging wake pattern made of shed vortex ring is the common trace of low aspect ratio oscillating wings (Dong *et al.* 2006; Buchholz & Smits 2008). This wake pattern clearly differs from the reverse Von-Kármán wake observed in 2D self-propelled plates (Alben & Shelley 2005; Hua *et al.* 2013).

We now turn our attention to the emergent dynamics found in the tandem simulations. A total of 24 tandem configurations were simulated. They are characterized by the follower's vertical offset, H, the phase shift, ϕ, and the equilibrium distance, $\overline{D}$. Under the initial separation distances considered (i.e., $D_0/C = [1.5 - 3]$), a single $\overline{D}$ was found for each ϕ, except for $\phi = 0°$, where two equilibrium distances co-existed

(a) (b)

FIGURE 3: (a) Flow visualization around the isolated, self-propelled, flapper at mid-downstroke. Flow is visualized in terms of iso-surfaces of the Q-criterion for $Q/f^2 = 0.1$. (b) Bending pattern of the flapper's chordline during the downstroke (solid) and upstroke (dashed). Dotted line corresponds to the trajectory of the leading edge.

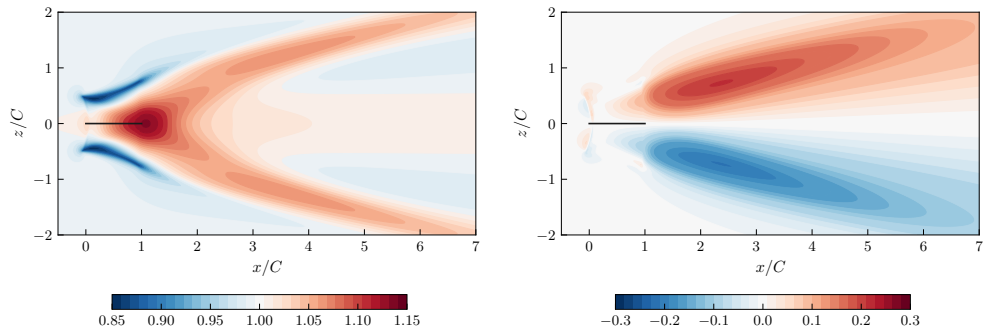

(a) $\langle u \rangle / \overline{U}_{p,s}$ (b) $\langle w \rangle / \overline{U}_{p,s}$

FIGURE 4: Velocity field of the isolated self-propelled flapper, averaged over 2 cycles and over $y/C = [-0.25, 0.25]$. (a) Horizontal component of the velocity, and (b) vertical component of the velocity. Black line correspond to the mean position of the flapper.

depending on D_0. In order to differentiate them, we assign $\phi = 0°$ to those configurations for which $\overline{D}/C \approx 1$, whereas $\phi = 360°$ is used for the tandem configurations where $\overline{D}/C \approx 3$.

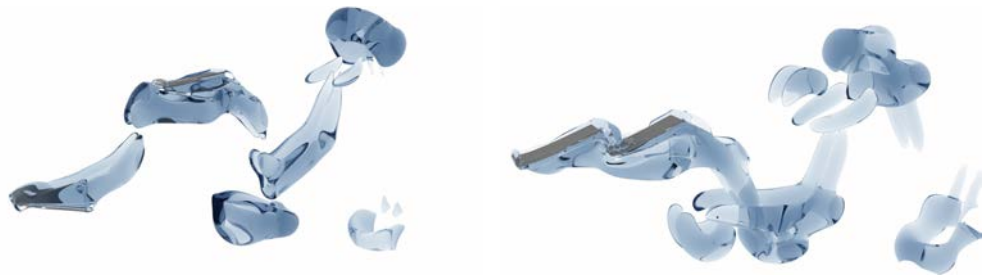

(a) (b)

FIGURE 5: Flow visualization around the flappers in tandem formation. Flow is visualized in terms of iso-surfaces of the Q-criterion for $Q/f^2 = 0.5$. (a) $H = 0.6C$, $\phi = 180°$ and (b) $H = 0$, $\phi = 0°$.

For illustration, figure 5 displays flow visualizations of two of the cases. Figure 5a displays the flow corresponding to the case $H = 0.6C$ and $\phi = 180°$, leading to $\overline{D}/C = 2.2$ (i.e., the horizontal gap between the trailing edge of the leader and the leading edge of the follower is approximately equal to C). It can be appreciated that the flow surrounding the leader is virtually unaffected by the follower, whereas the follower is *swimming* across the leader's wake vortices. Downstream of the follower, the wakes of the flappers interact yielding a different wake structure than for the isolated flapper. Figure 5b depicts the case $H = 0$ and $\phi = 0°$. In this case, the equilibrium distance is $\overline{D}/C = 1.01$ (i.e., the trailing edge of the leader and the leading edge of the follower are almost touching). Due to the proximity between the flappers, there is no clear distinction between the wakes of each plate. Instead, they appear to be merged. These two cases can be understood as the 3D counterparts of the *regular* and *compact* configurations reported by Zhu *et al.* (2014) for 2D tandem plates.

The performance of all the simulated configurations is summarized in figure 6. The data is presented in the form of ratios relating metrics of the performance in the tandem configuration to the corresponding metric of the isolated flapper, and using dashed lines to link configurations with the same phase shift, ϕ. Figures 6a and 6b display the input power required by the leader and the follower, respectively, as compared to that required by the isolated flapper. For configurations where $\overline{D}/C \geq 1.25$, the energy expenditure of the leader is virtually equal to that of the isolated flapper; whereas for the *compact* configurations (i.e., $\phi = 0°$ and $H \leq 0.3C$), a slightly higher mean power is required by the leader as compared to that in isolation. Contrary to that, for $H = 0.6C$ and $\phi = 0°$, the follower's and leader's leading edges are almost aligned, with $\overline{D} = 0.2C$, and the required power is equal for both flappers and slightly less than for the isolated flapper. The particularity of this *aligned* mode will be briefly discussed at the end of this subsection, § 3.1.

Nevertheless, the effect of the tandem configuration on the leader's power requirement is almost negligible, even for the *compact* configurations, as compared to the effect on the follower: figure 6a shows that the power requirements for the leader vary

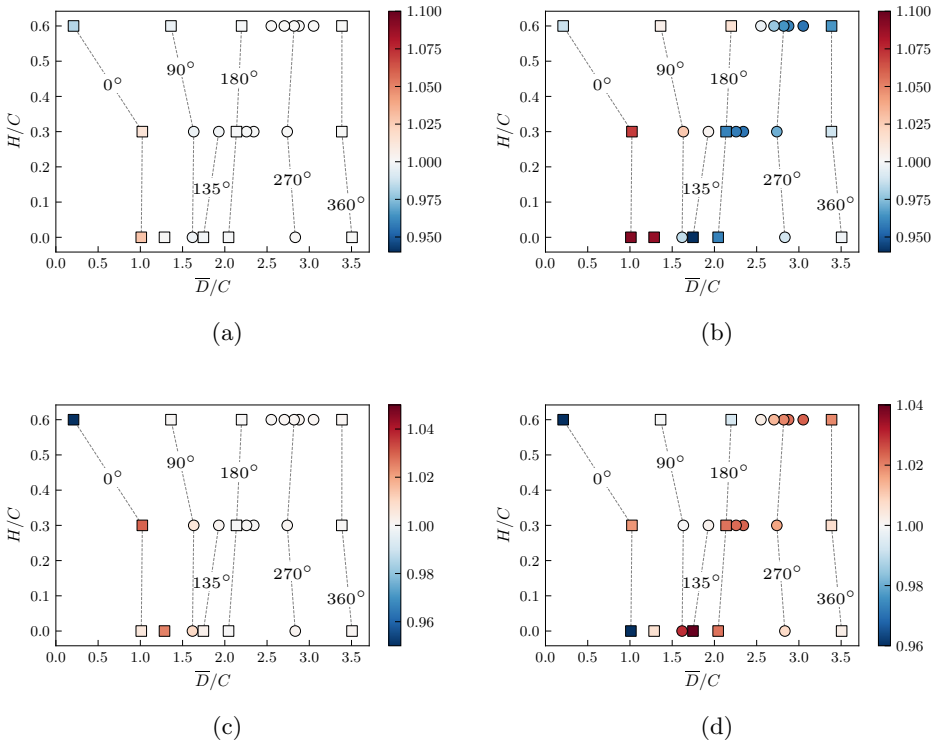

FIGURE 6: (a) Input power ratio of the leader (Π_l), (b) input power ratio of the follower (Π_f), and (c) propulsive speed ratio ($\overline{U}_p/\overline{U}_{p,s}$) for all the configurations explored. (d) Ratio of propulsive efficiency, η/η_s. The symbols stand for the resolution of the simulation: (▫) $\Delta x = C/80$; (○) $\Delta x = C/50$.

within ±1% of the value obtained for the isolated flapper, while figure 6b shows that the power requirement for the follower vary up to ±10%, depending on H and ϕ. In particular, depending on H there exists a ϕ below which the follower is able to take advantage from the fluid interaction such that their required energy is lower than that in isolation. From the performed simulations, it is found that this transition occurs roughly at $\phi > 30°$, 135° and 180° for $H = 0$, $0.3C$ and $0.6C$, respectively. On the other hand, the power spent by the follower in the *compact* configurations, considerably exceeds that of the isolated flapper (up to 10%).

The propulsive speed of the *regular* configurations (shown in figure 6c) is equal to that of the isolated flapper, consistently with previous 2D simulations (Zhu *et al.* 2014; Lin *et al.* 2019*b*; Ryu *et al.* 2020). For *compact* configurations (and $H = 0$, $\phi = 30°$), the propulsive speed is found to be up to 3% higher than $\overline{U}_{p,s}$. While the result is consistent with 2D simulations in the *compact* range and for $H = 0$, the increment in propulsive velocity of the 3D cases is more modest: Lin *et al.* (2019*b*) report propulsive

velocities up to 50% higher than in isolation for heaving and pitching rigid 2D-foils in *compact* configurations at $Re = 200$. Likewise, Ryu *et al.* (2020) find an increase of 40% in $\overline{U}_p$ for flexible plates at $Re = 100$, whereas Peng *et al.* (2018*a*) report a more modest increase of 10%, for flexible plates at $Re = 200$ in *compact* configurations. According to Lin *et al.* (2019*b*), the higher propulsive speed of the tandem airfoils in the *compact* configurations occurs because the foils behave as a single larger foil. Consequently, the problem might be equivalent to that of a plate with twice Re, thus a larger $\overline{U}_p$ would be expected (Park & Sung 2018; Lin *et al.* 2019*a*). However, in 3D, the two flappers would behave as a single flapper with twice the chord, but half the aspect ratio, $\mathit{AR} = b/C$. Since $\overline{U}_{p,s}$ decreases for decreasing AR (Yeh & Alexeev 2016), it might be the case that both the Re and AR counteracting effects lead to the small change observed for the present configurations.

As reported by Peng *et al.* (2018*a*), the significant increase of $\overline{U}_p$ in 2D *compact* configurations is enough to counteract the higher required power, leading to a higher overall efficiency of the *compact* configurations compared to isolated configurations (i.e., $\eta/\eta_s > 1$). However, in 3D, the results strongly depend on H and ϕ, as shown in figure 6d. For *regular* configurations higher η/η_s are obtained for cases where the follower extracts energy from the flow (i.e., $\Pi_f < 1$), as expected.

The aforementioned transition from *compact* to *aligned* for the cases with $\phi = 0°$ when H varies is also observed in 2D. In particular, Peng *et al.* (2018*a*) found that, for 2D flexible plates, when $\phi = 0°$ the stable position of the follower is $\overline{D}/C \approx 1$ below a certain H. However, for $H/C \geq 0.6$, both plates becomes aligned ($\overline{D}/C = 0$). In these cases, the required average power of each plate is equal and lower than that of the isolated plate, meanwhile $\overline{U}_p$ significantly decreases, leading to a loss of efficiency. In this regard, the same behaviour is observed in the present study for the *aligned* mode. Nonetheless, the dynamics differ between 2D and 3D. In 2D, the performance of both plates is symmetric with respect to each stroke and there is no leader or follower. On the contrary, in 3D the forces of the leader are nearly identical to that of the isolated case, whereas the follower is affected by the interaction of its trailing edge with the vortices shed by the leader. Finally, it is worth noting that the trends of the power ratios obtained by Peng *et al.* (2018*a*) (denoted herein as $\Pi_{i,2D}$) in the 2D *compact* configurations (namely, $H/C < 0.6$) are the opposite than the ones reported here in 3D. In both 2D and 3D, the flappers require more energy in the tandem configuration than if isolated (i.e., $\Pi_{l,2D}$, $\Pi_{f,2D} > 1$), entailing that the interaction is detrimental for both flappers. However, while Peng *et al.* (2018*a*) reports that this interaction is more detrimental for the leader (namely, $\Pi_{l,2D} > \Pi_{f,2D}$), our present 3D results shows the opposite trend (namely, $\Pi_l < \Pi_f$) as seen in figures 6a and 6b.

3.2. *Flow interaction mechanisms*

From the previous section it is clear that the follower is more affected by the collective behaviour than the leader, even for *compact* configurations. In order to understand the dependence of Π_f on H and ϕ, the temporal evolution of P_f is depicted in figure 7 for a few representative cases. In figure 7a the evolution for cases with constant $H/C = 0$ and different phase offset is shown, whereas figure 7b shows P_f for a constant offset, $\phi = 180°$ and different H. Note that, to allow a comparison with the isolated flapper

(grey dashed line in figures 7a and 7b), we define the variable $\hat{t} = t - \phi/(2\pi f)$ to shift the time reference of the follower so that its downstroke is synchronized with that of the isolated flapper. Qualitatively the required power behaves as a squared sine function over a cycle, being $P \approx 0$ at the beginning of the downstroke and upstroke, and maximum at mid-stroke. For $H = 0$ and $\phi = 0°$, the power ratio $\Pi_f > 1$ observed in figure 6b is due to an increase of the maximum required power at mid-stroke, as shown in figure 7a. However, for the optimum case, $H = 0$ and $\phi = 135°$, the power reduction is not due to a lower maximum required power at mid-stroke, but to a decrease of P_f after each mid-stroke. This can be better appreciated in figure 7c, which displays the difference $(P_f - P_s)$. In all cases, the follower spends more energy during the first half of the stroke than the isolated flapper. However, for the optimal case, this is largely counteracted during the second half of the stroke, yielding a total reduction of the required energy. Overall, it is observed that the difference $(P_f - P_s)$ monotonically decreases with increasing $\overline{D}$ (i.e., increasing ϕ) during the first half of a stroke. However, the power difference $(P_f - P_s)$ during the second half of a stroke does not follow the same behaviour: it decreases when ϕ varies from 0° to 135°, but it increases again when ϕ varies from 135° to 360°. As a consequence, for ϕ greater than the optimal one, Π_f increases towards 1, as illustrated by case $\phi = 360°$ in figure 7c.

Figure 7b allows to analyse the effect of H on the transition from $\Pi_f < 1$ to $\Pi_f > 1$ for a fixed ϕ. Note that $\overline{D}/C$ is similar for the cases displayed, as shown in figure 6. In figure 7b it is observed that for $H/C > 0$, P_f is not equal during the downstroke and the upstroke. In particular, the peak of the required power is higher during the downstroke and increases with H, whereas the peak during the upstroke remains approximately constant and equal to that of P_s. The larger power consumption during the donwstroke is not compensated during the upstroke for $H/C = 0.6$, as shown in figure 7d; whereas the lower peak for $H/C = 0.3$ during its downstroke, and a larger power reduction during the upstroke, allows this follower to outperform the isolated flapper

To summarize, the results from figures 7c and 7d suggest that, irrespective of the final power ratio, the follower always requires more power than the isolated flapper during the first half of the stroke, and less during part of the second half of the stroke. This is true for all the cases presented in this paper. The instantaneous power required by the follower, P_f, depends on the hydrodynamic forces and on the inertia and elasticity of the flapper. However, due to the choice of parameters of the present simulations (table 1), the influence of the hydrodynamic forces is dominant, and it should be possible to explain the behaviour of P_f in terms of the flow interactions. Moreover, since the inertia/elastic properties of the flapper and its prescribed kinematics are the same for both the follower and the isolated flapper, the difference $(P_f - P_s)$ must be ascribed to interactions of the follower with the leader's wake. Thus, we now proceed to analyse the flow surrounding the follower at different time instants.

Figure 8 depicts the pressure field and the velocity field near the follower at the beginning of the downstroke ($\hat{t}/T \approx 0.1$) for cases $H = 0$, and $\phi = 135°$ and $\phi = 0°$. For reference the case of the isolated flapper is also shown in the top part of the figure. Note that for the time instants considered $\dot{Z}_f < 0$, and the instantaneous

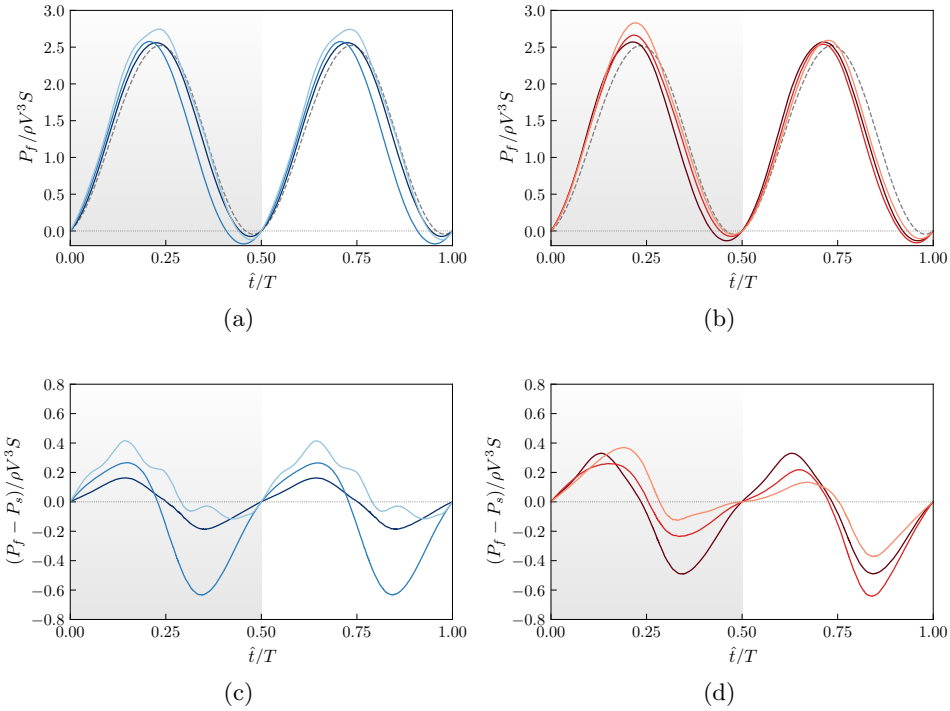

FIGURE 7: (a-b) Temporal evolution of the required power during a cycle, and (c-d) temporal evolution of the difference of the input power of the leader/follower and the isolated flapper. (a,c) $H = 0$ and (——) $\phi = 0°$; (——) $\phi = 135°$; and (——) $\phi = 360°$. (b,d) $\phi = 180°$ and (——) $H = 0$; (——) $H = 0.3C$; and (——) $H = 0.6C$. In (a-b), (- - -) corresponds to the power of the isolated flapper. Note that the time is shifted in each case so that 0 corresponds to the beginning of the downstroke for each flapper. For reference, the downstroke is indicated with a grey background.

required power of the follower exceeds that of the isolated flapper for both cases. The follower is interacting with the vortex ring (VR) shed during the leader's upstroke and, consequently, the VR circulation induces an upwards velocity jet. Due to the phase offset, the VR is located above the follower when $\phi = 135°$ (middle row) and below the follower for $\phi = 0°$ (bottom row). However, in both cases, the VR is *convecting* fluid against the flapper motion. This results in a flow pattern with a saddle point on the suction (pressure) side of the follower for $\phi = 135°$ ($\phi = 0°$). Note that this saddle point does not occur in the case of the isolated flapper (top row of figure 8).

Figure 9 displays the flow after the mid-downstroke ($\hat{t}/T \approx 0.3$), when the follower requires less power than the isolated flapper for $\phi = 135°$, but requires higher power for $\phi = 0°$. The middle row of figure 9 ($\phi = 135°$) shows that the VR shed during the leader's upstroke has travelled downstream meanwhile the VR shed during its

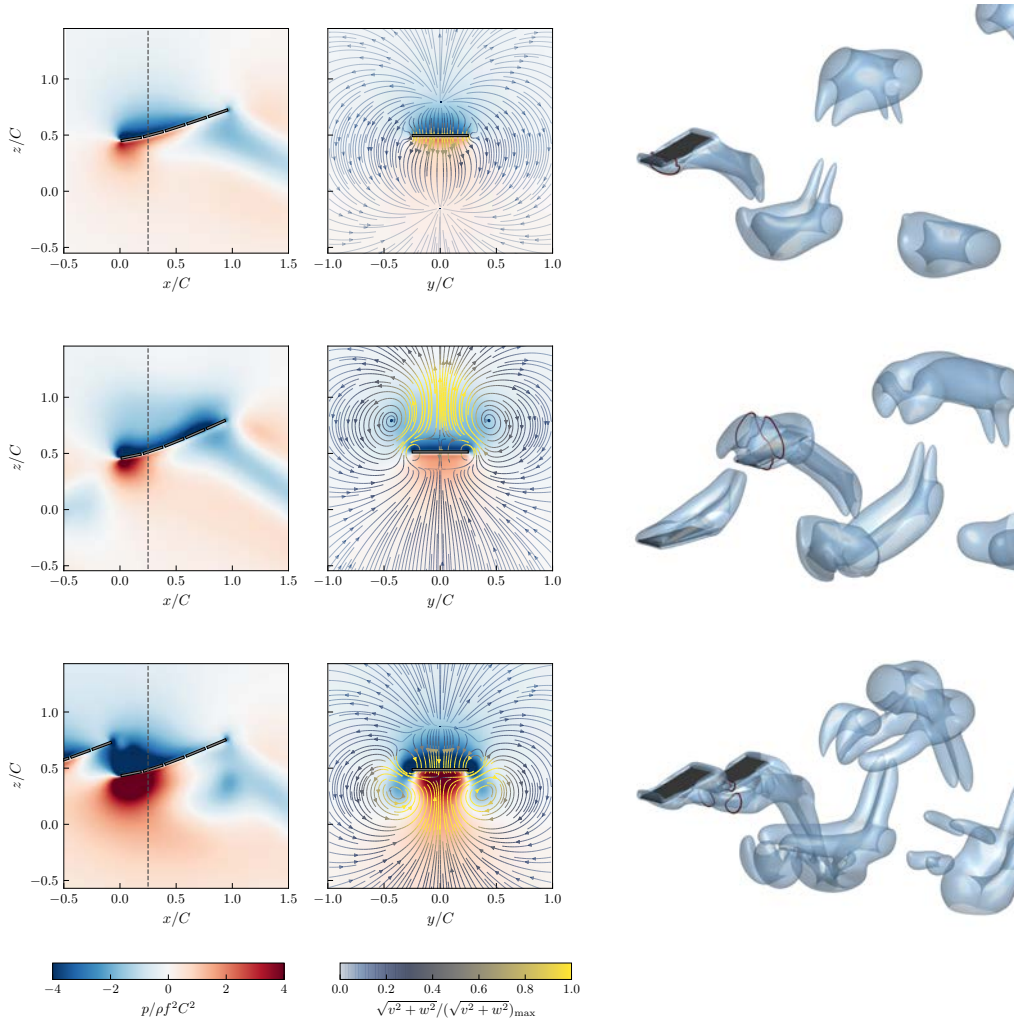

FIGURE 8: Flow visualization of different cases at a similar time instant $\hat{t}/T \approx 0.1$. From top to bottom: isolated flapper; tandem case with $H = 0$, $\phi = 135°$; and tandem case with $H = 0$, $\phi = 0°$. Left column corresponds to the pressure field at $y = 0$ plane around the isolated flapper for the top panel, and around the follower for the remaining panels. The dashed line indicates the plane shown in the center column panels. Center column displays the pressure in the $x = X_f + 0.25C$ plane. Superimposed to the pressure, the instantaneous streamlines of the *in-plane* velocity are displayed. The streamlines are coloured with the local velocity magnitude. Right column displays iso-surfaces of the Q-criterion for $Q/f^2 = 0.5$. Red lines stands for the intersection of the iso-surfaces with the $x = X_f + 0.25$ plane.

downstroke (with opposite circulation) starts interacting with the follower. Since both the follower's wing tip vortices and the VR have the same circulation, they seem to merge near the LE, and no saddle point is observed. This yields a downwards, high-velocity jet, which decreases the pressure on the follower's lower surface, thus explaining the lower P_f required with respect to P_s observed in figure 7c. This interaction is in agreement with the recently published work of Li *et al.* (2020), who reported that a following fish in tandem saved energy when its tail motion matches the direction of the induced velocity of the wake's VRs.

On the contrary, the bottom row of figure 9 ($\phi = 0°$) shows that the VR shed during leader's downstroke is still above the follower. Consequently, the VR is still inducing an upwards jet, whose overall result is a lower pressure on the upper surface. This leads to an increase of required power as compared to the isolated flapper. Note that, the saddle point is still present. Although not shown, for $\hat{t}/T \geq 0.36$, the VR is no longer affecting the flow above the follower's surface, and it starts interacting with the next VR, leading to a flow configuration similar to that of $\phi = 135°$. However, this beneficial interaction occurs during a shorter period of time, leading to an overall lower performance. Due to symmetry, an analogous behaviour is observed during the follower's upstroke.

Note also that, although only two cases have been presented here for the sake of brevity, the same qualitative behaviour is observed for the other cases. For $H > 0$, due to the lack of symmetry, the distance between the follower and the VR's during the upstroke and the downstroke is not the same, modulating the intensity of the interaction. But the nature of the interaction of the follower with the VR in the wake of the leader remains qualitatively the same.

Based on the results of figures 8 and 9, it is tempting to seek an estimate of the performance of the follower in the analysis of the wake of an isolated flapper. The key assumption is that the wake structure between the leader and the follower is governed by the flapping motion of the leader, with a weak effect of the follower. Therefore, the performance of the latter might be estimated superimposing its trajectory on the wake of an isolated flapper (Zhu *et al.* 2014; Peng *et al.* 2018*b*). This is done in figure 10, which displays the vertical velocity (w) in the wake of the isolated flapper at a vertical line with coordinates $y = 0$ and $x(t) = X_s(t) + D(t)$ (i.e., at the midspan of the leading edge of an hypothetical follower). Thus, the figure provides an estimation of the vertical velocity of the fluid just upstream of the leading edge of an hypothetical follower. Each panel in figure 10 corresponds to a different equilibrium position of the hypothetical follower, specified in terms of the values of H and ϕ. The corresponding trajectory of the hypothetical follower is also shown in each panel, with a black solid line. Note that the follower travels from right to left in the figure, implying that the rightmost position ($t = 0$) corresponds to the beginning of the follower's downstroke.

The first row of figure 10 (panels a to c) shows the same cases presented in figures 7a and 7c. Figure 10a shows that, for the case with $H = 0$ and $\phi = 0$, during roughly the first half of each stroke, the hypothetical follower encounters flow that opposes its motion: positive w during the first half of the downstroke, negative w during the first half of the upstroke). However, for cases $\phi = 135°$ and $\phi = 360°$ (figure 10b and c, respectively) the sign of w coincides better with the direction of

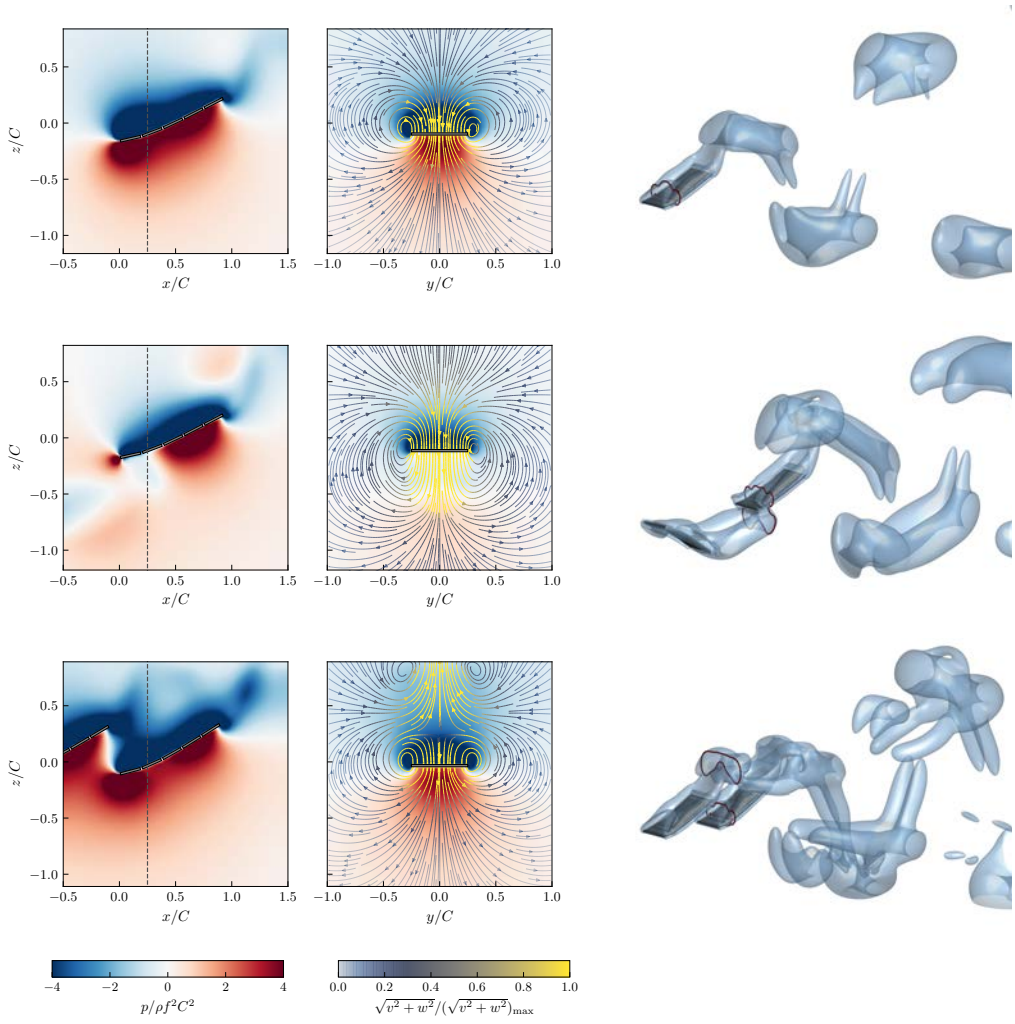

FIGURE 9: Flow visualization of various cases at a similar time instant $\hat{t}/T \approx 0.3$. From top to bottom: isolated flapper; tandem case with $H = 0$, $\phi = 135°$; and tandem case with $H = 0$, $\phi = 0°$. Caption as in figure 8.

the stroke of the follower. The difference between these two cases is the intensity of the vertical velocity fluctuations at the LE of the follower, larger for the case with $\phi = 135°$, which might explain its larger energy savings (as discussed in figure 7c).

The left and central panels of the second row of figure 10 (panels d and e) display the configurations analyzed in figure 7b and 7d, with $\phi = 180°$ and $H/C = 0.3$ and 0.6, respectively. Since $H > 0$, the flow encountered by the hypothetical follower during the downstroke and upstroke is no longer symmetric. The fraction of the stroke when the

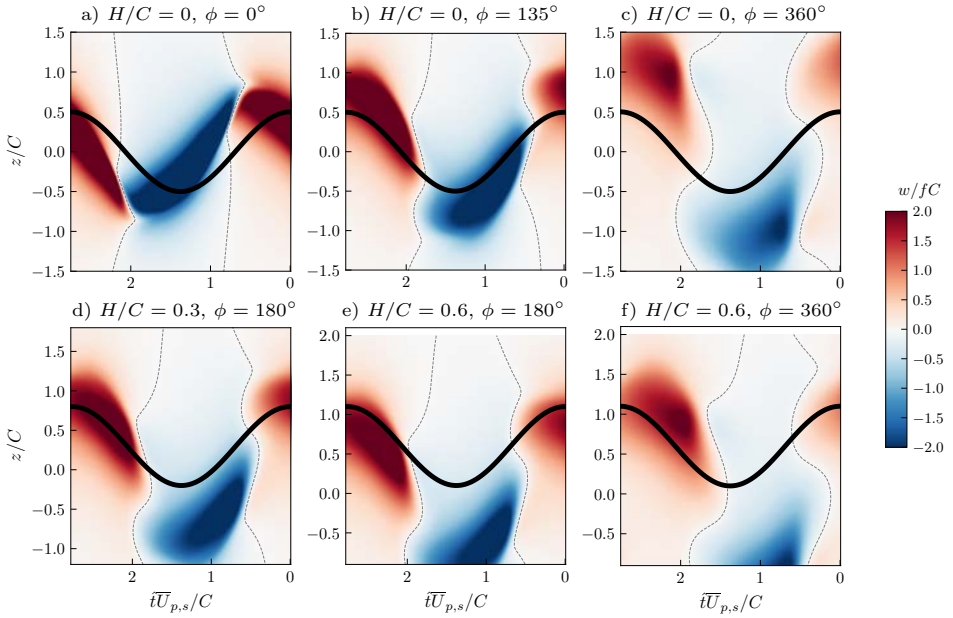

FIGURE 10: Vertical velocity field at $y = 0$ seen by the leading edge of the follower's flapper as if it where in the undisturbed wake of the isolated flapper. Black line denotes the vertical position of the follower's leading edge as a function of time, where $\hat{t} = 0$ is the beginning of the follower's downstroke. Dashed black lines are the contours for $w = 0$.

sign of the velocity of flapper and wake coincide is larger for the case $H/C = 0.3$ than for the case with $H/C = 0.6$, specially during the upstroke (note that the transition from positive to negative vertical velocity is indicated with dashed contour lines in figure 10). Additionally, whenever the sign of the velocities coincide, the value of w at the LE of the follower is higher for $H/C = 0.3$ than for $H/C = 0.6$. Both observations are in line with the behaviour of the required power in figure 7d, with larger power savings with respect to the isolated flapper in case $H/C = 0.3$ than in case $H/C = 0.6$.

Finally, panel figure 10f depicts the case $H = 0.6C$ and $\phi = 360°$. A comparison of panels e) and f) shows that, by increasing $\overline{D}$, the hypothetical follower is now swimming through a region where the flow velocity is better aligned with the LE's vertical motion. Thus, a larger value of the power ratio Π_f is expected for the case with $\phi = 360°$ than for the case with $\phi = 180°$, a result that is confirmed in the actual simulation (see results in figure 6b).

For reference, figure 11 shows the pressure fluctuation field seen by the hypothetical follower, obtained in the same fashion as the vertical velocity field in figure 10. These pressure fluctuation fields are analogous to those reported by other authors for 2D flows (Zhu *et al.* 2014; Peng *et al.* 2018*b*), and can be used to estimate the relative position

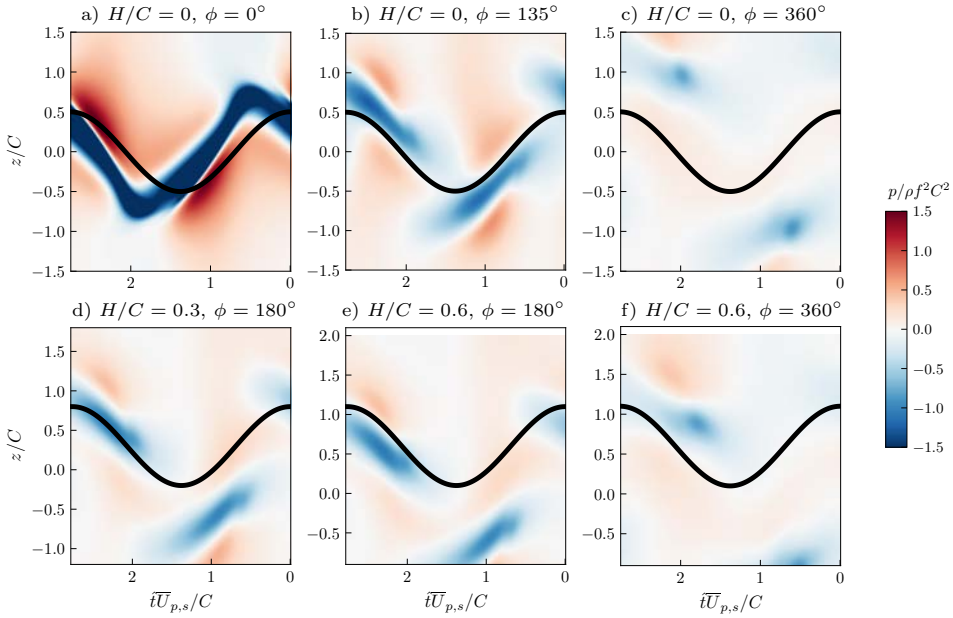

FIGURE 11: Caption as figure 10 but for the pressure field.

of the vortex ring (i.e., a low pressure region, in blue in the figure) with respect to the trajectory of the hypothetical follower (black line). However, this representation is not ideal since it does not show the direction of the jet induced by the vortex ring, which is important in determining if a vortical interaction is beneficial or not, as discussed in figures 8 and 9. Overall, figure 11 seems to suggest that the tandem configurations where the follower outperforms the isolated flapper correspond to cases where the vortex rings pass above the LE during its downstroke. As discussed in this section, this an oversimplification since not only the position, but also the sign of the circulation of the vortex ring matters.

3.3. *Modelling the follower's performance*

The results discussed in the previous sections have shown that the nature of the interaction of the follower with the leader's wake is qualitatively the same for all cases, including the *compact* configurations. Our results support the existing literature on the topic, confirming that the differences in the performance of the follower are linked to the different timing of the interaction of the follower with the vortex rings shed by the leader, which determines if the interaction is beneficial (in terms of power requirements) or not. In this section, a more quantitative analysis of the results is presented.

Figure 12a shows Π_f as a function of $\overline{D}$, for three values of H. Although the data presented in this figure was already reported in figure 6b, this alternative representation

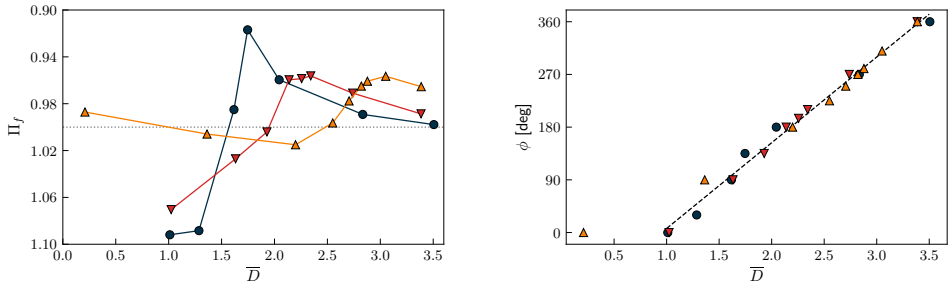

(a) (b)

FIGURE 12: (a) Input power ratio of the follower, Π_f, as a function of $\overline{D}$. Note that the vertical axis is reversed, such that maximums corresponds to cases where the follower outperforms the isolated flapper. (b) Relationship between ϕ and $\overline{D}$ for all cases. Symbols stand for the vertical offset: (●) $H/C = 0$; (▼) $H/C = 0.3$; and (▲) $H/C = 0.6$. In (b), dashed black line is the linear regression.

highlights other features of the present study. First of all, it is clear that for each H there exist a $\overline{D}$ (and consequently also a corresponding phase shift ϕ) for which the follower is able to extract the most energy from the flow interaction, as indicated by the corresponding peaks in figure 12a. This distance increases with H, due to the diverging pattern of the leader's wake. The optimum values are $\Pi_f = 0.917$, 0.960 and 0.957 for $H/C = 0$, 0.3 and 0.6, respectively. It is clear that the global optimum is obtained for $H = 0$ because the positive flow interaction occurs both during the upstroke and the downstroke. Also, it is clearly appreciated in figure 12a that Π_f is most sensitive to ϕ when the vertical offset is $H = 0$, with broader peaks for $H/C = 0.3$ and 0.6.

It is also noticeable (at least for $H/C = 0$ and 0.3) that Π_f tends to 1 relatively quickly as $\overline{D}$ increases, especially when compared to similar studies in 2D, (Park & Sung 2018; Lin *et al.* 2019*b*, 2020; Ryu *et al.* 2020). This is due to the diverging pattern of the wake in 3D: In the previous section, figure 11c shows that the follower of case $H = 0$, $\phi = 360°$ ($\overline{D}/C \approx 3.5$) is not directly interacting with the VRs, since the VRs are passing the follower too far away. In a 2D configuration with a reversed Von-Kármán vortex street, in which the vortices are advected in the streamwise direction with no wake bifurcation, a very similar interaction would be obtained for $\phi = 0°$ and for $\phi = 360°$.

Figure 12b shows $\overline{D}$ versus ϕ for the different vertical offsets. Although figure 6 revealed that $\overline{D}$ depended on both ϕ and H, it is clear from figure 12b that its main dependence is on ϕ. Particularly, $\overline{D}$ shows a linear dependency on ϕ for all cases except for the *aligned* mode case (i.e., the data point in the lower left corner of the figure). This trend is also observed for 2D schooling configurations (Newbolt *et al.* 2019; Lin *et al.* 2019*b*; Ryu *et al.* 2020), and can be linked to the wavelength of the

leader's wake, λ_l, as postulated in Portugal *et al.* (2014). This wavelength is defined as $\lambda_l \equiv fU_\lambda$, where f is the frequency of the flapping motion and U_λ is the horizontal advective velocity of the leader's wake. Indeed, Newbolt *et al.* (2019) propose

$$\phi = 2\pi S + \phi_0, \tag{9}$$

where ϕ_0 is an unknown constant and S is the schooling number (Ramananarivo *et al.* 2016), defined as the ratio of the horizontal distance between the leader's trailing edge and the follower's leading edge and λ_l. That is $S \equiv (\overline{D} - C)/\lambda_l$, which yields

$$\phi = 2\pi \left(\frac{\overline{D}}{C} - 1 \right) \frac{C}{fU_\lambda} + \phi_0. \tag{10}$$

A linear regression on the data shown in figure 12b, excluding the *aligned* mode case, yields $\phi_0 = 0.12$ and $U_\lambda = 0.78V = 0.89\overline{U}_{p,s}$. Note that, $\phi_0 \approx 0$ entails that, for $\phi = 0$, the equilibrium distance is $\overline{D}/C = 1$ (i.e., $S = 0$). This is of course consistent with the present results, and also with the literature: Ramananarivo *et al.* (2016); Peng *et al.* (2018*a*); Lin *et al.* (2019*b*); Newbolt *et al.* (2019), all of them find $S \approx 0$ for $\phi = 0$. On the other hand, these authors report $U_\lambda \approx \overline{U}_p$ for 2D configurations, somewhat larger than the value obtained here for 3D configurations. The origin of this discrepancy is unclear, but one possible source could be the different flow topology of the 2D and 3D wakes. Indeed, similar discrepancies for U_λ have been reported between 2D and 3D configurations with imposed gap distances and fixed free-stream velocities: $U_\lambda \approx 1.2U_\infty$ for 2D (Boschitsch *et al.* 2014), larger than $U_\lambda \approx 1.02U_\infty$ in 3D (Kurt & Moored 2018).

In § 3.2 we observed a relation between the vertical induced velocity of the VR and the required power of the follower. Motivated by figure 10, we hypothesise that the effect of the VR can be estimated from the averaged vertical velocity seen by the leading edge of a hypothetical follower swimming in the wake of an isolated flapper. This quantity is defined as

$$w_{LE,f}(t) = \int_{-b/2}^{b/2} w(X_f(t), y, Z_f(t); t) dy. \tag{11}$$

The discussion in section 3.2 suggests that higher power is required when the induced flow velocity is opposed to the direction of the follower's LE ($\dot{Z}_f$), and vice-versa. Thus, to estimate the goodness of a given configuration we define

$$\langle w_{LE,f} \dot{Z}_f \rangle = \frac{1}{T} \int_0^T w_{LE,f}(t) \dot{Z}_f(t) dt, \tag{12}$$

expecting large values of $\langle w_{LE,f} \dot{Z}_f \rangle$ to be linked to high performance cases (i.e., $\Pi_f < 1$), and low or negative values to be associated to low performing cases ($\Pi_f > 1$). Indeed, figure 13 displays $\langle w_{LE,f} \dot{Z}_f \rangle$ versus Π_f for all cases, showing a good correlation between these two variables (i.e., a linear regression yields $R^2 = 0.95$). Note that, in the plot $\langle w_{LE,f} \dot{Z}_f \rangle$ is normalized with the integral over a cycle of $\dot{Z}_f^2$, namely, $2\pi f^2 A^2$.

The correlation between $\langle w_{LE,f} \dot{Z}_f \rangle$ and Π_f indicates a route to the estimation of the performance of any given tandem configuration, by using $\langle w_{LE,f} \dot{Z}_f \rangle$ as a surrogate model of Π_f. Note that, the computation of $\langle w_{LE,f} \dot{Z}_f \rangle$ only requires the flow field of

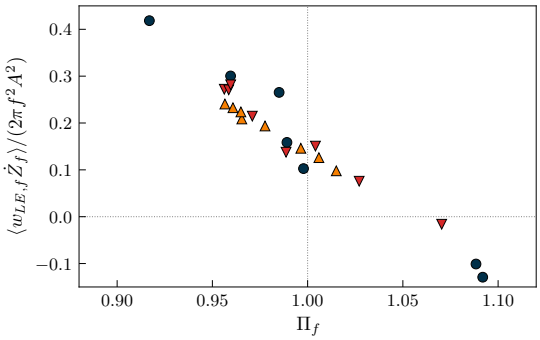

FIGURE 13: Follower's power ratio, Π_f, as a function of $\langle w_{LE,f}\dot{Z}_f\rangle$ for all cases. (●) $H/C = 0$; (▼) $H/C = 0.3$; and (▲) $H/C = 0.6$.

the isolated case and the position of the hypothetical follower's LE, $\boldsymbol{x}_f = (X_f, Z_f)$. In order to compute $\boldsymbol{x}_f$, we assume $X_f(t) \approx X_s(t) + \overline{D}$, which requires that the velocity of the leader is approximately equal to that of the isolated flapper (see figure 6c) and that $D(t) \approx \overline{D}$. The latter assumption is reasonable for the present cases, with $|D(t) - \overline{D}| \lesssim 0.17C$ for all cases reported here. Using these estimations, together with equations 10 and 1, the position of the hypothetical follower's LE can be expressed as

$$\boldsymbol{x}_f(t, H, \phi) = \left(X_s(t) + \frac{fU_\lambda}{2\pi}(\phi - \phi_0) + C, Z_f(t, H, \phi) \right), \tag{13}$$

where the dependence of Z_f on H, ϕ and t has been made explicit.

Figure 14a displays a map of $\langle w_{LE,f}\dot{Z}_f\rangle$ for hypothetical followers, as a function of the mean separation $\overline{D}$ and the height H. This map is computed using $U_\lambda = 0.78V$ and $\phi_0 = 0.12$ in equation 13 (i.e., with the values calculated from the linear regression in figure 12b), and shows good agreement between $\langle w_{LE,f}\dot{Z}_f\rangle$ and the values of Π_f obtained from the actual simulations. The map of $\langle w_{LE,f}\dot{Z}_f\rangle$ predicts a range of good performing hypothetical followers along a diagonal band, with a maximum occurring for $H = 0$. For configurations below this diagonal band, $\langle w_{LE,f}\dot{Z}_f\rangle$ decreases slowly, consistent with the slow drift of $\Pi_f \to 1$ as H decreases from the optimal value. Recall that this decrease in performance is associated to the loss of the beneficial interactions with the VR, and hence the performance of the follower tends monotonically to the performance of the isolated flapper. On the contrary, configurations above the optimal diagonal band show a sharp decrease of $\langle w_{LE,f}\dot{Z}_f\rangle$, consistent with the sudden degradation of the follower's performance as the interactions with the VR become damaging ($\Pi_f > 1$). Likewise, the map of $\langle w_{LE,f}\dot{Z}_f\rangle$ also predicts the sharp transition in performance for $H = 0$ previously discussed in figure 12a, when $\overline{D}/C$ decreases from the optimum value (i.e., $\overline{D}/C \approx 1.6$) to $\overline{D}/C \approx 1$.

It is interesting to note that the map of $\langle w_{LE,f}\dot{Z}_f\rangle$ predicts good performance for cases with $\overline{D}/C \approx 1$ and $H/C \approx [0.4, 0.6]$. Note however that figure 14a provides no information about the stability of a given configuration (i.e., a duplet $\overline{D} - H$). That

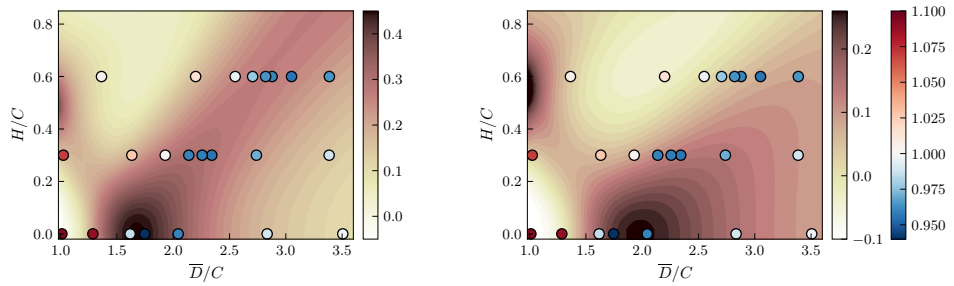

FIGURE 14: Contour of $\langle w_{LE,f}\dot{Z}_f\rangle/(2\pi f^2A^2)$ for a follower's LE trajectory computed with eq. (13). Values of $\boldsymbol{x}_f$ are computed assuming (a) $U_\lambda = 0.78V$, $\phi_0 = -0.12$, and (b) $U_\lambda = \overline{U}_{p,s}$, $\phi_0 = 0$. The simulated cases are superimposed, coloured with Π_f, as in figure 6b.

is, there is no warranty that equilibrium, self-propelled, tandem configurations can be obtained for the whole phase space $\overline{D}$-H plotted in figure 14a. Hence, it could be the case that configurations around this region are not stable, but develop into an *aligned* mode configuration (i.e., with $\overline{D} \to 0$).

Even though the previous model yields good predictive results, the values obtained not only depend on data of the isolated flapper. In addition a large number of tandem simulations has been required to estimate the values of U_λ and ϕ_0, via the linear regression in figure 12b. Therefore, it is interesting to explore what predictions can be made by using only data of the isolated flapper simulation. This can be done by assuming in eq. (13) the values of $U_\lambda = \overline{U}_{p,s}$, and $\phi_0 = 0$, which are reasonable estimations according to the literature (Newbolt *et al.* 2019; Peng *et al.* 2018*a*; Lin *et al.* 2019*b*). The results of this alternative model are presented in figure 14b. The agreement with the actual data of the tandem simulations is reduced, but nevertheless, the main features of the configuration space are satisfactorily predicted, at least in a qualitative way. Namely, the maximum performance follows a diagonal line with a clear maximum at $H = 0$; configurations above this line have a lower performance; and there exists a sharp transition at $H = 0$ from the optimum case to bad performing configurations as $\overline{D}/C \to 1$ (i.e., $\phi \to 0$). Finally, this model also predicts the good performance region for $\overline{D}/C = 1$ and $H/C \approx 0.6$ discussed in the previous paragraph.

4. Conclusions

In this work, the tandem configurations of two self-propelled flexible plates of finite span are explored by means of numerical simulations. The flappers self-propel due to an imposed vertical motion of their leading edges. We explore the stable tandem configurations that emerge in the parametric space of phase shift between the motion of each leading edge ($\phi \in [0° - 360°]$) and vertical offset between the mean vertical

position of the flappers ($H/C \in [0 - 0.6]$). For all the cases, the flappers self-propel at a mean constant speed and a mean equilibrium distance between the leader and the follower.

Two main patterns are found: *compact* and *regular* configurations, in agreement with similar two dimensional configurations (Zhu *et al.* 2014). In *compact* configurations the equilibrium is such that the leading edge of the follower and the trailing edge of the leader are almost touching. The propulsive speed of the *compact* configurations is slightly higher than that of the isolated flapper, but at the expense of a higher required power, both for the leader and the follower. On the other hand, *regular* configurations are characterized by larger equilibrium distances, propelling at the same speed as the isolated flapper. In this mode, the leader is virtually unaffected by the follower, such that it performs as an isolated flapper; on the contrary, the follower is affected by the leader's wake and its performance depends both on H and ϕ. For some values of these parameters the follower's required power is reduced compared to the isolated flapper. In summary, a 3% increase of the propulsive speed is found in *compact* configurations as compared to the case of the isolated flapper; and a maximum reduction of $\approx 10\%$ on the required power of the follower for the *regular* configurations. These gains are more modest than those found in 2D (Park & Sung 2018; Peng *et al.* 2018*a*; Lin *et al.* 2019*b*; Ryu *et al.* 2020), a fact that can be attributed to the different flow topology between the 2D and 3D wakes. This reduced energy harvesting from 2D to 3D is also reported in Verma *et al.* (2018).

To understand the effect of ϕ and H on the performance of the follower, the instantaneous required power of the latter is compared to that of the isolated flapper. It is found that, irrespective of the overall performance, the follower requires more power than the isolated flapper during the first half of each stroke. Good performing cases outperform the isolated flapper during the second half, thus counteracting the previous excess of required power, and leading to a lower averaged required power for the follower than for the isolated case.

These changes in the temporal evolution of the power are linked to the flow interaction of the follower with vortex rings (VR) in the leader's wake. The analysis of the flow field at different time instants reveals that the follower saves energy when it is moving (vertically) in the same direction of the jet induced by the VR interacting with the follower (i.e., beneficial interactions). Conversely, detrimental interactions are found when the jet induced by the VR points in the opposite direction to the motion of the follower, yielding larger energy requirements than in the isolated case. For the cases where the VR is too far away from the follower, the power requirements of the latter tend to those of the isolated flapper (i.e., no interactions).

A predictive model of the performance (in terms of required power) of the follower is presented based on the flow field of the isolated flapper. Two versions of the model are explored, one which makes use of data extracted from the tandem simulations and another which only relies on the data from the isolated flapper simulation. Although the first version of the model shows better agreement with the actual data from the simulations (as expected), the second version is still able to capture the main characteristics of the $\phi - H$ phase space, at least from a qualitative point of view.

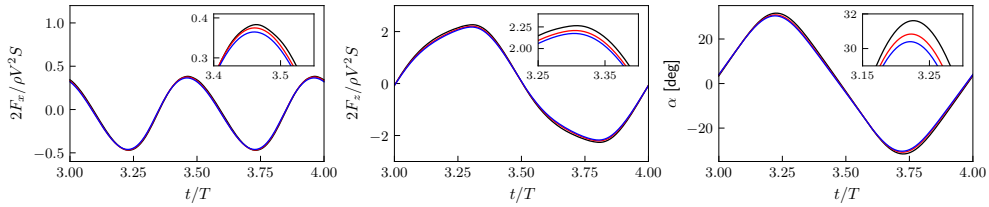

FIGURE 15: Grid sensitivity analysis on the (a) horizontal force, (b) vertical force, and (c) tip deflection angle (α), of an isolated flapper with a prescribed motion of its leading edge. Note that $S = bC$ is the planform area of the flapper. (——) $\Delta x = C/50$; (——) $\Delta x = C/80$; and (——) $\Delta x = C/120$.

Acknowledgements

This work was supported by the State Research Agency of Spain (AEI) under grant DPI2016-76151-C2-2-R including funding from the European Regional Development Fund (ERDF). The computations were partially performed at the supercomputer Caesaraugusta from the *Red Española de Supercomputación* in activity IM-2020-2-0005.

Appendix A. Grid sensitivity analysis

In order to determine the grid spacing to be employed in the simulations, a grid sensitivity study is performed. As a benchmark case, the simulation of a single flapper with an imposed vertical motion of its leading edge equal to that of the leader in eq. (1) and fixed along the horizontal direction, is considered. The properties of the flapper and of the fluid are those gathered in Table 1, and $U_\infty = 0.83V$.

Three different Δr are considered, $C/50$, $C/80$, and $C/120$. For each simulation $\Delta t f = 0.025 \Delta r/C$, ensuring $CFL = U_{\max}\Delta t/\Delta r < 0.2$ (where $U_{\max}$ is the maximum flow velocity in the domain). The grid sensitivity on the horizontal, F_x, and vertical force, F_z, is depicted in Fig. 15, as well as on the tip deflection angle, α (defined as the angle between the horizontal plane and the plane that joins the leading edge and the trailing edge (Arora *et al.* 2018)). It can be observed that the dynamics of the flapper are well captured with all employed grids. Table 2 gathers the variation with the grid spacing of the mean forces, their rms and the maximum value of the tip deflection angle over a cycle, $T = 1/f$. Note that, $F^* = 2F/\rho V^2 S$ (where $S = bc$), and $\overline{()}$ stands for the average over a cycle. Relative errors below 6% are obtained between the forces computed with $\Delta r = C/50$ and $\Delta r = C/120$; whereas this difference is reduced to 2% if the results from $\Delta r = C/80$ and $\Delta r = C/120$ are compared.

Table 3 shows, for illustration, the effect of the grid spacing on the performance of a tandem case with $H/C = 0.6$ and $\phi = 360°$. The difference in the propulsive speed from $\Delta r = C/50$ to $\Delta r = C/80$ is less than 1% and the difference in the equilibrium distance is $0.003C$, implying that the same tandem configuration is obtained for both grid spacings. The difference in the average power ($\overline{P_i^*} \equiv 2P_i/\rho V^3 S$) is below 4%,

Δr	$\overline{F_x^*}$	rms(F_x^*)	$\overline{F_z^*}$	rms(F_z^*)	$\alpha_{\max}$ [deg]
$C/50$	-0.033	0.305	1.479	1.626	31.61
$C/80$	-0.042	0.302	1.430	1.575	30.84
$C/120$	-0.044	0.296	1.401	1.544	30.38

TABLE 2: Statistics of the forces for an isolated flapper with imposed motion as a function of the grid size.

Δr	$\overline{U}_p/V$	$\overline{P_s^*}$	$\overline{D}/C$	$\overline{P_l^*}$	$\overline{P_f^*}$	Π_l	Π_f
$C/50$	0.874	0.648	3.383	0.649	0.627	1.001	0.967
$C/80$	0.879	0.624	3.386	0.625	0.603	1.001	0.966

TABLE 3: Statistics of the tandem configuration, $H/C = 0.6$, $\phi = 360°$, for different grid sizes.

however when comparing the power ratio, the difference is lower than 0.2%. Similar results are obtained for the other tandem simulations presented herein.

In view of the results from tables 2 and 3, the simulations are performed with $\Delta r = C/50$. Only for those configurations where flow visualizations and temporal histories of force and power are presented, the simulations are performed with $\Delta r = C/80$.

REFERENCES

ALBEN, S. & SHELLEY, M. 2005 Coherent locomotion as an attracting state for a free flapping body. *Proc. Natl. Acad. Sci. USA* **102** (32), 11163–11166.

ARORA, N., KANG, C.-K., SHYY, W. & GUPTA, A. 2018 Analysis of passive flexion in propelling a plunging plate using a torsion spring model. *J. Fluid Mech.* **857**, 562–604.

ARRANZ, G., FLORES, O. & GARCÍA-VILLALBA, M. 2021 A weakly coupled immersed boundary method and dynamic algorithm for the fluid-structure interaction of multi-body systems. Submitted to J. Comput. Phys.

BEAL, D. N., HOVER, F. S., TRIANTAFYLLOU, M. S., LIAO, J. C. & LAUDER, G. V. 2006 Passive propulsion in vortex wakes. *J. Fluid Mech.* **549**, 385–402.

BECKER, A. D., MASOUD, H., NEWBOLT, J. W., SHELLEY, M. & RISTROPH, L. 2015 Hydrodynamic schooling of flapping swimmers. *Nature Comm.* **6** (1), 8514.

BERMAN, G. J. & WANG, Z. J. 2007 Energy-minimizing kinematics in hovering insect flight. *J. Fluid Mech.* **582**, 153–168.

BOSCHITSCH, B., DEWEY, P. & SMITS, A. 2014 Propulsive performance of unsteady tandem hydrofoils in an in-line configuration. *Phys. Fluids* **26** (5), 051901.

BUCHHOLZ, J. & SMITS, A. 2008 The wake structure and thrust performance of a rigid low-aspect-ratio pitching panel. *J. Fluid Mech.* **603**, 331–365.

DAGHOOGHI, M. & BORAZJANI, I. 2015 The hydrodynamic advantages of synchronized swimming in a rectangular pattern. *Bioinspir. Biomim.* **10** (5), 056018.

DAI, L., HE, G., ZHANG, X. & ZHANG, X. 2018 Stable formations of self-propelled fish-like

swimmers induced by hydrodynamic interactions. *J. Royal Soc. Interface* **15** (147), 20180490.

Dong, H., Mittal, R. & Najjar, F. M. 2006 Wake topology and hydrodynamic performance of low-aspect-ratio flapping foils. *J. Fluid Mech.* **566**, 309–343.

Featherstone, R. 2014 *Rigid body dynamics algorithms*. Springer.

Felis, M. 2017 RBDL: an efficient rigid-body dynamics library using recursive algorithms. *Auton. Robot.* **41** (2), 495–511.

Gazzola, M., Chatelain, P., van Rees, W. M. & Koumoutsakos, P. 2011 Simulations of single and multiple swimmers with non-divergence free deforming geometries. *J. Comput. Phys.* **230** (19), 7093–7114.

Heathcote, S. & Gursul, I. 2007 Flexible flapping airfoil propulsion at low Reynolds numbers. *AIAA J.* **45** (5), 1066–1079.

Hoover, A. P., Cortez, R., Tytell, Eric D. & Fauci, L. J. 2018 Swimming performance, resonance and shape evolution in heaving flexible panels. *J. Fluid Mech.* **847**, 386–416.

Hua, R.-N., Zhu, L. & Lu, X.-Y. 2013 Locomotion of a flapping flexible plate. *Phys. Fluids* **25** (12), 121901.

Kurt, M., A., Eslam P. & Moored, K. W. 2020 Flow interactions between low aspect ratio hydrofoils in in-line and staggered arrangements. *Biomimetics* **5** (2).

Kurt, M. & Moored, K. 2018 Flow interactions of two- and three-dimensional networked bio-inspired control elements in an in-line arrangement. *Bioinspir. Biomim.* **13** (4), 045002.

Lentink, D., Dickson, W. B., van Leeuwen, J. L. & Dickinson, M. H. 2009 Leading-edge vortices elevate lift of autorotating plant seeds. *Science* **324** (5933), 1438–1440.

Li, G., Kolomenskiy, D., Liu, H., Thiria, B. & Godoy-Diana, R. 2019 On the energetics and stability of a minimal fish school. *Plos One* **14** (8), e0215265.

Li, L., Nagy, M., Graving, J, M., Bak-Coleman, J., Xie, G. & Couzin, I. D. 2020 Vortex phase matching as a strategy for schooling in robots and in fish. *Nature Comm.* **11**, 5408.

Liao, J. C., Beal, D. N., Lauder, G. V. & Triantafyllou, M. S. 2003 The kármán gait: novel body kinematics of rainbow trout swimming in a vortex street. *J. Exp. Biol.* **206** (6), 1059–1073.

Lin, X., Wu, J. & Zhang, T. 2019*a* Performance investigation of a self-propelled foil with combined oscillating motion in stationary fluid. *Ocean Eng.* **175**, 33–49.

Lin, X., Wu, J., Zhang, T. & Yang, L. 2019*b* Phase difference effect on collective locomotion of two tandem autopropelled flapping foils. *Phys. Rev. Fluids* **4**, 054101.

Lin, X., Wu, J., Zhang, T. & Yang, L. 2020 Self-organization of multiple self-propelling flapping foils: energy saving and increased speed. *J. Fluid Mech.* **884**, R1.

Maertens, A. P., Gao, A. & Triantafyllou, M. S. 2017 Optimal undulatory swimming for a single fish-like body and for a pair of interacting swimmers. *J. Fluid Mech.* **813**, 301–345.

Mora, T., Walczak, A. M., Del Castello, L., Ginelli, F., Melillo, S., Parisi, L., Viale, M., Cavagna, A. & Giardina, I. 2016 Local equilibrium in bird flocks. *Nature Phys.* **12** (12), 1153–1157.

Moriche, M., Flores, O. & García-Villalba, M. 2017 On the aerodynamic forces on heaving and pitching airfoils at low Reynolds number. *J. Fluid Mech.* **828**, 395–423.

Muscutt, L., Weymouth, G. & Ganapathisubramani, B 2017 Performance augmentation mechanism of in-line tandem flapping foils. *J. Fluid Mech.* **827**, 484–505.

Newbolt, J. W., Zhang, J. & Ristroph, L. 2019 Flow interactions between uncoordinated

flapping swimmers give rise to group cohesion. *Proc. Natl. Acad. Sci. USA* **116** (7), 2419–2424.

Park, S. G. & Sung, H. J. 2018 Hydrodynamics of flexible fins propelled in tandem, diagonal, triangular and diamond configurations. *J. Fluid Mech.* **840**, 154–189.

Peng, Z.-R., Huang, H. & Lu, X.-Y. 2018*a* Collective locomotion of two closely spaced self-propelled flapping plates. *J. Fluid Mech.* **849**, 1068–1095.

Peng, Z.-R., Huang, H. & Lu, X.-Y. 2018*b* Collective locomotion of two self-propelled flapping plates with different propulsive capacities. *Phys. Fluids* **30** (11), 111901.

Peng, Z.-R., Huang, H. & Lu, X.-Y. 2018*c* Hydrodynamic schooling of multiple self-propelled flapping plates. *J. Fluid Mech.* **853**, 587–600.

Platzer, M. F., Jones, K. D., Young, J. & Lai, J. C. S. 2008 Flapping wing aerodynamics: Progress and challenges. *AIAA J.* **46** (9), 2136–2149.

Portugal, S. J., Hubel, T. Y., Fritz, J., Heese, S., Trobe, D., Voelkl, B., Hailes, S., Wilson, A. M. & Usherwood, J. R. 2014 Upwash exploitation and downwash avoidance by flap phasing in ibis formation flight. *Nature* **505** (7483), 399–402.

Quinn, D. B., Lauder, G. V. & Smits, A. J. 2014 Scaling the propulsive performance of heaving flexible panels. *J. Fluid Mech.* **738**, 250–267.

Quinn, D. B., Lauder, G. V. & Smits, A. J. 2015 Maximizing the efficiency of a flexible propulsor using experimental optimization. *J. Fluid Mech.* **767**, 430–448.

Ramananarivo, S., Fang, F., Oza, A., Zhang, J. & Ristroph, L. 2016 Flow interactions lead to orderly formations of flapping wings in forward flight. *Phys. Rev. Fluids* **1**, 071201.

Ryu, J., Yang, J., Park, S. G. & Sung, H. J. 2020 Phase-mediated locomotion of two self-propelled flexible plates in a tandem arrangement. *Phys. Fluids* **32** (4), 041901.

Streitlien, K., Triantafyllou, G. S. & Triantafyllou, M. S. 1996 Efficient foil propulsion through vortex control. *AIAA J.* **34** (11), 2315–2319.

Taylor, G. K., Nudds, R. L. & Thomas, A. L. R. 2003 Flying and swimming animals cruise at a Strouhal number tuned for high power efficiency. *Nature* **425** (6959), 707–711.

Uhlmann, M. 2005 An immersed boundary method with direct forcing for the simulation of particulate flows. *J. Comput. Phys.* **209** (2), 448–476.

Vejdani, H. R., Boerma, D. B., Swartz, S. M. & Breuer, K. S. 2018 The dynamics of hovering flight in hummingbirds, insects and bats with implications for aerial robotics. *Bioinspir. Biomim.* **14** (1), 016003.

Verma, S., Novati, G. & Koumoutsakos, P. 2018 Efficient collective swimming by harnessing vortices through deep reinforcement learning. *Proc. Natl. Acad. Sci. USA* **115** (23), 5849–5854.

Weihs, D. 1973 Hydromechanics of fish schooling. *Nature* **241** (5387), 290–291.

Weimerskirch, H., Martin, J., Clerquin, Y., Alexandre, P. & Jiraskova, S. 2001 Energy saving in flight formation. *Nature* **413** (6857), 697–698.

Yeh, P. D. & Alexeev, A. 2014 Free swimming of an elastic plate plunging at low Reynolds number. *Phys. Fluids* **26** (5), 053604.

Yeh, P. D. & Alexeev, A. 2016 Effect of aspect ratio in free-swimming plunging flexible plates. *Comput. Fluids* **124**, 220–225.

Zhang, J., Liu, N.-S. & Lu, X.-Y. 2010 Locomotion of a passively flapping flat plate. *J. Fluid Mech.* **659**, 43–68.

Zhu, X., He, G. & Zhang, X. 2014 Flow-mediated interactions between two self-propelled flapping filaments in tandem configuration. *Phys. Rev. Lett.* **113**, 238105.